

# Investigation of Ground Moving Target Indication Techniques for a Multi-Channel Synthetic Aperture Radar



Prepared by:

Katlego Ernest Mosito  
MSTKAT005

Supervised by:

Dr. Mohammed Yunus Abdul Gaffar  
Department of Electrical Engineering (UCT)  
and

Dr. Josias Jacobus de Witt  
Radar and Electronic Warfare (CSIR)

A dissertation submitted to the Department of Electrical Engineering,  
University of Cape Town,  
for partial fulfilment of the degree of  
*Master of Engineering in Radar and Electronic Defence*

February 2020

The copyright of this thesis vests in the author. No quotation from it or information derived from it is to be published without full acknowledgement of the source. The thesis is to be used for private study or non-commercial research purposes only.

Published by the University of Cape Town (UCT) in terms of the non-exclusive license granted to UCT by the author.

## Declaration

1. I know that plagiarism is wrong. Plagiarism is to use another's work and pretend that it is one's own.
2. I have used the IEEE convention for citation and referencing. Each contribution to, and quotation in, this dissertation from the work(s) of other people, has been attributed and has been cited and referenced.
3. This dissertation is my own work.
4. This dissertation has been submitted to the *Turnitin* module (or equivalent similarity and originality checking software) and I confirm that my supervisor has seen my report and any concerns revealed by such have been resolved with my supervisor.
5. I have not allowed, and will not allow, anyone to copy my work with the intention of passing it off as their own work or part thereof.

Signed by candidate

Signature of Author

CSIR Pretoria  
February 2020

## EBE Faculty: Assessment of Ethics in Research Projects (Rev2)

Any person planning to undertake research in the Faculty of Engineering and the Built Environment at the University of Cape Town is required to complete this form before collecting or analysing data. When completed it should be submitted to the supervisor (where applicable) and from there to the Head of Department. If any of the questions below have been answered YES, and the applicant is NOT a fourth year student, the Head should forward this form for approval by the Faculty EIR committee: submit to Ms Zulpha Geyer ([Zulpha.Geyer@uct.ac.za](mailto:Zulpha.Geyer@uct.ac.za); Chem Eng Building, Ph 021 650 4791). NB: A copy of this signed form must be included with the thesis/dissertation/report when it is submitted for examination

*This form must only be completed once the most recent revision EBE EIR Handbook has been read.*

Name of Principal Researcher/Student: **Katlego Ernest Mosito** Department: **Electrical Engineering**

Preferred email address of the applicant: **katlegomosito@gmail.com**

If a Student: **MSTKAT005** Degree: **MEng in Radar** Supervisor: **Dr. Mohammed Yunus Abdul Gaffar**

If a Research Contract indicate source of funding/sponsorship:

Research Project Title: **Investigation of Ground Moving Target Indication (GMTI) Techniques using a Multichannel Synthetic Aperture Radar (SAR)**

### Overview of ethics issues in your research project:

Question 1: Is there a possibility that your research could cause harm to a third party (i.e. a person not involved in your project)?	YES	<input checked="" type="checkbox"/> NO
Question 2: Is your research making use of human subjects as sources of data? If your answer is YES, please complete Addendum 2.	YES	<input checked="" type="checkbox"/> NO
Question 3: Does your research involve the participation of or provision of services to communities? If your answer is YES, please complete Addendum 3.	YES	<input checked="" type="checkbox"/> NO
Question 4: If your research is sponsored, is there any potential for conflicts of interest? If your answer is YES, please complete Addendum 4.	YES	<input checked="" type="checkbox"/> NO

If you have answered YES to any of the above questions, please append a copy of your research proposal, as well as any interview schedules or questionnaires (Addendum 1) and please complete further addenda as appropriate. Ensure that you refer to the EIR Handbook to assist you in completing the documentation requirements for this form.

I hereby undertake to carry out my research in such a way that

- there is no apparent legal objection to the nature or the method of research; and
- the research will not compromise staff or students or the other responsibilities of the University;
- the stated objective will be achieved, and the findings will have a high degree of validity;
- limitations and alternative interpretations will be considered;
- the findings could be subject to peer review and publicly available; and
- I will comply with the conventions of copyright and avoid any practice that would constitute plagiarism.

Signed by:

	Full name and signature	Date
Principal Researcher/Student:	<b>Katlego Ernest Mosito</b> <div style="border: 1px solid black; padding: 2px; display: inline-block;">Signed by candidate</div>	<b>20-02-2017</b>

This application is approved by:

Supervisor (if applicable):	<i>Dr. M.Y. Abdul Gaffar</i>	<b>20-02-2017</b>
HOD (or delegated nominee): <i>Final authority for all assessments with NO to all questions and for all undergraduate research.</i>	<i>E BOSE</i>	<b>28/2/17</b>
Chair : Faculty EIR Committee For applicants other than undergraduate students who have answered YES to any of the above questions.		

## Acknowledgements

Firstly, I would like to thank the Council for Scientific and Industrial Research (CSIR) for awarding me the opportunity to pursue a master's degree and giving me all the needed support.

I would also like to extend my sincere gratitude to my supervisors Dr. Mohamed Yunus Abdul Gaffar from the University of Cape Town and Dr. Josias Jacobus de Witt from REW-DPSS at the CSIR. Your guidance and support were highly appreciated. I am also grateful to Dr. Ciara Blaauw and the SAR team for assisting me with the measurement of the practical radar data.

## Abstract

Synthetic Aperture Radar (SAR) is an imaging technique that creates two dimensional images of the scattering objects in the illuminated ground scene. The objects in the illuminated ground scene may be truly stationary, e.g. buildings etc. or in motion relative to these stationary objects, e.g. cars on a highway. In SAR, the radar platform is moving during the imaging period, hence everything that the radar illuminates has motion relative to the radar platform. In order to specifically detect objects on the ground that are moving relative to stationary ground objects (often termed clutter), processing techniques called Ground Moving Target Indication (GMTI) techniques are required. This is especially required for targets that are moving at relative velocities lower than the stationary clutter's relative velocity to the radar platform (endo-clutter detection). This dissertation investigates five multichannel GMTI techniques being Displaced Phase Centre Antenna (DPCA), Along Track Interferometry (ATI), Iterative Adaptive Approach (IAA), Space Time Adaptive Processing (STAP) and Velocity SAR (VSAR) in literature and assesses the performance of two selected GMTI techniques (ATI and DPCA) on simulated and measured radar data to compare them and identify their strengths and weaknesses. The radar data were measured with a C-band FMCW radar in a controlled environment with known parameters and cooperating targets.

The performances of the techniques were assessed in terms of moving target detection within clutter and sensitivity to inaccuracies in the physical system setup. The DPCA technique exhibited some attractive characteristics over the ATI technique. These included its robustness against false alarm in noise dominated cells - ATI exhibited large phase residuals in noise dominated cells, due to the random nature of the phase in these cells. Furthermore, DPCA seem to not suffer from false alarms due to volumetric scattering of vegetation to the extent that was observed with ATI. Lastly, DPCA exhibited more robustness against temporal misalignment errors introduced between the measurement channels, compared to ATI.

These observations lead to the conclusion that DPCA would be a practically better choice to implement for the purpose of moving target detection, compared to ATI. However, a double threshold approach, which used DPCA as a pre-processing step to ATI, proved to be superior to DPCA alone in terms of moving target indication within clutter and noise. This approach was verified through implementation on the measured radar data in this study.

# Contents

<b>1</b>	<b>Introduction</b>	<b>1</b>
1.1	Background . . . . .	1
1.1.1	Synthetic Aperture Radar . . . . .	1
1.1.2	Inverse Synthetic Aperture Radar . . . . .	3
1.1.3	Ground Moving Target Indication . . . . .	4
1.2	Objectives . . . . .	7
1.3	Methodology . . . . .	7
1.4	Limitations . . . . .	8
1.5	Layout of the study . . . . .	8
<b>2</b>	<b>Literature Review</b>	<b>11</b>
2.1	Introduction . . . . .	11
2.2	GMTI using Displaced Phase Center Antenna . . . . .	11
2.3	GMTI using Along-Track Interferometry . . . . .	18
2.4	GMTI using Space Time Adaptive Processing . . . . .	21
2.5	GMTI using Iterative Adaptive Approach . . . . .	25
2.6	GMTI using Velocity SAR . . . . .	27
2.7	Conclusion . . . . .	29
<b>3</b>	<b>Methodology</b>	<b>31</b>
<b>4</b>	<b>GMTI Technique Evaluation Criterion</b>	<b>33</b>
4.1	Introduction . . . . .	33
4.2	Moving Target Indication within Clutter . . . . .	33
4.3	Sensitivity to Practical Implementation Non-idealities . . . . .	34
4.4	Conclusion . . . . .	34
<b>5</b>	<b>Radar Simulations and Experiment Setup</b>	<b>36</b>
5.1	Introduction . . . . .	36
5.2	Radar Data Simulations . . . . .	36
5.3	Experiment Setup Description . . . . .	41

5.4	Conclusion . . . . .	45
<b>6</b>	<b>Pre-processing of the Measured Radar Data for GMTI</b>	<b>46</b>
6.1	Introduction . . . . .	46
6.2	The Imaged Scene . . . . .	46
6.3	Data Pre-processing . . . . .	48
6.3.1	Channel Co-registration . . . . .	48
6.3.2	Channel Balancing . . . . .	51
6.4	Conclusion . . . . .	56
<b>7</b>	<b>Performance Comparison of GMTI Techniques with Simulated Data</b>	<b>57</b>
7.1	Introduction . . . . .	57
7.2	GMTI using DPCA Technique on Simulated Data . . . . .	57
7.2.1	Processing Overview . . . . .	57
7.2.2	DPCA Detection of Moving Targets within Clutter . . . . .	59
7.2.2.1	Scenario 1 Pulse No. 12000: Target moving west, parallel and opposite direction to the radar . . . . .	60
7.2.2.2	Scenario 1 Pulse No. 24200: Target moving west, parallel and opposite direction to the radar . . . . .	62
7.2.2.3	Scenario 2 Pulse No. 2048: Target moving east, pa- rallel and same direction as the radar . . . . .	65
7.2.2.4	Scenario 2 Pulse No. 18000: Target moving east, pa- rallel and same direction as the radar . . . . .	67
7.2.2.5	Results Summary . . . . .	69
7.2.3	Sensitivity Analysis for DPCA . . . . .	72
7.3	GMTI using ATI Technique on Simulated Data . . . . .	74
7.3.1	Processing Overview . . . . .	74
7.3.2	ATI Detection of Moving Targets within Clutter . . . . .	75
7.3.2.1	Scenario 1 Pulse No. 12000: Target moving west, parallel and opposite direction to the radar . . . . .	75
7.3.2.2	Scenario 1 Pulse No. 24200: Target moving west, parallel and opposite direction to the radar . . . . .	77
7.3.2.3	Scenario 2 Pulse No. 2048: Target moving east, pa- rallel and same direction as the radar . . . . .	79
7.3.2.4	Scenario 2 Pulse No. 18000: Target moving east, pa- rallel and same direction as the radar . . . . .	81
7.3.2.5	Results Summary . . . . .	82
7.3.3	Sensitivity Analysis for ATI . . . . .	83
7.4	Comparison of DPCA and ATI Performance . . . . .	84

7.5	Conclusion . . . . .	90
<b>8</b>	<b>Performance Comparison of GMTI Techniques with Measured Radar Data</b>	<b>92</b>
8.1	Introduction . . . . .	92
8.2	GMTI using DPCA Technique on Measured Radar Data . . . . .	92
8.2.1	Processing Overview . . . . .	92
8.2.2	DPCA Detection of Moving Targets within Clutter . . . . .	93
8.2.2.1	Scenario 1 Pulse No. 12000: Target moving west, parallel and opposite direction to the radar . . . . .	93
8.2.2.2	Scenario 1 Pulse No. 24200: Target moving west, parallel and opposite direction to the radar . . . . .	97
8.2.2.3	Scenario 2 Pulse No. 2048: Target moving east, parallel and same direction as the radar . . . . .	100
8.2.2.4	Scenario 2 Pulse No. 18000: Target moving east, parallel and same direction as the radar . . . . .	104
8.2.2.5	Results Summary . . . . .	106
8.2.3	Sensitivity Analysis of DPCA Technique . . . . .	108
8.3	GMTI using ATI Technique on Measured Radar Data . . . . .	112
8.3.1	Processing Overview . . . . .	113
8.3.2	ATI Detection of Moving Targets within Clutter . . . . .	113
8.3.2.1	Scenario 1 Pulse No. 12000: Target moving west, parallel and opposite direction to the radar . . . . .	114
8.3.2.2	Scenario 1 Pulse No. 24200: Target moving west, parallel and opposite direction to the radar . . . . .	116
8.3.2.3	Scenario 2 Pulse No. 2048: Target moving east, parallel and same direction as the radar . . . . .	117
8.3.2.4	Scenario 2 Pulse No. 18000: Target moving east, parallel and same direction as the radar . . . . .	119
8.3.2.5	Results Summary . . . . .	121
8.3.3	Sensitivity Analysis of ATI Technique . . . . .	122
8.4	Comparison of DPCA and ATI Performance on Measured Data . . . . .	124
8.5	GMTI using DPCA and ATI Techniques Combined . . . . .	127
8.5.1	Scenario 1 Pulse No. 12000: Target moving west, parallel and opposite direction to the radar . . . . .	128
8.5.2	Scenario 1 Pulse No. 24200: Target moving west, parallel and opposite direction to the radar . . . . .	129

8.5.3	Scenario 2 Pulse No. 2048: Target moving east, parallel and same direction as the radar . . . . .	131
8.5.4	Scenario 2 Pulse No. 18000: Target moving east, parallel and same direction as the radar . . . . .	133
8.6	Conclusion . . . . .	134
<b>9</b>	<b>Conclusion</b>	<b>135</b>
	<b>References</b>	<b>137</b>

# List of Figures

1.1	SAR system setup [6]. . . . .	2
1.2	SAR stripmap setup showing cross-range and ground range [6]. . . . .	2
1.3	ISAR system setup [6]. . . . .	4
1.4	SAR GMTI system setup [7]. . . . .	5
1.5	Battlefield surveillance using a SAR GMTI system [8]. . . . .	6
2.1	3 channel system setup with standard data collection mode [11]. . . . .	12
2.2	2 channel system setup with double baseline data collection mode [11]. . . . .	13
2.3	3 channel system setup with ping pong data collection mode [11]. . . . .	13
2.4	Steps followed in applying DPCA for GMTI [10]. . . . .	14
2.5	Steps followed in applying ATI for GMTI [10] . . . . .	19
2.6	STAP data cube . . . . .	22
2.7	Fourier Transform of the data cube showing the clutter ridge [21]. . . . .	23
2.8	VSAR configuration [31]. . . . .	27
2.9	VSAR processor block diagram [31]. . . . .	28
3.1	Flowchart showing the methodology of the study. . . . .	32
5.1	Simulated scene with a stationary scatterer and a moving target. . . . .	37
5.2	Expected radial velocity change of targets at all simulated pulse instances. (1) Pulse no.2048 and (2) Pulse no.18000 for east moving target, (3) Pulse no.12000 and (4) Pulse no.24200 for target moving west, (5) Pulse no.12000 and (6) Pulse no.22000 for target moving orthogonal towards radar. . . . .	40
5.3	Expected range and radial velocity change of targets over the simulation period. (1) and (2) for target moving east, (3) and (4) for target moving west, (5) and (6) for target moving orthogonal towards the radar . . . . .	41
5.4	The image of the radar and the moving platform from the back. . . . .	43
5.5	Top view map of the experiment setup for real data measurement. . . . .	44
6.1	View of the experimental setup scene where radar data were measured. . . . .	47
6.2	A labelled range-Doppler map of the imaged scene. . . . .	47

6.3	Channel 1 range-Doppler map. . . . .	49
6.4	Channel 2 range-Doppler map. . . . .	49
6.5	Channel 1 and Channel 2 before channel balancing. . . . .	50
6.6	Flowchart of the adaptive 2D-Calibration technique. . . . .	53
6.7	Channel 1 and Channel 2 after channel balancing. . . . .	54
6.8	Range-Doppler map of channel 1 after channel balancing. . . . .	54
6.9	Range-Doppler map of channel 2 after channel balancing. . . . .	55
7.1	Steps followed in applying DPCA. . . . .	58
7.2	Simulated scene with a stationary scatterer and a moving target (copy of Figure 5.1). . . . .	59
7.3	(b) Expected range and (a) Expected radial velocity of target moving west at pulse number 12000. . . . .	60
7.4	Range-Doppler map of target moving west at pulse number 12000. . .	61
7.5	PDFs for target moving west from pulse 12000. (a) Clutter plus Noise PDF and Target plus Noise PDF before DPCA, (b) Clutter plus Noise PDF and Target plus Noise PDF after DPCA. . . . .	62
7.6	(b) Expected range and (a) Expected radial velocity at pulse number 24200 for target moving west. . . . .	63
7.7	Range-Doppler map of target moving west at pulse number 24200. . .	63
7.8	The PDFs for target moving west from pulse 24200. (a) Clutter plus Noise PDF and Target plus Noise PDF before DPCA, (b) Clutter plus Noise PDF and Target plus Noise PDF after DPCA. . . . .	64
7.9	(b) Expected range and (a) Expected radial velocity at pulse number 2048 for target moving east (target 1). . . . .	65
7.10	Range-Doppler map of target moving east at pulse number 2048. . . .	66
7.11	The PDFs for target moving east from pulse 2048. (a) Clutter plus Noise PDF and Target plus Noise PDF before DPCA, (b) Clutter plus Noise PDF and Target plus Noise PDF after DPCA. . . . .	67
7.12	(b) Expected range and (a) Expected radial velocity at pulse number 18000 for target moving east (target 1). . . . .	68
7.13	Range-Doppler map of target moving east at pulse number 18000. . .	68
7.14	The PDFs for target moving east from pulse 18000. (a) Clutter plus Noise PDF and Target plus Noise PDF before DPCA, (b) Clutter plus Noise PDF and Target plus Noise PDF after DPCA. . . . .	69
7.15	DPCA response against target radial velocity ( $V_{rP0}$ ) for a west moving target (target 2). . . . .	71

7.16	DPCA response against target radial velocity ( $V_{r_{P0}}$ ) for an east moving target (target 1). . . . .	72
7.17	Residual clutter plotted against pulse shift number. . . . .	73
7.18	Flowchart followed in the application of the ATI technique. . . . .	74
7.19	Interferogram of a target moving west (target 2) at pulse number 12000. . . . .	76
7.20	Phase PDF of clutter plus noise and phase PDF of target plus noise, for a target moving west (target 2) at pulse number 12000 after applying ATI. . . . .	77
7.21	Interferogram of a target moving west (target 2) at pulse number 24200. . . . .	78
7.22	Phase PDF of clutter plus noise and phase PDF of target plus noise, for a target moving west (target 2) at pulse number 24200 after applying ATI. . . . .	78
7.23	Interferogram of a target moving east (target 1) at pulse number 2048. . . . .	79
7.24	Phase PDF of clutter plus noise and phase PDF of target plus noise, for a target moving east (target 1) at pulse number 2048 after applying ATI. . . . .	80
7.25	Interferogram of a target moving east (target 1) at pulse number 18000. . . . .	81
7.26	Phase PDF of clutter plus noise and Phase PDF of target plus noise, for a target moving east (target 1) at pulse number 18000 after applying ATI. . . . .	82
7.27	Residual clutter phase against pulse shift number for co-registration. . . . .	84
7.28	Overlaid power PDFs of target and clutter at pulse 12000 after DPCA. . . . .	85
7.29	Overlaid phase PDFs of target and clutter at pulse 12000 after ATI. . . . .	86
7.30	Overlaid power PDFs of target and clutter at pulse 24200 after DPCA. . . . .	87
7.31	Overlaid phase PDFs of target and clutter at pulse 24200 after ATI. . . . .	88
7.32	(a) Target and clutter phase PDFs without co-registration errors, (b) Target and clutter phase PDFs with co-registration errors, (c) Target and clutter power PDFs without co-registration errors, (d) Target and clutter power PDFs with co-registration errors. . . . .	89
7.33	Probability of false alarm against probability of detection (ROC curves) for ATI and DPCA technique. . . . .	90
8.1	DPCA processing applied on measured radar data (copy of Figure 7.1). . . . .	93
8.2	(b) Calculated range and (a) calculated radial velocity, for a target moving west at pulse number 12000. . . . .	94
8.3	Range-Doppler map of a target moving west (target 2) before DPCA processing at pulse 12000. . . . .	95

8.4	Range-Doppler map of a target moving west (target 2) after DPCA processing at pulse 12000. . . . .	95
8.5	Range-Doppler map of a detected target after applying DPCA and a threshold. . . . .	96
8.6	(b) Expected range and (a) Expected radial velocity at pulse number 24200, for target moving west. . . . .	97
8.7	Range-Doppler map of a target moving west (target 2) before DPCA processing at pulse 24200. . . . .	98
8.8	Range-Doppler map of a target moving west (target 2) after DPCA processing at pulse 24200. . . . .	98
8.9	Range-Doppler map of a detected target after applying DPCA and a threshold at pulse number 24200. . . . .	99
8.10	Top view map of the experiment setup for real data measurement (copy of Figure 5.5). . . . .	100
8.11	(b) Calculated range and (a) calculated radial velocity at pulse number 2048, for target moving east (target 1). . . . .	101
8.12	Range-Doppler map of a target moving east (target 1) before DPCA processing at pulse 2048. . . . .	102
8.13	Range-Doppler map of a target moving east (target 1) after DPCA processing at pulse 2048. . . . .	102
8.14	Range-Doppler map of a detected target after applying DPCA and a threshold at pulse number 2048. . . . .	103
8.15	(b) Expected range and (a) Expected radial velocity at pulse number 18000, for target moving east (target 1). . . . .	104
8.16	Range-Doppler map of a target moving east (target 1) before DPCA processing at pulse 18000. . . . .	105
8.17	Range-Doppler map of a target moving east (target 1) after DPCA processing at pulse 18000. . . . .	106
8.18	Moving target DPCA response. . . . .	108
8.19	Mean clutter power before and after DPCA for data with target moving east along target path 1 . . . . .	109
8.20	Mean clutter power before and after DPCA for data with target moving west along target path 2 . . . . .	110
8.21	Range-Doppler map after DPCA processing with co-registration errors on data with a target moving west (target 2). . . . .	112
8.22	Flowchart of the ATI technique (copy of Figure 7.18). . . . .	113
8.23	Interferogram of a target moving west processed from pulse number 12000. . . . .	114

8.24	Phase image of a target moving west processed from pulse number 12000 with a phase threshold. . . . .	115
8.25	Interferogram of a target moving west processed from pulse number 24200. . . . .	116
8.26	Interferogram of a target moving west processed from pulse number 24200 with a phase threshold. . . . .	117
8.27	Interferogram of a target moving east processed from pulse number 2048.	118
8.28	Phase image of a target moving east processed from pulse number 2048 with a phase threshold. . . . .	119
8.29	Interferogram of a target moving east processed from pulse number 18000. . . . .	120
8.30	Interferogram of a target moving east with a phase threshold. . . . .	120
8.31	Residual clutter phase after applying the ATI technique. . . . .	123
8.32	Interferogram after applying ATI technique on channel miss-aligned data. . . . .	123
8.33	Phase image of a target moving west with a phase threshold. . . . .	128
8.34	Phase image of a target moving west after applying double threshold.	129
8.35	Phase image of a target moving west with a phase threshold. . . . .	130
8.36	Interferogram of a target moving west after double thresholding. . . .	130
8.37	Phase image of a target moving east with a phase threshold. . . . .	131
8.38	Interferogram of a target moving east after double thresholding. . . .	132
8.39	Interferogram of a target moving east with a phase threshold. . . . .	133
8.40	Interferogram of a target moving east after double thresholding. . . .	133

# List of Tables

6.1	Summary of the performance of the adaptive 2D-calibration technique.	56
7.1	Summary of DPCA SCR improvement results. . . . .	70
7.2	Summary of the clutter phase cancellation performance of the ATI technique. . . . .	83
8.1	Summary of DPCA SCR improvement results obtained from measured data. . . . .	107
8.2	Summary of the ATI technique clutter cancellation extent achieved on measured radar data. . . . .	121

# List of Symbols

$a$	-	Amplitude of the return signal
$a_r$	-	Radial acceleration
$\alpha$	-	Vector with unknown amplitude and phase
$\mathbf{A}$	-	Steering matrix
$B$	-	Bandwidth
$\mathbf{B}$	-	Antenna baseline
$c$	-	Speed of light
$d$	-	Spacing between the channels
$\delta$	-	Grazing angle
$\Delta CR$	-	Cross-range resolution
$D_t$	-	Physical length of antenna
$\mathbf{e}$	-	Vector containing interference plus noise
$\epsilon$	-	Convergence threshold
$f_d$	-	Doppler frequency
$F$	-	Noise Figure
$G$	-	Antenna gain
$k$	-	Boltzman's constant
$L_s$	-	Swath length
$\lambda$	-	Wavelength
$n_p$	-	Number of pulses
$\varphi$	-	Phase of the return signal
$\mathbf{P}$	-	Power matrix
$P_d$	-	Probability of detection
$P_{fa}$	-	Probability of false alarm
$P_t$	-	Transmitted power

$R_{slant}$	-	Slant range to middle of swath
$\Delta R$	-	Range resolution
$\sigma$	-	Clutter intensity
$\theta_{int}$	-	Integration angle
$\theta_{tgt}$	-	Target phase
$\Delta t$	-	Change in time
$T$	-	Threshold
$T_k$	-	Standard temperature (Kelvin)
$T_{CPI}$	-	Coherent processing time
$T_\theta$	-	Phase threshold
$V_{blind}$	-	Blind velocity
$V_p$	-	Platform velocity
$V_r$	-	Radial velocity
$V_{r_{unamb}}$	-	Unambiguous target radial velocity
$V_{r_{P0}}$	-	Radial velocity of target with zero platform velocity
$V_t$	-	Target velocity
$\mathbf{y}$	-	Measured data vector
$z$	-	SAR image
$z_{DPCA}$	-	Power after DPCA

# List of Abbreviations

ATI	-	Along Track Interferometry
AWGN	-	Additive White Gaussian Noise
CNR	-	Clutter-to-Noise Ratio
CSIR	-	Council for Scientific and Industrial Research
DoA	-	Direction of Arrival
DPCA	-	Displaced Phase Center Antenna
FMCW	-	Frequency Modulated Continuous Waves
GMTI	-	Ground Moving Target Indication
IAA	-	Iterative Adaptive Approach
ISAR	-	Inverse Synthetic Aperture Radar
MDV	-	Minimum Detectable Velocity
MIMO	-	Multiple Input Multiple Output
MTI	-	Moving Target Indication
NULA	-	Non-uniform Linear Antenna Array
PDF	-	Probability Density Function
PRF	-	Pulse Repetition Frequency
PRI	-	Pulse Repetition Interval
RADAR	-	Radio Detection And Ranging
RCS	-	Radar Cross Section
ROC	-	Receiver Operating Characteristics
SAR	-	Synthetic Aperture Radar
SCR	-	Signal-to-Clutter Ratio
SIMO	-	Single-Input Multiple-Output
SINR	-	Signal-to-Interference-plus-Noise Ratio
STAP	-	Space Time Adaptive Processing
UAV	-	Unmanned Aerial Vehicle
VSAR	-	Velocity Synthetic Aperture Radar

# Chapter 1

## Introduction

### 1.1 Background

A radar is a system that works by transmitting radiofrequency (RF) electromagnetic waves towards an object which has the ability to reflect the waves [1]. The reflected or scattered electromagnetic waves are then used to determine the presence of the scattering object (target) and its range relative to the radar receiver [1]. The unique ability of electromagnetic waves to penetrate through various materials and to not be affected by weather conditions and light intensity made the radar system the best invented tool for detection of military ships and aircraft during World War II [1]. The discovery of the Doppler shift of electromagnetic waves by Christian Doppler allowed the development of a radar system to estimate the relative velocity of moving targets [2].

A radar system can be designed to be a continuous wave radar which transmits unmodulated continuous signals or Frequency Modulated Continuous Waves (FMCW) [3]. A radar can also be designed to be a pulsed radar which transmits pulse modulated signals or intra-pulse modulated signals [3]. A radar system can be used as a search radar, imaging radar, navigational radar, weather radar or tracking radar [3]. Each pulsed radar type has a unique Pulse Repetition Frequency (PRF), antenna aperture size, bandwidth, rotation speed, antenna type and beamwidth to enable it to efficiently and effectively execute its set task [4].

#### 1.1.1 Synthetic Aperture Radar

Radar systems have advanced substantially from only target detection and ranging, as performed during World War II, to now also include the ability to perform target imaging. There are two main techniques employed by imaging radars, namely Synthetic Aperture Radar (SAR) and the Inverse Synthetic Aperture Radar (ISAR).

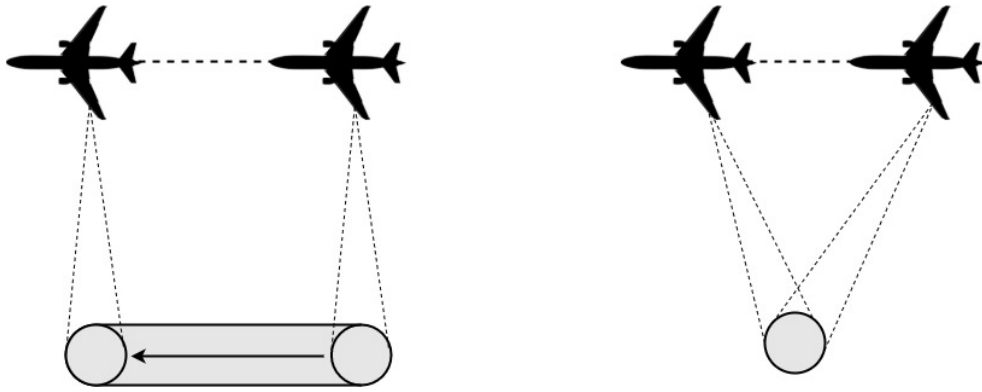


Figure 1.1: SAR system setup [6].

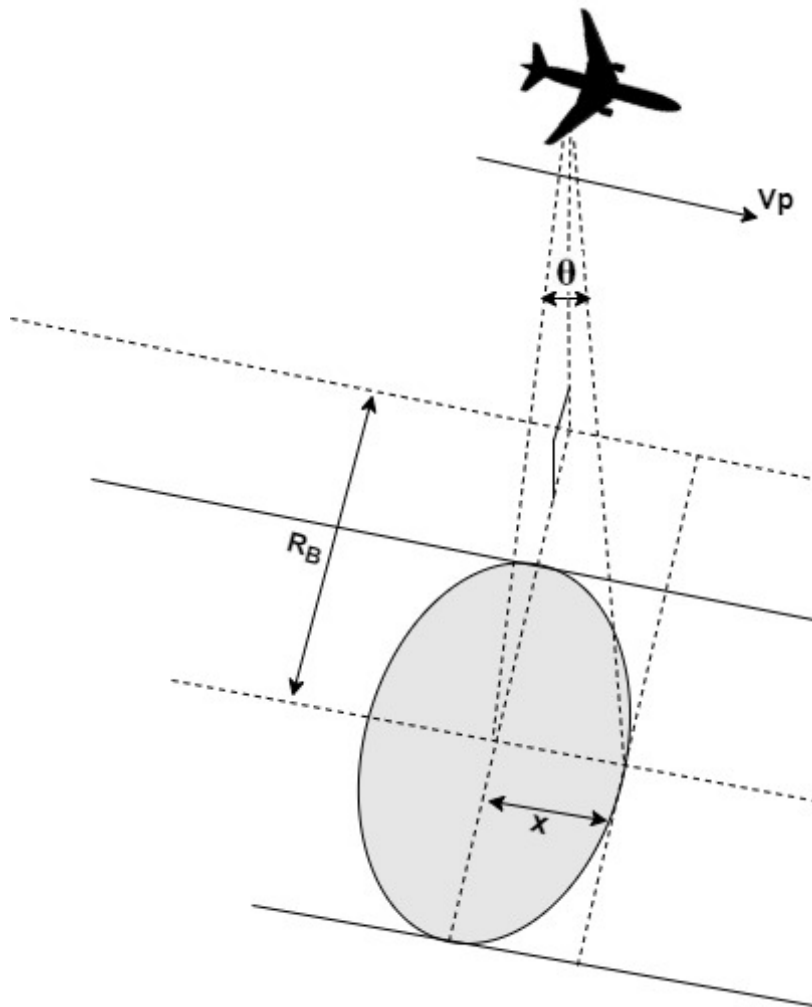


Figure 1.2: SAR stripmap setup showing cross-range and ground range [6].

SAR is a technique that uses the movement of the radar system mounted on a platform to synthesize a large antenna aperture for imaging a stationary area on the ground, typically with fine cross-range resolution and slant-range resolution [5]. The SAR system setup is presented in Figure 1.1. SAR can operate either in stripmap mode as shown in the left image or spotlight mode as depicted on the right image of Figure 1.1 [6]. Figure 1.2 presents the SAR stripmap setup with the defined flight path and flight velocity ( $V_p$ ), cross-range ( $x$ ), ground range ( $R_B$ ) and an antenna beamwidth ( $\theta$ ).

Research and development into SAR technology was started by Carl Wiley in the 1950s and it still continues today [5]. This imaging technique creates two dimensional images called SAR images. A SAR image is a map of the scattering intensity of objects in the illuminated image scene [2]. The achieved cross-range resolution is a result of processing many pulses that are recorded at different spatial positions such that they synthesize a large virtual antenna aperture. Cross-range resolution ( $\Delta CR$ ) is given by Equation (1.1) [5]

$$\Delta CR = \frac{\lambda R_{slant}}{2D_{SAR}} \quad (1.1)$$

where:

- $R_{slant}$  - slant range to middle of swath.
- $D_{SAR}$  - effective aperture size resulting from the spatial displacement over which the pulses were integrated to form the SAR image.

The slant-range resolution ( $\Delta R$ ) is a function of the transmit signal's bandwidth as shown in Equation (1.2) [5]

$$\Delta R = \frac{c}{2B} \quad (1.2)$$

The scene illuminated by the SAR system scatters (reflects) energy back to the radar and the energy is recorded and processed to a two-dimensional (typically intensity) image consisting of the cross-range dimension and the slant-range dimension [2]. The SAR imaging technique is used, amongst others, for landscape imaging, crop monitoring, urban area mapping and classifications and Moving Target Indication (MTI).

### 1.1.2 Inverse Synthetic Aperture Radar

ISAR is a two-dimensional high resolution imaging radar technique that uses the movement of a target to create an image [4]. The radar system remains nominally stationary, the motion of the illuminated target and the resultant Doppler changes of

its scattering centers are used to form an image of that illuminated target [4]. Figure 1.3 shows the ISAR setup observing a ship moving across the ocean. The motion of the ship and its Doppler histories were used to image the ship [6]. ISAR is used for detection, identification and recognition of targets such as ships, military aircrafts and missiles [5].

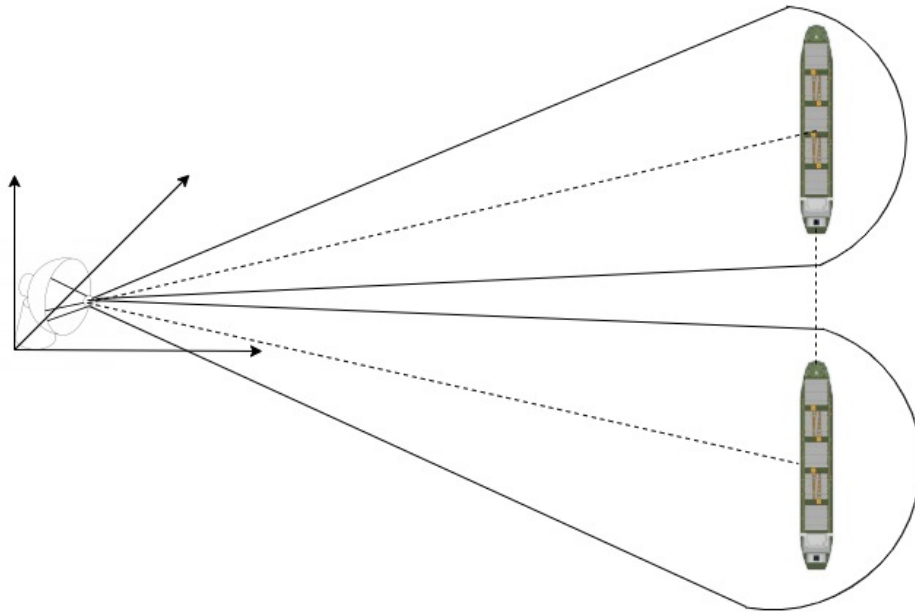


Figure 1.3: ISAR system setup [6].

### 1.1.3 Ground Moving Target Indication

Moving Target Indication (MTI) is a technique used to detect scattering objects which are in motion and estimate their radial velocity with respect to the radar system. The scattering objects that are in motion are called moving targets while any other stationary scattering object results in undesired return signals (clutter) since they are not of interest to MTI [2]. A MTI technique employed from an airborne platform such as a satellite or an aircraft can be used to detect scattering objects that are moving on the ground resulting in a technique called Ground Moving Target Indication (GMTI).

A SAR system can employ a GMTI technique, however, in SAR the radar platform is moving hence everything that the radar illuminates has motion relative to the radar platform. This makes it difficult for traditional MTI techniques to separate moving objects from stationary objects. The aim of SAR GMTI is to detect

targets that are moving on the ground with a certain radial velocity due to the radar platform motion and target ground motion and importantly, detect the targets that are moving at a radial velocity lower than the clutter's maximum radial velocity (termed endo-clutter detection). The SAR GMTI system setup is shown in Figure 1.4 [7].

Figure 1.4 shows the radar baseline  $\mathbf{B}$  between the antenna  $A_0$  and  $A_1$  as the platform travels with a velocity  $V_p$ .  $V_r$  is the moving object radial velocity detected by the radar at the initial position  $[x_0, y_0, h]$  on the ground.  $\Delta t$  is the amount of time it takes the platform to travel the set antenna baseline. The radar system is mounted on a moving platform and it is imaging the ground consisting of moving and stationary objects [7].

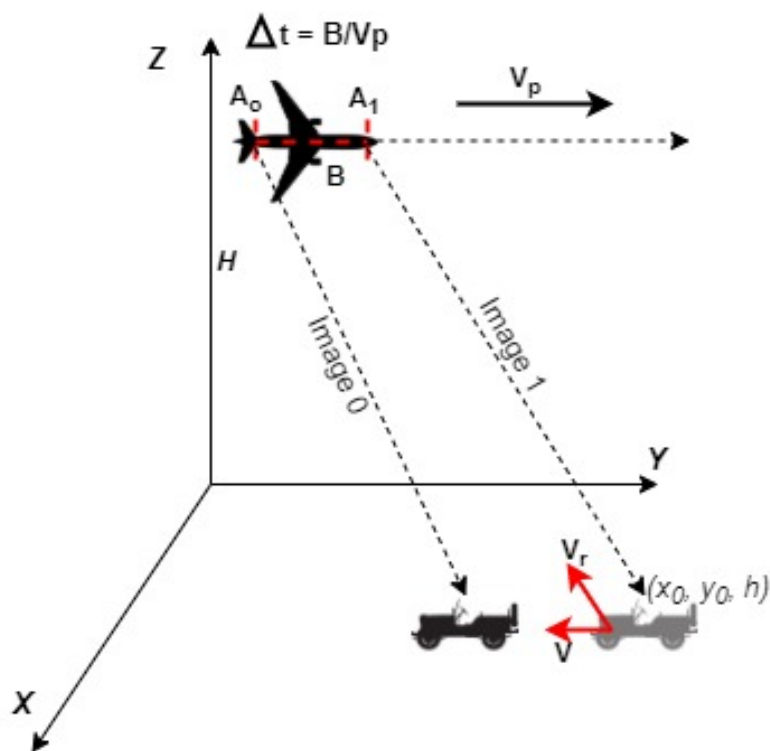


Figure 1.4: SAR GMTI system setup [7].

SAR GMTI is mainly developed for surveillance of a ground patch of interest. The surveyed area can be a battlefield, an enemy military camping base or a game reserve for animal movement monitoring [8]. SAR GMTI significantly improves the accuracy of fighter jet bombing technology as it can be observed on Figure 1.5 [8]. The figure shows an Unmanned Aerial Vehicle (UAV) equipped with SAR GMTI technology which relays the information to a central point for evaluation and then the information is sent to a fighter jet which then can accurately eliminate enemy ground moving

objects on the battle field [8].

In GMTI, ground clutter could mask the desired signal returns from ground moving targets hence making it difficult to detect the targets and distinguish them. This occurs when the radial velocity of the target detected by the radar is lower than the radial velocity of the ground patch that the radar illuminates, i.e, the moving target and the ground clutter occupy the same Doppler space by exhibiting the same relative velocity, at that particular point in time.

There have been several techniques investigated and employed for clutter suppression in GMTI. These techniques include Space Time Adaptive Processing (STAP), Displaced Phase Center Antenna (DPCA), Non-uniform Linear Antenna Array (NULA), Along Track Interferometry (ATI), Iterative Adaptive Approach (IAA) and many other methods [9]. These GMTI methods are outlined in detail in the following chapter.

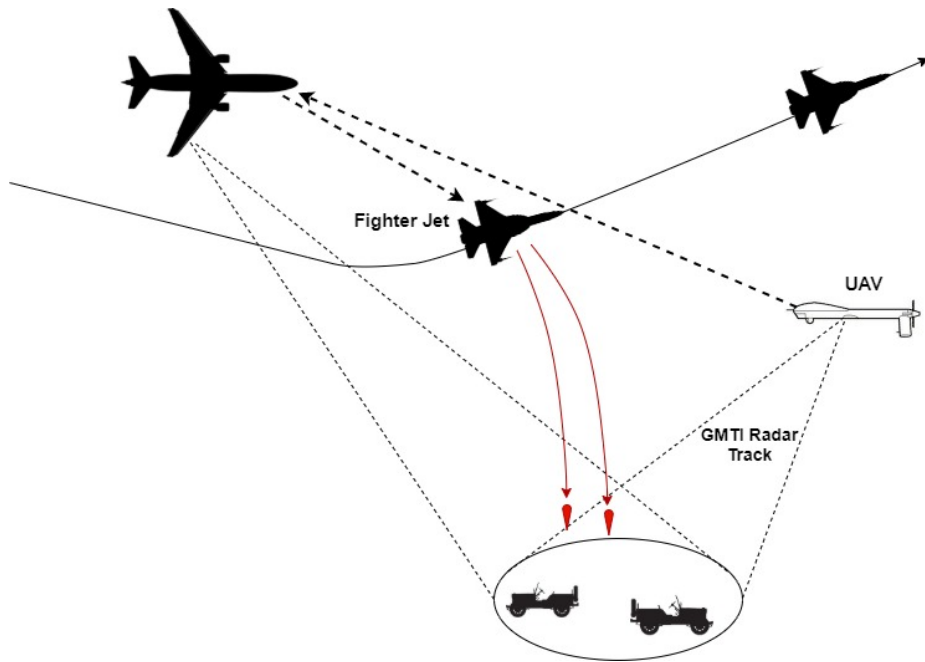


Figure 1.5: Battlefield surveillance using a SAR GMTI system [8].

SAR GMTI techniques are implemented with specific antenna channel configurations. The configurations can be implemented using a multi-pass single channel SAR system or multi-channel single-pass SAR system. In a multi-pass single channel SAR system two passes are required to form two SAR images of the same ground patch since the radar consist of only one channel. In this SAR system a steady and identical flight path is required to maintain the channel baseline. This study, however, investigates

the Multi-channel single-pass SAR GMTI techniques.

A multi-channel system consist of two or more channels on the radar platform maintaining a constant baseline through the flight path. Since the channels are on the same platform only a single pass is required to form multiple SAR images of the same ground patch. The multiple channels transmit and receive signals and allows for coherent integration and processing. A multi-channel system also increases the degree of freedom of the SAR GMTI system.

## 1.2 Objectives

The objectives of this study are to:

- assess and verify the performance of two GMTI techniques on simulated radar data and on measured radar data.
- identify and compare the strengths and weaknesses of the two GMTI techniques on simulated radar data and on measured radar data and indicate a practically better performing technique between the two.

## 1.3 Methodology

In this study, multichannel SAR GMTI techniques are implemented and tested with simulated radar data and measured radar data. The performance of the implemented GMTI techniques (both simulated and practically measured) are compared to the theoretical expected results and agreement is shown.

The simulated raw radar data were generated using a radar simulator environment developed by the Council for Scientific and Industrial Research (CSIR). This simulator, however, only provides the raw data samples and thus all subsequent signal processing is done from first principles, as part of the contribution of this study.

Real radar data were measured using a CSIR developed C-band radar system, in a controlled environment on the CSIR campus in Pretoria. The radar parameters, geometry and target movement characteristics were kept identical (to the best of the author's ability) between the simulated and real radar experiments, as to allow one to one comparison between the results.

The simulated raw radar data and the measured radar data were processed into

range-Doppler images which were then used to investigate the performance of the GMTI techniques. A GMTI technique with superior performance characteristics, specifically in terms of moving target indication within clutter and its sensitivity to practical implementation non-idealities was identified.

## **1.4 Limitations**

This study is limited to the investigation of five SAR GMTI techniques together with their system setup and specifications in literature. Two of the five SAR GMTI techniques were selected based on the system setup they require for data collection and the implementation complexity of their algorithm on simulated data and measured radar data. The two selected techniques were investigated using simulated radar data and real radar data measured in a controlled environment. The controlled experiment had limitations in terms of geometries which include the maximum height and speed of the radar platform, the length of the radar platform rail as well as the clear area that the radar can illuminate. The simulated scene was chosen to reflect the same geometries that were used for practical radar data measurement. The radar system used for real data measurements in a controlled experiment is a two receiver system which set limits on the number of receive channels that the experiment can use. The simulated data were generated using a radar simulator developed by the CSIR. The simulations were limited to simple clutter modelling for testing together with additive white Gaussian noise (AWGN).

## **1.5 Layout of the study**

This study is organized as follows:

### **Chapter 2: Literature Review**

In this chapter, five GMTI techniques are reviewed in-depth. These techniques are: DPCA, ATI, STAP algorithm, IAA algorithm and Velocity SAR (VSAR) for GMTI. Each technique is briefly introduced and then its mode of operation as well as its system setup is discussed in detail. The governing equations of each technique are outlined. The performances and the limitations of the techniques are also outlined.

### **Chapter 3: Methodology**

The methodology followed in this study is outlined in this chapter. The methodology states how the study developed and the criterion of how the two techniques that were tested with simulated data and measured radar data were chosen. This chapter also provides an overview of the performance characteristics that were investigated and how the performance was assessed. The simulated data used for testing the techniques are also briefly introduced.

#### **Chapter 4: GMTI Technique Evaluation Criterion**

In this chapter the assessment criterion for the performance of the GMTI techniques are presented. The criterion includes the GMTI characteristics such as the ability of the techniques to indicate a moving target within clutter and the co-registration sensitivity requirements for GMTI. The criterion is then used to assess the performance of the GMTI techniques on simulated data and on measured radar data.

#### **Chapter 5: Radar Simulations and Experiment Setup**

This chapter presents the details of the data that is simulated. The simulated scene that is illuminated by the radar is presented together with the direction of motion of the radar platform. The experimental setup for radar data measurements in a controlled environment is also outlined. The parameters of the simulated data and experimental setup are presented in detail and the abilities of the radar simulator are presented.

#### **Chapter 6: Pre-processing of the Measured Radar Data for GMTI**

This chapter presents the recorded radar data of the controlled GMTI experiment that was conducted. The data results are processed to range-Doppler map level. Co-registration and channel calibration technique used to prepare the recorded data for GMTI techniques are presented in detail. The results of co-registration and channel balancing/calibration are then presented.

#### **Chapter 7: Performance Comparison of GMTI Techniques with Simulated Data**

The results of the two techniques that were chosen for testing with simulated data are outlined in this chapter. The ability of each technique to indicate the presence of moving targets within clutter is presented. The performance of the two techniques

on data with co-registration errors is also presented. The performance of the two techniques with simulated data is then assessed side-by-side.

## **Chapter 8: Performance Comparison of GMTI Techniques with Measured Radar Data**

The performance of two GMTI techniques being DPCA and ATI are assessed with real radar data in this chapter. The data were measured in a controlled environment with co-operating moving targets placed on the scene. The GMTI techniques are assessed in-terms of their ability to indicate moving targets within clutter and their sensitivity to channel misalignment or co-registration errors. The performance of the GMTI techniques on measured radar data is also compared to the performance of the techniques on simulated data. A combination of the DPCA and the ATI technique called the double threshold approach is also briefly discussed and analysed with measured radar data in this chapter. The methodology of how to correctly apply the GMTI techniques on measured radar data is outlined in this chapter and the subsequent results are evaluated.

## **Chapter 9: Conclusion**

A summary of how the investigation developed and how the GMTI techniques were assessed is given. The performance of the two GMTI techniques on the simulated data and real radar data is briefly discussed and the performance characteristics of the identified GMTI technique are discussed.

# Chapter 2

## Literature Review

### 2.1 Introduction

In this chapter five multi-channel SAR GMTI techniques were discussed in detail with emphasis into the design specifications and operation parameters of each system. The performance of each technique was also assessed together with the advantages and disadvantages of the technique. The constraints and limitations of each technique were addressed with the goal to determine the SAR GMTI techniques to implement and test with simulated data and measured SAR data.

### 2.2 GMTI using Displaced Phase Center Antenna

The main challenge with GMTI is suppressing or filtering the radar returns from the ground and other stationary scatterers in order to isolate the moving scatterers. These signal returns are termed clutter [10]. One of the earliest and simplest methods used for clutter filtering in GMTI is DPCA [10]. DPCA is a non-adaptive, two-dimensional filtering method that is used in multi-channel side-looking SAR to suppress the clutter and enhance moving target returns [11]. The main principle of DPCA is to compare radar data collected from the same point in space at different times [10]. This method requires two or more receive channels for it to be implemented.

Data from the same point in space at different times is obtained by timing the position of the second receive channel on a given pulse to electronically align with the 1st channel on the next pulse. This requires precise pulse-to-pulse timing control and sets restrictions on the Pulse Repetition Interval (PRI) [11]. The data can be collected in three modes being;

- the standard mode,
- double baseline mode and
- the ping-pong mode [11].

The standard mode requires that only one antenna transmits and receives while the other antennas just receive energy. Figure 2.1 presents the standard data collection mode with channel 1 transmitting and receiving indicated with the double-headed red arrows (mono-static) and channel 2 and 3 receiving only indicated with red arrows pointing up. For standard mode, the receiving antenna 2 has to travel half the baseline for every PRI to align with the position of channel 1 [11].

The double baseline mode works in such a way that the two antennas take turns in transmitting and receiving from PRI-to-PRI. This means while the first antenna transmits the second antenna receives in that PRI then the second antenna transmits while the first antenna receives in the next PRI. Figure 2.2 presents the double baseline mode with the red arrows pointing down indicating the transmitting channel and red arrows pointing up indicating the receiving channel.

Ping pong mode employs mono-static antennas where each channel transmits and receives its own pulses [11]. For ping pong mode, the channels travel the full baseline for them to image the same point in space at different times. The diagram presented on Figure 2.3 shows a three channel DPCA system setup and concept with a ping-pong data collection mode.

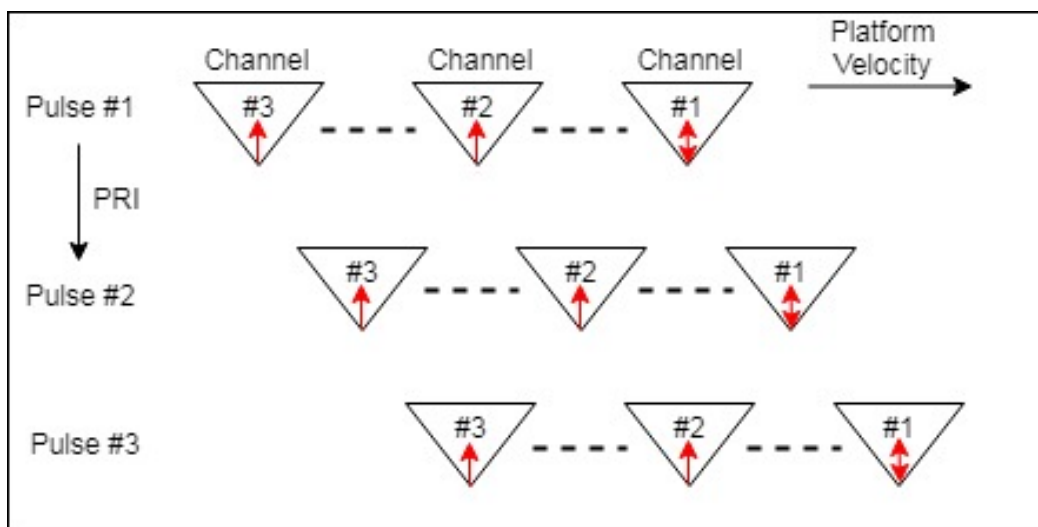


Figure 2.1: 3 channel system setup with standard data collection mode [11].

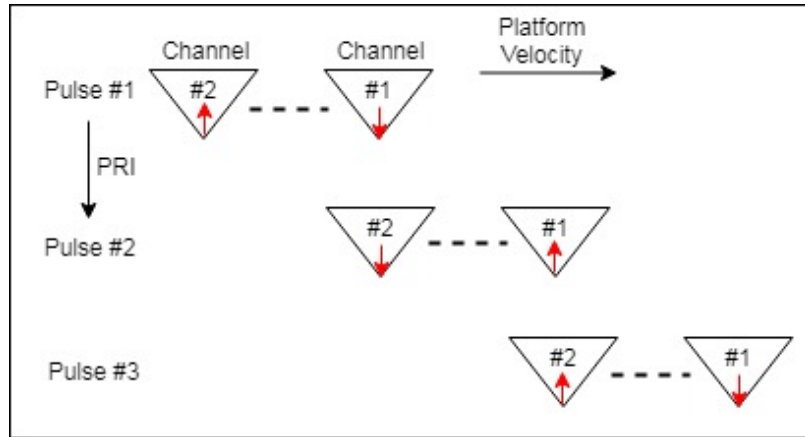


Figure 2.2: 2 channel system setup with double baseline data collection mode [11].

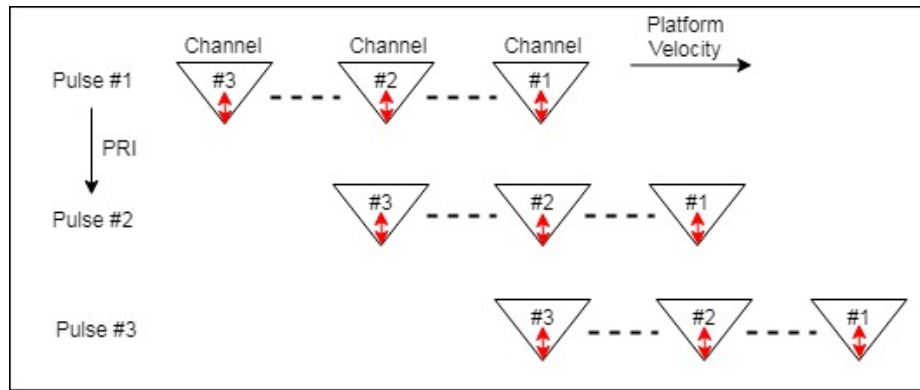


Figure 2.3: 3 channel system setup with ping pong data collection mode [11].

Figure 2.3 shows that as the three channel platform moves in the indicated direction from pulse-to-pulse, the radar channels align in space. As observed in pulse #2, channel 2 was aligned with channel 1 from the first transmitted pulse (Pulse #1) and channel number 2 on the first pulse was aligned with channel number 3 of the second pulse. This aligned channels collect data from the same point in space at different times hence allowing any changes that happen from pulse-to-pulse to be detected.

Once echo returns are received, typical SAR imaging algorithms such as chirp scaling and range-Doppler algorithms are used to focus them into images [12]. The SAR images obtained from each receive channel are then channel balanced and co-registered in order to make sure that the pixels of the images are aligned and the motion due to the radar platform is arrested [12]. This will ensure that all stationary objects within the imaged scene are aligned in all SAR images that were created with data from the same point in space (images from radar channels that are aligned). This

will allow the two images from two aligned channels to be subtracted from each other and hence cancel out the clutter present in both of them while leaving the moving targets in the image since they will be changing position from pulse-to-pulse unlike stationary ground clutter [10]. Figure 2.4 outlines the steps followed in applying the DPCA method for clutter suppression.

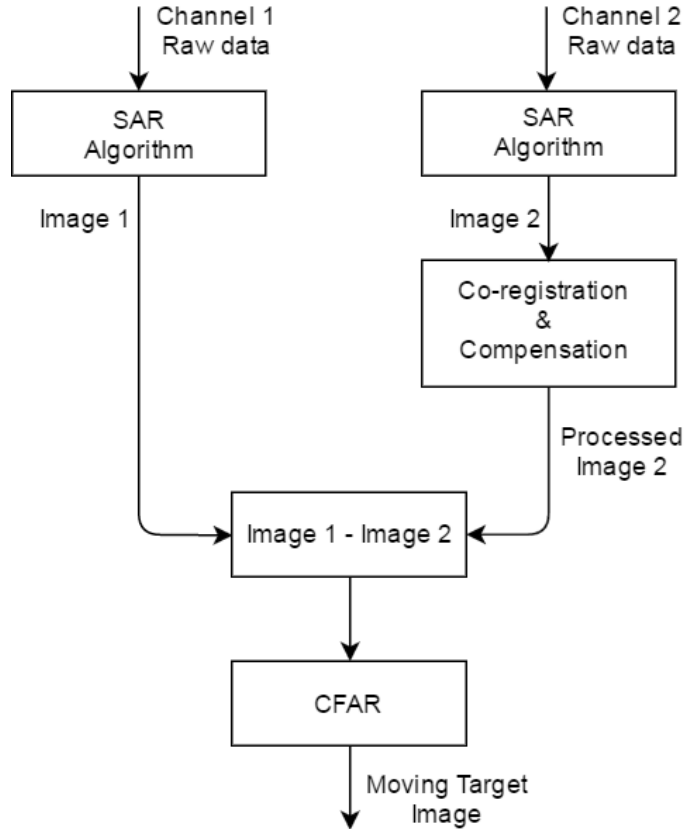


Figure 2.4: Steps followed in applying DPCA for GMTI [10].

The moving target response in the SAR image created from each radar channel can be represented by Equation (2.1) and Equation (2.3) below for channel 1 and channel 2 respectively [12]. The target has a radial velocity  $V_r$  over a PRI time span until it is imaged by channel 2. The PRI is given by the time it takes for channel 2 to align with channel 1 in space which depends on the platform velocity ( $V_p$ ) and the distance between the channels ( $d$ ). Hence, the signals received by channel 2 has an additional phase value induced by the target's change in range as given by Equation (2.3).

$$z_1 = ae^{j\varphi} \quad (2.1)$$

$$z_2 = ae^{j\left(\varphi + \frac{2\pi PRI V_r}{\lambda}\right)} \quad (2.2)$$

$$z_2 = ae^{[j(\varphi + \frac{2\pi dV_r}{\lambda V_p})]} \quad (2.3)$$

Where:

- $a$  - amplitude of the return signal.
- $\varphi$  - phase of the return signal.
- $d$  - spacing between the channels.
- $\lambda$  - wavelength.
- $V_p$  - platform velocity.
- $V_r$  - target radial velocity.

After subtracting the two SAR images represented by  $z_1$  and  $z_2$ , the DPCA results obtained can be represented by Equation (2.4) [12].

$$z_{DPCA} = |z_1 - z_2| = \left| a \sin \left( \frac{\pi d V_r}{\lambda V_p} \right) \right| \quad (2.4)$$

DPCA filtering is typically followed by a detection method applying Constant False Alarm Rate (CFAR) thresholding algorithm on the magnitude values of the DPCA results. CFAR processing allows the maximum tolerated probability of false alarm ( $P_{fa}$ ) to be set and hence provide a target threshold ( $T$ ) that will be used to indicate the presence of the target given that it exceeds the set threshold [12]. This is assuming that the clutter is Gaussian distributed and correlated from pulse to pulse. Equation (2.5) below is used to calculate the target threshold given the probability of false alarm ( $P_{fa}$ ) and the average clutter intensity after DPCA around the target ( $\sigma$ ) [12].

$$T = \sqrt{\frac{-4}{\pi} \sigma^2 \ln(P_{fa})} = k\sigma \quad (2.5)$$

A moving target will be detected if its magnitude exceeds the determined threshold ( $T$ ), that is,

$$\left| a \sin \left( \frac{\pi d V_t}{\lambda V_p} \right) \right| > k\sigma \quad (2.6)$$

The magnitude of the moving target in the SAR image ( $z_{DPCA}$ ) depends on the target's original amplitude ( $a$ ) and the target's radial velocity ( $V_r$ ) according to Equation (2.4), therefore the higher the radial velocity of a target the higher its intensity and

the easier it is to be detected [12]. Rearranging Equation (2.6), the SCR is obtained as  $a/\sigma$ , hence for a moving target to be detected

$$SCR = \frac{a}{\sigma} > \frac{k}{|\sin(\pi dV_r)/(\lambda V_p)|}. \quad (2.7)$$

DPCA filtering method requires precise hardware matching of all receive channels and precise pulse-to-pulse timing control in order to suppress clutter sufficiently [11]. The pulse-to-pulse timing control is achieved by satisfying Equation (2.8) which presents the relationship between the system PRI, the platform velocity ( $V_p$ ) and the spacing between the system channels ( $d$ ). Equation (2.8) means with each PRI, the platform must travel the distance of the antenna channel spacing in order to collect data from the same point in space, this data collection mode is called "ping-pong" [11]. For standard data collection mode, the antennas must travel half the baseline to image the same point in space at different times.

$$PRI = \frac{d}{V_p} \quad (2.8)$$

This means careful considerations should be taken in setting the channel spacing and the velocity of the platform to achieve the required PRI. However, due to platform velocity perturbations, the PRI will have to be varied in real time to accommodate the platform velocity changes given the fixed antenna spacing.

The chosen PRI given the antenna spacing and the platform velocity limits the maximum radial velocity of ground moving targets that can be detected correctly by the DPCA technique [13]. This is due to the blind velocity that is associated with the chosen PRI given by Equation (2.9) [13]. Targets that are moving at a radial velocity greater than the blind velocity will be detected with a wrong radial velocity due to velocity ambiguity.

$$V_{blind} = \frac{\lambda}{2PRI} \quad (2.9)$$

There are also other pulse timing constraints that must be satisfied due to the radars specific operation. For example, on a strip-map SAR mode, eclipsing and range ambiguities play an important role in choosing the optimum PRI [14]. Eclipsing is a situation whereby a strip-map SAR is receiving swath data from one pulse while busy transmitting another pulse [14]. This will result in a loss of data since during transmission of one pulse the receiving chain of the radar is switched off. Range

ambiguity is when the SAR system receives main-beam signals from current pulse while also still receiving swath data from the previous pulse [14]. This will result in ambiguity in range. Both these conditions are due to the chosen PRI of the SAR system. The PRI must be chosen such that all the desired signal returns from a swath length are received from the current pulse before the swath data from the next pulse starts. Hence, the chosen PRI must satisfy the constraints given in Equation (2.10) and Equation (2.11) to avoid eclipsing and range ambiguity [14].

$$PRI \geq \frac{2L_s \cos \delta}{c} \quad (2.10)$$

$$PRI < \frac{D_l}{2V_p} \quad (2.11)$$

Where:

- $L_s$  - swath length.
- $\delta$  - grazing angle.
- $d$  - spacing between the channels.
- $D_l$  - physical length of antenna.
- $V_p$  - platform velocity.

These constraints related to the PRI and hence the PRF places rigid restrictions on the design parameters for data collected for DPCA GMTI technique. DPCA requires coherent difference of measurements at the same point in space at different times and this requires a strict relationship between the PRI, the antenna spacing, the platform velocity and the side-looking SAR collection geometry [11]. This is one of the disadvantages of DPCA as compared to Non-Uniform Linear Antenna (NULA) technique. Another disadvantage is the required precise hardware matching of the receiving channels [11]. The receiving channels are sensitive to mismatches and this can result in significant residual clutter which will make the DPCA method prone to false alarms and hence reduce its sensitivity to slow moving targets [10].

DPCA is the simplest and computationally efficient technique to use for clutter suppression in SAR GMTI. DPCA avoids the complications of having relative motion of the ground clutter due to the motion of the radar platform. DPCA clutter cancellation method acts as a notch filter with maximum suppression at zero velocity when viewed in terms of the target velocity [11]. In [15], the DPCA algorithm is used for SAR GMTI. However the velocity of the ground moving target is not estimated by this technique [15].

DPCA is an ideal method to use when dealing with systems limited in size and

complexity since it requires at least two antenna channels to be employed. The efficiency and effectiveness of DPCA in clutter suppression can also be improved by combining it with other GMTI clutter suppressing methods such as ATI and others [10].

## 2.3 GMTI using Along-Track Interferometry

ATI is a multi-channel SAR technique that was traditionally implemented for sea surface observations to measure the currents on the ocean surface and to investigate wave behaviour [16]. In this application the velocity of the ocean surface currents are measured by detecting the difference in phase of the return signals received by two or more channels from the same ocean surface patch [17]. The Doppler frequency shift that is caused by the motion of the ocean surface produces the difference in phase which is then used to determine the velocity of the ocean waves and surface [17].

Hence, similar to DPCA, ATI requires two or more receive channels in order to be implemented. The ability of ATI to detect small ocean current velocities lead the technique to also be adapted for GMTI.

The processing chain of ATI is similar to that of DPCA as shown in Figure 2.5. The antenna channels are required to be placed along-track the motion of the SAR platform. The antenna channels spacing as well as the radar PRI should be designed such that the channels align from pulse to pulse as the SAR platform moves forward. This will allow the aligned channels to measure data from the same point in space but at different times [10].

The main difference between the processing chain of ATI compared to DPCA, is that instead of subtracting the two complex SAR images after co-registration, an interferogram is formed by multiplying one image with the complex conjugate of the other [18]. This results in the residual phase of zero for stationary targets in the imaged scene and non-zero phase for moving targets which is related to their radial velocities [18]. The ability of the ATI technique to indicate the presence of moving targets within clutter depends on the SCR of the data. A low SCR will result in the phase of the moving target being contaminated and corrupted by the phase of clutter and the target phase being undistinguishable [19]. This corrupt target phase will also give incorrect radial velocity of the moving target [10]. This signifies that the ATI technique is clutter limited.

The ATI technique, just like the DPCA technique, has three modes in which it can collect data for GMTI [19]. The three modes are the "ping-pong" mode, "standard" mode and "double baseline" mode, as discussed in Section 2.2.

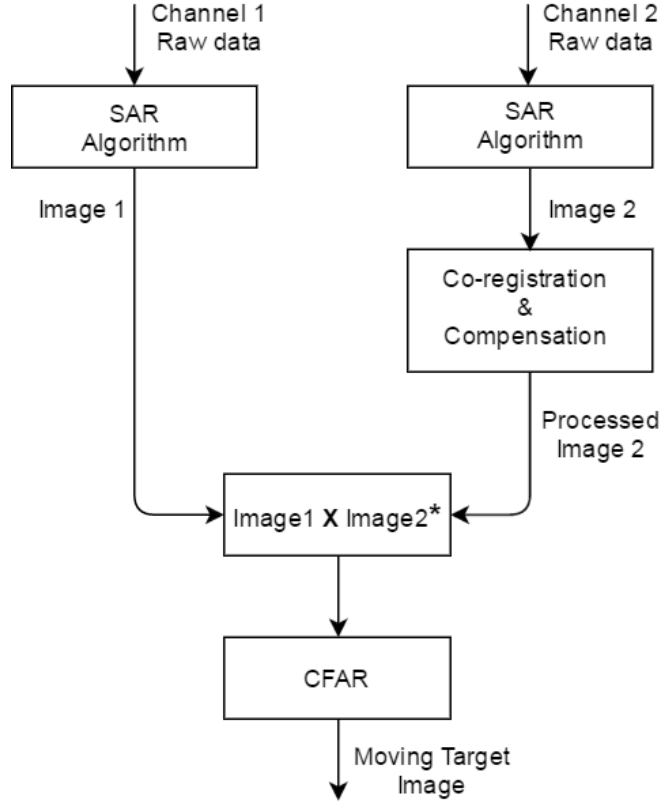


Figure 2.5: Steps followed in applying ATI for GMTI [10]

Each of the three ATI data collection modes are governed by a set of equations to make sure that the data collected is from the same point in space at a different time. The data collection mode that was chosen to be simulated in this study is the standard data collection mode. This mode uses two receive only channels and one transmit channel which allowed for generation of simulated radar data that is similar to the practically measured radar data.

The standard data collection mode requires that the SAR antenna spacing (baseline) and the velocity of the platform be selected according to Equation (2.12) such that the same ground patch is imaged by at least two different channels at a different time determined by the system PRI. The moving target at that ground patch will have a Doppler frequency in both the channels. The Doppler frequency of the target ( $f_d$ ) as well as the time difference (PRI) between the formation of the two images

creates an interferometric phase or phase difference ( $\theta_{tgt}$ ) between the two channels given by Equation (2.13) [19].

$$PRI = \frac{d}{2V_p} \quad (2.12)$$

$$\theta_{tgt} = 2\pi f_d PRI \quad (2.13)$$

Substituting the Doppler frequency formula ( $f_d = \frac{2V_r}{\lambda}$ ) and the PRI formula given by Equation (2.12) into Equation (2.13) produces Equation (2.14) below which represents the interferometric phase in terms of platform velocity ( $V_p$ ), target radial velocity ( $V_r$ ), channel separation baseline ( $d$ ) and transmitted wavelength ( $\lambda$ ).

$$\theta_{tgt} = \frac{2\pi V_r d}{\lambda V_p} \quad (2.14)$$

Rearranging Equation (2.14), one can obtain the target radial velocity from the obtained phase difference using the platform velocity and the channel separation distance as given by Equation (2.15).

$$V_r = \frac{\theta_{tgt} \lambda V_p}{2\pi d} \quad (2.15)$$

Doppler frequency ambiguities exist because of the phase folding every  $2\pi$ , hence the maximum unambiguous phase difference is given by  $\theta_{tgt_{unamb}} = 2\pi$ . Substituting this maximum unambiguous phase into Equation (2.15) results in the maximum unambiguous target radial velocity that the ATI GMTI technique can detect given by Equation (2.16) [19]. A target moving at a radial velocity greater than that presented in Equation (2.16) will be detected ambiguously.

$$V_{r_{unamb}} = \frac{\lambda V_p}{d} \quad (2.16)$$

The minimum target velocity that can be detected by the standard ATI data collection mode is determined by setting a phase threshold,  $T_\theta$ . The phase threshold is determined by the required probability of false alarm ( $P_{fa}$ ) from the probability density function of the recorded phase [19]. The MDV of a ground moving target is then calculated using Equation (2.17). On the formed phase image (interferogram)

after applying the ATI technique, any phase that is below the set phase threshold is forced to zero and anything above that is declared as a ground moving target.

$$MDV = \frac{\lambda V_p T_\theta}{2\pi d} \quad (2.17)$$

ATI technique for GMTI is mainly based on the phase created by the target and the clutter. The phase is unaffected by the amplitude of the clutter [10]. This makes ATI a powerful technique in suppressing strong and heterogeneous clutter such as that produced by buildings in urban areas and mountainous terrains. ATI is also computationally efficient and simple to implement similar to DPCA [10]. The ATI detection provides direct measurement of the target radial velocity from the target phase given that the target phase is not entirely corrupted by clutter phase and that the phase is measured unambiguously. This radial velocity measurement can assist in resolving the ambiguity between target azimuth angle and radial velocity in the Doppler coordinate equation for geo-location [10].

The clutter suppression effectiveness of this technique deteriorates when operating in conditions where clutter decorrelates from pulse to pulse [16]. This phase inconsistency is usually associated with volumetric scattering, e.g. from vegetation. The inter-relationship between the MDV, the channel separation distances and the PRI affects the extent of target velocities that can be detected by this technique. However the fact that this technique is simple to implement, physically and mathematically, and does not require assumptions or prior knowledge about the clutter conditions makes it attractive.

## 2.4 GMTI using Space Time Adaptive Processing

Space Time Adaptive Processing (STAP) is a well-known clutter suppressing technique that optimizes SINR. It is a two dimensional adaptive clutter filtering technique that uses spatial samples from the elements of an antenna array and the temporal samples from the multiple pulses of a coherent processing interval [21]. The first optimum STAP filtering technique was described by Brennan and Reed in 1973 as presented in [22].

The ground clutter returns of a moving SAR platform fall within a ridge in the angle-Doppler domain due to the coupling of the angular position of a stationary scatterer with Doppler frequency [5]. STAP aims at suppressing clutter and any other interference (e.g jamming) at the specific angle and Doppler frequency where it

is present (the ridge for clutter) and increase the gain at the angle and Doppler frequency where the target is [21]. This will then increase the SINR and hence maximize the probability of target detection.

STAP uses a multi-channel array of transmitting and receiving elements that are arranged along the direction of motion of the SAR platform to measure the spatial characteristics [5]. The time in STAP is measured and distinguished in two ways, the fast time and the slow time [5]. Fast time is the round trip time the electromagnetic wave signal makes to and from a target and the slow time is the time between transmission of pulses (repetition interval of pulses or PRI) [5]. STAP processes a cube of data consisting of the three mentioned dimensions, the spatial, slow time and fast time dimensions. Figure 2.6 depicts a basic data cube processed by STAP.

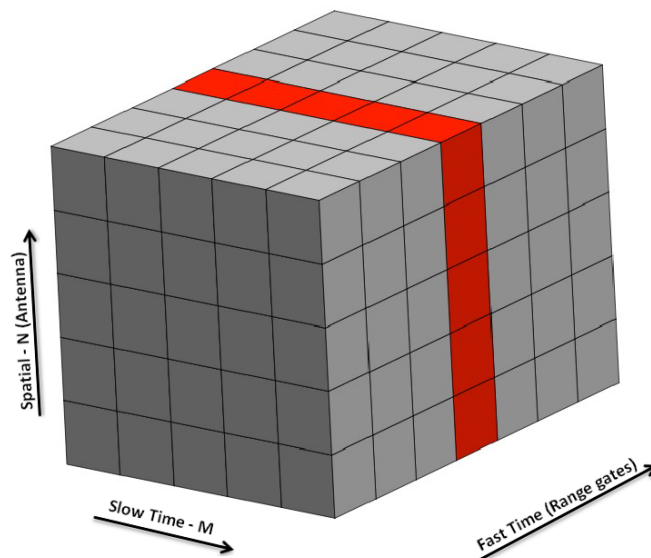


Figure 2.6: STAP data cube

The blocks along the slow time dimension of the data cube represents the pulses transmitted ( $M$  dimension), hence in this data cube 5 pulses were transmitted. The blocks in the spatial dimension represent the number of array antennas that are transmitting and receiving signals ( $N$  dimension), in this case there are five antennas in the array. The blocks in the fast time represent the range gates available in each transmitted pulse, in this case there are seven range gates in each pulse. The red blocks on the fast time along each transmitted pulse indicates a stationary target detected in range gate number four by all five antennas. The Fourier Transform of the spatial samples provides the angle dimension, the Fourier Transform of the slow time samples provides the Doppler dimension, while the fast time samples provides

the range dimension [5].

Figure 2.7 shows an illustration of the information obtained by taking the Fourier Transform of the data cube presented in Figure 2.6 [21]. The coupling of the angular position of clutter with Doppler frequency is shown in Figure 2.7 by the diagonal clutter line across the angle and Doppler domain. Possible presence of jamming across all frequencies along a constant angular position is also illustrated in the Figure [21]. A moving target detected with negative Doppler frequency is also depicted in Figure 2.7 within all the interference present [21]. STAP technique is applied in such situations to unmask the detected target from all the interference shown in Figure 2.7.

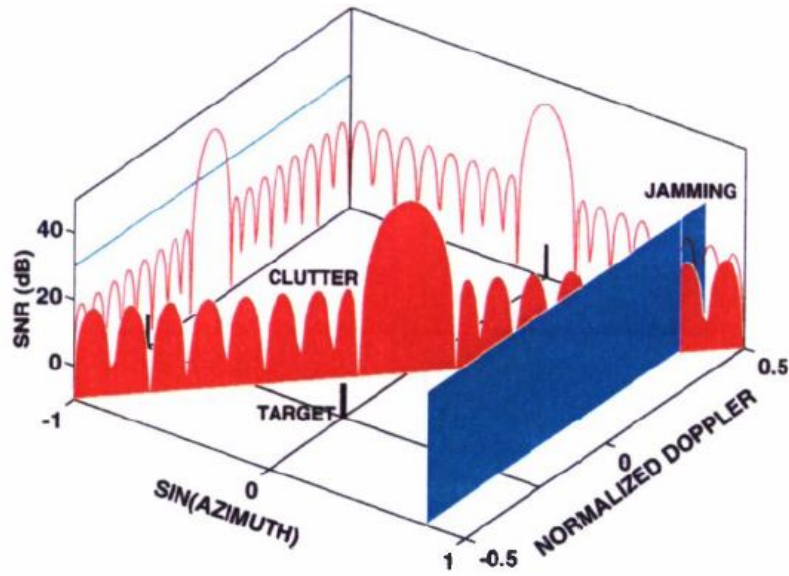


Figure 2.7: Fourier Transform of the data cube showing the clutter ridge [21].

STAP endeavours to form a null at the interference angle and Doppler response region to suppress that interference [21]. A null in a specific angle is formed by combining the spatial samples from all the receiving antennas to form a beam with a null at the angles with interference (clutter and jamming interference). The temporal samples from the pulses in slow time are combined to form a Doppler filter with a null at the frequency with interference [21]. This null formation is calculated using a STAP algorithm.

A STAP algorithm consist of three major components namely; the training strategy, weight computation and weight application [21]. A weight vector,  $\mathbf{w}$ , consists of  $\mathbf{M}$  number of pulses from each  $\mathbf{N}$  number of antenna elements for each Coherent Processing Interval (CPI), hence it is an  $\mathbf{M} \times \mathbf{N}$  vector [21]. A STAP algorithm

works on adaptively computing and optimising the weight vector  $\mathbf{w}$  from the training data and applying it to the CPI data of interest.

The training strategy of the STAP algorithm consist of a set of training rules. The main aim of the training strategy is to calculate the best estimate of clutter interference that is present at a certain range gate of interest within a CPI. The training rules are applied on the CPI data from the  $\mathbf{M}$  pulses of the  $\mathbf{N}$  elements to produce new data called the training data [21]. The interference-plus-noise covariance matrix is then estimated from the training data and then the weight vector  $\mathbf{w}$  is calculated. The training strategy uses data from several neighbouring range gates to estimate the interference that is present at the range gate of interest. The number of range gates used for the estimation must be enough to provide a sufficiently accurate estimate of interference [21]. This dependence in the number of range gates available in each CPI means the training strategy is affected by the chosen system PRI and the instantaneous bandwidth [21]. The training data computed by the training rules from the CPI data changes with the non-stationarity of the interference, hence for each change in the training data, a new weight vector is calculated [21].

The interference-plus-noise covariance matrix is not known during real time operation, and has to be estimated from the training data [23]. Therefore the training data should not contain the signal of interest since it will be mistaken for interference and be nulled by the weighting vector together with the real interference [23]. To avoid this, enough guard gates around the range gate of interest must be specified together with enough range gates for interference estimation. Clutter in most cases is not homogeneous, therefore taking many range gates for the estimation of the interference matrix might give poor results. The non-stationarity or the heterogeneity of clutter makes it impossible to be suppressed entirely from an imaged scene [23]. STAP works well with stationary or homogeneous clutter and unfortunately clutter is not always homogeneous.

The abrupt changes in the clutter characteristics within each CPI results in a new training data set which requires re-computation of the weighting vector and hence a new estimate of the covariance interference matrix [22]. This is computationally intense when working with radar systems taking large samples or snapshots of areas of interest. Reducing the dimensions of the adaptive weight vector ( $\mathbf{M} \times \mathbf{N}$ ) will reduce the computation intensity of STAP but at the cost of limiting available range gates for the estimation of the covariance interference matrix, resulting in suboptimal interference suppression [23].

## 2.5 GMTI using Iterative Adaptive Approach

Iterative Adaptive Approach (IAA) is a technique that was originally developed for source localizations [24]. Source localization involves estimating the location and signal power spectrum of sources in an observed field [24]. In array processing IAA is used for the estimation of the direction of arrival (DoA) of waveforms [24]. Recently IAA has been applied in radar imaging and missing data estimation [25]. IAA is a non-parametric iterative method that is based on a weighted least squares approach for spectral estimation [26]. The adaptation of IAA to radar imaging requires a multi-channel imaging radar.

The echoes from an observed ground swath received by the multi-channels are used to estimate the amplitude and phase of the scattering objects in that snapshot with high resolution and low sidelobes in both the cross-range and range dimension [27]. This then results in a clear separation of the clutter ridge and the slow ground moving targets outside the clutter ridge [27]. The IAA algorithm assumes that the echo signals from the ground is arranged in a data vector described by Equation (2.18) [26].

$$\mathbf{y} = \mathbf{A}\boldsymbol{\alpha} + \mathbf{e} \quad (2.18)$$

Where:

- $\mathbf{y}$  - measured data vector.
- $\mathbf{A}$  - steering matrix.
- $\boldsymbol{\alpha}$  - vector containing unknown amplitude and phase.
- $\mathbf{e}$  - vector containing interference plus noise.

The steering matrix  $\mathbf{A}$  is made up of steering vectors  $\mathbf{a}(\theta_k)$  where  $\theta$  is the azimuth angle between the target and the radar line of sight,  $k$  is the range bin number of the illuminated swath [27][28]. The steering matrix is an  $[M \times k]$  matrix where  $M$  is the number of antennas along-track. In one CPI, the angle  $\theta$  is constant for each range bin  $k$  of interest [27]. The vector  $\boldsymbol{\alpha}$  contains the scattering coefficients  $\alpha_k$  of each range gate with amplitude and phase, making it a  $[k \times 1]$  column vector. The measured data vector  $\mathbf{y}$  then becomes a  $[M \times 1]$  vector. The steering vectors  $\mathbf{a}(\theta_k)$  are given by Equation (2.19) below [26][29].

$$\mathbf{a}(\theta_k) = [e^{-j(2\pi f/c)d_1 \sin \theta_k}, \dots, e^{-j(2\pi f/c)d_M \sin \theta_k}]^T \quad (2.19)$$

Equation (2.19) is a column vector consisting of  $M$  number of rows which represent the number of antennas in the array and one column representing the range gate  $k$  of interest making a  $[M \times 1]$  column vector [29]. From Equation (2.19),  $d_M$  represents the antenna spacing from the first antenna  $d_1$ .

The IAA algorithm works such that it iteratively estimates the back scattering coefficients  $\alpha_k$  with accuracy and low sidelobes [27]. From the estimated scattering coefficients the signal power is given by  $p_k = |\alpha_k|^2$ . The signal power is then updated in a diagonal power matrix  $\mathbf{P}$  [26]. The updated power is then subtracted from the power of the previous iteration and the difference is compared to a convergence threshold,  $\epsilon$ . When the power difference from two successive iterations is smaller than the convergence threshold, the IAA algorithm has converged. The steps of the IAA algorithm are given below.

- Step 0: Initialize,  $i = 0$ ,  $\alpha_{(i)} = \mathbf{A}^H \mathbf{y}$  then  
Calculate,  $\mathbf{P}_i = \text{diag}(|\alpha_{(i)}|^2)$ .

- Step 1: Increment  $i$ .  
Calculate  $\mathbf{R}_{(i)} = \mathbf{A} \mathbf{P}_{(i-1)} \mathbf{A}^H$

- Step 2: For all  $k = 1, \dots, K$ ,

$$\text{Calculate } \alpha_{(k,i)} = \frac{\mathbf{a}_k^H \mathbf{R}_{(i)}^{-1} \mathbf{y}}{\mathbf{a}_k^H \mathbf{R}_{(i)}^{-1} \mathbf{a}_k}$$

$$\text{Update } \mathbf{P}_{(i)} = \text{diag}(|\alpha_{(k,i)}|^2)$$

- Step 3: Evaluate  $\|\mathbf{P}_{(i)} - \mathbf{P}_{(i-1)}\|^2 < \epsilon$

Repeat from Step 1 until convergence.

The IAA algorithm is not a clutter suppressing algorithm but a high resolution algorithm for estimating the scattering coefficient of objects in the illuminated scene as can be observed in [27]. It can be observed that after applying IAA on the simulated point targets and distributed targets in [27], the targets are displayed with high resolution, accuracy and low sidelobes. However the targets that can be classified as clutter, at zero range and azimuth, are still present in the processed image. For GMTI, IAA algorithm is usually incorporated with a clutter removing or nulling algorithm. The RELAX algorithm can be used to estimate the intensity of the clutter and cancel it from the measured data and then apply the IAA algorithm after as executed in [29], hence isolating targets that are not on the clutter ridge.

The IAA algorithm can also be used together with STAP algorithm as depicted in [30]. The IAA algorithm is used to estimate the clutter plus noise covariance matrix from the training data and then the covariance matrix is used to design the STAP

filter for clutter suppression and moving target indication [30]. IAA algorithm works in both homogeneous and heterogeneous clutter [28]. The high resolution spectral estimates of both clutter and moving targets for each range bin calculated by IAA algorithm is used as a clutter plus noise covariance matrix which aids STAP to create an effective clutter suppressing filter and detect ground moving targets [30].

## 2.6 GMTI using Velocity SAR

Velocity SAR (VSAR) is a radar imaging system that can detect and focus scatterers that are in motion while rejecting the scatterers that are stationary on the ground surface [31]. VSAR employs linear antenna arrays and it is able to construct a 3-dimensional image consisting of the range, azimuth and velocity domains [31]. VSAR is a single-output multiple-input radar, which means it consists of one transmitting element and multiple receive only elements along track the radar direction of motion [32]. The ability of VSAR to construct a 3-dimensional image with range, azimuth and velocity, and its ability to reject stationary scatterers (clutter) on the ground qualifies as a MTI system [31]. VSAR configuration is presented in Figure 2.8.

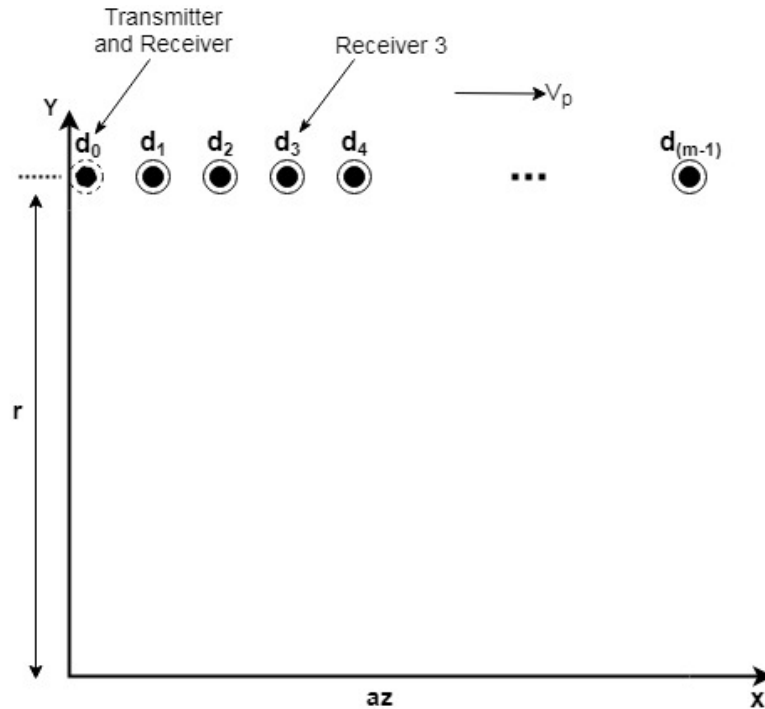


Figure 2.8: VSAR configuration [31].

Figure 2.8 shows that the transmitter and first receiver are co-located at position  $d_0$ , the other subsequent receivers are located at distances  $d_1, d_2, d_3, d_4$  until  $d_{(m-1)}$  ( $m$

is the total number of antennas used) on the same platform along the direction of motion of the radar. The multiple receive antennas each receive pulses from the same location in space at different times, hence they all image the same area. A single complex SAR image from one receive antenna consists of the range and azimuth dimensions only,  $z_m(r, az)$  ( $m = 1, 2, 3..$ ) [32].

VSAR works by combining the complex SAR images from all the receive antennas into a 3-dimensional matrix consisting of range, azimuth and space,  $z_m(r, az, m)$  [31]. A Fourier transform of this 3-dimensional matrix along the  $m$  dimension results in a range, azimuth and velocity matrix,  $Z(r, az, v)$ . Then each radial velocity plane along the velocity dimension of the matrix is shifted by a radial velocity proportional to the velocity of the radar platform to compensate for the azimuth displacement that was induced by the motion of the platform [31]. After the compensation, all scatterers will then be at their right radial velocity planes for the radial velocity that they induced if they were in motion and all stationary clutter will be at the zero radial velocity plane on the matrix  $Z(r, az, v)$ . The zero radial velocity plane will be the first plane along the velocity dimension of the matrix  $Z(r, az, v)$  [32]. To suppress the stationary clutter, the zero radial velocity plane is removed and replaced by zeros hence cancelling the amplitude and phase contributions of the stationary clutter [32] [33]. The block diagram of the VSAR system is presented in Figure 2.9 [31].

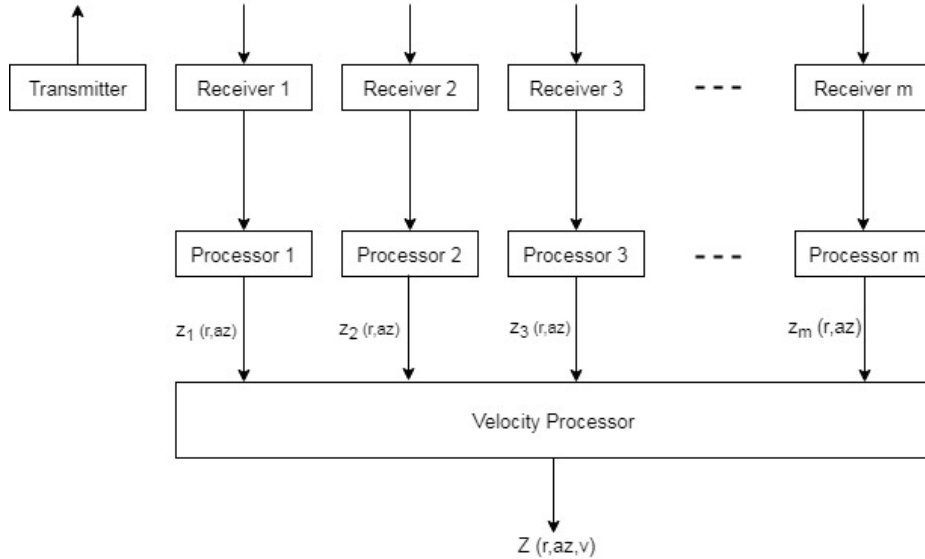


Figure 2.9: VSAR processor block diagram [31].

The constant distance between the multiple receive antennas,  $d$ , is determined by the velocity of the radar platform ( $V_p$ ), the coherent integration time ( $T_{cpi}$ ) and the total

number of receive antenna used ( $m$ ) as shown by Equation 2.20 [31]. This constant spacing determines the maximum unambiguous radial velocity that the VSAR system can estimate. The maximum unambiguous radial velocity is calculated by Equation 2.21 [31].

$$d = \frac{2V_p T_{cpi}}{m} \quad (2.20)$$

$$V_{r_{unamb}} = \frac{V_p \lambda}{d} \quad (2.21)$$

Substituting Equation 2.20 into Equation 2.21 results in Equation 2.22 which illustrates that as the number of receive antennas increase, the maximum unambiguous radial velocity increases. This means that faster ground moving targets can be detected unambiguously by using more receive antennas. Equation 2.23 also shows that the radial velocity resolution increases as more receive antennas are used [31].

$$V_{r_{unamb}} = \frac{m \lambda}{2T_{cpi}} \quad (2.22)$$

$$v_{res} = \frac{2V_{r_{unamb}}}{m} \quad (2.23)$$

The performance of VSAR increases as the receive antennas increases however, increasing the number of receivers increases the cost and the complexity of the system [33] [34]. The weight of the system and the size also increases as the number of antennas increase [31]. VSAR also has a disadvantage of potentially cancelling fast moving targets which allias to the zero radial velocity plane due to Doppler ambiguities [32] [33] [34]. The number of computations to focus the received data into SAR images also increases as the number of receive elements increases, hence, a compromise has to be reached in the design of a VSAR system which optimizes the effective system size, computational performance, detection performance and cost.

## 2.7 Conclusion

Five GMTI techniques were presented and explored in detail in this chapter. The advantages and disadvantages of each technique under investigation were outlined and this enables a selection of two GMTI techniques to be investigated further with simulated data and real measured radar data. The DPCA technique and the ATI

technique allows for implementation with only two receive channels while STAP and VSAR techniques require more than two receive channels to be implemented. The IAA algorithm like STAP, is computationally intensive as it runs iteratively until convergence. The following chapter looks at how two GMTI techniques will be selected from the explored five for further analysis, and provides the methodology that will be followed in their investigation.

# Chapter 3

## Methodology

The purpose of this study is to investigate multichannel GMTI techniques in terms of their performance . In the previous chapter, a literature review of five multichannel SAR GMTI techniques were presented, focussing on their capability to indicate moving targets within clutter, their implementation complexity, efficiency and how sensitive they are to errors in their practical realisation (mechanical, assumed platform velocity, etc.). The limitations of the techniques have also been noted.

From the five techniques investigated in the literature review, two techniques are now selected to be investigated further with simulated radar data as well as measured radar data. The two techniques are;

- DPCA
- ATI

DPCA and ATI were chosen due to the simplicity of their implementation and their wide applicability in practical GMTI radar system. Both of these techniques can be implemented on a two-receiver radar system, which allows their practical evaluation using the CSIR measurement radar that is available for this purpose.

By using simulated and real radar data, the performance of the two techniques will be evaluated and compared in terms of a specific criterion. This criterion include the ability of the techniques to indicate the moving target within clutter and their sensitivity to system setup non-idealities. Chapter 4 discusses this evaluation criterion in more detail.

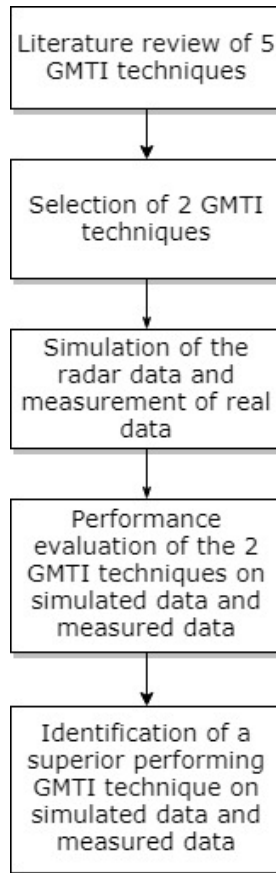


Figure 3.1: Flowchart showing the methodology of the study.

The flowchart in Figure 3.1 summarizes the followed methodology of this study. The simulated data were generated with a radar data simulator, developed by the CSIR. The description of the simulator and the data set it produces is outlined in Chapter 5. The experimental setup for controlled, practical radar data measurements is also outlined in Chapter 5.

The practical experiment had limitations in terms of geometries which include the maximum height and speed of the radar platform, the length of the radar platform rail as well as the clear area that the radar can illuminate. The simulated scene was chosen to reflect the same geometries that were used for practical radar data measurement. This enabled the simulated data and the measured radar data to be comparable one-to-one and between DPCA and ATI.

# Chapter 4

## GMTI Technique Evaluation Criterion

### 4.1 Introduction

In this study, the two selected GMTI techniques are applied to simulated data as well as real radar data measured in a controlled environment. This chapter presents a criterion that was used to evaluate the performance of these techniques on simulated data and measured radar data.

### 4.2 Moving Target Indication within Clutter

The main objective of GMTI techniques is to reject returns from stationary clutter and detect moving targets that could reside inside the Doppler spectrum of the clutter (endo-clutter targets) or outside the clutter Doppler spectrum (exo-clutter targets). The ability of the GMTI techniques to indicate moving target signals within clutter will be used as one of the selection performance qualities. The DPCA technique indicates moving targets using magnitude while the ATI technique indicates the moving target using the resulting interferometric phase as outlined in Chapter 2.

The DPCA technique achieves this target indication by suppressing the magnitude of the clutter signals and improving the SCR. The SCR improvement is the measure of how the DPCA technique improved the dominance of the target signal by reducing that of the clutter signal. Hence, indicating the moving target.

The ATI technique achieves moving target indication by subtracting the identical phase from stationary clutter that is present in two complex radar images to zero radians. This exposes the phase anomaly resulting from the moving target. The

moving target creates this phase anomaly by inducing a different phase in each complex radar image which doesn't cancel down to zero radians when the two images are conjugately multiplied. The measure of the residual clutter phase as compared to the measure of the moving target phase after applying ATI shows the performance and ability of the ATI technique to indicate moving targets within clutter.

The simulated data and the measured radar data were focused into range-Doppler maps. The power received was extracted from the range-Doppler maps before and after applying each GMTI technique. This allowed an assessment of how much clutter is left after GMTI processing as compared to the detected target signal.

### **4.3 Sensitivity to Practical Implementation Non-idealities**

Multichannel SAR GMTI techniques need accurate knowledge of the arrangement of the radar's antennas, their spacing, the PRF that the radar system operates at and the velocity of the platform that carries the radar system. In practice, however, these parameters may differ from their theoretical or designed values.

Simulation will be used to investigate the effect of antenna spacing errors. Data will be simulated which has slightly misaligned antenna spacing. This data set will be used to analyse the sensitivity of each GMTI technique to platform system errors. A favourable technique would effectively indicate moving targets within clutter even under non-ideal conditions.

Using the recorded radar data, intentional misalignment between the radar channels will be introduced. This will represent a case where either the radar platform velocity is different from the constant required velocity or where a wrong or different PRF is used for data recording. The two receive channels will not be exactly illuminating the same point in space at different times and hence result in co-registration errors. This will result in less effective clutter suppression and phase cancellation when performing GMTI processing. The sensitivity of the GMTI techniques will then be assessed with this channel misaligned data.

### **4.4 Conclusion**

The evaluation criterion for assessing the performance of the GMTI techniques on simulated data and on real measured radar data was discussed. The criterion con-

sists of two GMTI quality measures being distinguishing moving targets from ground clutter as well as sensitivity to practical implementation non-idealities. In the next chapter, the setup for the simulated data will be discussed as well as the setup for the measurement of practical radar data in a controlled environment.

# Chapter 5

## Radar Simulations and Experiment Setup

### 5.1 Introduction

This chapter presents the radar system setup for simulated data and the controlled experimental setup for radar data measurements. The parameters used for data simulation are presented together with the details and parameters of the controlled experiment.

### 5.2 Radar Data Simulations

The simulations in this study were performed using a radar simulator designed and implemented previously at the CSIR. The simulator is implemented in MATLAB for generation of raw radar data only and has been used for testing and development of an image focusing SAR processor [35]. The raw data simulator has the ability to simulate different sensor configurations with different radar parameters. The output of the radar simulator is the radar's received samples, i.e. before any digital signal processing [35]. In this study, this raw radar data output was focused into range-Doppler maps for GMTI processing and analysis.

In this study, the simulator was used to simulate a multichannel radar scenario with stationary point scatterers on the ground representing stationary clutter and ground moving scatterers as moving targets. The simulator only simulates point scatterers hence the simulated ground clutter and moving target were represented as point scatterers with AWGN added. It is noted that modelling clutter as a point scatterer with AWGN added is not a sufficient way to represent the scattering characteristics, amplitude distribution characteristics and space correlation characteristics of real radar

clutter. The stationary scatterer simulated represent a discrete point and in order for the target and clutter to influence each other in the simulations, the complex clutter range-Doppler cell was added to the complex target range-Doppler cell. This way the magnitude and phase of the radar signal returns for clutter and target had influence on each other given that they were initially simulated at different locations. This is a simplified approach to model stationary ground clutter as a discrete clutter point whose RCS varies with aspect angle and frequency. Identical processing is applied to both the clutter and the target.

Figure 5.1 illustrates the simulated scenarios. Each scenario had a target either moving east (target 1), west (target 2) or orthogonal (target 3) relative to the radar. The radar setup simulated had two receive only antennas and one transmit only antenna. The data collection mode for the simulation was the "standard mode", as discussed in Chapter 2 Subsection 2.2.1, whereby one dedicated transmit antenna is used with two dedicated receive antennas.

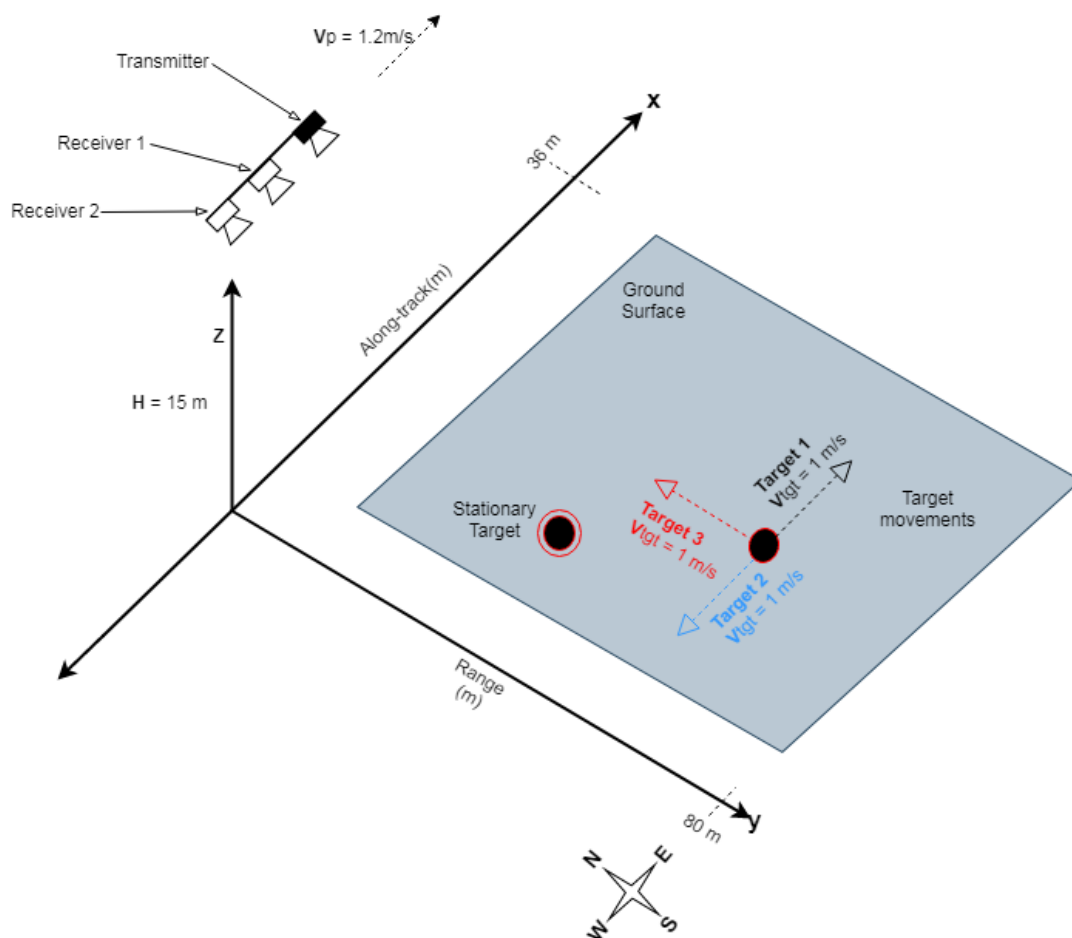


Figure 5.1: Simulated scene with a stationary scatterer and a moving target.

The assumptions made in simulating the data were that the platform moved along a straight trajectory that was level and the data were collected in a strip-map SAR mode configuration. Zero squint angle was also assumed. The two receive antennas and the transmit antenna were also assumed to be positioned on a straight line along-track the platform motion and were separated by a predetermined baseline. Only two scatterers were simulated and the atmospheric effects were not included in the simulation.

The simulation parameters were chosen and calculated to be the same as those used to measure real radar data during the radar experiment (as discussed in Chapter 3).

The performance parameters for the simulated scenario are as follows;

- Center Frequency,  $f = 5.5$  GHz
- Pulse Repetition Frequency,  $PRF = 1501.5$  Hz
- Duty Cycle,  $T_{dc} = 100\%$
- Transmitted power,  $P_t = 10$  W
- Instantaneous pulse bandwidth,  $B = 100$  MHz
- Analogue to digital sampling rate,  $f_s = 200$  MHz
- Noise Figure,  $F = 15$  dB
- Transmit and receive antenna beamwidth,  $\theta_B = 34.72^\circ$  (0.61 radians)
- Simulation duration,  $t = 30$  s
- Measured scene size,  $R_{ms} = 36$  m
- Platform Velocity,  $V_p = 1.2$  m/s
- Number of receive channels,  $Chn_{Rx} = 2$
- Number of transmit channels,  $Chn_{Tx} = 1$
- Antenna physical spacing (baseline),  $d = 118.5$  mm
- Radar look angle towards scene center,  $\phi_{elev} = 61.05^\circ$
- Number of moving targets,  $tgt = 1$
- Moving target ground velocity,  $V_{tgt} = 1$  m/s

- Number of stationary scatterers, clutter = 1
- Initial Position of moving Target 1 [x y z],  $PoT_1 = [0 \ 117 \ 0]$  m
- Initial Position of moving Target 2 [x y z],  $PoT_2 = [19 \ 129 \ 0]$  m
- Initial Position of moving Target 3 [x y z],  $PoT_3 = [0 \ 145 \ 0]$  m
- Initial Position of radar Platform [x y z],  $PoP = [-18 \ 0 \ 15]$  m
- Position of Stationary Scatterer [x y z],  $PoS = [13 \ 125 \ 0]$  m

The above performance parameters were chosen to result in a cross range resolution ( $\Delta CR$ ) of 0.05 m using Equation (1.1) and a slant-range resolution ( $\Delta R$ ) of 1.5 m using Equation (1.2). A PRF of 1501.5 Hz was used during the simulation of the raw radar data and during the measurement of real radar data. This specific value was chosen to make sure that the sweep rate of the real radar used with a high pass filter in the front-end does not cut-off the near ranges in the measured data. The decimals in the PRF are due to the radar clocks in the real radar being integer multiples. The center frequency was constrained to 5.5 GHz due to the radar hardware that was available. The simulated noise figure of 15 dB was also from the hardware setup of the radar used for real data measurement.

Since the measured ground scene is 80 m wide, the radar channel measurement had 53 range gates. The simulation represented 30 s worth of data with a PRI of 0.666 ms, which results in 45045 pulses per simulation. Hence, the simulated radar raw data matrix was  $53 \times 45045$  in size for each channel.

Three scenarios were simulated, each one with a target moving at 1 m/s in various direction as depicted on Figure 5.1. Each moving target was simulated with an RCS of a triangular trihedral with 30 cm dimensions. According to Equation 5.1, the peak RCS ( $\sigma_{RCS}$ ) of the triangular trihedral is  $13.6 \text{ m}^2$  at a frequency of 5.5 GHz and dimension length,  $A$ , of 30 cm [36]. These trihedrals were also used in the controlled experiment for measurement of radar data.

$$\sigma_{RCS} = \frac{4\pi A^4}{3\lambda^2} \quad (5.1)$$

Each simulated target scenario was expected to have a unique radial velocity change and slant range change throughout the 30 s simulation time. Figure 5.2 shows the

expected radial velocity change over 30 s (45045 pulses) for target moving east (blue line), target moving west (red line) and target moving orthogonal (green line). A plot of the expected change in slant range of the targets, relative to the radar, over the 30 s simulation period is presented in Figure 5.3.

The simulated raw data were not processed for the whole 30 s (45045 pulses), instead, only selected intervals were used, as indicated in Figure 5.2. The selected intervals (interval (1) to (6)) in Figure 5.2 corresponds to the range and radial velocity in Figure 5.3, taking only 4096 pulses ( $2^{12}$  pulses) from the indicated pulse number. This way the GMTI techniques were investigated at various azimuth angles and target positions yielding different target radial velocities for different moving target scenarios.

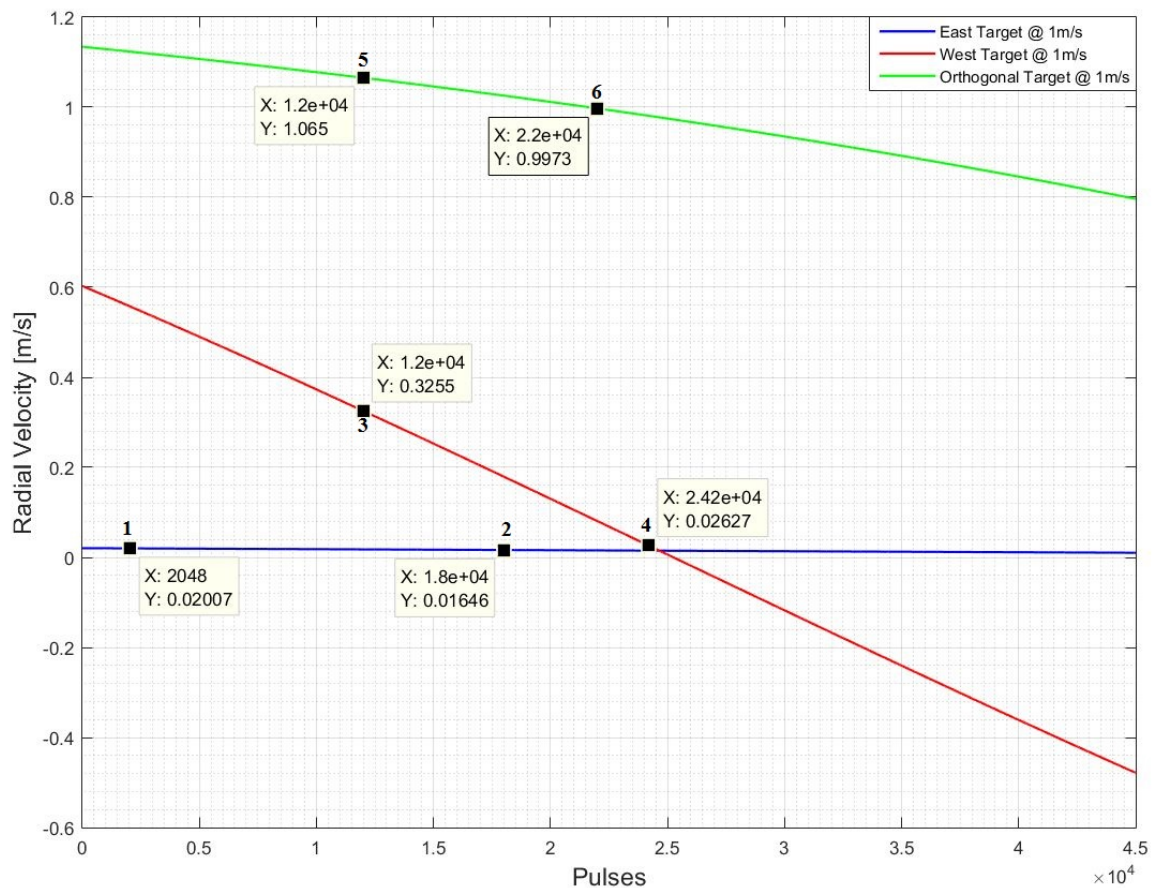


Figure 5.2: Expected radial velocity change of targets at all simulated pulse instances. (1) Pulse no.2048 and (2) Pulse no.18000 for east moving target, (3) Pulse no.12000 and (4) Pulse no.24200 for target moving west, (5) Pulse no.12000 and (6) Pulse no.22000 for target moving orthogonal towards radar.

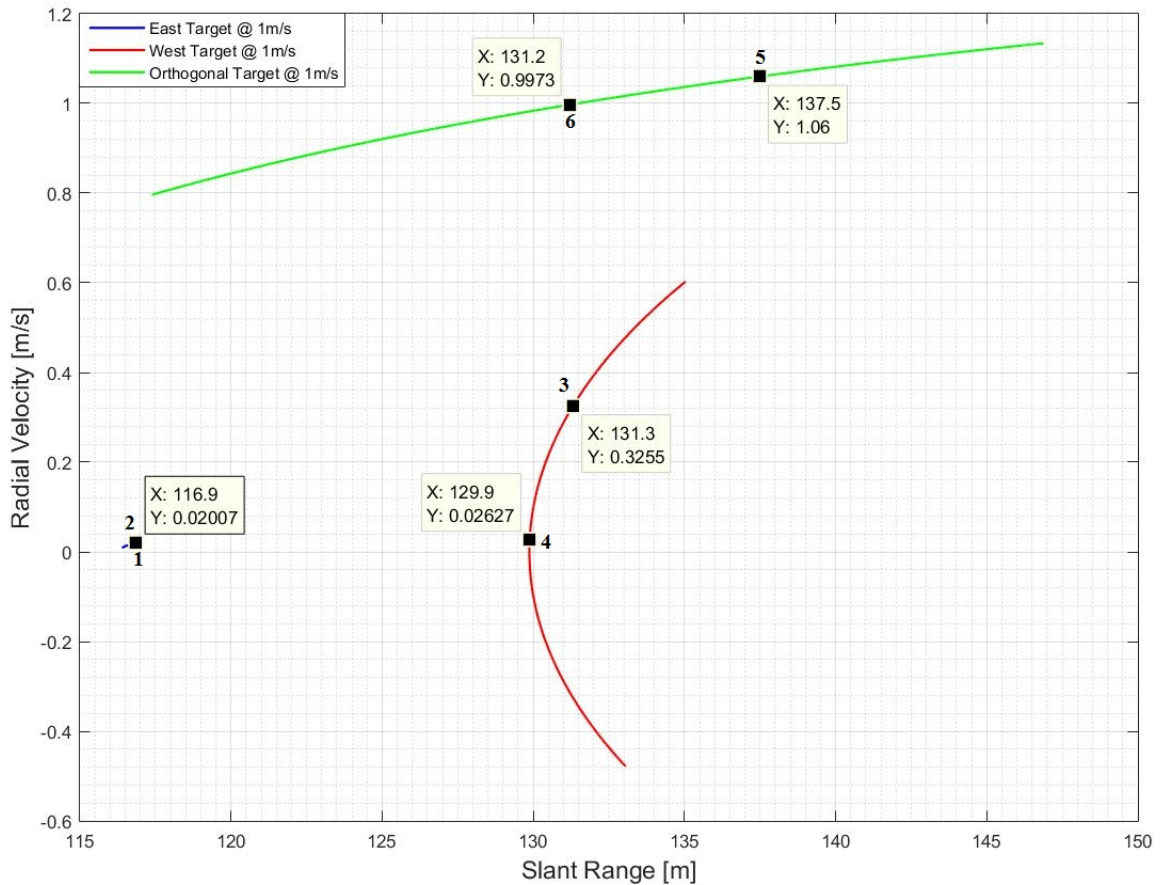


Figure 5.3: Expected range and radial velocity change of targets over the simulation period. (1) and (2) for target moving east, (3) and (4) for target moving west, (5) and (6) for target moving orthogonal towards the radar

### 5.3 Experiment Setup Description

The performance of the GMTI techniques investigated in this study was assessed with simulated data and with real measured data using the same parameters. For the practical experimentation, the radar data were measured in an experimentally controlled environment with known moving target, target speed and clutter features. This enabled the GMTI techniques to be investigated with measured radar data of known properties.

The system parameters used for the recording of measured radar data are presented as follows;

- Center Frequency,  $f = 5.5$  GHz

- Pulse Repetition Frequency,  $PRF = 1501.5$  Hz
- Duty Cycle,  $T_{dc} = 100\%$
- Transmitted power,  $P_t = 10$  W
- Bandwidth,  $B = 100$  MHz
- Sampling rate,  $f_s = 200$  MHz
- Transmit and receive antenna beamwidth,  $\theta_B = 34.3^\circ$
- Recording duration,  $t = 30$  s
- Measured scene size,  $R_{ms} = 36$  m
- Platform Velocity,  $V_p = 1.2$  m/s
- Number of receive channels,  $Chn_{Rx} = 2$
- Number of transmit channels,  $Chn_{Tx} = 1$
- Antenna physical spacing (baseline),  $d = 118.5$  mm
- Radar look angle towards scene center,  $\phi_{elev} = 61.05^\circ$
- Polarization - VV
- Number of moving targets,  $tgt = 1$
- Moving target ground velocity,  $V_{tgt} = 1$  m/s

The radar used during the controlled experiment employed a multichannel configuration. Two receive channels and a dedicated transmit channel were used. For both transmit and receive, horn antennas with a nominal  $34.3^\circ$  beamwidth in the E-plane and H-plane were used. The horn antennas had a gain of 13.8 dB at 5.5 GHz.

The two receive channels were separated by 118.5 mm from phase centre to phase centre along track the radar motion. The data collection mode employed was the standard mode, as discussed in Chapter 2, Subsection 2.2.1. The radar employed a Frequency Modulated Continuous Wave (FMCW) mode operation, which means that the radar was continuously transmitting and receiving at the same time. This data measurement mode allowed for the performance investigation of DPCA GMTI technique and ATI GMTI technique.



Figure 5.4: The image of the radar and the moving platform from the back.

The radar was mounted on a platform moving on a 150 m rail on the roof of a building on the CSIR campus in Pretoria, South Africa, with its antennas pointing exactly perpendicular to the direction of motion of the radar platform. Figure 5.4 presents the image of the radar and the trolley it was mounted on, which facilitated the movement.

For the moving target, a triangular trihedral (corner reflector) was carried by a person that walked on the ground below the radar. The corner reflector had RCS of  $13.6 \text{ m}^2$  as determined by Equation 5.1. The moving target travelled in the same predetermined directions as the simulated moving targets outlined in Figure 5.1. The illuminated ground had vegetation, carports and a tar road making the resulting clutter heterogeneous. Figure 5.5 illustrates the experimental setup and the top view photo of the location for the practical radar data measurement.



Figure 5.5: Top view map of the experiment setup for real data measurement.

Figure 5.5 shows the three paths marked with dotted yellow arrow lines that the moving targets used during the experiment. The target paths are labelled target path 1, target path 2 and target path 3.

- Target path 1 represents the target that moved east, parallel and same direction as the radar platform, at an average velocity of 1 m/s while carrying a corner reflector.
- Target path 2 represents the target that moved west, parallel and opposite direction to the motion of the radar platform, at an average velocity of 1 m/s while carrying a corner reflector.
- Target path 3 is for a target that moved orthogonal, towards the radar platform, at an average velocity of 1 m/s without a corner reflector enhancing the radar returns.

These target positions and target paths correspond to that of the simulated data, and they produced distinct radial velocities and slant ranges relative to the radar as depicted in Figure 5.3. The radar platform was approximately 15 m high above the ground level where the ground targets moved, which results in a look angle of  $61.05^\circ$ . The radar platform was travelling at an average velocity of 1.2 m/s on a 150 m long rail indicated in Figure 5.5. During the experiment, only about 36 m of this rail was used, as indicated with green lines on Figure 5.5. The radar system moved east for every radar data recording while illuminating the ground scene depicted in Figure 5.5.

## 5.4 Conclusion

The simulated scenario and the radar data measurement experiment with the multi-channel SAR setup was presented in this chapter. The parameters used in the data simulations and radar data measurements were also outlined. In the next chapter, the results obtained from the practical measured scene are presented. The radar data pre-processing required before applying the GMTI techniques is also outlined.

# Chapter 6

## Pre-processing of the Measured Radar Data for GMTI

### 6.1 Introduction

This chapter presents the pre-processing of the practically measured raw radar data outlined in Chapter 5 under the experimental setup description subsection. Details of the data and the type of pre-processing performed on it before GMTI processing are outlined. The exact imaged area is depicted with labels on a range-Doppler map.

### 6.2 The Imaged Scene

The experimental setup description from Chapter 5 detailed how the experimental data were measured and illustrated the scene of interest to be measured to obtain SAR data for GMTI under a known controlled environment. The actual scene that was illuminated and measured by the radar is the one presented in Figure 6.1 below. The image in Figure 6.1 was obtained from Google Earth. From Figure 6.1 one can clearly see the position of the radar and its distance from labelled objects of interest. One target was used in this data measurement and display. The target was moving east along the yellow dotted arrow line (target path 1) indicated on the image. A stationary corner reflector was placed on the ground as observed and there was a vertical metal pole next to it. A bush creating a diagonal line across the imaged scene can also be observed together with a corrugated iron parking bay. These structures mentioned were one of the points of interest that marked the experimental scene.

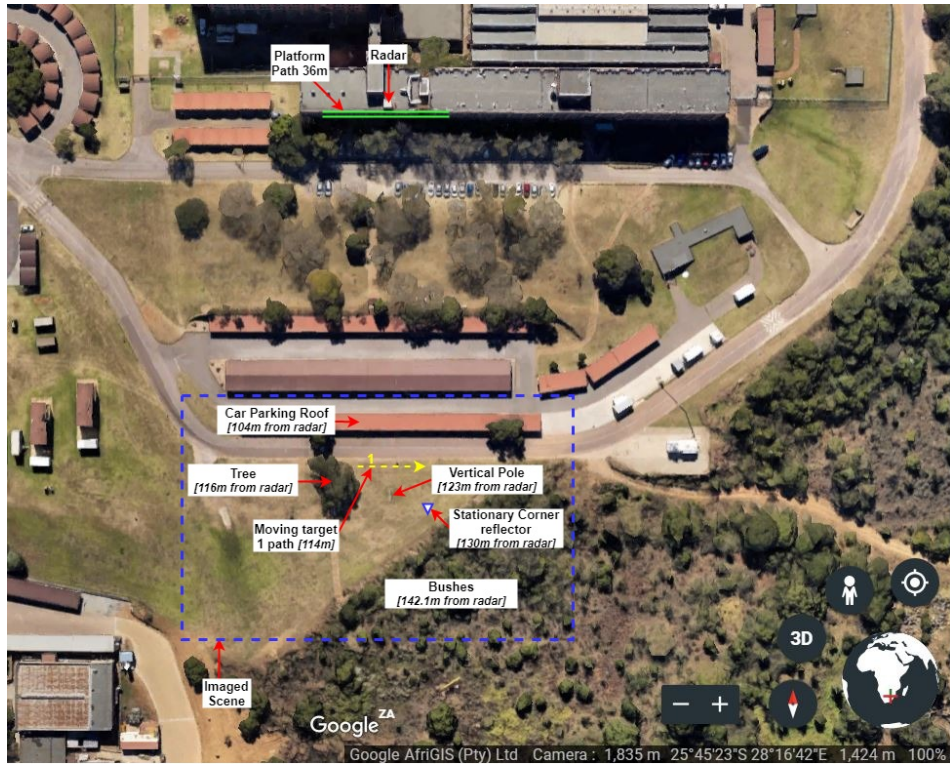


Figure 6.1: View of the experimental setup scene where radar data were measured.

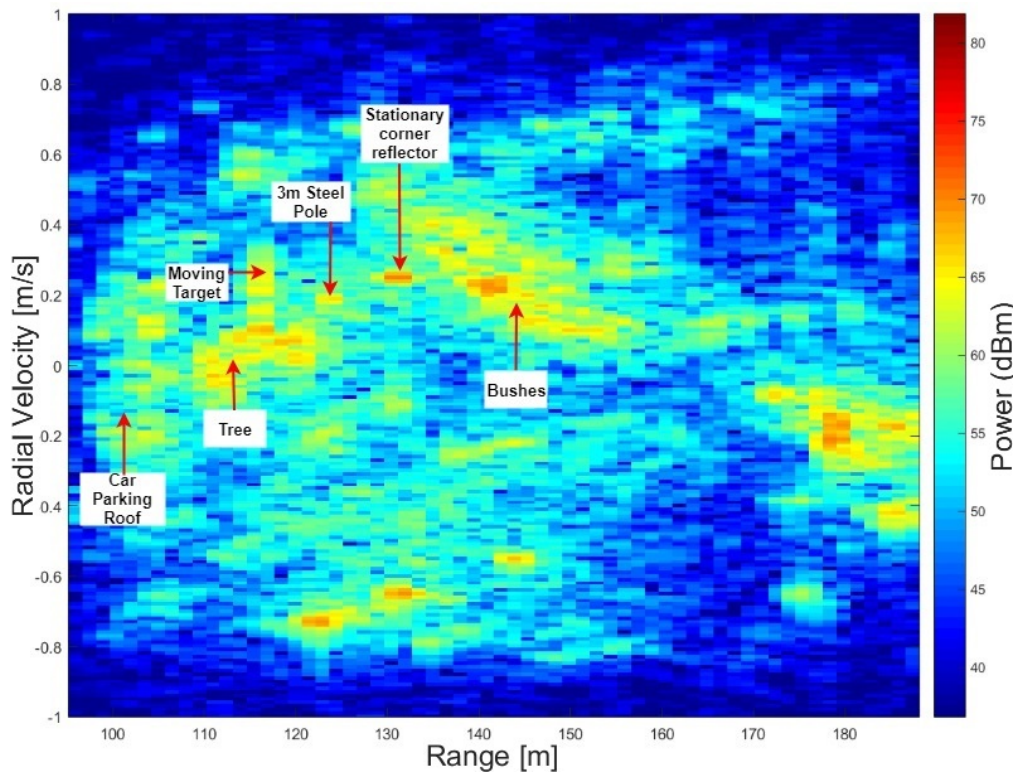


Figure 6.2: A labelled range-Doppler map of the imaged scene.

Figure 6.2 presents the range-Doppler map of the imaged scene with all the structures of interest labelled. The corrugated iron roofed parking as well as the diagonal bush is clearly visible in the range-Doppler image. The stationary corner reflector and the steel pole can also be observed. The moving target in-front of the corrugated iron roofed parking is seen smearing across range and Doppler bins as it was in motion during coherent integration.

## 6.3 Data Pre-processing

When using multiple radar channels to image the same point in space at different time instances, the multiple channel receive chains are required to be equal in terms of their frequency responses, so as to enable the detection of any change occurring in the area observed [37]. In practice, however, RF systems differ slightly in their frequency responses, due to component tolerances, regardless of how similar in built the systems are [37]. Figure 6.3 and Figure 6.4 present the range-Doppler maps formed using receive channel 1 and channel 2 data recorded from the depicted scene in Figure 6.1. Clearly, it can already be observed that the power intensity of the two range-Doppler maps are different, indicating a difference in the analogue gain of the two receive channels, since the digital processing applied to both were the same. This difference can also be observed from Figure 6.5 which shows the power level of a single range bin across all the pulses, for channel 1 and channel 2. For GMTI, the different frequency responses of the multiple receive channels must be corrected so as to be sensitive to changes in the scene that occurred over time, using multiple channels. This correction can be achieved by channel balancing/equalization.

In order to detect and indicate the ground moving targets within stationary clutter using two or more channels, the channels must be co-registered and balanced over frequency, so as to achieve significant clutter suppression. Radar channel balancing and co-registration are two crucial steps in multi-channel SAR GMTI.

### 6.3.1 Channel Co-registration

Channel co-registration is performed first before channel balancing, and is required to ensure that the received signals of both channels are compared when each is at exactly the same point in space. Channel co-registration can be performed in the time domain or via multiplication with a suitable phase in the Doppler domain [38].

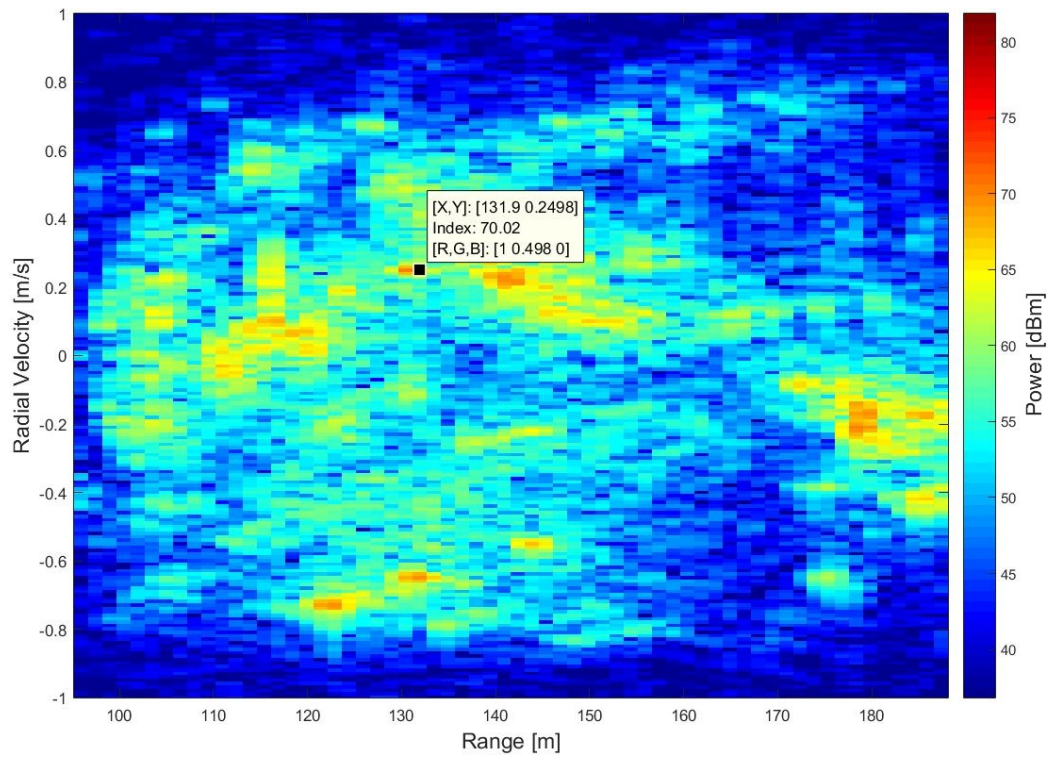


Figure 6.3: Channel 1 range-Doppler map.

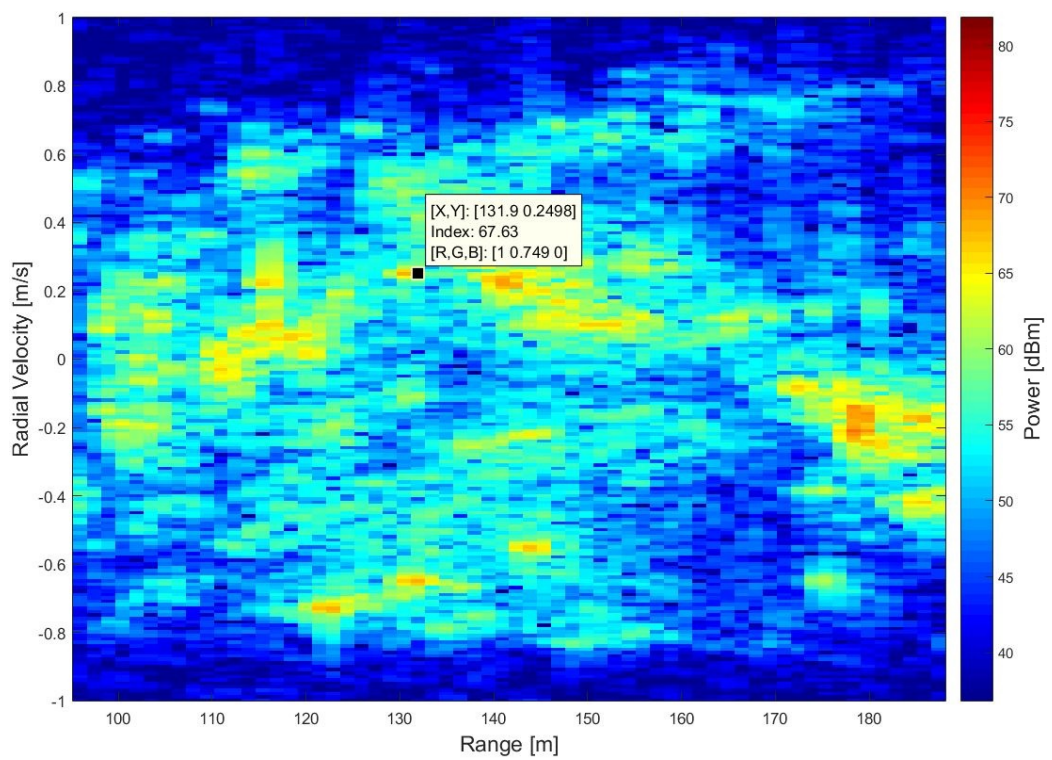


Figure 6.4: Channel 2 range-Doppler map.

In the time domain, channel co-registration is performed by discarding the first few pulses of the aft radar channel so as to account for the radar platform velocity, the spacing (baseline) between the channels and the PRF used in capturing the data. The number of pulses to discard are calculated by determining the time delay ( $t_d$ ) it takes the aft antenna to travel the set channel baseline ( $d$ ) from phase center to phase center ( $t_d = d/V_p$ ), then dividing that time delay by the system PRI ( $t_d/PRI$ ) for ping-pong data collection mode [38]. For standard data collection mode, the time delay is calculated for travelling half the antenna baseline ( $t_d = d/2V_p$ ).

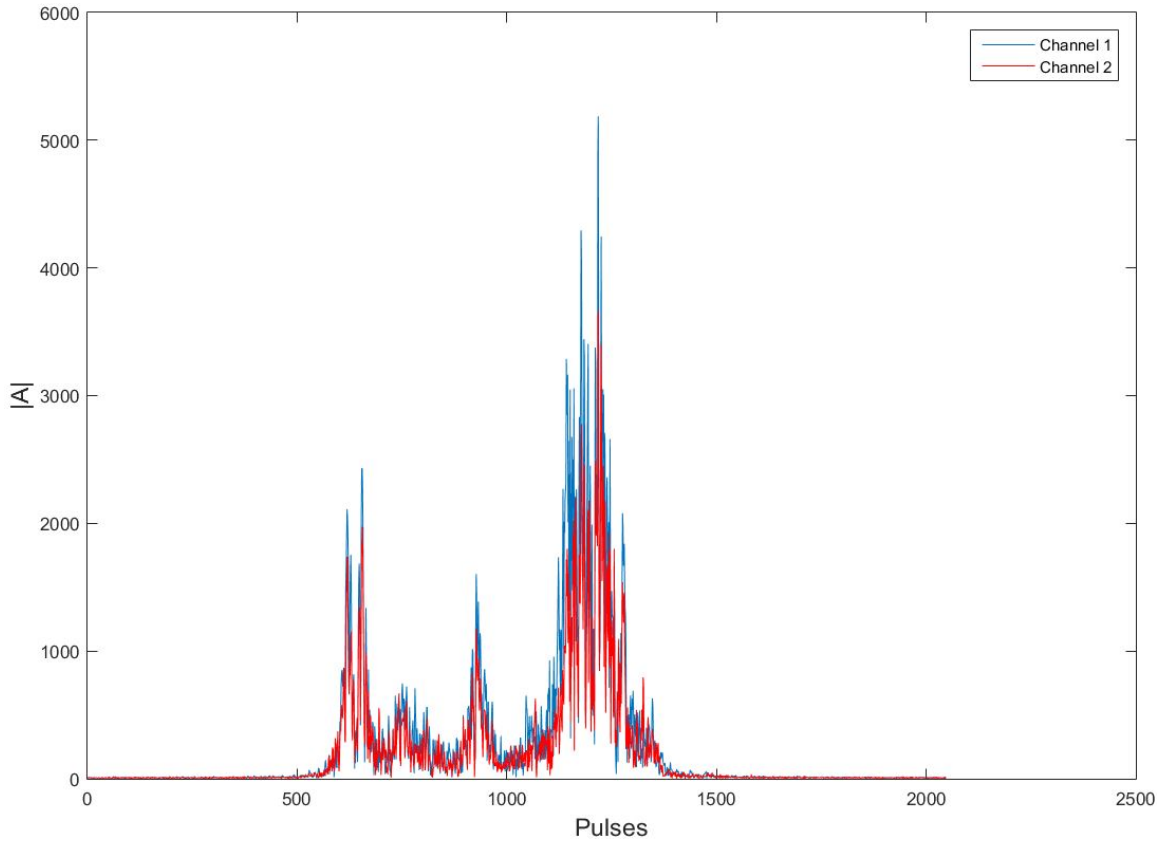


Figure 6.5: Channel 1 and Channel 2 before channel balancing.

In the Doppler domain, the time delay ( $t_d$ ) due to the antenna baseline corresponds to a systematic azimuth phase ( $\phi_d = -V_r d / \lambda V_p$ ) for standard data collection mode. For ping-pong mode, the azimuth phase is ( $\phi_d = -2dV_r / \lambda V_p$ ) [38]. Multiplying the aft channel data with the conjugate exponential term  $\exp(j\phi_d)$  co-registers the radar channels and removes the azimuth phase ramp due to the antenna baseline [38]. Co-registration was performed in the time domain on the images of Figure 6.3 and Figure 6.4 hence the maximum scatterer indicated (corner reflector) is at the same range and Doppler bin on both images.

### 6.3.2 Channel Balancing

In order to achieve channel equalization, algorithms such as linear fitting algorithm, eigen-decomposition algorithm and adaptive 2-dimensional algorithm have been suggested in previous GMTI experiments [39]. For the eigen-decomposition algorithm proposed and implemented by Gierull in [38], the author found that the compression of the entire clutter energy for each Doppler frequency into a one-dimensional subspace can be achieved by determining the spectral density matrix (power spectral matrix) of rank one for the recorded clutter [38]. The eigenvector that corresponds to the largest eigenvalue from the spectral density matrix can then be used to estimate azimuthal phase errors and calibrate the radar channels [38, 39]. This algorithm only operates on the phase of the two radar channels [38]

The linear fitting algorithm suggested by Deng and Zhang in [40], estimates the compensating function for channel calibration using the minimal-power criterion and linear fitting [40]. Minimal-power criterion is used to extract the compensation vector of the aft channel using the complex image of the aft channel and the fore channel (reference channel). The compensation vector is unwrapped then linear fitting is performed on it to form a compensating function for the aft channel data [40]. The aft channel data is then multiplied by the compensate function in the frequency domain for calibration and equalization with the reference channel [40]. According to Deng and Zheng in [40], this algorithm works best when three radar receive channels are used and the middle channel is used as a reference for the other two channels.

Adaptive 2D-calibration is a technique proposed by Ender in [41]. It is a digital iterative channel equalization technique that calibrates the amplitude and phase of the received radar signals [41, 38]. This technique operates across both range and Doppler domains and attempts to equalize the spectral responses of two channels [41, 42]. The spectral responses are equalized by adjusting one channel's spectral response and minimizing the square of the difference between the two channels across both Doppler and range [41, 38].

In this study, channel equalization was performed using adaptive 2D-calibration technique. This technique is used because it adaptively calibrates both the phase and the magnitude of the radar channels unlike the eigen-decomposition algorithm suggested by Gierull in [38] which only calibrates the phase. The linear fitting algorithm by Deng and Zhang [40] works best with three receive radar channels and only two channels are available in this study.

Equation 6.1 and Equation 6.2 below indicates how the adaptive 2D-calibration technique adjusts the spectral response of channel 2 ( $z_2$ ) iteratively across Doppler and range respectively [38].

$$z_2^{(n+1)}(r, f_d) = z_2^{(n)}(r, f_d) \times \frac{\int z_1(r, f_d) \times z_2^{(n)*}(r, f_d) df_d}{\int |z_2^{(n)}(r, f_d)|^2 df_d} \quad (6.1)$$

$$z_2^{(n+2)}(r, f_d) = z_2^{(n+1)}(r, f_d) \times \frac{\int z_1(r, f_d) \times z_2^{(n+1)*}(r, f_d) dr}{\int |z_2^{(n+1)}(r, f_d)|^2 dr} \quad (6.2)$$

Where:

- $n$  - 0, 1, 2, ... (iterator).
- $z_1(r, f_d)$  - channel 1 spectral data.
- $z_2^{(n)*}(r, f_d)$  - complex conjugate of channel 2 data.
- $z_2^{(n)}(r, f_d)$  - iteratively improved channel 2 spectral data across Doppler ( $f_d$ ) and range ( $r$ ).

The ratio of integrals from Equation 6.1 determines the Doppler ( $f_d$ ) calibration weights. These Doppler calibration weights are a measure of complex coherence between channel 1 ( $z_1$ ) and channel 2 ( $z_2$ ) [38]. The calibration weights are then multiplied with channel 2, which is the channel that is being iteratively improved to balance with channel 1. The ratio of integrals in Equation 6.2 are also calibration weights across the range ( $r$ ) domain which also measure the complex coherence of the channels across range [38]. Channel 2 is then also multiplied by this range calibration weights. The Doppler and range calibration weights are calculated and used to adjust channel 2 until the mean difference between the calibration weights are below a set convergence threshold ( $\epsilon$ ), which is the least acceptable complex coherence error between channel 1 and channel 2.

Figure 6.6 presents the flowchart of the adaptive 2D-calibration technique. The variables `weights_D` and `weights_R` are the Doppler calculated weights and the range calculated weights respectively. These weights are initialized such that their difference is above the set convergence threshold on the zeroth iteration. The variables **Ch1** and **Ch2** are the recorded channel 1 data matrix and channel 2 data matrix respectively with range on the first dimension and Doppler on the second dimension. **H1** and **H2** are the weighing factors populated into a matrix. Convergence is reached when the mean difference of the weights becomes less than the convergence threshold (Thresh

$= \epsilon$ ) on the technique, and the number of iterations it took to achieve convergence is displayed. The convergence threshold is chosen to ensure that the mean difference of the weights is less than 0.01% ( $1 \times 10^{-4}$ ), which is the maximum tolerable calibration error between the two radar channels.

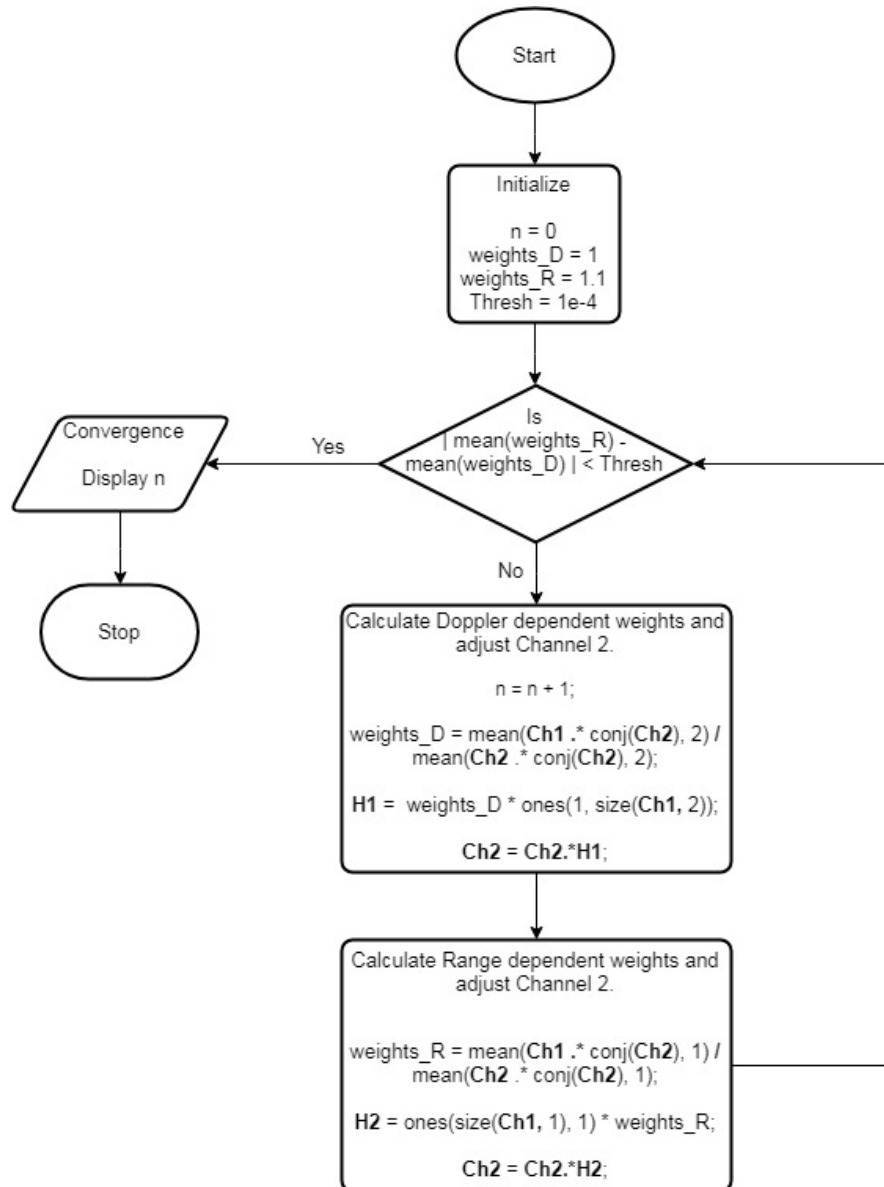


Figure 6.6: Flowchart of the adaptive 2D-Calibration technique.

Applying the adaptive 2D-calibration technique on the data recorded with channel 1 and channel 2 and iteratively adjusting the spectral response of channel 2 gives the results presented in Figure 6.7. It can be observed that after channel balancing the two channels have the same amplitude responses on Figure 6.7 as compared to before on Figure 6.5.

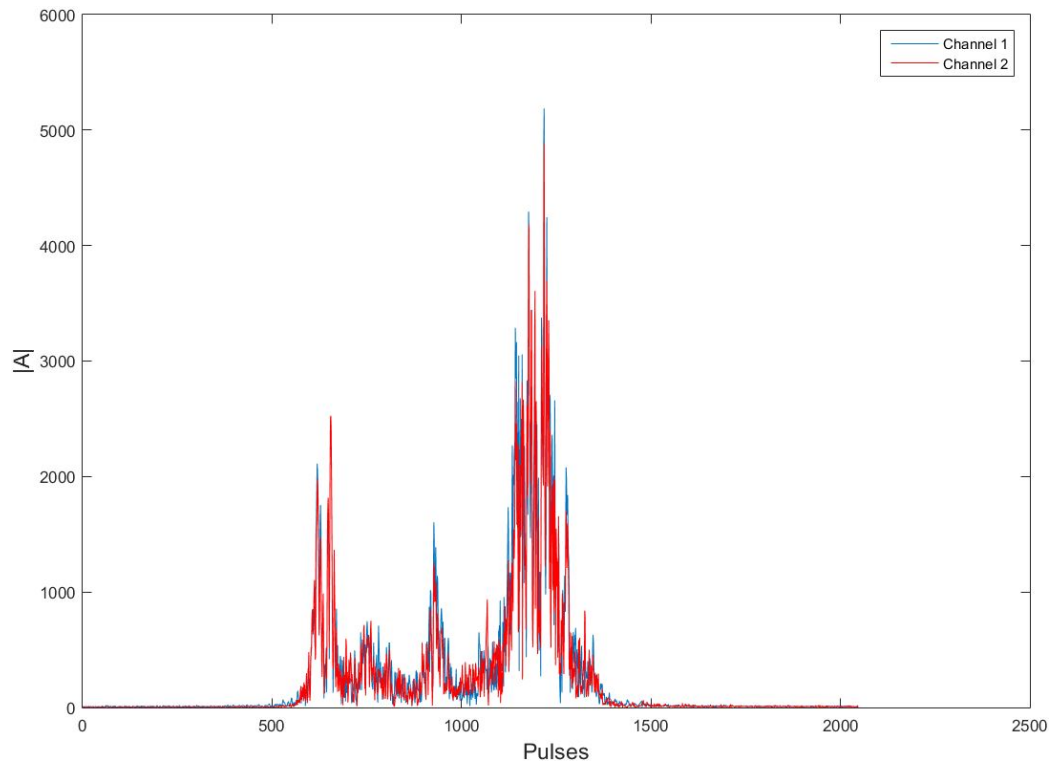


Figure 6.7: Channel 1 and Channel 2 after channel balancing.

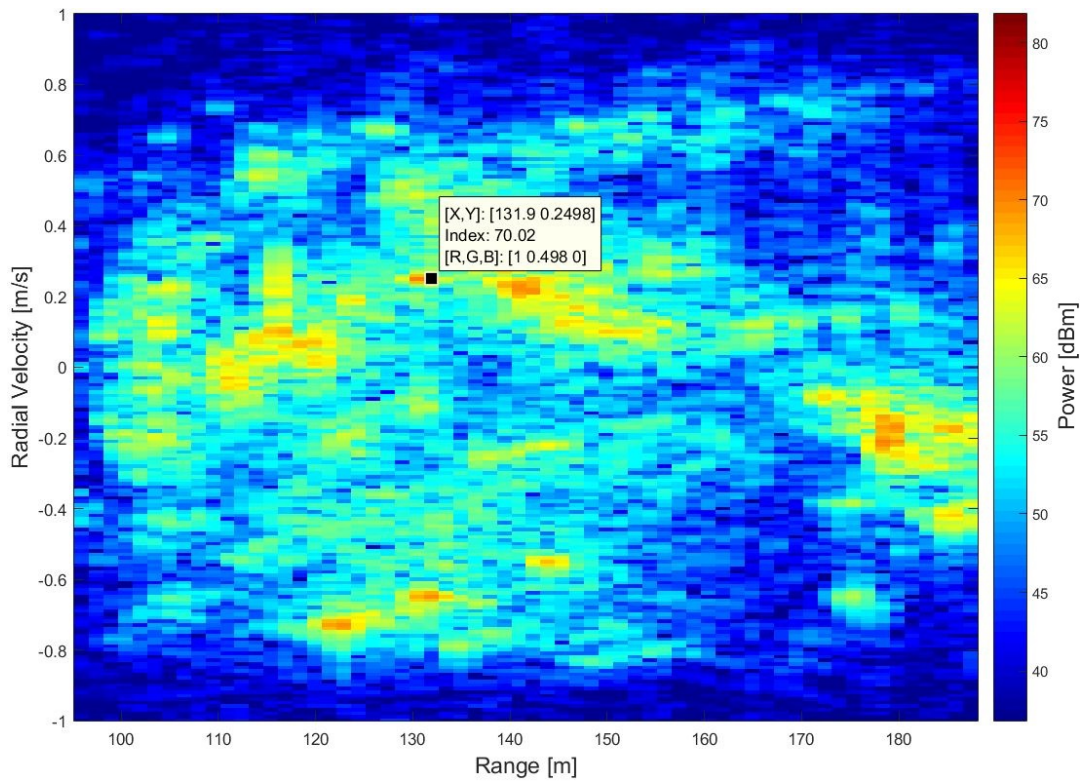


Figure 6.8: Range-Doppler map of channel 1 after channel balancing.

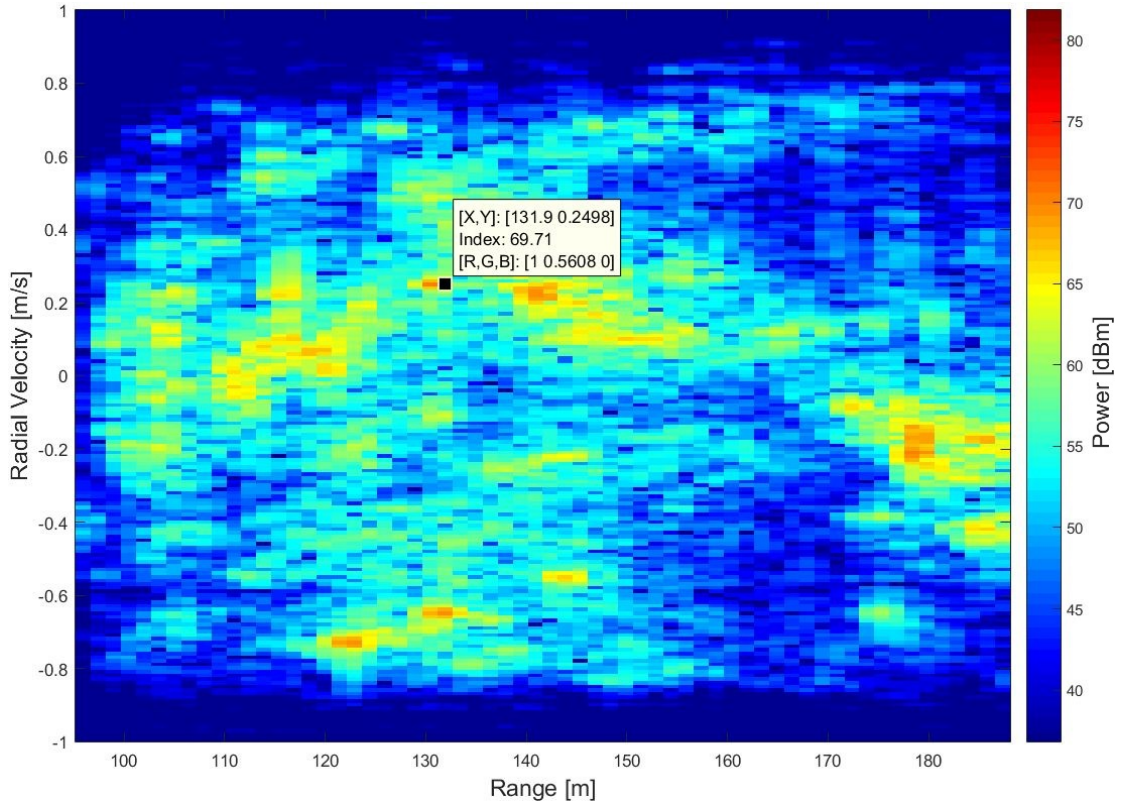


Figure 6.9: Range-Doppler map of channel 2 after channel balancing.

Figure 6.8 and Figure 6.9 display the obtained range-Doppler maps for channel 1 and channel 2 after channel balancing. The dominant clutter scatterer (corner reflector) is displayed with a power level of 70.02 dBm on channel 1 and a power level of 69.71 dBm on channel 2 after channel balancing. The dominant scatterer is at the same location on the two range-Doppler maps of Figure 6.8 and 6.9.

Table 6.1 presents a summary of the channel differences before and after applying the adaptive 2D-calibration technique. The differences are determined with reference to the dominant clutter scatterer in channel 1. The table shows that the two channels have been equalized down to a 0.31 dB difference, which equates to an error of 0.44% for a single range-Doppler cell containing the dominant scatterer. Before channel balancing, the error between the two channels was 3.41% as Table 6.1 outlines. The phase of channel 2 also show that it was corrected from 1.0357 radians to -2.9392 radians for the dominant clutter scatterer to balance with the phase of channel 1. Hence, the channel balancing technique was applied correctly and it managed to equalize the two radar channels. After co-registration and channel balancing, the GMTI techniques can be applied to suppress the clutter and indicate the ground moving target.

Table 6.1: Summary of the performance of the adaptive 2D-calibration technique.

	<b>Before Calibration</b>	<b>After Calibration</b>
<b>Channel 1 Power</b>	70.02 dBm	70.02 dBm
<b>Channel 2 Power</b>	67.63 dBm	69.71 dBm
<b>Channel Power Difference</b>	2.39 dB	0.31 dB
<b>Power Balance Error</b>	3.41%	0.44%
<b>Channel 1 Phase</b>	-2.9265 radians	-2.9265 radians
<b>Channel 2 Phase</b>	1.0357 radians	-2.9392 radians

## 6.4 Conclusion

The imaged scene and all its features were depicted and the resulting range-Doppler map was also presented with labels of the structures of interest. The position of the structures were verified to be at the expected distance on the range-Doppler map as indicated on the scene image. Pre-processing of the SAR GMTI data using the adaptive 2D-calibration technique and co-registration was outlined in detail in this chapter. A 3.41% power imbalance error was observed before channel calibration and after channel calibration, the power imbalance error was reduced to 0.44%. The following chapter presents the performance evaluation of the two GMTI techniques using simulated data.

# Chapter 7

## Performance Comparison of GMTI Techniques with Simulated Data

### 7.1 Introduction

In this chapter the two selected GMTI techniques, namely DPCA and ATI, are evaluated using simulated data. Each technique's performance is assessed in terms of its ability to indicate moving targets within clutter and its sensitivity to system errors as per the methodology discussed in Chapter 3. The two techniques are tested with the same simulated data in order to enable comparison of the two techniques. The geometry and the radar system parameters for this simulated data were described previously in Chapter 5.

### 7.2 GMTI using DPCA Technique on Simulated Data

#### 7.2.1 Processing Overview

The simulated data used in testing this technique represents two radar channels operating at a centre frequency of 5.5 GHz and a PRF of 1501.5 Hz. The size of the area imaged is 80 m. Recall that the radar data simulator simulates point scattering sources. As stated in Chapter 5, the complex range-Doppler map cell (amplitude and phase) of clutter is added to the complex range-Doppler map cell of the target in order for the clutter to influence the target. Identical processing is applied to both the clutter and the target. The clutter and target power before and after applying the technique is extracted from focused range-Doppler images for analysis.

The DPCA technique was applied by firstly introducing a time delay of 49.375 ms on

the received radar returns of channel 2. With a PRI of 0.666 ms, this is equivalent to shifting the received pulses of channel 2 by 74 pulses. The shift allows the returns of channel 2 to be spatially aligned and co-registered with the returns of channel 1 by travelling half the baseline distance between the two channels. After co-registration, the two channels are focused using range-Doppler processing and the complex values are subtracted from each other.

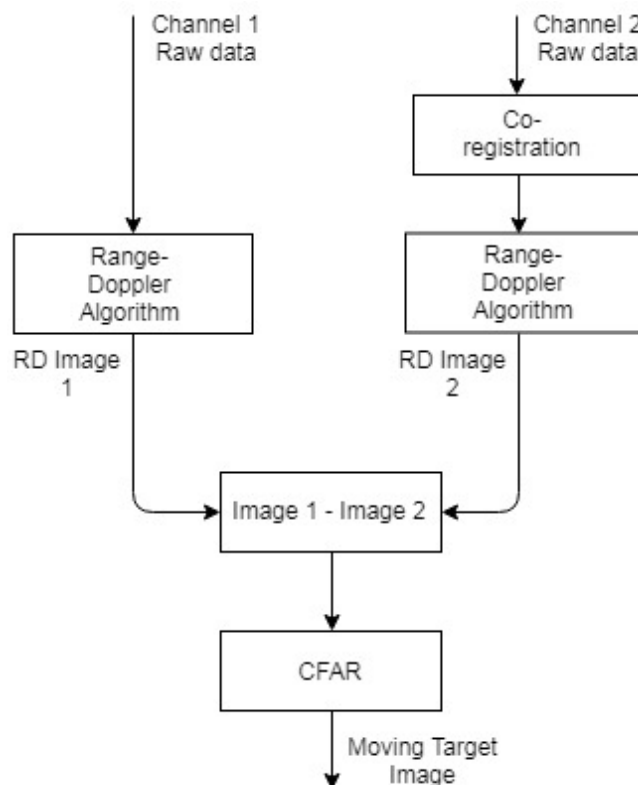


Figure 7.1: Steps followed in applying DPCA.

During analysis, the received target and clutter power before DPCA processing is extracted from the range-Doppler maps to indicate the SCR before DPCA processing. The target and clutter power is also extracted from the range-Doppler maps after DPCA processing to observe how the technique improved the SCR and indicated the presence of the moving target.

Using 500 Monte Carlo simulation runs, the extracted target and clutter power before and after DPCA processing are plotted as a Probability Density Function (PDF) because both the extracted power values are influenced by Gaussian noise in the simulated data sets. From this, the mean power before and after DPCA processing were used to assess the performance of the technique.

## 7.2.2 DPCA Detection of Moving Targets within Clutter

Three data sets with one ground moving target each were simulated. One ground moving target was simulated moving east and parallel to the radar in one simulation case, the other target was simulated moving orthogonal towards the radar platform in another simulation case and in the last case the moving target was simulated moving west, parallel and opposite the direction of motion of the radar platform. These simulated cases are illustrated in Figure 7.2. Each case with a moving target was simulated for a period of 30 seconds, recording a total of 45045 pulses with a PRF of 1501.5 Hz. Simulation over a period of 30 seconds allows the radar to observe the ground moving target at various azimuth angles and slant ranges which yields different target radial velocities.

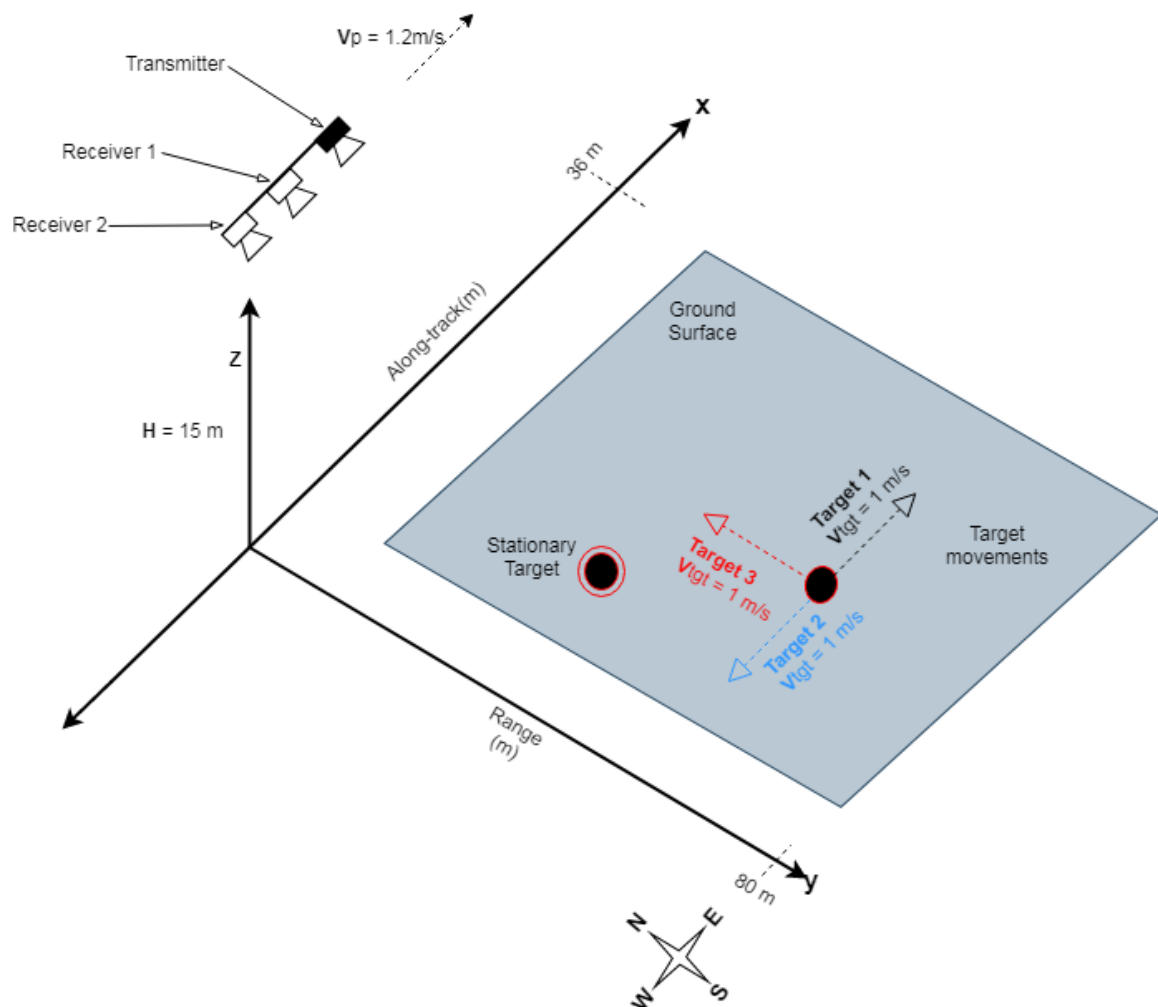


Figure 7.2: Simulated scene with a stationary scatterer and a moving target (copy of Figure 5.1).

### 7.2.2.1 Scenario 1 Pulse No. 12000: Target moving west, parallel and opposite direction to the radar

Considering the simulated data of a target moving west, parallel and opposite direction to the radar and processing 4096 pulses ( $2^{12}$  pulses) from pulse number 12000, results in the range-Doppler map in Figure 7.4. Pulse number 12000 is chosen because at this point the radar has travelled a distance of 9.59 m from its starting point and the velocity of the radar platform has stabilized at an average velocity of 1.2 m/s. The position ( $[x \ y \ z]$ ) of the radar at pulse number 12000 is  $PoP = [(-18+9.59) \ 0 \ 15]$ . The ground target moving west had travelled a distance of 7.99 m from its starting point and its position is  $PoT_2 = [(19-7.99) \ 129 \ 0]$  at pulse number 12000.

Figure 7.3(a) and Figure 7.3(b) show that at this pulse number (12000), the target is expected at a range of approximately 131.3 m with a radial velocity of approximately 0.3255 m/s. Considering the range-Doppler map in Figure 7.4, the moving target is circled with black and stationary target circled with white. From this figure, is seen that the moving target is at the expected range and radial velocity as per Figure 5.3 and Figure 7.3(b).

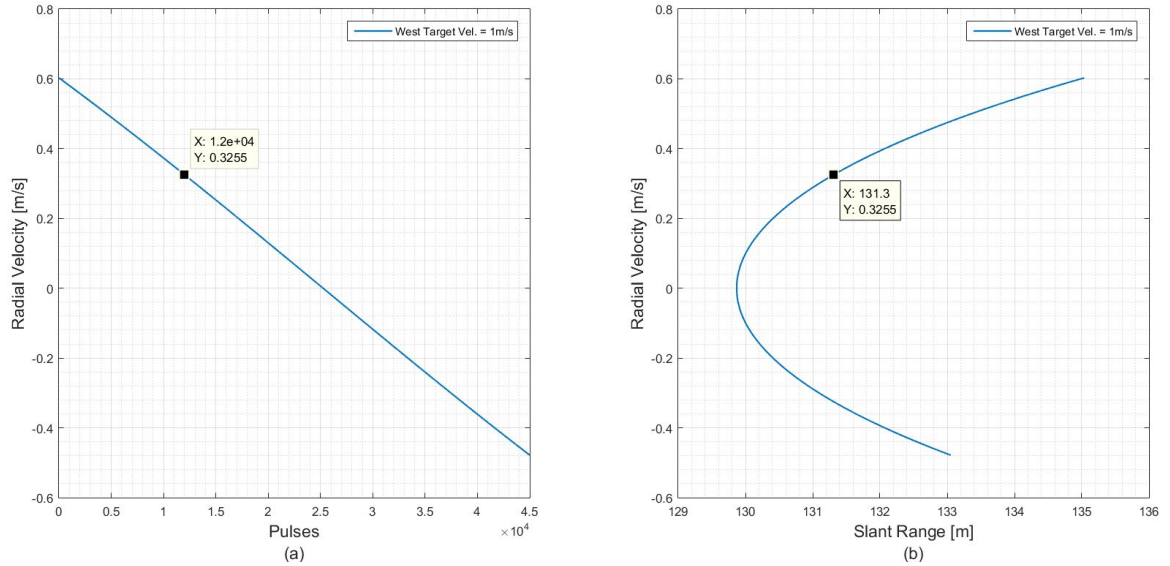


Figure 7.3: (b) Expected range and (a) Expected radial velocity of target moving west at pulse number 12000.

Extracting the target plus noise power and clutter plus noise power from 500 Monte Carlo simulations, before applying DPCA, at pulse number 12000 results in the PDFs presented in Figure 7.5(a). The mean of the target plus noise PDF from Figure 7.5(a)

is 6.04 dBm and the mean of the clutter plus noise PDF is 6.26 dBm before applying DPCA. Subtracting this mean power values provides a SCR of -0.22 dB.

Following the processing steps outlined in the flowchart in Figure 7.1 to apply DPCA and extract the target plus noise power and clutter plus noise power result in the PDFs of Figure 7.5(b). Subtracting the mean power values of Figure 7.5(b) results in a SCR of 11.52 dB after applying DPCA. The total SCR improvement achieved by applying DPCA for a target moving west is found as 11.74 dB. This SCR improvement is for a target at an azimuth angle of  $81.44^\circ$  and a radial velocity of 0.3 m/s as detected by the radar. This azimuth angle was determined by the position of the radar and target at pulse number 12000. The DPCA technique was able to improve the presence of the signal power to the clutter power by 11.74 dB and hence indicating the moving target within clutter.

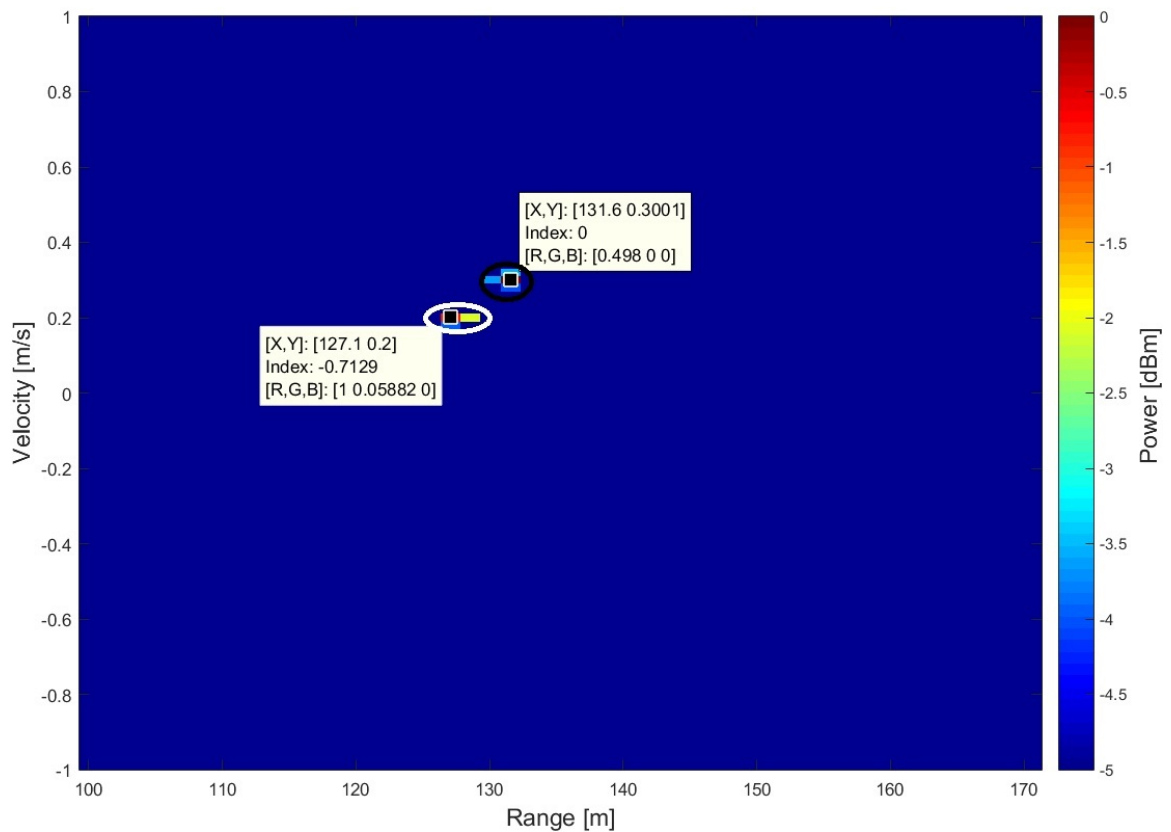


Figure 7.4: Range-Doppler map of target moving west at pulse number 12000.

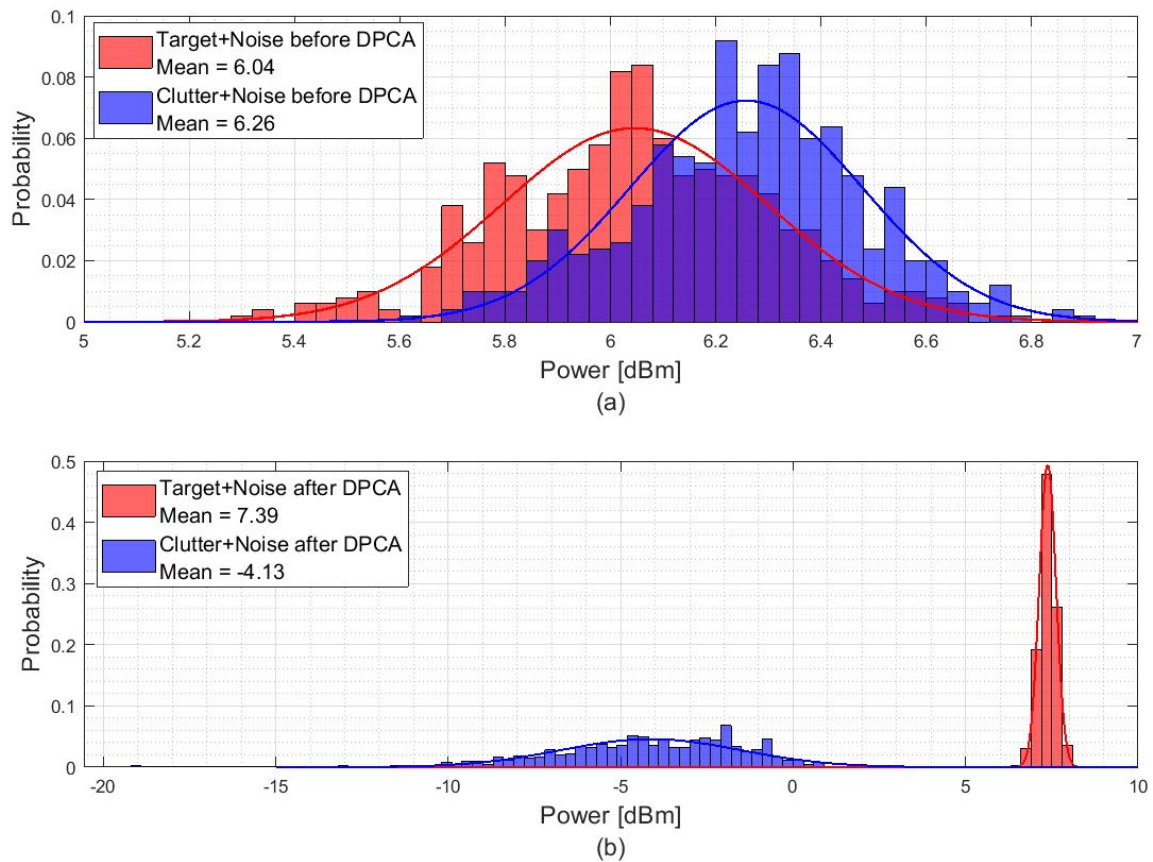


Figure 7.5: PDFs for target moving west from pulse 12000. (a) Clutter plus Noise PDF and Target plus Noise PDF before DPCA, (b) Clutter plus Noise PDF and Target plus Noise PDF after DPCA.

### 7.2.2.2 Scenario 1 Pulse No. 24200: Target moving west, parallel and opposite direction to the radar

The SCR improvement after applying DPCA for a target moving west was also explored at a different radar and target position and hence a different azimuth angle relative to the radar. This was achieved by processing the simulated data from pulse number 24200 of a target moving west.

Figure 7.6(a) and Figure 7.6(b) show that from pulse number 24200, the moving target is expected at a range of approximately 129.9 m with a radial velocity of approximately 0.02627 m/s.

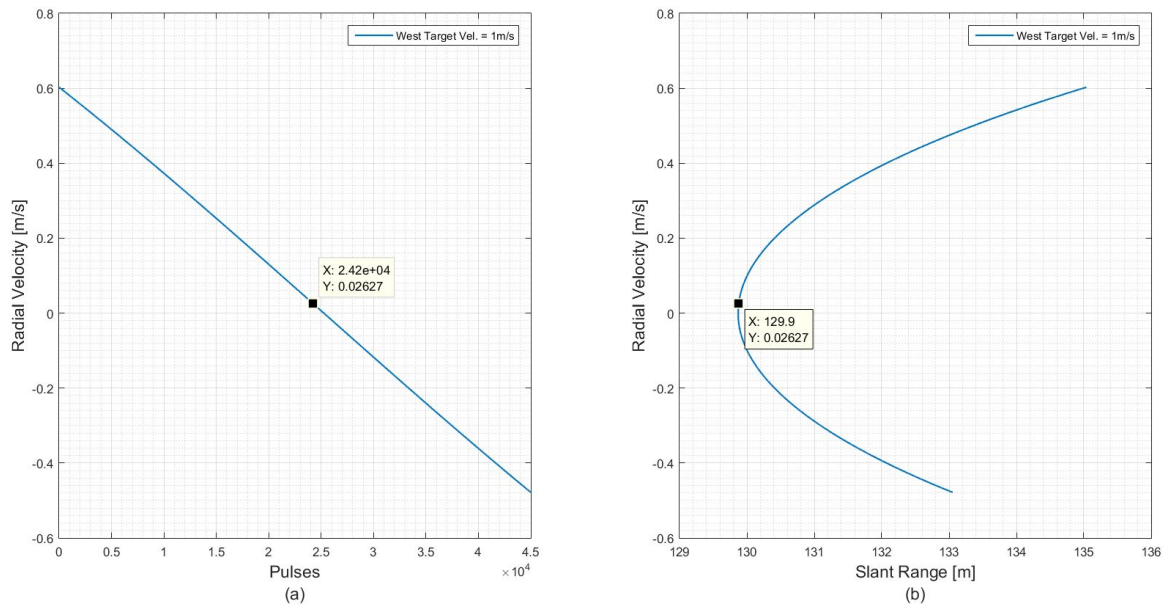


Figure 7.6: (b) Expected range and (a) Expected radial velocity at pulse number 24200 for target moving west.

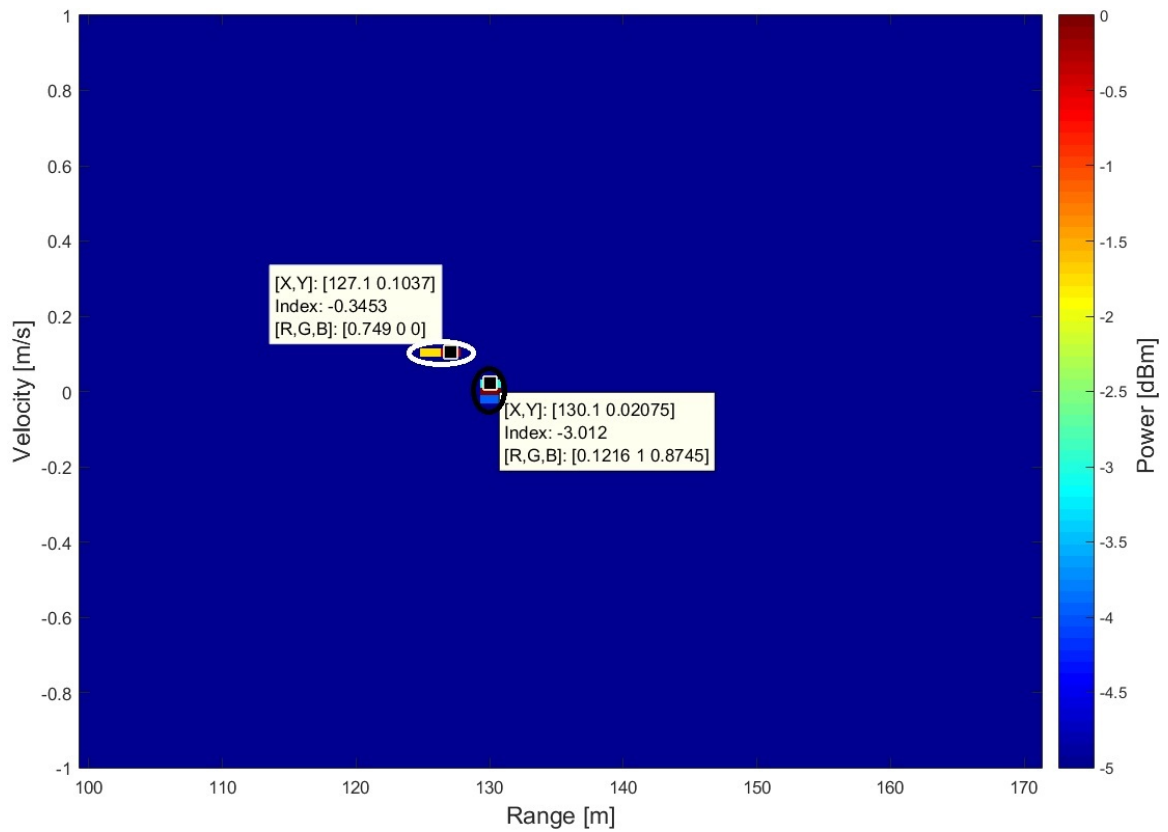


Figure 7.7: Range-Doppler map of target moving west at pulse number 24200.

Figure 7.7 presents a range-Doppler map with a stationary clutter circled with white and a moving target circled with black. The moving target is observed as being at the expected range and radial velocity after processing 4096 pulses from pulse number 24200. The radar had travelled 19.34 m from its starting point at pulse number 24200, putting it at position  $PoP = [(-18+19.34) \ 0 \ 15]$ . The target had travelled 16.12 m from its initial position placing it at position  $PoT_2 = [(19-16.12) \ 129 \ 0]$ . The azimuth angle to the target, in reference to the radar, is found to be  $89.32^\circ$  at a start pulse number of 24200.

The PDFs resulting from extracting the target plus noise and clutter plus noise power from the range-Doppler maps of a target moving west from pulse number 24200 are presented in Figure 7.8(a) before applying DPCA.

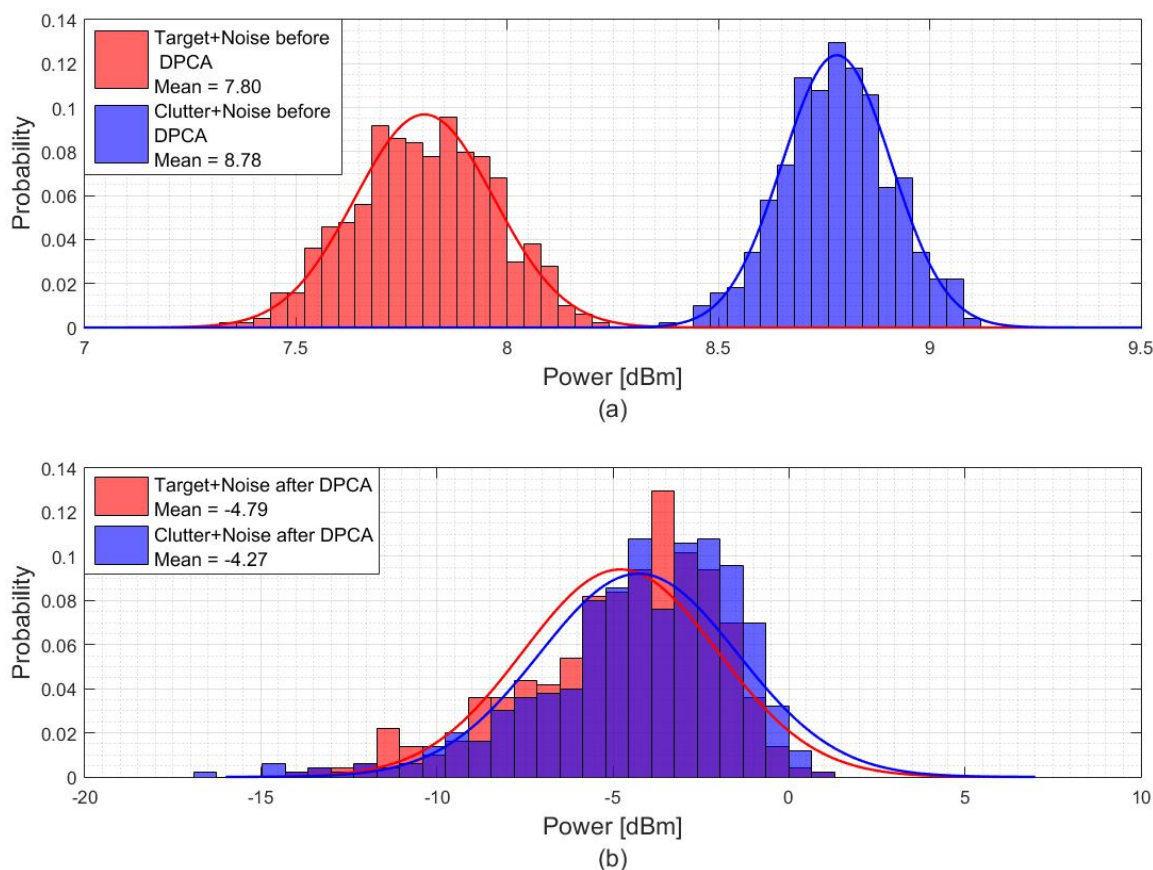


Figure 7.8: The PDFs for target moving west from pulse 24200. (a) Clutter plus Noise PDF and Target plus Noise PDF before DPCA, (b) Clutter plus Noise PDF and Target plus Noise PDF after DPCA.

The SCR before applying DPCA is calculated as -0.98 dB using the mean power values of Figure 7.8(a). After co-registering the two channels and applying DPCA, the

PDFs in Figure 7.8(b) are obtained. The SCR after DPCA processing is calculated as -0.52 dB using the mean power values of Figure 7.8(b). The total SCR improvement is found as 0.46 dB for a target moving west at an azimuth angle of  $89.32^\circ$  and a radial velocity of 0.02 m/s.

It can be observed that the SCR improvement of the DPCA technique and hence the ability of the technique to indicate moving targets within clutter decreases as the azimuth angle to the moving target increases towards  $90^\circ$ . This is expected, since the radial velocity observed by the radar approaches zero and eventually the radar observes the target as stationary (in terms of radial velocity) at an azimuth angle of  $90^\circ$ .

### 7.2.2.3 Scenario 2 Pulse No. 2048: Target moving east, parallel and same direction as the radar

The SCR improvement of the DPCA technique was investigated further on data simulated with a ground target moving east, parallel and same direction as the radar (target 1 from Figure 5.1). Figure 7.9(a) and Figure 7.9(b) present the expected radial velocity change and slant range change of a target moving east, parallel and same direction as the radar for a duration of 30 s over 45045 pulses. Processing 4096 pulses of the simulated data from pulse 2048 gives the range-Doppler map in Figure 7.10 with stationary clutter circled with white and moving target circled with black.

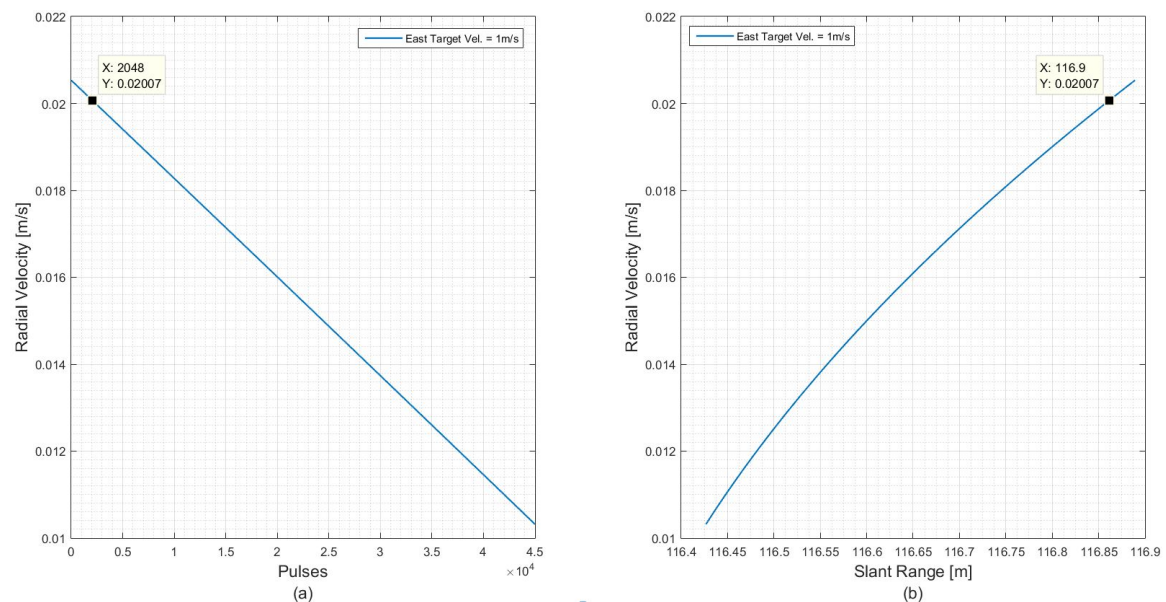


Figure 7.9: (b) Expected range and (a) Expected radial velocity at pulse number 2048 for target moving east (target 1).

At pulse 2048, the radar had travelled a distance of 1.64 m from its starting position, placing it at position  $PoP = [(-18+1.64) \ 0 \ 15]$ . The ground moving target had travelled 1.36 m from its initial position, placing it at position  $PoT_1 = [(-6+1.36) \ 115.3 \ 0]$ . The expected range and radial velocity of the target at this pulse number is approximately 116.9 m and 0.02 m/s respectively. From the range-Doppler map in Figure 7.10 one can observe that the range and radial velocity of the target is as expected in Figure 7.9(b).

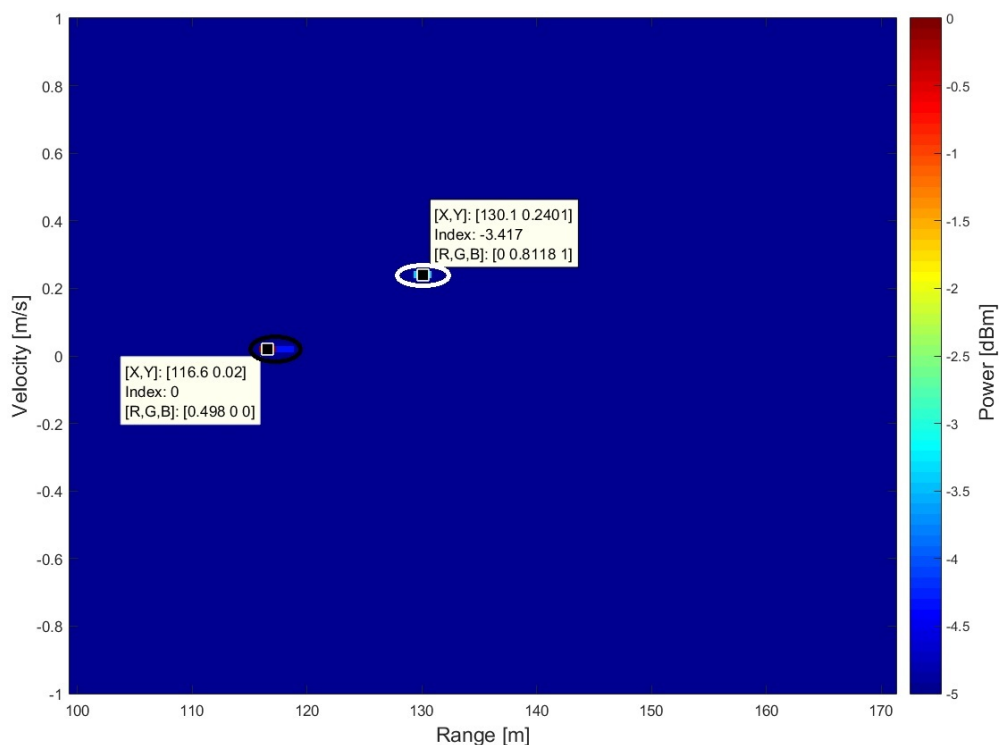


Figure 7.10: Range-Doppler map of target moving east at pulse number 2048.

Figure 7.11(a) presents the PDFs of clutter plus noise power and target plus noise power, plotted from 500 Monte Carlo simulations of a target moving east from pulse number 2048. The difference of the mean power indicated in Figure 7.11(a) give a SCR of 2.56 dB before DPCA processing. Co-registering the radar channels and applying DPCA technique results in a SCR of 13.79 dB as evaluated from the mean power levels indicated in Figure 7.11(b). The total SCR improvement achieved by DPCA technique is 11.23 dB for a target moving east processed from pulse number 2048 over 4096 pulses ( $2^{12}$ ). This SCR improvement show that the DPCA technique is able to suppress clutter and enhance the presence of a moving target as the mean power of the target in Figure 7.11(b) is observed to be higher than the mean power of clutter. The azimuth angle to the target at this pulse number is calculated as  $84.19^\circ$  and the radial velocity detected by the radar is 0.02 m/s.

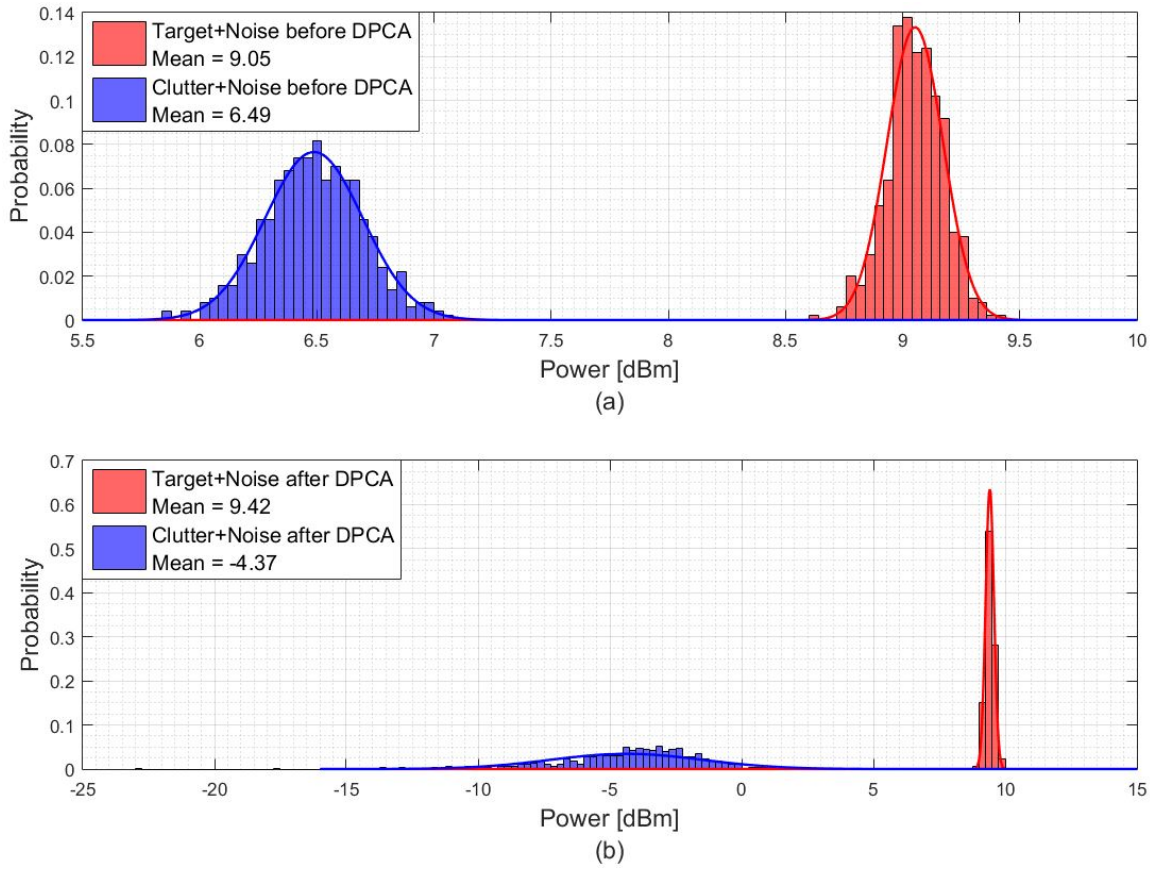


Figure 7.11: The PDFs for target moving east from pulse 2048. (a) Clutter plus Noise PDF and Target plus Noise PDF before DPCA, (b) Clutter plus Noise PDF and Target plus Noise PDF after DPCA.

#### 7.2.2.4 Scenario 2 Pulse No. 18000: Target moving east, parallel and same direction as the radar

The data simulated with a target moving east, parallel and same direction as the radar, was again processed at a different start pulse number and hence a different radar and target position. The data were processed from pulse number 18000. At this pulse number, the azimuth angle to the target relative to the radar is found as  $85, 24^\circ$ . The expected range and radial velocity of an east moving target at this pulse number is approximately 116.7 m and 0.0165 m/s respectively as shown in Figure 7.12. Figure 7.13 presents the range-Doppler map of a target moving east processed from pulse number 18000 over 4096 pulses. The moving target is circled with black at the expected range and radial velocity and the stationary scatterer is circled with white.

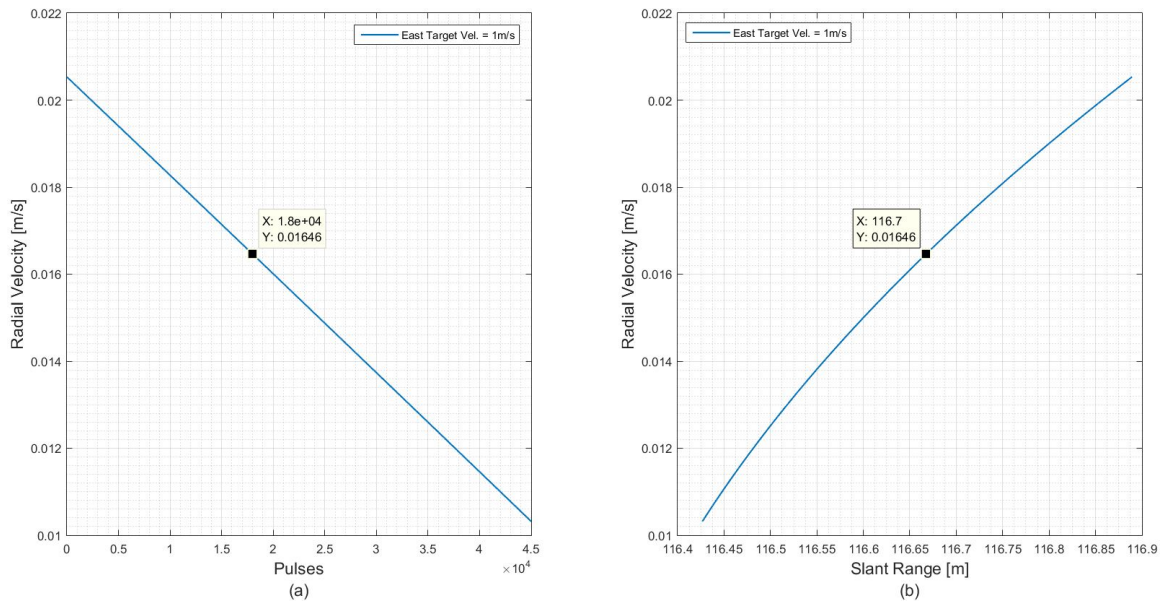


Figure 7.12: (b) Expected range and (a) Expected radial velocity at pulse number 18000 for target moving east (target 1).

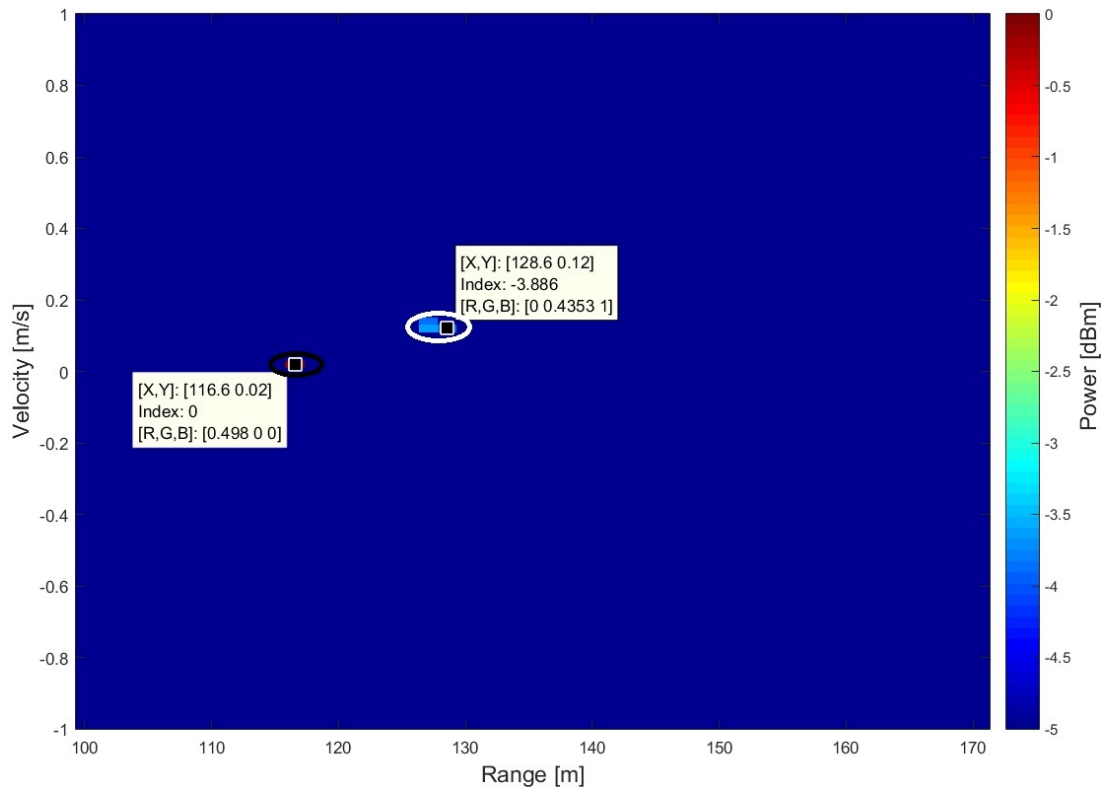


Figure 7.13: Range-Doppler map of target moving east at pulse number 18000.

Figure 7.14(a) presents the PDFs plotted with clutter plus noise and target plus noise

from 500 Monte Carlo simulation at pulse number 18000 before DPCA processing. The difference of the mean power values of Figure 7.14(a) give a SCR of 2.54 dB before DPCA processing. After DPCA processing, the SCR is improved to 13.36 dB. This gives a total SCR improvement of 10.82 dB for the target azimuth angle of  $85, 24^\circ$  in reference to the radar and detected radial velocity of 0.016 m/s. It can be observed that as the azimuth angle to the target increases towards  $90^\circ$  and the radial velocity detected by the radar decreases, the SCR improvement decreases. This is because the target starts to be suppressed by the DPCA technique similar to the stationary clutter and hence hinders the detection of the moving target.

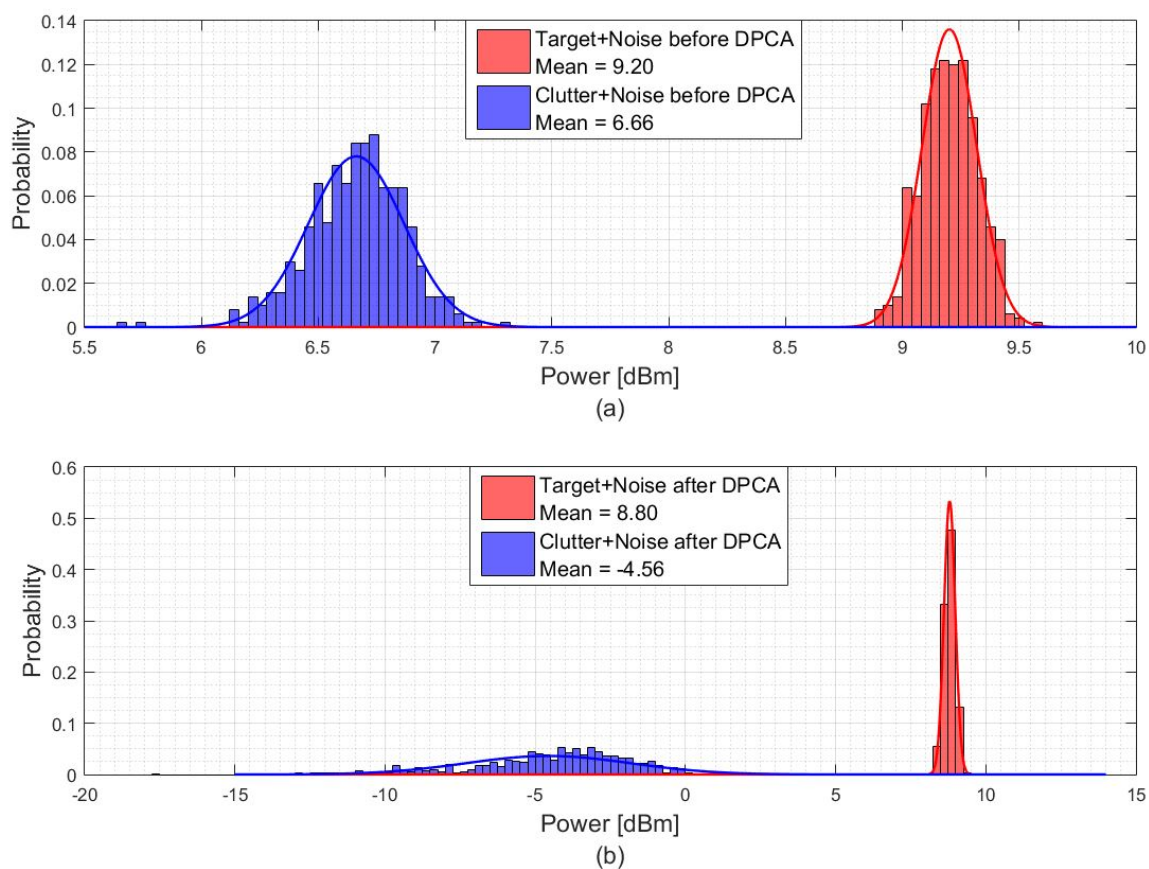


Figure 7.14: The PDFs for target moving east from pulse 18000. (a) Clutter plus Noise PDF and Target plus Noise PDF before DPCA, (b) Clutter plus Noise PDF and Target plus Noise PDF after DPCA.

### 7.2.2.5 Results Summary

Table 7.1 presents a summary of the results obtained from the conducted investigation above. The DPCA technique is able to improve the SCR and indicate the ground moving target for targets moving east (target 1) and targets moving west (target 2).

However, the SCR improvement and hence ability to distinguish moving targets from stationary scatterers, depend on the resulting radial velocity ( $V_{r_{P0}}$ ) of the moving target with the platform velocity arrested. This radial velocity ( $V_{r_{P0}}$ ) is calculated after arresting the motion of the radar platform. The motion of the radar platform is arrested by introducing a pulse shift in the aft channel and co-registering the two channels. This radial velocity decreases to zero as the azimuth angle between the radar and the moving target tends to  $90^\circ$ . The radial velocity,  $V_r$ , is determined by taking both the radar platform velocity and the moving target ground velocity into consideration. Equation 7.1 introduced in Chapter 2 Subsection 2.2.2 describes the expected DPCA response of a moving target [12].

$$z_{DPCA} = \left| a \sin \left( \frac{\pi d V_{r_{P0}}}{\lambda V_p} \right) \right| \quad (7.1)$$

Table 7.1: Summary of DPCA SCR improvement results.

Target Dir.	Pulse No.	Azimuth Angle	Radial Vel. ( $V_r$ )	Radial Vel. ( $V_{r_{P0}}$ )	SCR bef. DPCA	SCR aft. DPCA	SCR Imp.
West	12000	$81.44^\circ$	0.33 m/s	0.15 m/s	-0.22 dB	11.52 dB	11.74 dB
West	24200	$89.32^\circ$	0.02 m/s	0.014 m/s	-0.98 dB	-0.52 dB	0.46 dB
East	2048	$84.19^\circ$	0.02 m/s	-0.10 m/s	2.56 dB	13.79 dB	11.23 dB
East	18000	$85.24^\circ$	0.016 m/s	-0.082 m/s	2.54 dB	13.36 dB	10.82 dB

The green graph from Figure 7.15 plots the expected DPCA response presented by Equation 7.1 for a target moving west and opposite direction to the radar (target 2) against radial velocity ( $V_{r_{P0}}$ ). It can be observed that the target power received is expected to decrease as  $V_{r_{P0}}$  of the target tends to zero. This is because the DPCA technique attenuates the target power of slow moving targets. The blue graph from Figure 7.15 plots the obtained DPCA response using the simulated data. It can be observed that the power received from the simulated data also decreases as  $V_{r_{P0}}$  decreases towards zero following the trend of the expected DPCA response, hence explaining the observed behaviour of the DPCA SCR improvement for a target moving west, parallel and opposite direction to the radar. The graphs of Figure 7.15 also indicates that the obtained results correspond to the theoretical results expected.

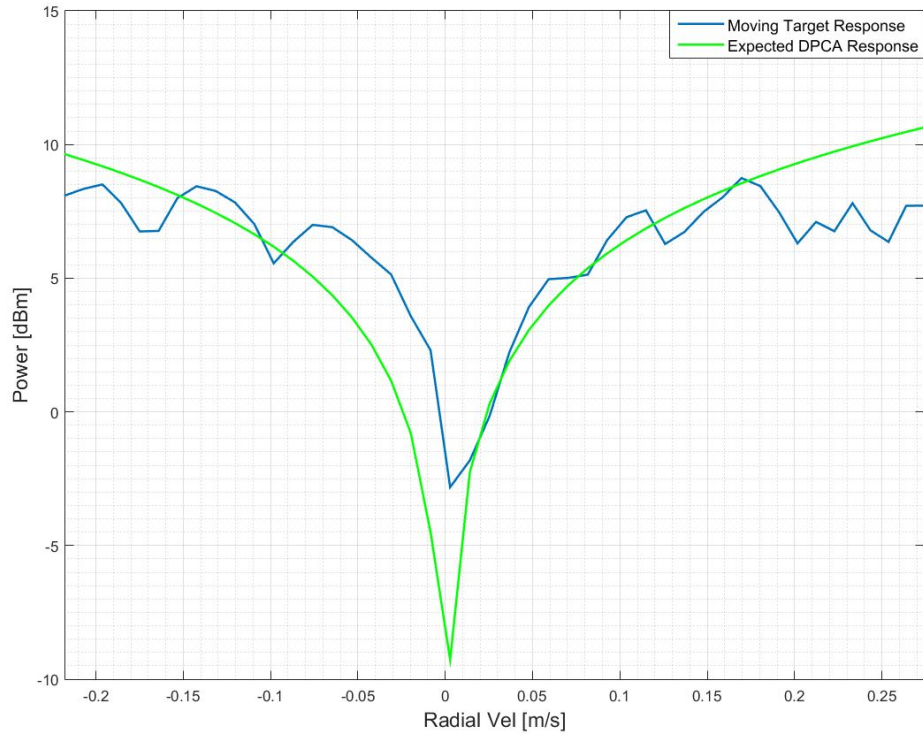


Figure 7.15: DPCA response against target radial velocity ( $V_{rP0}$ ) for a west moving target (target 2).

Figure 7.16 presents the DPCA response for a target moving east and same direction as the radar (target 1). The green graph from Figure 7.16 presents the expected DPCA response for a target moving same direction as the radar using Equation 7.1. The DPCA response plotted show that for the simulated time period (30 s), the radar platform does not pass the position of the east ground moving target (target 1) hence the plotted response does not pass through zero radial velocity ( $V_{rP0}$ ) like the response for a west moving target (target 2). The DPCA response obtained from the simulated data also follow the trend of the theoretical DPCA response as the blue graph from Figure 7.16 shows. It can be seen that the DPCA technique does not attenuate the power of the east moving target at the rate that it attenuates the power of the west moving target. This is due to the fact that the radial velocity of the east moving target does not decrease as fast as that of the west moving target for the simulated period of 30 s. Hence, the SCR improvement for an east moving target (target 1) get less affected than that of the west moving target as observed from Table 7.1.

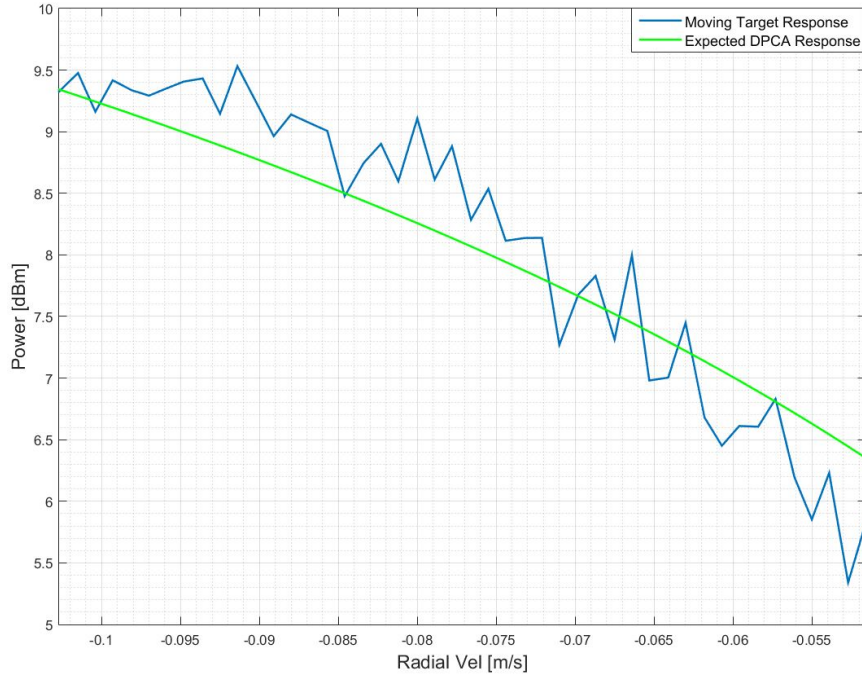


Figure 7.16: DPCA response against target radial velocity ( $V_{r_{P0}}$ ) for an east moving target (target 1).

Ciu and Livingstone in [43] presented that targets are classified as slow moving targets when their radial velocity  $V_r < \lambda V_p / 8d$ . Applying the parameters used to generate the simulated data in this study with antenna baseline  $d = 118.5$  mm, platform velocity  $V_p = 1.2$  m/s and wavelength  $\lambda = 0.0545$  m, the radial velocity ( $V_r$ ) for slow moving targets is found as  $V_r = 0.069$  m/s. This indicates the minimum detectable velocity for the radar used.

### 7.2.3 Sensitivity Analysis for DPCA

The DPCA technique requires precise PRF, platform velocity ( $V_p$ ) and antenna spacing ( $d$ ) match as described by Equation (2.8) in order for it to effectively suppress clutter. Equation (2.8) governs the ping-pong data collection mode discussed in Chapter 2 for correct channel co-registration and application of DPCA. The standard data collection mode is governed by Equation (7.2) for optimal channel co-registration and application of DPCA technique. A mismatch in any of the mentioned parameters ( $V_p$ ,  $d$  and PRF) results in co-registration errors. Co-registration errors are channel misalignments from pulse to pulse which result in an increase in residual clutter after DPCA processing. In this study, the co-registration errors were investigated by introducing additional time delays or pulse shifts on the aft antenna and monitoring the residual clutter after applying DPCA.

The required antenna spacing is  $d = 118.5$  mm from one channel phase center to the other for a PRF of 1501.5 Hz with a platform speed of 1.2 m/s. Data simulated with the standard data collection mode requires that the aft antenna travel half the baseline between the two antenna phase centres. Half the antenna baseline is 59.25 mm and it took 49.375 ms for the phase center of the aft channel to travel half the baseline at radar platform velocity of 1.2 m/s according to Equation (7.2).

$$\Delta T = \frac{d}{V_p} \quad (7.2)$$

For correct channel co-registration in the time domain, the data collected by the aft antenna must be delayed by 49.375 ms. This delay is achieved by discarding the first 74 pulses received by the aft antenna for a PRF of 1501.5 Hz. This ensures that the aft and fore channel are co-registered and optimal clutter suppression is achieved.

Figure 7.17 presents the residual clutter for various pulse shift delays after applying DPCA on data simulated with a target moving east and parallel to the radar. It can be observed that optimal clutter suppression is achieved at pulse shift number 74 as calculated by Equation 7.2. A time delay smaller or greater than 49.375 ms (74 pulses at PRF of 1501.5 Hz) results in an increased residual clutter due to co-registration errors after DPCA processing as Figure 7.17 indicates. An increasing residual clutter decreases the SCR improvement and hence hinders ground moving target detection for DPCA.

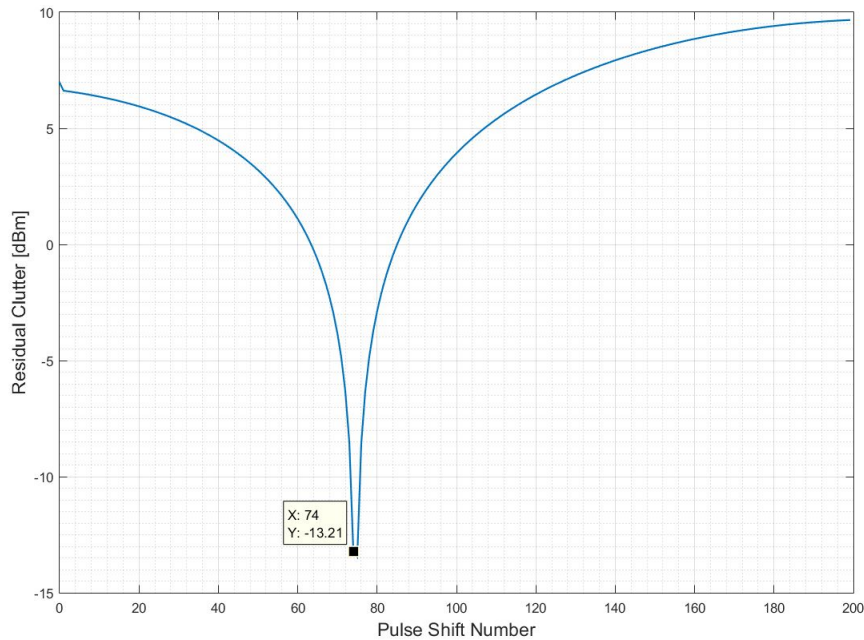


Figure 7.17: Residual clutter plotted against pulse shift number.

## 7.3 GMTI using ATI Technique on Simulated Data

### 7.3.1 Processing Overview

ATI creates a phase interferogram from two SAR images, or two range-Doppler maps. The SAR images are formed from two or more distinct radar channels separated by a distance,  $d$ , in the along track dimension. The channel spacing is designed such that the channels take measurements from the same point in space at very controlled time difference, as described by the data collection modes in Chapter 2. This allows the changes that occur in the scene between the measurements of the two channels from the same point in space, to be detected. The change detected in this case, is the change in phase of a moving target, due to its change in position between observations by the various channels.

The ATI technique is applied by multiplying the conjugate SAR image of channel 1 by the SAR image of channel 2, forming a phase interferogram. This results in zeroing of all phase angles that are equal in channel 1 and channel 2. Equal phase angles from channel 1 and channel 2 will be a result of objects which are stationary. Moving targets will have different phase values in channel 1 and channel 2 (after time delay compensation/co-registration) which will result in non-zero phase residues after conjugate multiplication. Figure 7.18 presents the flowchart followed in applying the ATI technique.

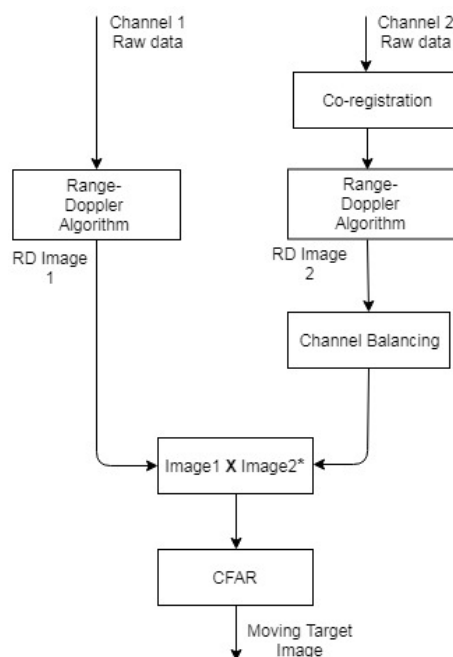


Figure 7.18: Flowchart followed in the application of the ATI technique.

The clutter point scatterer and the moving target point scatterer are simulated in separate positions and hence appear in different range-Doppler bins. As stated in Chapter 5, the complex range-Doppler map cell (amplitude and phase) of clutter is added to the complex range-Doppler map cell of the target in order for the clutter phase to influence the target phase in this study. This is done for both the ATI technique and DPCA technique performance assessment. The two range-Doppler maps are then conjugate multiplied to form an interferogram. This way the phase histories of the moving target will be influenced by the clutter magnitude and phase.

### **7.3.2 ATI Detection of Moving Targets within Clutter**

The data used in this study were simulated over a 30 s period with a PRF of 1501.5 Hz resulting in a total of 45045 pulses. Only a certain portion of this data were processed and used for this investigation. The portions processed correspond to those used in the DPCA technique's investigation. This was done to ensure that the results obtained with the DPCA technique can be compared with the results obtained with the ATI technique.

The clutter phase cancellation extent of the ATI technique was assessed by the phase PDFs plotted from the clutter plus noise phase after applying ATI. The target phase was also assessed using the phase PDFs to determine the mean phase induced by a ground moving target after applying the ATI technique. The resulting target phase was compared to the resulting clutter phase after applying the ATI technique to observe how the technique was able to distinguish the clutter phase from the target phase and indicate the presence of the moving target.

#### **7.3.2.1 Scenario 1 Pulse No. 12000: Target moving west, parallel and opposite direction to the radar**

The data simulated with a target moving west (target 2) was processed from pulse number 12000 over 4096 pulses to form an interferogram. Figure 7.19 presents the interferogram with a moving target phase circled with black and stationary clutter phase circled with white. It can be seen from the interferogram of Figure 7.19 that the phase induced by noise is not cancelled down to zero. This makes the ATI technique prone to false alarms.

The PDF of the mean phase difference of the moving target is presented in Figure 7.20 as well as the mean phase difference of clutter after ATI processing. The phase induced by the target and the clutter are extracted from the positions at which they

were simulated at on the range-Doppler map. It can be observed that the mean noise and clutter phase difference is found as 0.03 radians after applying ATI. The target plus noise mean phase difference is found as 2.16 radians. These residual phase difference results are achieved at a radar azimuth angle of  $81.44^\circ$  to the target. At the exact positions where clutter and target were simulated, it can be observed that the ATI technique is able preserve and indicate the phase of the moving target at 2.16 radians from that of the stationary clutter at 0.03 radians. However, the performance of the ATI technique deteriorates in areas where there is only noise with no stationary scatterers. This is because noise is random and independent from channel to channel hence it does not get cancelled down to zero radians when ATI is applied. This then hinders the visibility and detection of the phase of a moving target in the interferogram as observed in Figure 7.19. Hence without the knowledge of the position and radial velocity of the moving target, the phase of the moving target can not be distinguished from that of noise after applying ATI as Figure 7.19 shows.

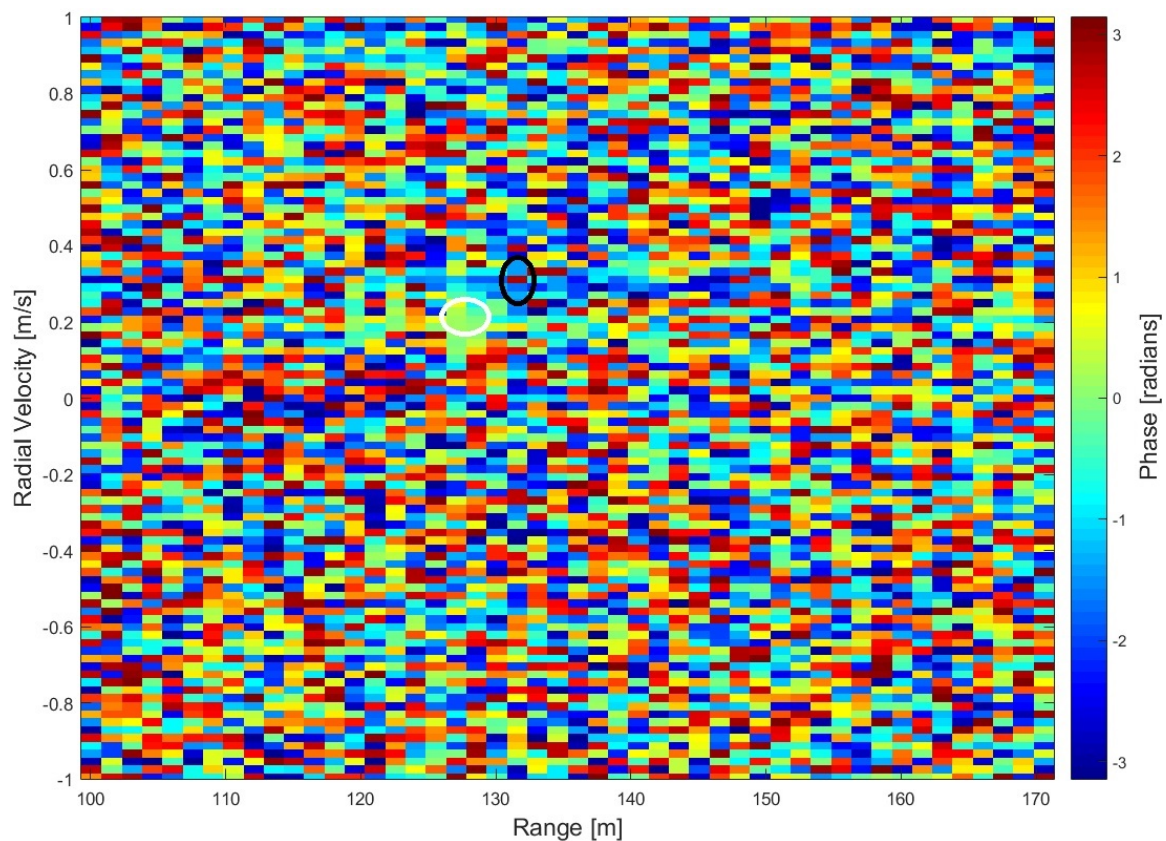


Figure 7.19: Interferogram of a target moving west (target 2) at pulse number 12000.

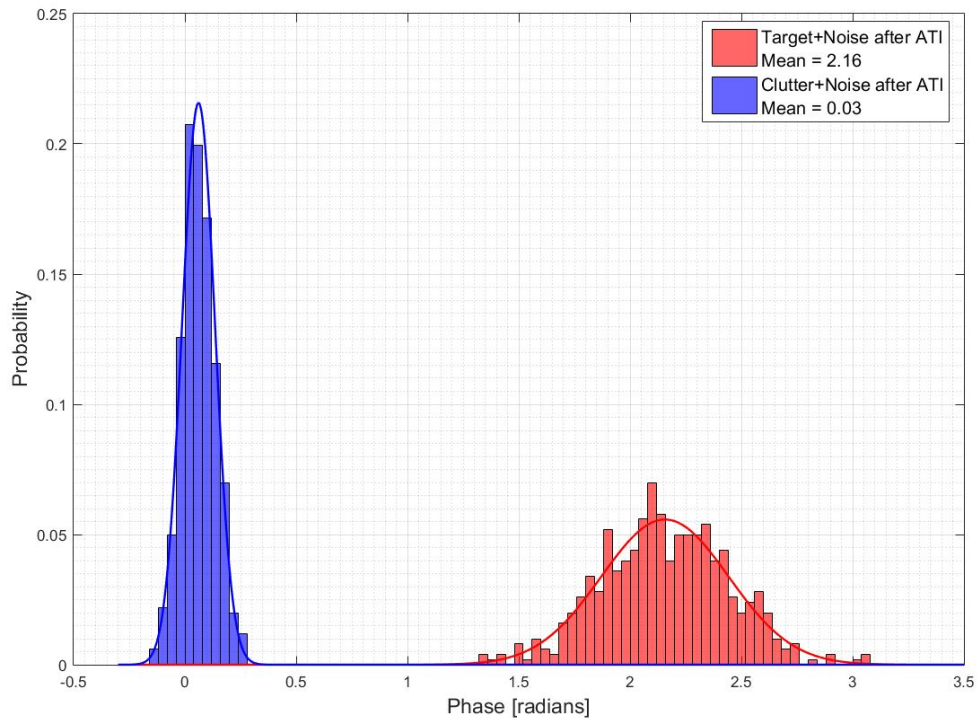


Figure 7.20: Phase PDF of clutter plus noise and phase PDF of target plus noise, for a target moving west (target 2) at pulse number 12000 after applying ATI.

### 7.3.2.2 Scenario 1 Pulse No. 24200: Target moving west, parallel and opposite direction to the radar

The simulated data for a target moving west, parallel and opposite direction to the radar (target 2), was also processed from pulse number 24200 over 4096 pulses. At this pulse number, the radar was observing the ground moving target at an azimuth angle of  $89.32^\circ$ .

Applying the ATI technique and forming an interferogram gave the results presented in Figure 7.21. It can be observed that the phase difference induced by the moving target is not distinguishable from the phase difference of noise after applying the ATI technique. The PDFs in Figure 7.22 display the residual clutter plus noise phase difference and target plus noise phase difference at their expected positions after applying the ATI technique. The mean of the clutter plus noise phase after applying ATI is found as 0.02 radians as observed from Figure 7.22.

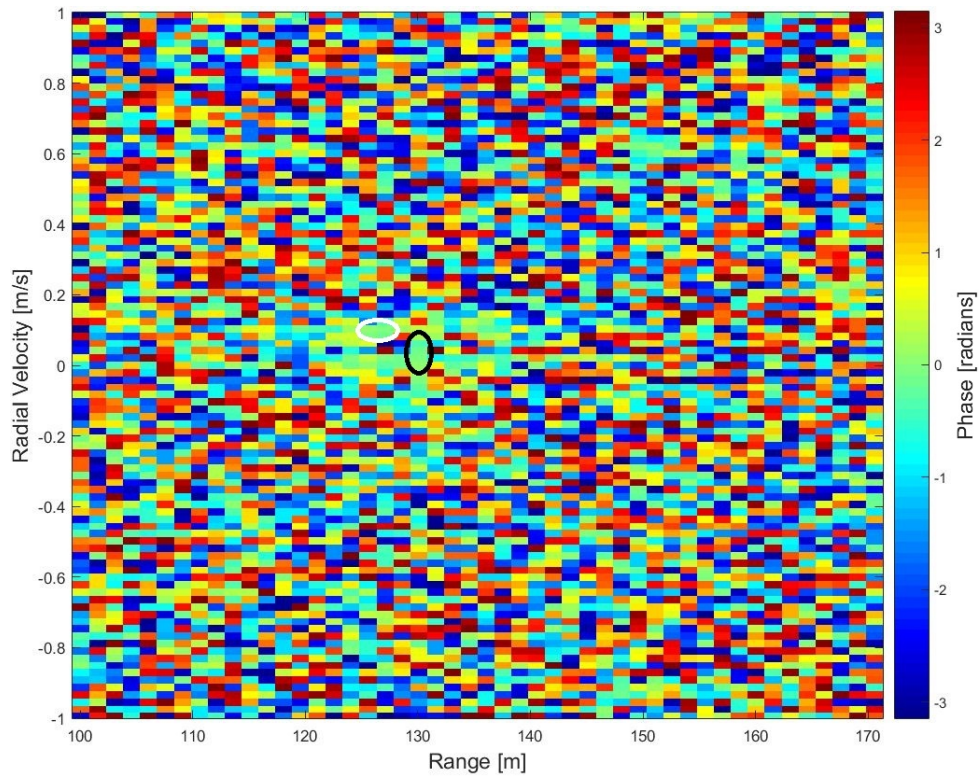


Figure 7.21: Interferogram of a target moving west (target 2) at pulse number 24200.

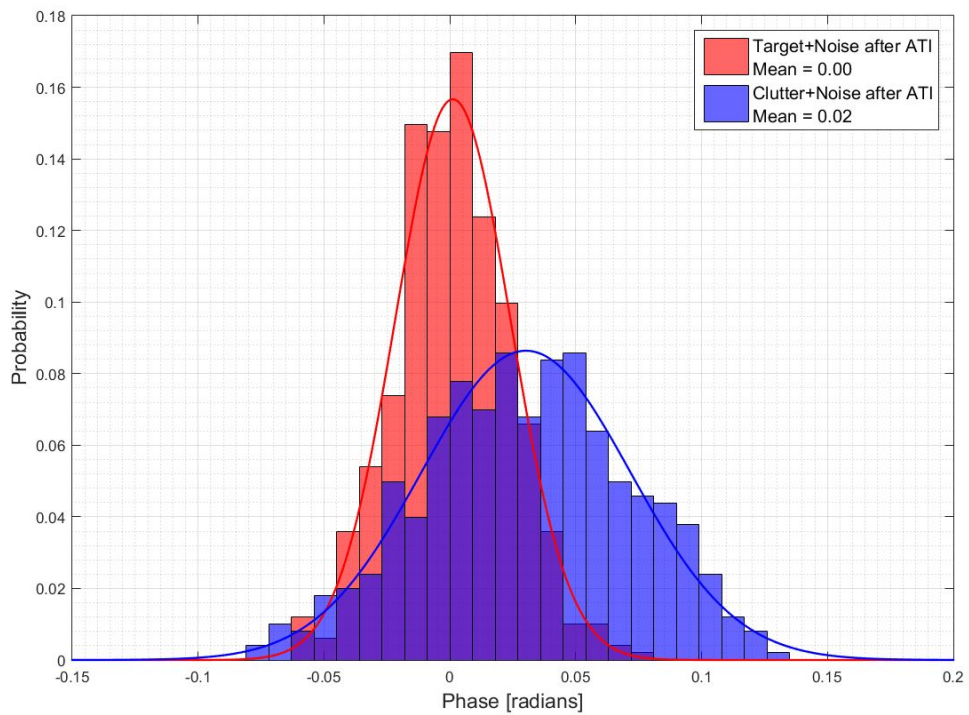


Figure 7.22: Phase PDF of clutter plus noise and phase PDF of target plus noise, for a target moving west (target 2) at pulse number 24200 after applying ATI.

The moving target mean phase after applying the ATI technique is also found as 0.00 radians as shown in Figure 7.22. This is due to the fact that at an azimuth angle of  $89.32^\circ$ , the radial velocity detected by the radar is approaching zero and hence the radar observes the ground moving target as stationary. The presence of random and independent phase noise observed in Figure 7.21 also hinders the ATI technique from indicating the presence of the moving target at this radar azimuth angle. Applying the ATI technique zeros the phase induced by the moving target together with the clutter phase, hence resulting in the interferogram presented in Figure 7.21.

### 7.3.2.3 Scenario 2 Pulse No. 2048: Target moving east, parallel and same direction as the radar

The ability of the ATI technique to achieve a phase difference of zero for stationary clutter and detect the non-zero phase of a ground moving target was also investigated with data simulated with a ground target moving east, parallel and same direction as the radar (target 1). This allowed for the ATI technique to be assessed with a different geometry of the target and radar and also different azimuth angles of the radar to the target.

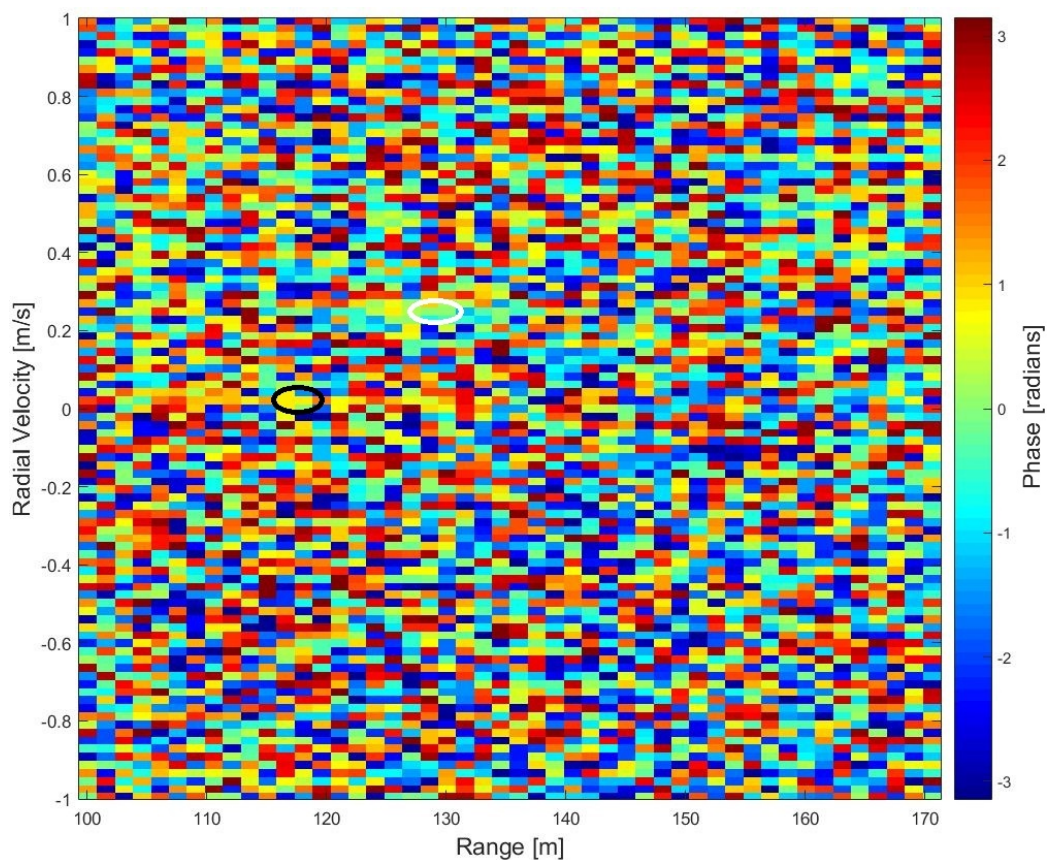


Figure 7.23: Interferogram of a target moving east (target 1) at pulse number 2048.

The data simulated with a target moving east was processed from pulse number 2048 over 4096 pulses to form complex data range-Doppler maps. The ATI technique was then applied to the range-Doppler maps to form an interferogram. The resulting interferogram from data processed from pulse number 2048 is presented in Figure 7.23. At this pulse number the radar is observing the moving target at an azimuth angle of  $84.19^\circ$ . It is seen from Figure 7.23 that the phase of the moving target is undistinguishable from the phase induced by noise after applying the ATI technique. The AWGN present induces random phase which does not subtract to zero when an interferogram is formed because the noise is independent in the two receive channels used to form the interferogram.

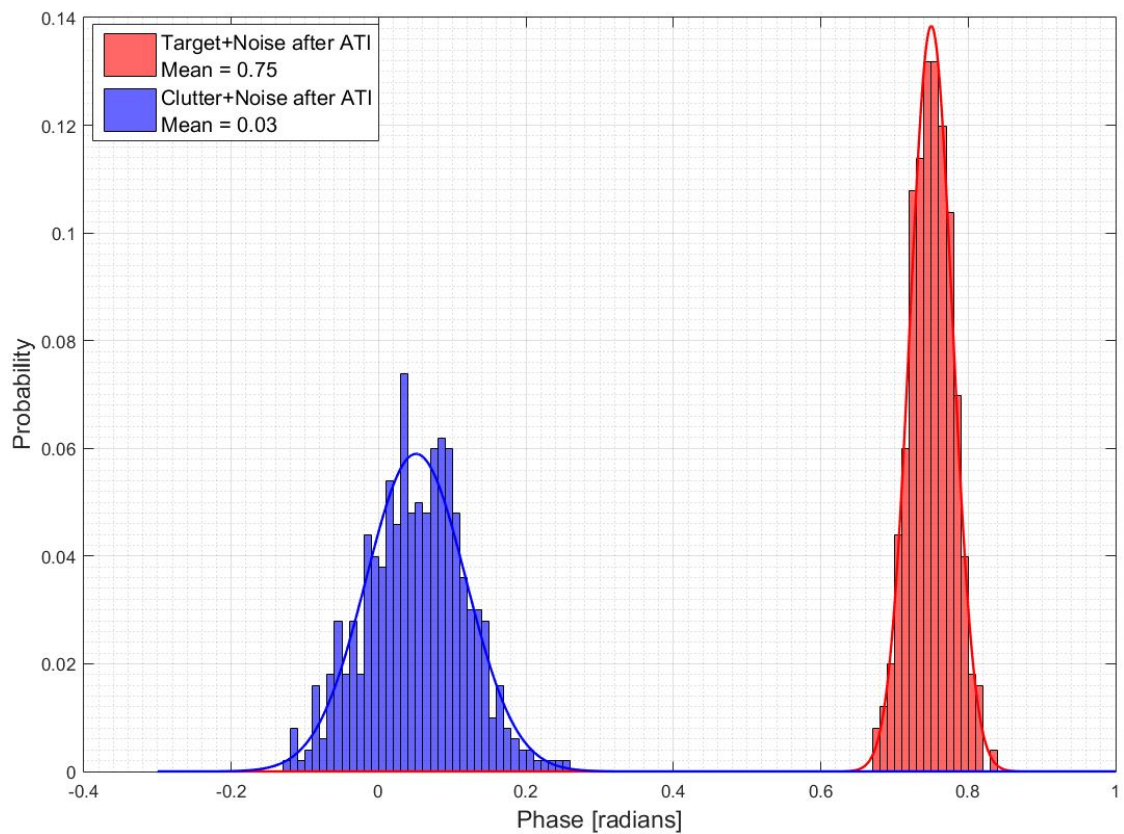


Figure 7.24: Phase PDF of clutter plus noise and phase PDF of target plus noise, for a target moving east (target 1) at pulse number 2048 after applying ATI.

Extracting the residual clutter plus noise phase from the interferograms of 500 Monte Carlo simulations and plotting it into a PDF gave Figure 7.24. The clutter power is extracted from the positions where the clutter was simulated at in generation of the data. It can be observed from Figure 7.24 that after ATI processing the mean clutter phase difference is 0.03 radians. The mean phase difference of the target plus noise

PDF in Figure 7.24 is indicated as 0.75 radians. These results are achieved at the radar azimuth angle of  $84.19^\circ$  to the target.

#### 7.3.2.4 Scenario 2 Pulse No. 18000: Target moving east, parallel and same direction as the radar

The clutter phase cancellation extent of the ATI technique and its ability to indicate moving targets within clutter was investigated further by processing data simulated with a target moving east (target 1) from pulse number 18000 over 4096 pulses. At this pulse number the azimuth angle of the radar to the target was calculated as  $85.24^\circ$ . Applying the ATI technique to the complex range-Doppler map data gave the interferogram shown in Figure 7.25.

Plotting a PDF of clutter plus noise after applying the ATI technique from 500 Monte Carlo simulations gave the PDFs in Figure 7.26. It can be seen that the clutter phase difference after applying the ATI technique is down to a mean of 0.02 radians. The resulting mean target phase difference after applying ATI is found as 1.68 radians from Figure 7.26.

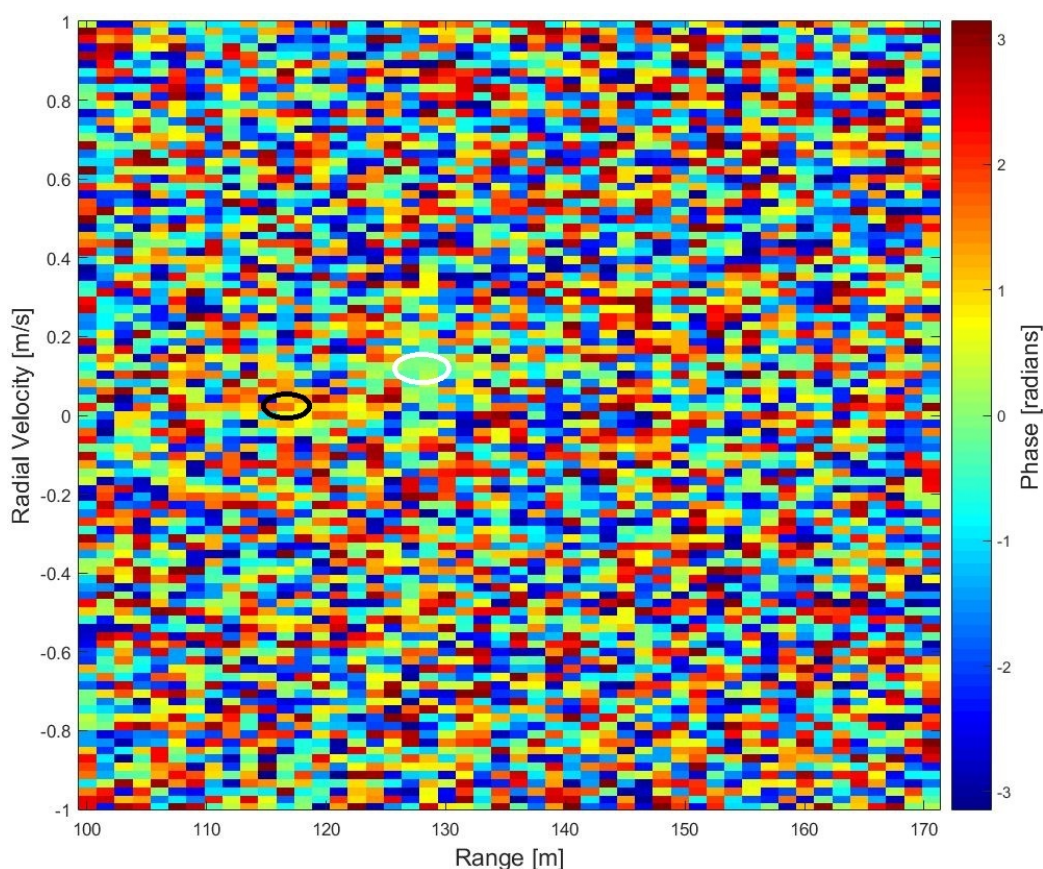


Figure 7.25: Interferogram of a target moving east (target 1) at pulse number 18000.

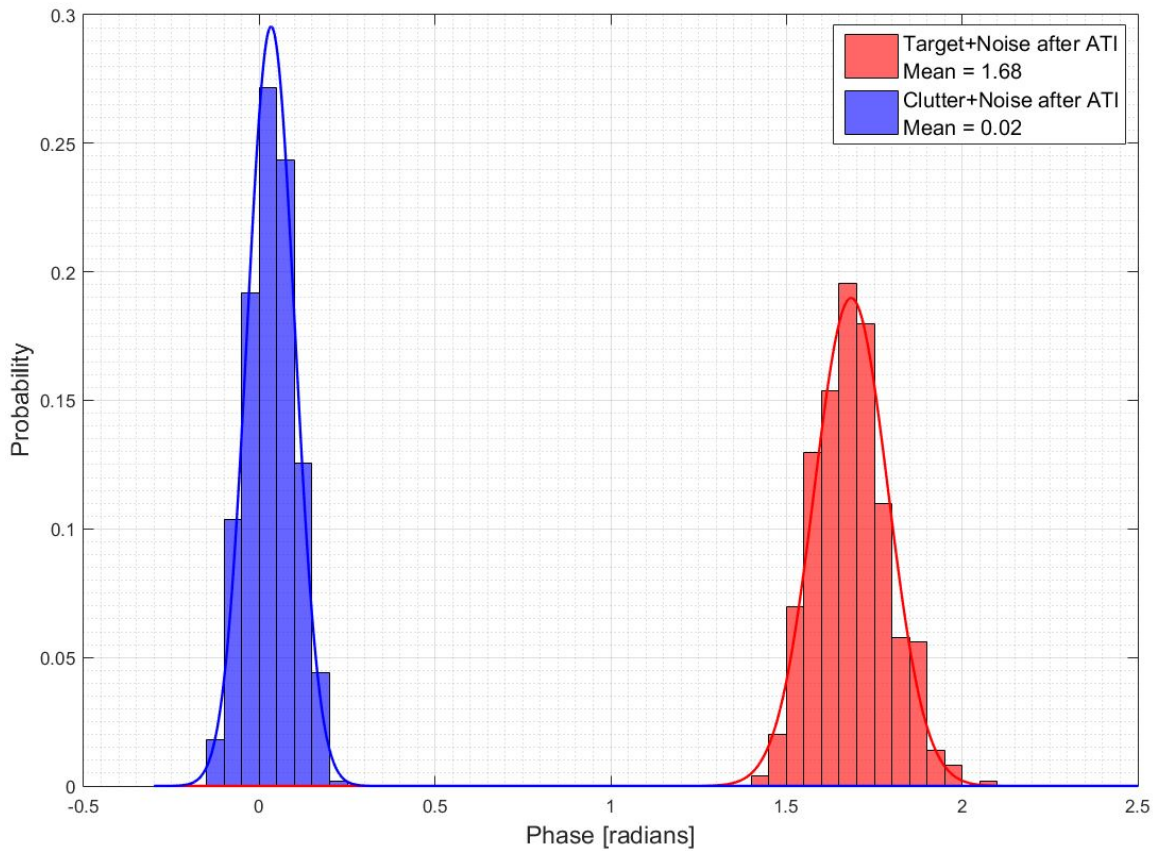


Figure 7.26: Phase PDF of clutter plus noise and Phase PDF of target plus noise, for a target moving east (target 1) at pulse number 18000 after applying ATI.

### 7.3.2.5 Results Summary

The results obtained after applying the ATI technique to the simulated scenarios from Chapter 5 are summarized in Table 7.2. ATI technique was applied on data at different radar and target positions, different azimuth angles and different radial velocities ( $V_r$  and  $V_{rP_0}$ ) to deduce the clutter phase zeroing performance and ability to indicate the moving target phase as the angle between the radar and target changes. The radial velocity,  $V_r$ , is calculated taking into account the radar platform velocity as well as the moving target velocity as plotted on the interferograms. The radial velocity,  $V_{rP_0}$ , is calculated by taking into account only the moving target velocity after arresting the motion of the radar platform by introducing a pulse shift on the aft radar channel and co-registering the two radar channels.

It can be observed from the summary in Table 7.2 that the ATI technique is able to cancel the phase of stationary scatterers at their simulated positions at various azimuth angles and radial velocities ( $V_{rP_0}$ ), however, the ATI technique has a high

false alarm rate due to the phase induced by noise. These phase cannot be subtracted down to zero radians when forming an interferogram because it is random and independent in each channel. To reduce the false alarm rate of the ATI technique, a double threshold approach has to be applied which uses an amplitude threshold together with a phase threshold to distinguish the phase of moving targets from that of clutter and noise as suggested in [19].

Table 7.2: Summary of the clutter phase cancellation performance of the ATI technique.

Target Direction	Pulse Number	Azimuth Angle	Radial Vel. ( $V_r$ )	Radial Vel. ( $V_{rP0}$ )	Clutter Phase After ATI	Target Phase After ATI
West	12000	81.44°	0.33 m/s	0.15 m/s	0.03 radians	2.16 radians
West	24200	89.32°	0.02 m/s	0.014 m/s	0.02 radians	0 radians
East	2048	84.19°	0.02 m/s	-0.10 m/s	0.03 radians	0.75 radians
East	18000	85.24°	0.016 m/s	-0.082 m/s	0.02 radians	1.68 radians

### 7.3.3 Sensitivity Analysis for ATI

The data used in this investigation were simulated with the standard data collection mode presented in Chapter 2. The data were simulated with a PRF of 1501.5 Hz with an antenna spacing of 118.5 mm on a radar platform travelling at 1.2 m/s. The standard data collection mode requires that the aft antenna must travel half the baseline distance between the antennas in order for the data to be able to be used with the ATI technique for ground moving target indication. This ensures that the aft antenna images the same area as the fore antenna at different times and hence detect change that occur in the imaged area.

The requirement of the standard data collection mode for ATI application ensures that the data collected by fore antenna is co-registered with the data collected with the aft antenna. Co-registration of the fore and aft antenna data is important in GMTI and in the application of the ATI technique. Without channel co-registration, the phase of the stationary scatterers from the two radar channels will not subtract down to zero radians because the two radar channels will not be imaging the exact same point in space. The co-registration errors result in an increased amount of residual clutter phase which in turn hinders the phase detection of ground moving targets.

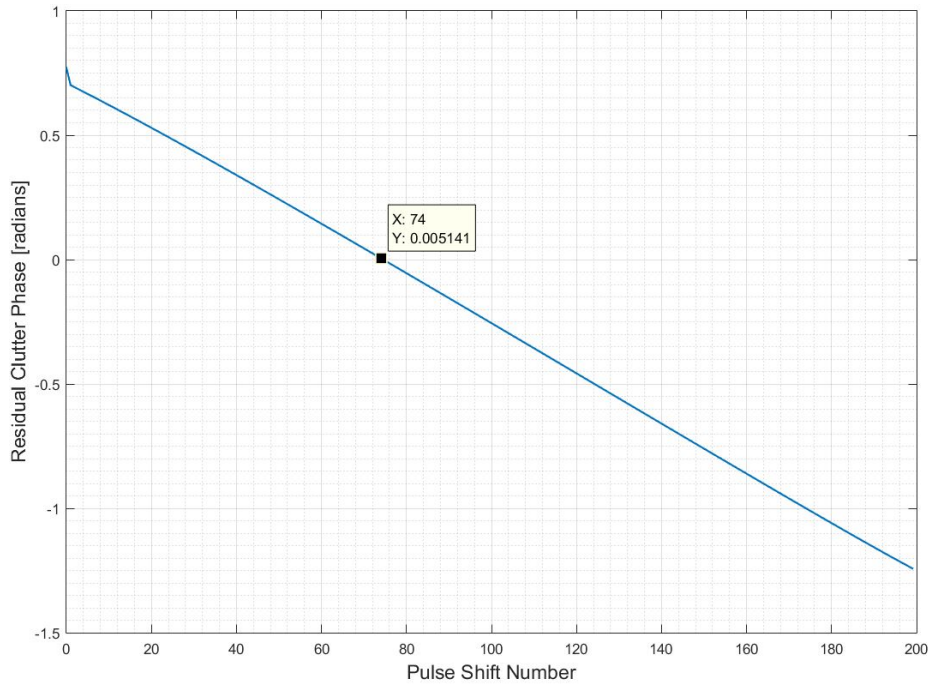


Figure 7.27: Residual clutter phase against pulse shift number for co-registration.

To apply the ATI technique on data simulated with a PRF of 1501.5 Hz, an antenna spacing of 118.5 mm and radar platform velocity of 1.2 m/s, the aft channel data must be delayed by 49.375 ms. This is the time it takes the aft channel to travel half the antenna baseline distance. A time delay of 49.375 ms is equivalent to discarding the first 74 pulses of the aft channel. Figure 7.27 presents a plot of various pulse shifts (time delays) and the residual clutter phase resulting after applying ATI. It can be seen from Figure 7.27 that the clutter phase is cancelled to a minimum of 0.005141 radians at pulse shift number 74, meaning that optimum clutter phase cancellation is achieved at this pulse shift.

## 7.4 Comparison of DPCA and ATI Performance

Two GMTI techniques namely, the ATI technique and the DPCA technique, were implemented and applied on the same simulated multichannel radar data. The GMTI techniques were assessed in terms of their ability to indicate and distinguish moving targets from clutter and sensitivity to errors in their system setup. DPCA technique's ability to indicate moving targets was evaluated based on the residual amplitude and the ATI technique's ability to indicate moving targets was assessed in terms of the resulting interferometric phase from the same two channels.

From the results in Section 7.2, the DPCA technique improved the SCR by 11.74 dB for a target moving west along target path 2 at radial velocity,  $V_r$ , of 0.33 m/s as detected by the radar which corresponds to  $V_{rP0}$  of 0.15 m/s with the platform velocity arrested. For data simulated with a target moving east along target path 1 and processed at a radar azimuth angle of  $84.19^\circ$ , the DPCA technique improved the SCR by 11.23 dB for radial velocity,  $V_r$ , of 0.02 m/s and  $V_{rP0}$  of -0.10 m/s with the platform velocity arrested. This improvement in the signal power presence relative to the clutter power shows that the DPCA technique at this azimuth angle and radial velocity ( $V_{rP0}$ ) is able to indicate and detect moving targets within clutter. Figure 7.28 shows a PDF of target power overlaid with a PDF of clutter power after DPCA processing and it can be observed that the target power is clearly separated and indicated from the clutter power. The PDFs of Figure 7.28 are of a target moving west at pulse number 12000 obtained from the line plots of Figure 7.5(b). This trend is also observed for a target moving east at pulse 2048 and azimuth angle of  $84.19^\circ$ .

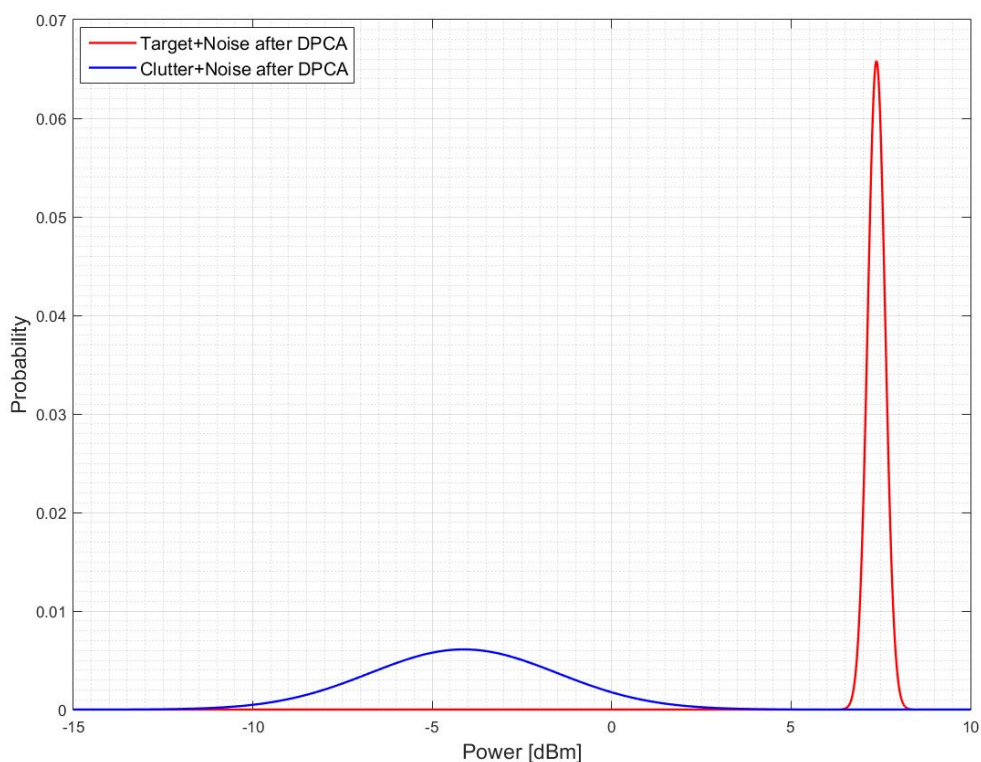


Figure 7.28: Overlaid power PDFs of target and clutter at pulse 12000 after DPCA.

The ATI technique uses the clutter and target phase, not the amplitude information. Stationary clutter phase after ATI processing is expected to be at zero radians since the conjugate multiplication of the same complex data results in cancellation of the phase. The phase of the moving target changes between observations, and thus results

in a non-zero residual phase. For data simulated with a target moving west at an azimuth angle of  $81.44^\circ$ , the phase difference of stationary clutter is found as 0.03 radians after applying the ATI technique. The moving target is detected with a phase of 2.16 radians hence indicating the presence of the target in the data.

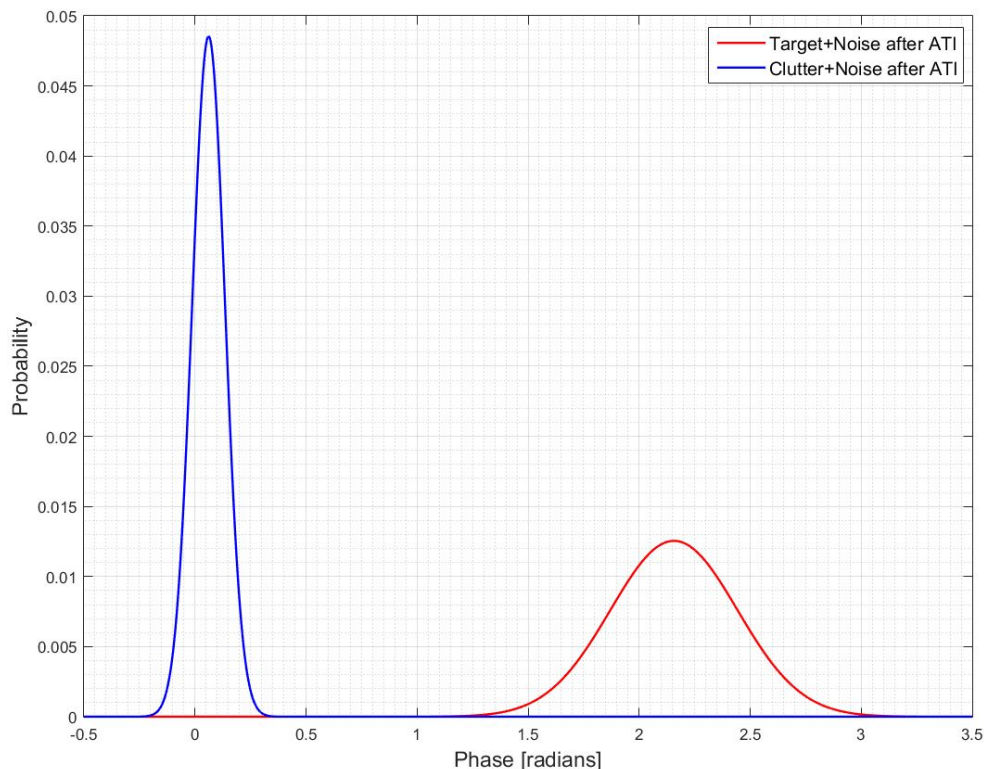


Figure 7.29: Overlaid phase PDFs of target and clutter at pulse 12000 after ATI.

The overlaid phase PDFs in Figure 7.29 illustrates how the ATI technique is able to separate and indicate the target phase from the clutter phase at the azimuth angle of  $81.44^\circ$  and  $V_{rP0}$  of 0.15 m/s. These PDFs are for a target moving west at pulse number 12000 obtained from the line plots of Figure 7.20. This trend is also observed for a target moving east at azimuth angle of  $84.19^\circ$ .

However, at a radar azimuth angle of  $89.19^\circ$  to the target, the residual phase of the moving target at the position that it was simulated at is zero as well as that of the stationary clutter. This shows that as the azimuth angle approaches  $90^\circ$ , the radial velocity ( $V_{rP0}$ ) also approaches zero, hence the radar observes the ground moving target as being stationary. The DPCA technique also has a low SCR improvement of 0.46 dB at this radar azimuth angle and radial velocity of the target. The PDF of the target power and clutter power after DPCA processing displayed in Figure 7.30

show that at the azimuth angle of  $89.19^\circ$ , the technique fails at separating the moving target returns from that of clutter hence giving a poor probability of detection. Figure 7.31 also show the phase PDFs of the target and clutter after ATI processing at the azimuth angle of  $89.19^\circ$  and it can be seen that the target phase and clutter phase are not separated, hence giving a poor target detection probability as well.

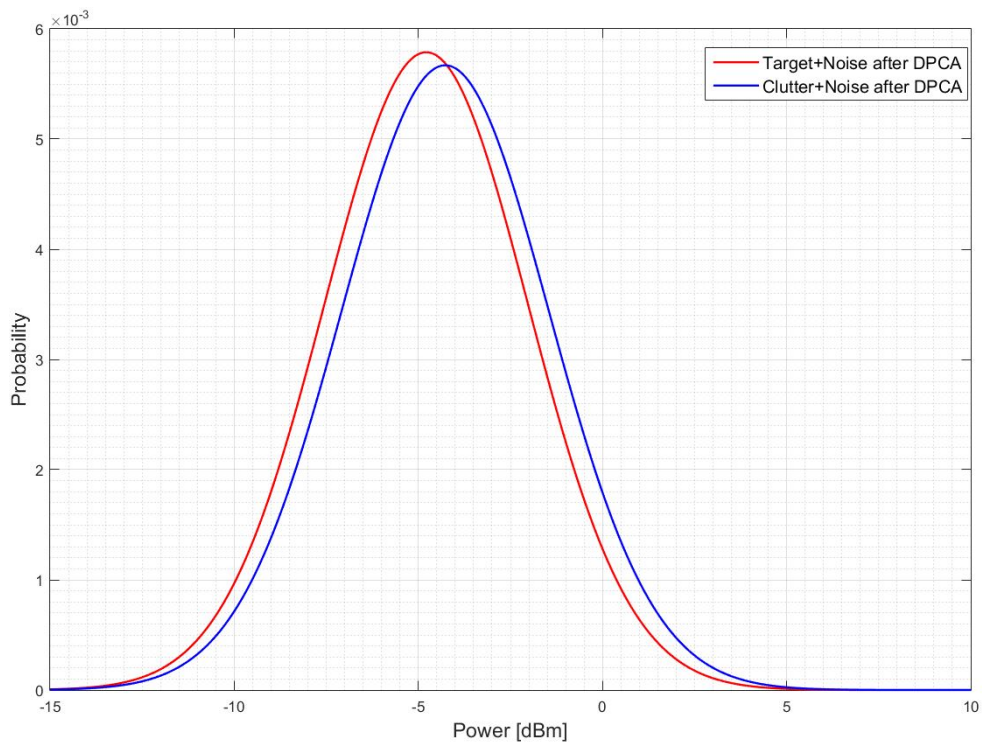


Figure 7.30: Overlaid power PDFs of target and clutter at pulse 24200 after DPCA.

This means that the performance of both the DPCA technique and the ATI technique deteriorates as the radial velocity ( $V_{rP0}$ ) approaches zero. This was verified by Equation 7.1 and Figure 7.15 showing the theoretically expected DPCA response as well as the simulated data DPCA response as the radial velocity ( $V_{rP0}$ ) changes. The results obtained with the simulated data used in this study corresponds to the theoretical expected DPCA response.

At azimuth angles smaller than  $90^\circ$ , both the techniques are able to indicate the ground moving targets within clutter at their simulated positions. However, the ATI technique has high false alarms due to the phase induced by the samples dominated by noise as seen in the interferograms from Subsection 7.3.2. These false alarms can be reduced by using a double threshold approach as outlined in [19]. The DPCA

technique is less sensitive to noise and hence performs superior to ATI in terms of moving target indication in this regard.

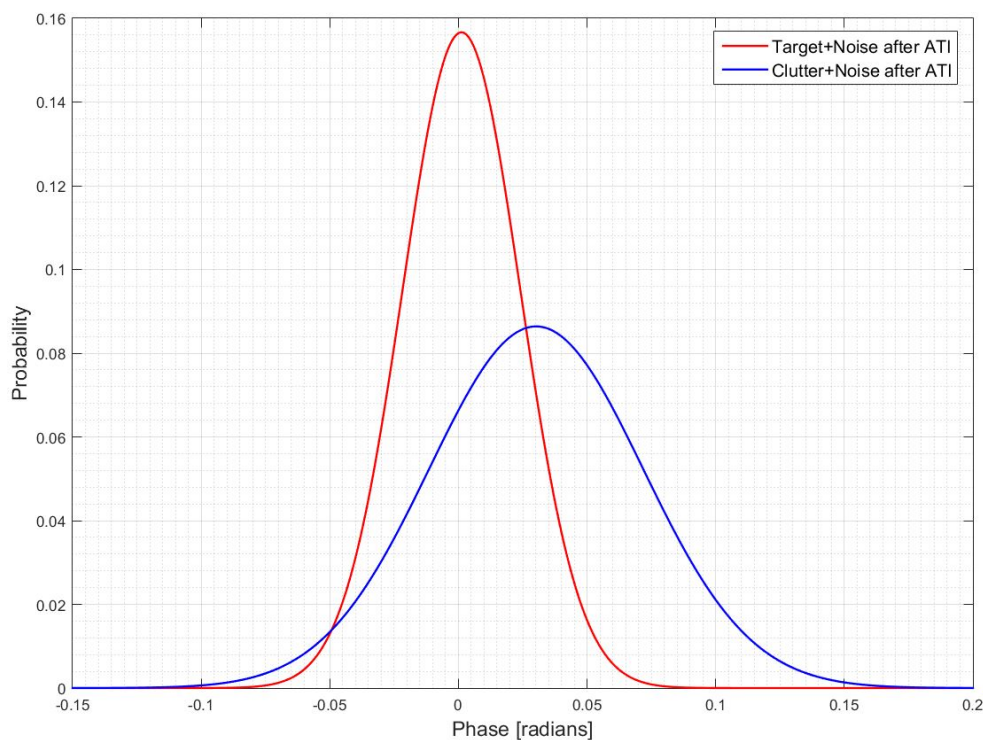


Figure 7.31: Overlaid phase PDFs of target and clutter at pulse 24200 after ATI.

The DPCA technique suppresses clutter well below the power of the ground moving target and the ATI technique indicates the presence of a moving target by zeroing the residual phase of the stationary clutter. However, this is only valid for data collected under ideal conditions. The residual clutter power and clutter phase increases when errors occur during data collection for both the techniques. One example of potential practical non-idealities in the implementation of the techniques can be induced by varying radar platform velocity or channel spacing. The decrease in the clutter cancellation means an increase in the residual clutter power and clutter phase. The increase in the residual clutter power and residual clutter phase result in the increase of false moving target detections.

The DPCA technique and the ATI technique both displayed a degradation of performance as the residual clutter power and residual clutter phase increased due to co-registration errors. Figure 7.32(b) presents the resulting PDFs of target phase and clutter phase after applying ATI technique to data with co-registration errors. This is for a target moving west at pulse 12000 and azimuth angle  $81.44^\circ$ . It can be observed that the target phase is submerged under the clutter phase when ATI is applied to

data with co-registration errors. Comparing Figure 7.32(b) to Figure 7.32(a), it can be observed that the target phase is no longer separated from the clutter phase like in Figure 7.32(a), hence hindering the detection of the phase of the moving target. It is however noted that for ATI, both the positive and negative non-zero residual phase can result in detection of moving targets.

Figure 7.32(d) displays the resulting target and clutter PDFs overlaid for data with co-registration errors after DPCA processing. This is also for a target moving west at pulse 12000 and azimuth angle of  $81.44^\circ$ . Comparing Figure 7.32(d) to Figure 7.32(c), it can be observed that the PDF of the target power after DPCA in Figure 7.32(d) is not as separated and distinguished from the clutter power as it is in Figure 7.32(c). This is due to the co-registration errors which deteriorates the detection probability of the moving target.

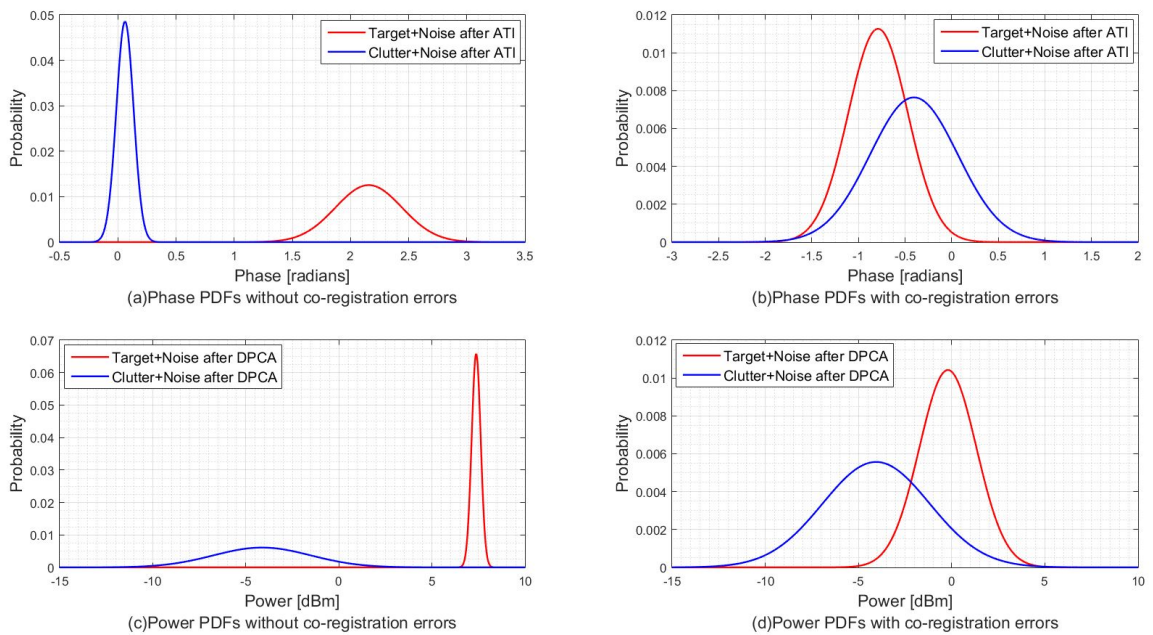


Figure 7.32: (a) Target and clutter phase PDFs without co-registration errors, (b) Target and clutter phase PDFs with co-registration errors, (c) Target and clutter power PDFs without co-registration errors, (d) Target and clutter power PDFs with co-registration errors.

Figure 7.33 shows a plot of the probability of false alarm ( $P_{fa}$ ) against the probability of detection ( $P_d$ ) (Receiver Operating Characteristics (ROC) curves) of the ATI technique as well as the DPCA technique. This is plotted from data with co-registration errors displayed in Figure 7.32(b) and Figure 7.32(d). It can be observed from Figure 7.33 that at a  $P_{fa}$  of 0.1517, the ATI technique has a  $P_d$  of 34.53% while

DPCA technique has a Pd of 80.04%. This shows that the ATI technique is more sensitive to co-registration errors than the DPCA technique, hence making the DPCA technique superior in this regard.

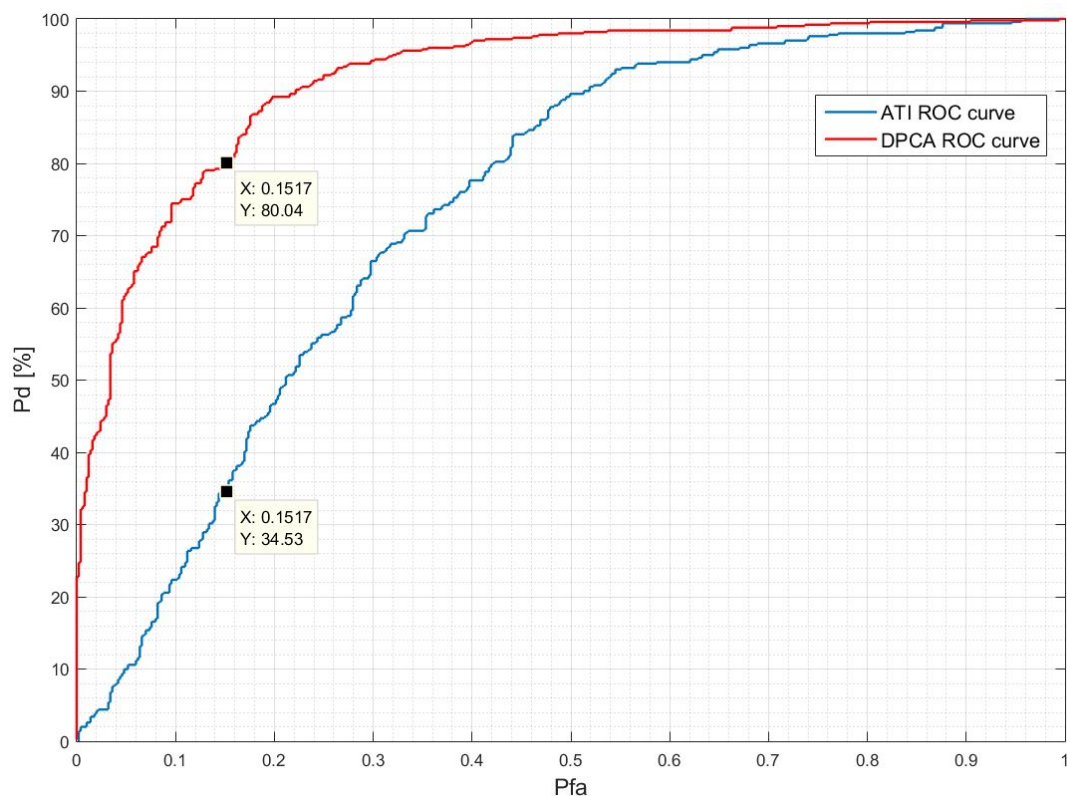


Figure 7.33: Probability of false alarm against probability of detection (ROC curves) for ATI and DPCA technique.

## 7.5 Conclusion

The performance results of DPCA and ATI techniques were discussed separately and presented in detail in this chapter. The two techniques were tested with similar simulated data and both the techniques performed well in enabling the detection of ground moving targets. It was also observed that the two techniques are unable to indicate moving targets at azimuth angles approaching  $90^\circ$  due to the radial velocity ( $V_{rP0}$ ) of the moving target being approximately 0 m/s. The two techniques are affected by co-registration errors, however, the ATI technique showed that it is more sensitive to co-registration errors as it was observed on the plotted ROC curves. Due to this, it is concluded that the DPCA technique on its own is a practical better choice. However, the double threshold approach discussed in [19] performs better than both the ATI technique and the DPCA techniques on their own, in terms of

indicating moving targets within clutter. This approach involves applying DPCA as a preprocessing step to the ATI process and will be discussed in more detail in Chapter 8 Subsection 8.5, where it will be implemented on real radar data. The same GMTI performance assessment performed on simulated data in this chapter will also be conducted on real measured radar data in the following chapter.

# Chapter 8

## Performance Comparison of GMTI Techniques with Measured Radar Data

### 8.1 Introduction

In this chapter, the DPCA and ATI GMTI techniques are applied and evaluated on actual measured radar data. The measured radar data were recorded in a controlled environment with specific structures of interest and moving targets as outlined in Chapter 5. The GMTI techniques are assessed in terms of their ability to indicate and detect moving targets within clutter and their sensitivity to errors due to misaligned system parameters on measured radar data.

### 8.2 GMTI using DPCA Technique on Measured Radar Data

#### 8.2.1 Processing Overview

The steps followed in applying DPCA technique on measured data are as presented in Figure 8.1. The measured radar data are firstly pre-processed before applying the DPCA GMTI technique as observed on the flow diagram in Figure 8.1. The performed pre-processing which includes co-registration and channel balancing was discussed in Chapter 6. The data were recorded over a period of 30 s with a PRF of 1501.5 Hz. The total number of pulses recorded over this period is 45045. In this study, only certain portions of the measured data were processed to investigate the DPCA GMTI technique. The selected portions to be investigated were presented in Figure 5.2 and Figure 5.3 of Chapter 5. These are the same subsections of simulated data that were used to investigate the DPCA technique. This was done so that the

results obtained with simulated data can be compared with the results obtained with measured data.

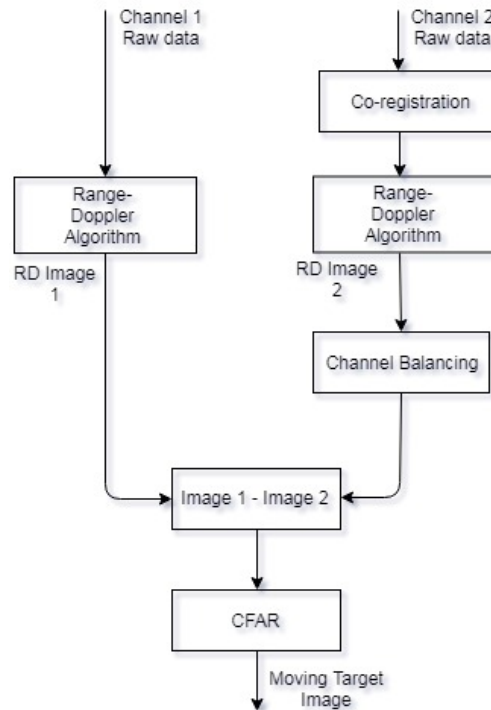


Figure 8.1: DPCA processing applied on measured radar data (copy of Figure 7.1).

## 8.2.2 DPCA Detection of Moving Targets within Clutter

SCR is the ratio of the desired target signal power to the undesired clutter power. SCR can be improved by reducing the amount of the undesired signal (clutter) present in the data without affecting the desired signal. In these measured radar data, clutter signals contaminates the moving target's range-Doppler cell before and after DPCA processing. This limits the calculated SCR. The DPCA technique improves the SCR by suppressing signals from the stationary scatterers (clutter) within the imaged scene while minimally affecting the signal of the moving target. This enables the indication of ground moving targets within clutter. The SCR improvement is used to assess the performance and ability of the DPCA technique to indicate and detect the moving target signal in this study.

### 8.2.2.1 Scenario 1 Pulse No. 12000: Target moving west, parallel and opposite direction to the radar

The scenario of a target moving west, parallel and opposite direction to the radar (target 2) that was simulated in Chapter 5 was also practically measured with a

radar system. The radar setup and parameters were identical to the one used in the simulated data. The measured radar data of a target moving west (target 2) was processed from the data portion starting at pulse number 12000, spanning 4096 pulses. The position  $([x \ y \ z])$  of the radar at this pulse number was  $PoP = [(-18+9.59) \ 0 \ 15]$  meters and the ground moving target was at position  $PoP_2 = [(19-7.99) \ 129 \ 0]$  meters. These are the same radar and target positions investigated with the simulated data. The radar azimuth angle to the target at this position was  $81.44^\circ$ . At this position, the moving target was expected to be at range 131.3 m with radial velocity of 0.3255 m/s as shown in Figure 8.2 displaying the calculated range and radial velocity of a target moving west (target 2) over a period of 30 s.

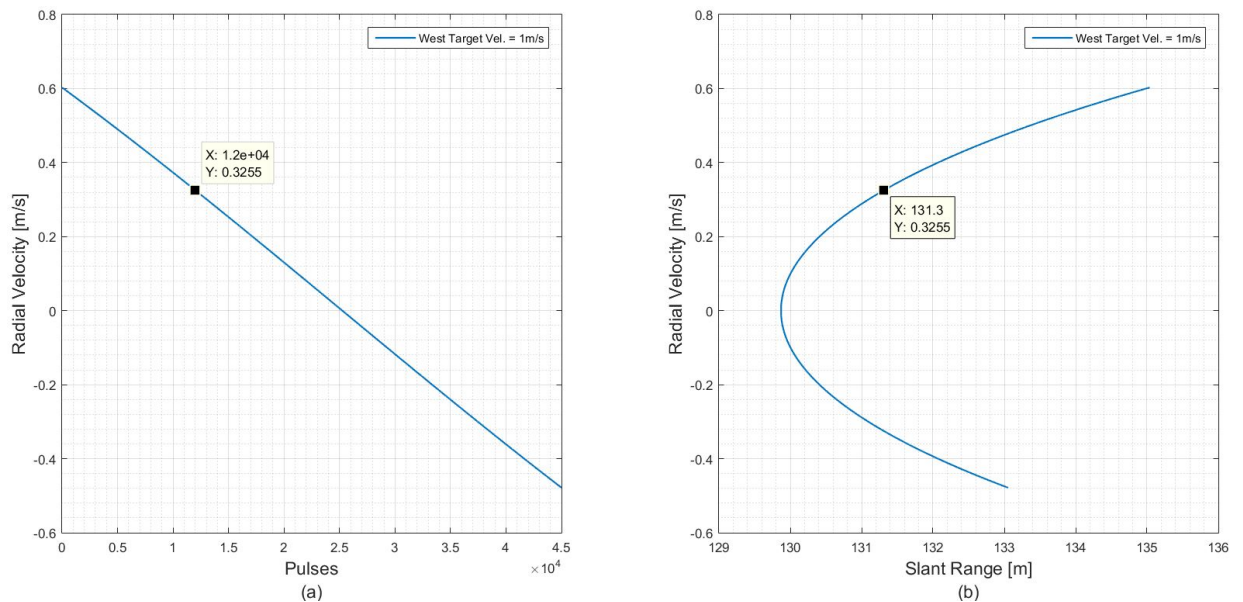


Figure 8.2: (b) Calculated range and (a) calculated radial velocity, for a target moving west at pulse number 12000.

The measured data of a target moving west, parallel and opposite direction to the radar (target 2) was processed and focused into a range-Doppler map presented in Figure 8.3. The range-Doppler map of Figure 8.3 shows the stationary corner reflector circled with white at position 128.9 m, radial velocity of 0.1798 m/s with a power value of 68.46 dBm before DPCA processing. This stationary corner reflector is a dominant clutter scatterer and hence it was used as a clutter power reference in this study. Other clutter scatterers like the bush area and the trees are fluctuating from pulse to pulse and channel to channel, hence they can not be used as reliable clutter references as they decorrelate within a short space of time. However the effects that these fluctuating scatterers have on the ability of the DPCA technique to detect ground moving targets are noted and observed.

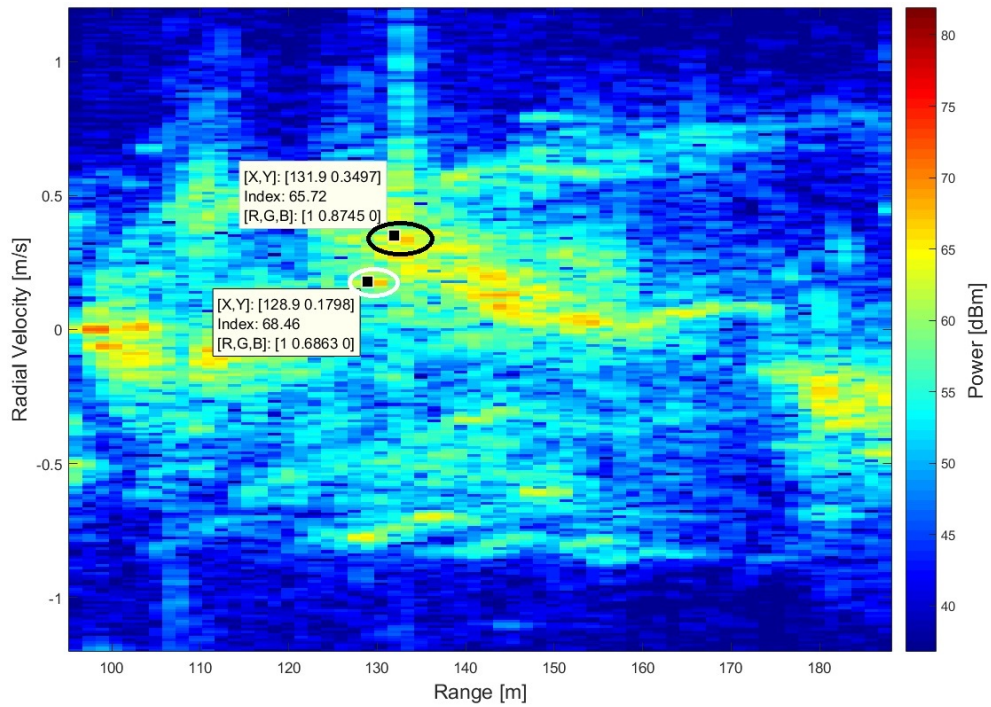


Figure 8.3: Range-Doppler map of a target moving west (target 2) before DPCA processing at pulse 12000.

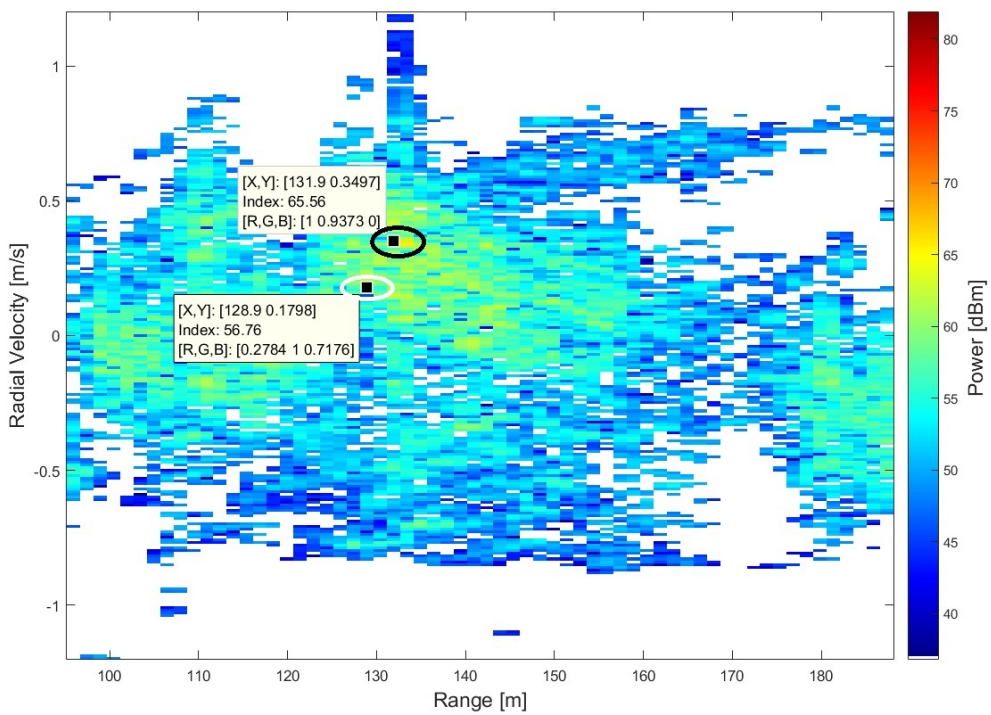


Figure 8.4: Range-Doppler map of a target moving west (target 2) after DPCA processing at pulse 12000.

The moving target, circled with black, is located at range 131.9 m and radial velocity 0.3497 m/s with a power value of 65.72 dBm in Figure 8.3 before DPCA processing. This gave a SCR of -2.74 dB before DPCA processing at a radar detected radial velocity of 0.3497 m/s and azimuth angle of  $81.44^\circ$  to the target.

Following the steps in Figure 8.1 and applying the DPCA technique, the range-Doppler map in Figure 8.4 is formed. It can be observed that the dominant stationary clutter scatterer (corner reflector) is suppressed down to 56.76 dBm while the moving target is detected with a power value of 65.56 dBm. The resulting SCR after DPCA is then calculated as 8.8 dB. The total SCR improvement at a radar azimuth angle of  $81.44^\circ$  to the target and radial velocity of 0.3497 m/s is 11.54 dB.

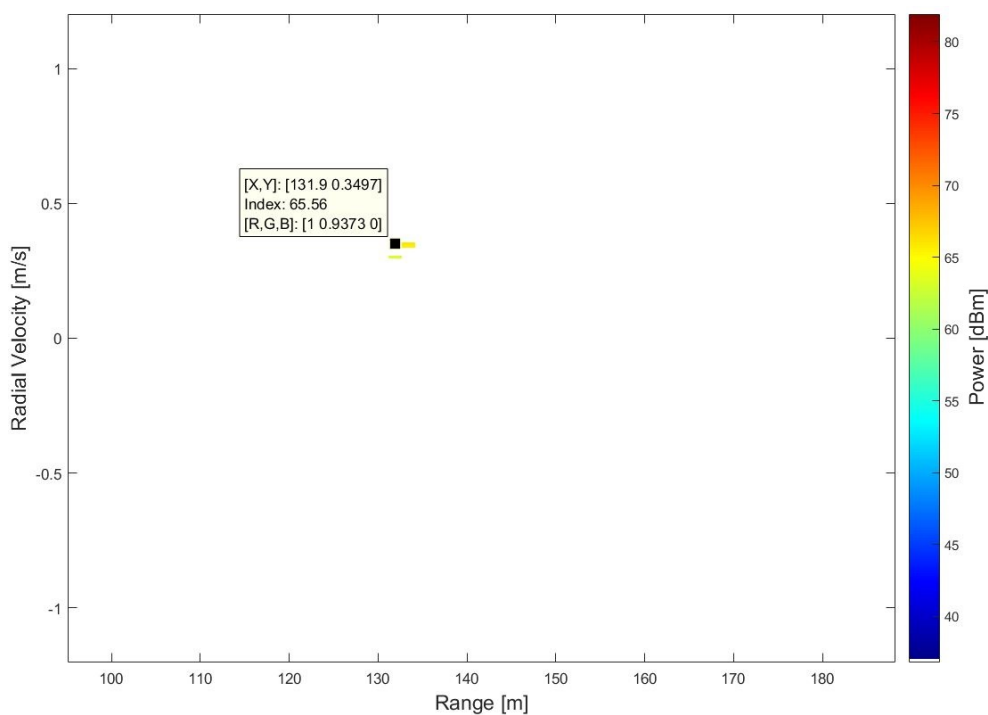


Figure 8.5: Range-Doppler map of a detected target after applying DPCA and a threshold.

The residual clutter power observed around the target in Figure 8.4 is due to a number of factors, including:

- movement of tree leaves and branches causing decorrelation of the clutter between the two observations,
- residual imperfections after the channel balancing step.

These factors limit the ability of the DPCA technique to suppress clutter. Applying a power threshold of 62 dBm clearly separates the moving target from the residual non-stationary (fluctuating) clutter power present in Figure 8.4. Figure 8.5 presents the moving target after applying a threshold. The plot of Figure 8.2 predicted that at the position the radar and the moving target will be at pulse number 12000, the moving target will be detected at range 131.3 m with a radial velocity of 0.3255 m/s. It can be observed that the moving target is detected at a range of 131.9 m and radial velocity of 0.3497 m/s. This indicates a good correlation between the controlled experiment and the results expected from the theoretical calculations.

### 8.2.2.2 Scenario 1 Pulse No. 24200: Target moving west, parallel and opposite direction to the radar

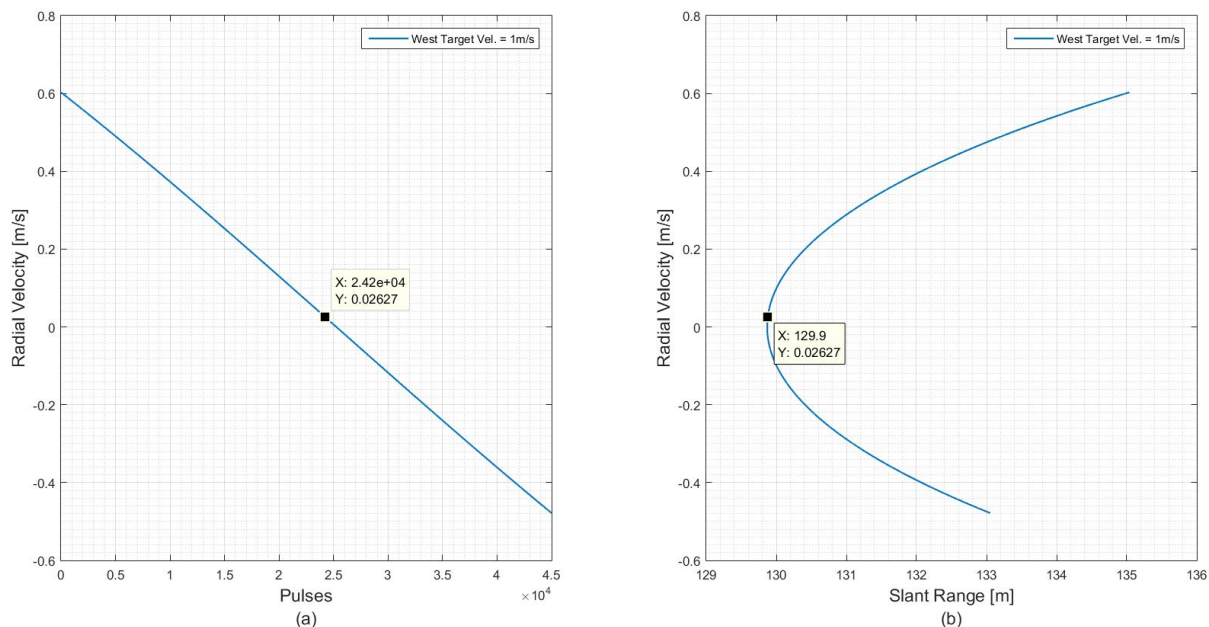


Figure 8.6: (b) Expected range and (a) Expected radial velocity at pulse number 24200, for target moving west.

The measured data of a target moving west, parallel and opposite direction to the radar (along target path 2), was processed from pulse number 24200 over 4096 pulses to form a range-Doppler map presented in Figure 8.7 before DPCA processing. At this pulse number, the radar was calculated to be at position  $PoP = [(-18+19.34) \ 0 \ 15]$  and the west moving target at position  $PoT_2 = [(19-16.12) \ 129 \ 0]$ . The radar azimuth angle to the target at this position is found as  $89.32^\circ$ . Figure 8.6 shows that the expected range and radial velocity of the target at pulse number 24200 is 129.9 m and 0.02627 m/s respectively.

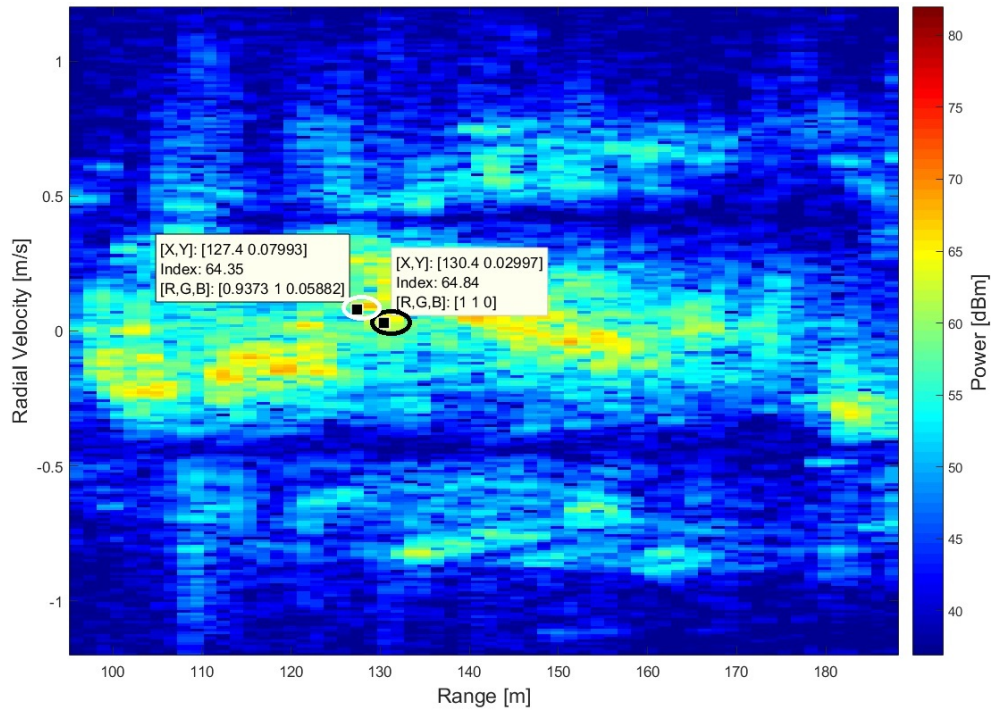


Figure 8.7: Range-Doppler map of a target moving west (target 2) before DPCA processing at pulse 24200.

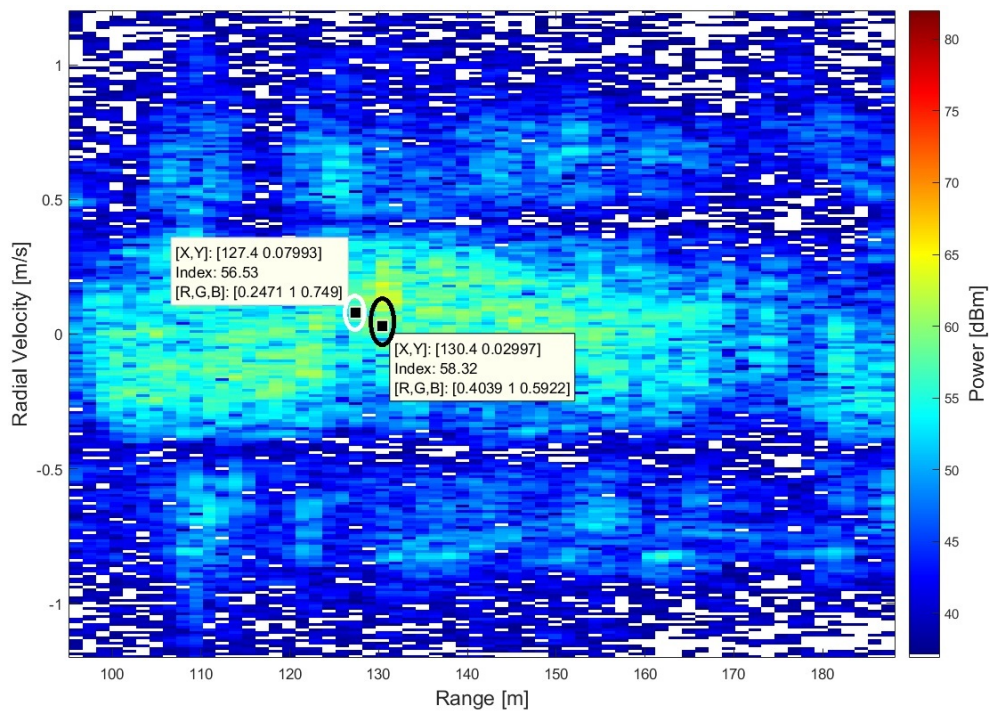


Figure 8.8: Range-Doppler map of a target moving west (target 2) after DPCA processing at pulse 24200.

Figure 8.7 shows the dominant clutter scatterer (stationary corner reflector) circled with white, at range 127.4 m and radial velocity 0.07993 m/s with a power value of 64.35 dBm before DPCA processing. The moving target within clutter circled with a black, is located at range 130.4 m and radial velocity 0.02997 m/s with a power value of 64.84 dBm. The SCR before DPCA processing is found as 0.49 dB at an azimuth angle of  $89.32^\circ$  and detected radial velocity of 0.02997 m/s.

Figure 8.8 presents the range-Doppler map after applying the DPCA technique on data processed from pulse number 24200 of a target moving west (along target path 2). It can be observed that the power of the dominant clutter scatterer circled with white has been reduced to 56.53 dBm and the moving target, at its previous indicated position, is also reduced to a power value of 58.32 dBm. This gives a SCR of 1.79 dB after DPCA processing. The total SCR improvement is calculated as 1.3 dB at a radial velocity of 0.02997 m/s and an azimuth angle of  $89.32^\circ$ . Applying a threshold of 63 dBm after DPCA processing indicates the power signature of the moving target as shown in Figure 8.9.

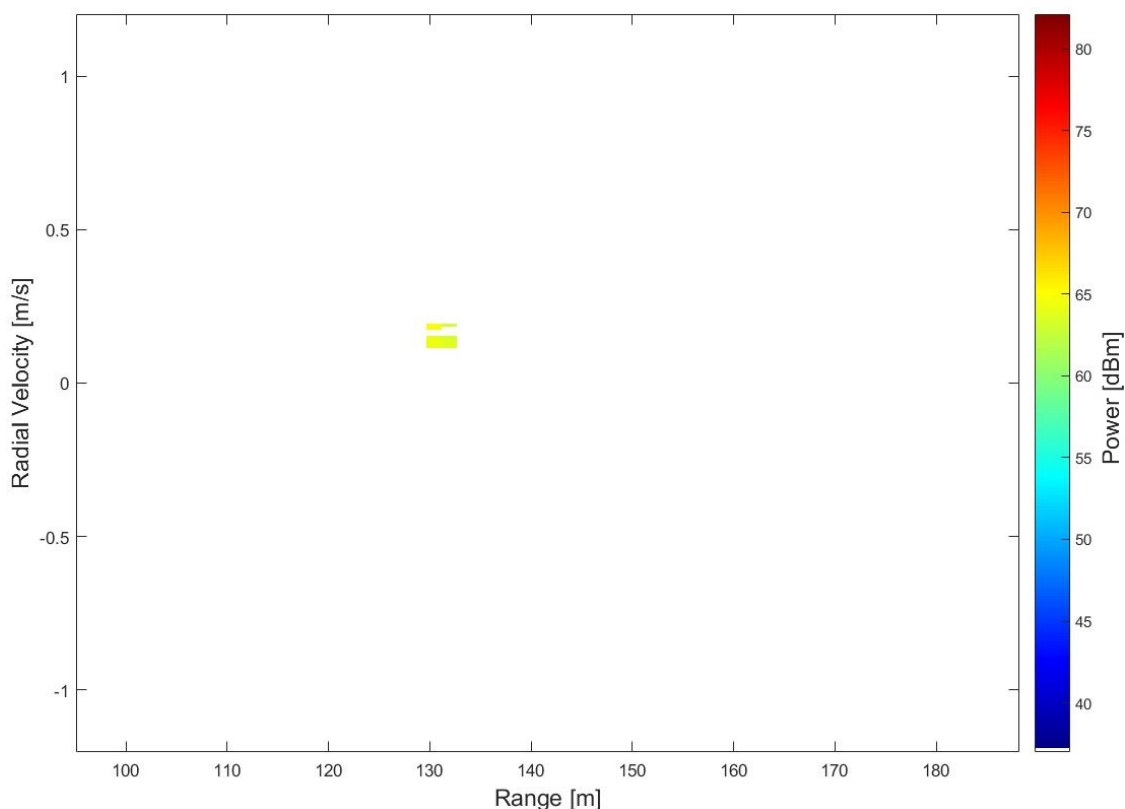


Figure 8.9: Range-Doppler map of a detected target after applying DPCA and a threshold at pulse number 24200.

### 8.2.2.3 Scenario 2 Pulse No. 2048: Target moving east, parallel and same direction as the radar

The measured data with a target travelling east, parallel and same direction as the radar (along target path 1), was also processed and used to investigate the DPCA technique. In this specific measured data, an additional experimental target was introduced during the data recording. The additional target was a person moving orthogonal and towards the radar along target path 3 on Figure 8.10. The walking person was not holding a corner reflector or any metallic objects to enhance the reflection of radar signals. This extra target was added so as to investigate if the radar can detect a person walking at approximately 1 m/s, with no radar signal reflection enhancer (corner reflector).



Figure 8.10: Top view map of the experiment setup for real data measurement (copy of Figure 5.5).

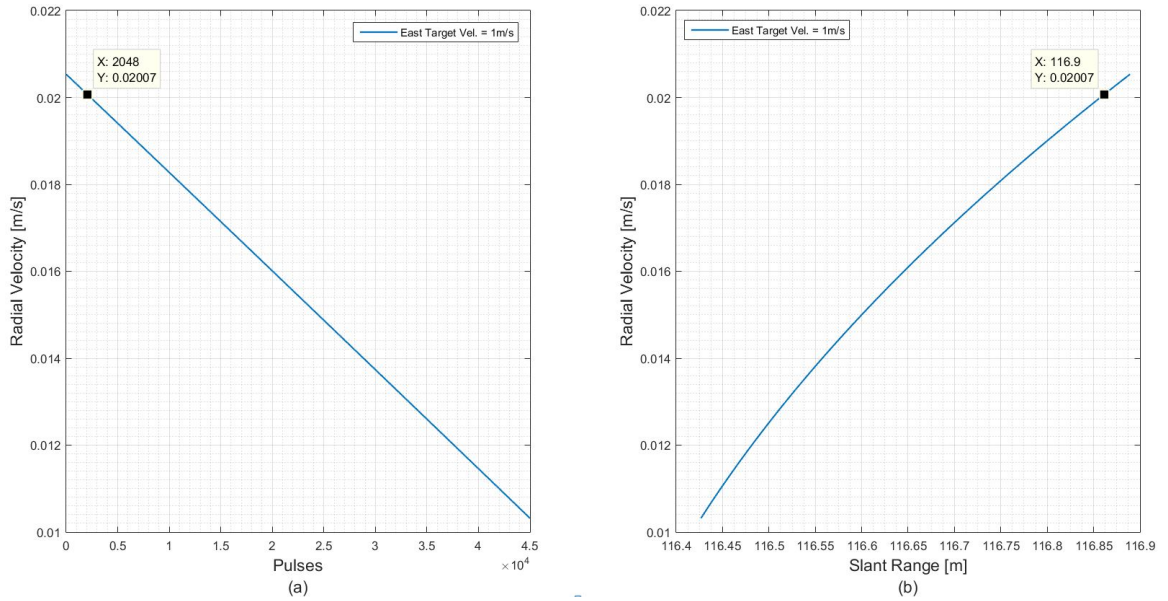


Figure 8.11: (b) Calculated range and (a) calculated radial velocity at pulse number 2048, for target moving east (target 1).

The measured data in this instance was processed from pulse number 2048, using 4096 pulses to form a range-Doppler map presented in Figure 8.12 before DPCA processing. The target moving east, parallel and same direction as the radar with a corner reflector (along target path 1) from position  $PoT_1 = [-6 \ 115.3 \ 0]$ , is expected to be at position  $PoT_1 = [(-6+1.3640) \ 115.3 \ 0]$  at pulse number 2048. The radar, from a starting position of  $PoP = [-18 \ 0 \ 15]$ , is expected to be at position  $PoP = [(-18+1.6368) \ 0 \ 15]$  at pulse number 2048. Figure 8.11 shows that the calculated range and radial velocity that the moving target is expected to be at in the range-Doppler map at pulse number 2048 is 116.9 m and 0.02 m/s respectively.

Figure 8.12 shows a range-Doppler map of a target moving east, parallel and same direction as the radar, circled with black at the expected range of 116.9 m and radial velocity of 0.01998 m/s. The stationary scatterer (corner reflector) is circled with white at range 130.4 m and radial velocity 0.2398 m/s. The additional orthogonal moving target signature is circled with red at range 143.9 m and radial velocity 0.3397 m/s. The SCR before DPCA processing for a target moving east is -1.69 dB at a radar detected radial velocity of 0.2 m/s. At pulse number 2048, the azimuth angle of the radar to the target is calculated as  $84.19^\circ$ .

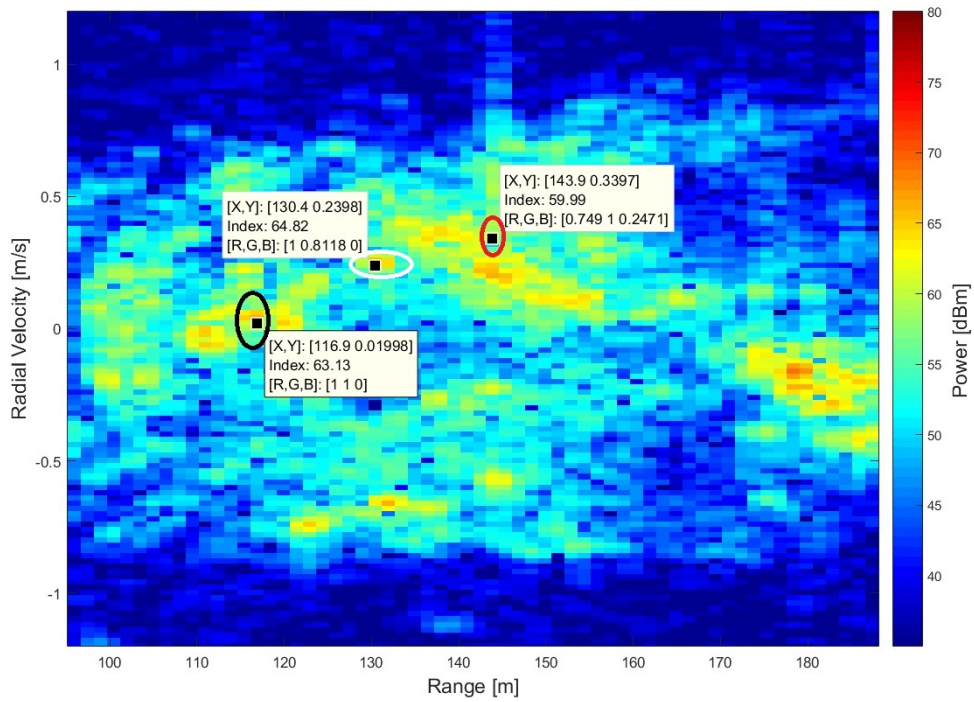


Figure 8.12: Range-Doppler map of a target moving east (target 1) before DPCA processing at pulse 2048.

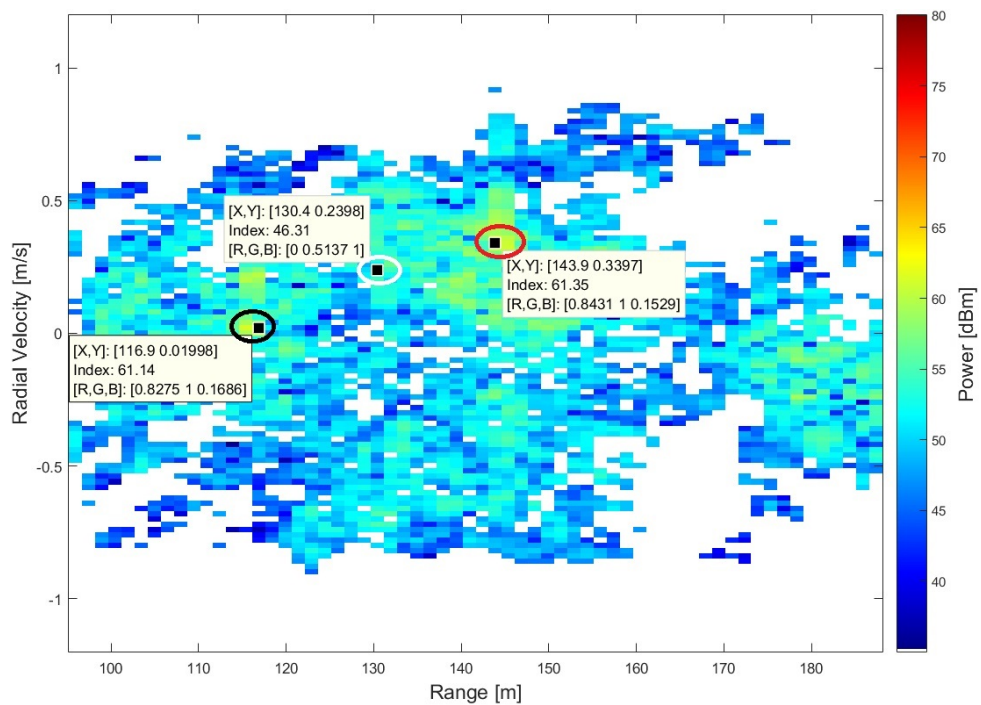


Figure 8.13: Range-Doppler map of a target moving east (target 1) after DPCA processing at pulse 2048.

Following the steps in Figure 8.1 and applying the DPCA technique to the data of a target moving east, from pulse number 2048, gives the range-Doppler map in Figure 8.13. It can be observed that the dominant stationary clutter scatterer power (corner reflector) is suppressed down to 46.31 dBm circled with white. The target moving east is circled with black at its expected range and radial velocity with a power level of 61.14 dBm. The additional orthogonal moving target circled with red is also detected above clutter with a power level of 61.35 dB. The resulting SCR after applying DPCA technique is found as 14.83 dB for the east moving target at azimuth angel of  $84.19^\circ$  to the radar and radial velocity of 0.02 m/s. The total SCR improvement is then found as 16.52 dB at this target and radar position.

Figure 8.14 presents the range-Doppler map obtained after applying DPCA technique and a threshold of 61 dBm. It can be seen that the east moving target is clearly detected and indicated with a black circle at the expected range and radial velocity as calculated in Figure 8.11. The additional orthogonal moving target is also detected and indicted with a red circle in Figure 8.14. The DPCA technique has shown that it can suppress stationary clutter and successfully detect a moving target with a corner reflector (east moving target) and a moving person (orthogonal moving target) without a corner reflector.

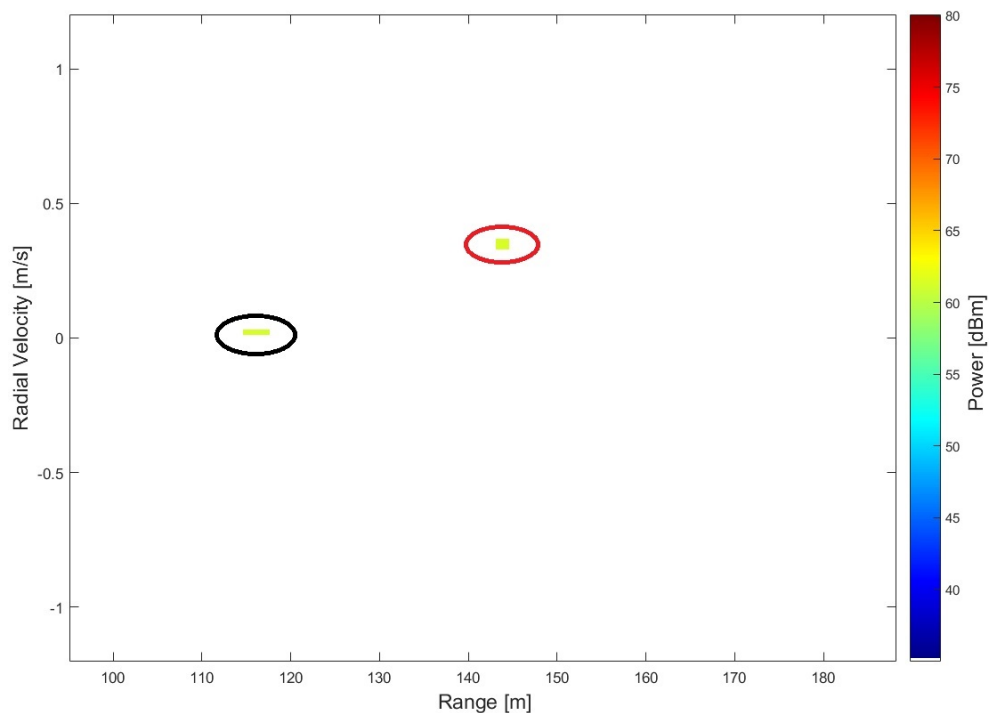


Figure 8.14: Range-Doppler map of a detected target after applying DPCA and a threshold at pulse number 2048.

### 8.2.2.4 Scenario 2 Pulse No. 18000: Target moving east, parallel and same direction as the radar

The DPCA technique was also applied on data measured with a target moving east from pulse number 18000. At this pulse number, the east moving target was at position  $PoT_1 = [(-6+11.988) \ 115.3 \ 0]$  and the radar was at position  $PoP = [(-18+14.3856) \ 0 \ 15]$ . The azimuth angle of the radar to the target at this position was calculated as  $85.24^\circ$ . The additional orthogonal moving target was also present during the measurement of this data. The additional target moving orthogonal towards the radar was still a person walking on the ground (along target path 3 in Figure 8.10) without a corner reflector. Figure 8.15 displays the expected range and radial velocity of the east moving target calculated at the position of pulse number 18000. The east moving target is expected at range 116.7 m and radial velocity 0.01646 m/s on the range-Doppler map of data processed from pulse 18000 over 4096 pulses.

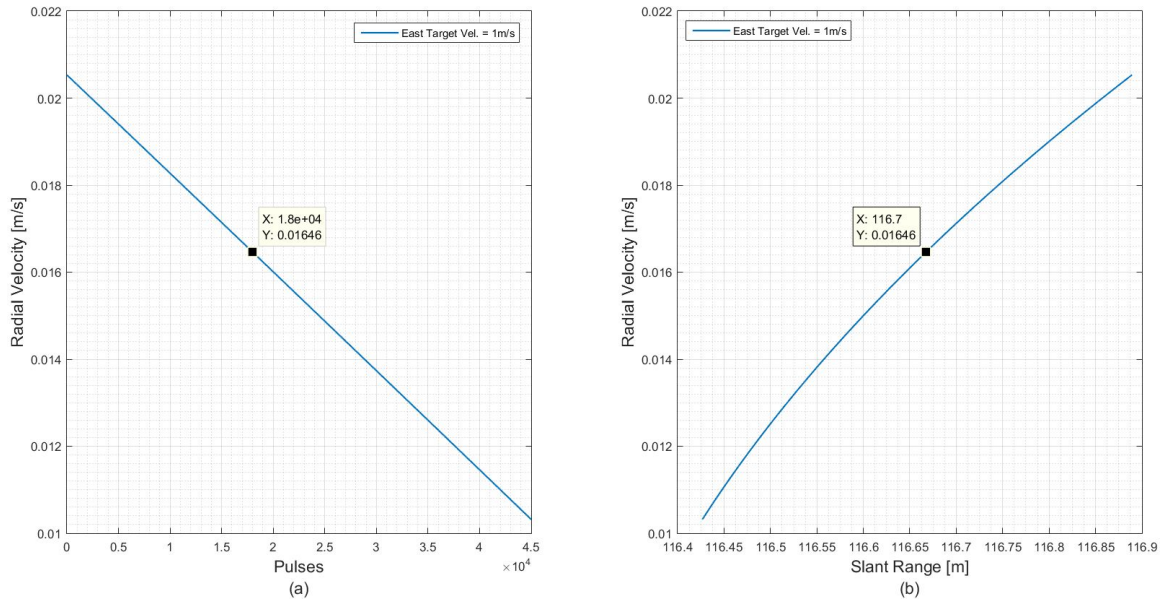


Figure 8.15: (b) Expected range and (a) Expected radial velocity at pulse number 18000, for target moving east (target 1).

The range-Doppler map resulting after processing 4096 pulses from pulse number 18000 of data measured with a target moving east is presented in Figure 8.16. The stationary dominant clutter scatterer (corner reflector) is indicated with a white circle at range 127.4 m and radial velocity 0.1299 m/s with a power of 64.57 dBm. The east moving target circled with black is shown at 116.9 m at its expected range, radial velocity of 0.01 m/s and power level of 62.23 dBm. The orthogonal moving target is circled with red at range 133.4 m and radial velocity 0.759 m/s. The resulting SCR

of this processed data is -2.34 dB at a radar detected radial velocity of 0.01 m/s and azimuth angle of  $85.24^\circ$  to the target.

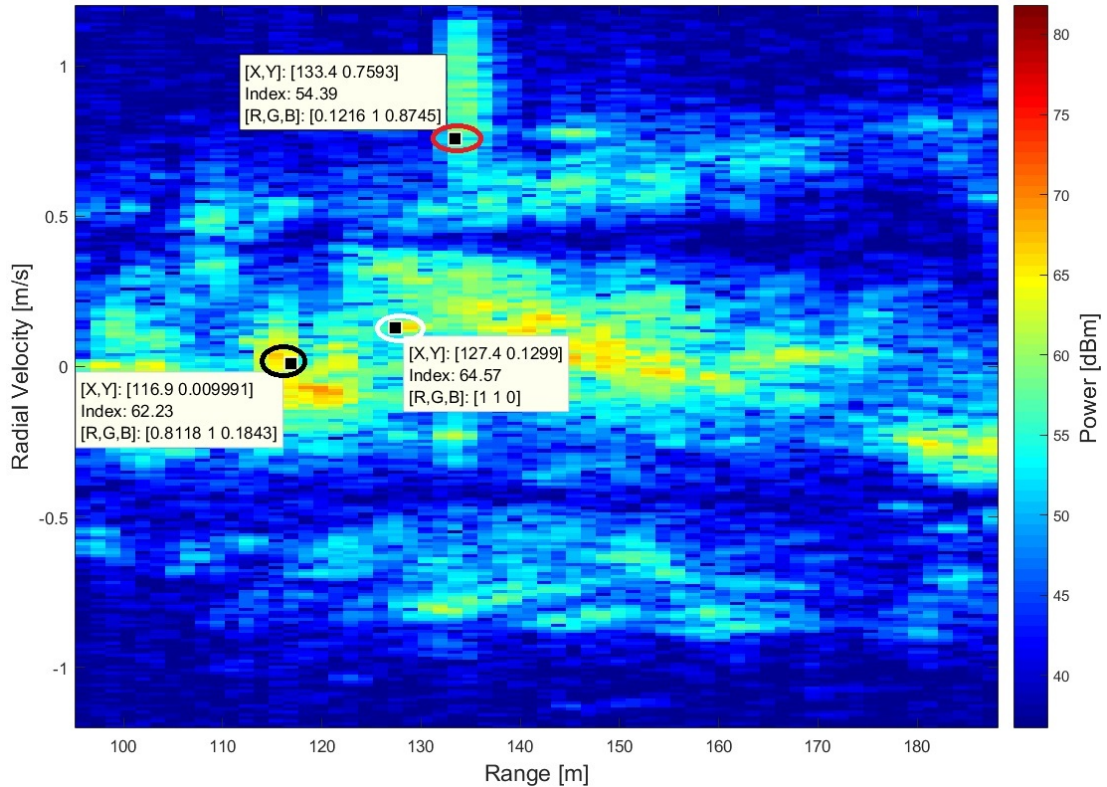


Figure 8.16: Range-Doppler map of a target moving east (target 1) before DPCA processing at pulse 18000.

Figure 8.17 is obtained after applying the DPCA technique. It can be observed that the east moving target circled with black is distinguished above stationary clutter with a power level of 59.59 dBm from Figure 8.17. The power of the stationary corner reflector circled with white is suppressed down to 55.2 dBm after DPCA processing. The resulting SCR after applying DPCA is calculated as 4.39 dB at the radar azimuth angle of  $85.24^\circ$  to the target and radial velocity of 0.01 m/s. The SCR improvement at this radar and target position is then calculated as 6.73 dB. The additional orthogonal moving target circled with red is indicated with a lower power level of 54.95 dBm after DPCA processing. The moving target power and the total SCR improvement after DPCA show a decreasing trend as the radial velocity detected by the radar decreases and as the azimuth angle to the target increases towards  $90^\circ$ . This is because the moving target power signature start to get suppressed together with stationary clutter as the radial velocity decreases due to an increasing radar azimuth angle to the target.

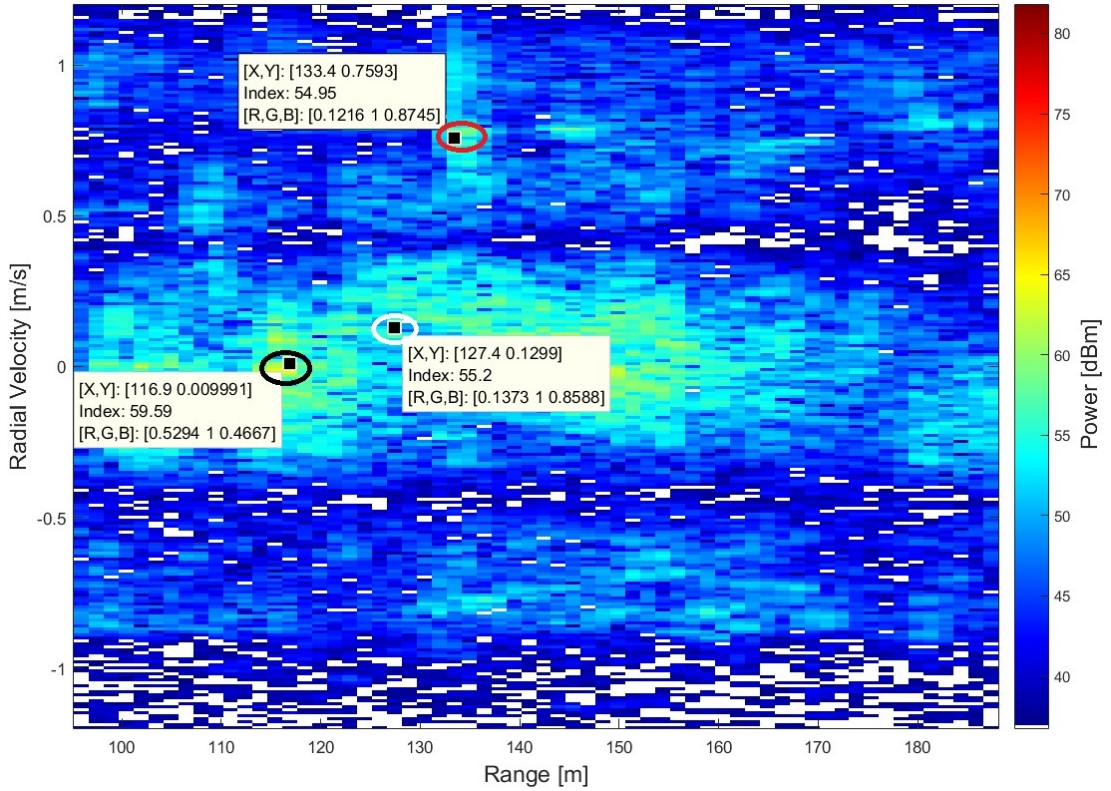


Figure 8.17: Range-Doppler map of a target moving east (target 1) after DPCA processing at pulse 18000.

### 8.2.2.5 Results Summary

Table 8.1 presents a summary of the results achieved by applying the DPCA technique on measured data at different radar and target positions. It can be observed that the DPCA technique is able to suppress clutter, improve the SCR and indicate ground moving targets on measured radar data. The SCR improvement of the DPCA technique, however, depends on the target radial velocity ( $V_{rP0}$ ) after arresting the motion of the radar platform and the azimuth angle to the target. The radial velocity,  $V_{rP0}$ , is calculated by taking the ground velocity of the moving target alone and projecting it on the radar line of sight without the influence of the radar platform velocity. This is because the radar platform velocity was arrested by introducing a pulse shift on the aft antenna and hence co-registering the two receive channels. The radial velocity,  $V_r$ , is calculated with both the target ground velocity and the radar platform velocity taken into account.

Table 8.1: Summary of DPCA SCR improvement results obtained from measured data.

Target Direction	Pulse Number	Azimuth Angle	Radial Vel. ( $V_r$ )	Radial Vel. ( $V_{rP0}$ )	SCR bef. DPCA	SCR aft. DPCA	SCR Imp.
West	12000	81.44°	0.34 m/s	0.15 m/s	-2.74 dB	8.8 dB	11.54 dB
West	24200	89.32°	0.0299 m/s	0.014 m/s	0.49 dB	1.79 dB	1.3 dB
East	2048	84.19°	0.02 m/s	-0.10 m/s	-1.69 dB	14.83 dB	16.52 dB
East	18000	85.24°	0.01 m/s	-0.082 m/s	-2.34 dB	4.39 dB	6.73 dB

Table 8.1 show that the SCR improvement decreases as the target radial velocity ( $V_{rP0}$ ) detected by the radar decreases. The SCR improvement decreases because as the radial velocity decreases the received moving target power gets attenuated by the DPCA technique as presented by Equation 8.1 [12].

$$z_{DPCA} = \left| \text{asin} \left( \frac{\pi d V_{rP0}}{\lambda V_p} \right) \right| \quad (8.1)$$

Equation 8.1 shows the relationship between radial velocity ( $V_{rP0}$ ) and the target power received. Plotting Equation 8.1 for various radial velocity results in the green graph of Figure 8.18. This is the ideal response of DPCA technique for a target moving west (target 2), given a channel spacing ( $d$ ) of 118.5 mm, platform velocity ( $V_p$ ) of 1.2 m/s and wavelength ( $\lambda$ ) of 0.0545 m. It is observed that as  $V_{rP0}$  decreases to zero, the target received power also decreases and makes a notch at around 0 m/s. The blue plot in Figure 8.18 show the power received from the measured radar data used to assess the performance of DPCA. It can be observed that the received target power from the measured data also decreases as the radial velocity ( $V_{rP0}$ ) decreases and follows the ideal DPCA response plotted in green. Hence, the results of the DPCA technique obtained with measured radar data correspond with the theoretical expected response of DPCA as presented by Equation 8.1. Assessment of the DPCA technique with simulated data from Chapter 7 also gave a DPCA response that corresponds to the one achieved with real measured radar data.

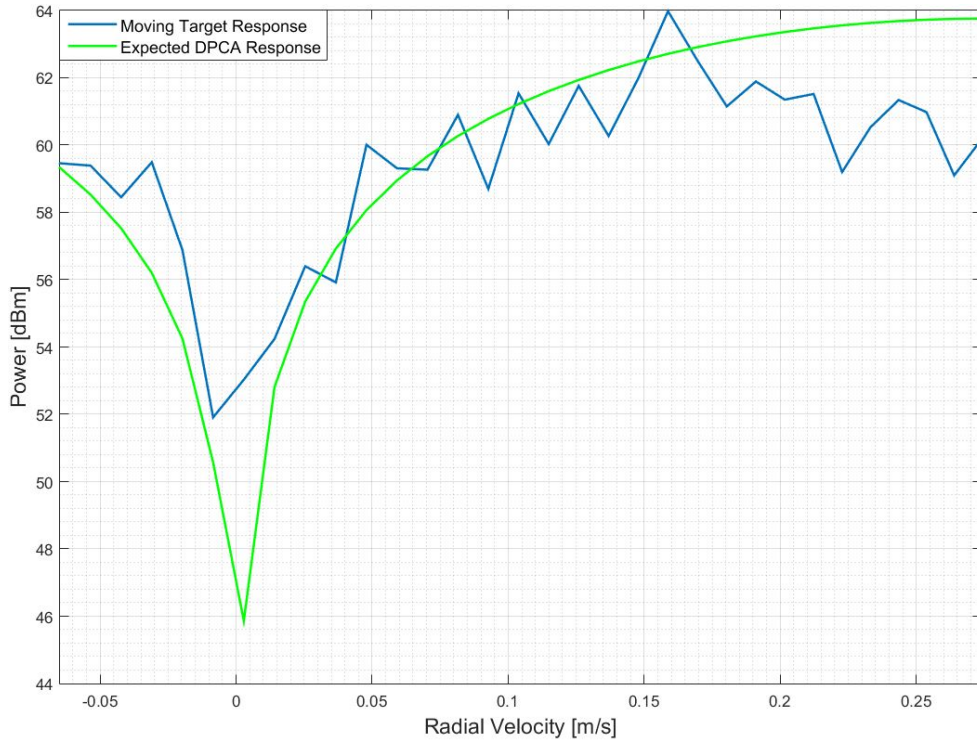


Figure 8.18: Moving target DPCA response.

The DPCA response represented by Equation 8.1 show that the DPCA technique does not only suppress stationary clutter but also attenuates targets that are moving slow at a radial velocity close to zero. Chiu and Livingstone in [43], presented that targets are considered slow moving if their radial velocity  $V_r < \lambda V_p / 8d$ , which is the minimum detectable velocity. With the parameters used to measure data in this experiment, the minimum detectable velocity is calculated as 0.069 m/s.

### 8.2.3 Sensitivity Analysis of DPCA Technique

DPCA technique requires that the radar data recorded with multiple channels be well co-registered and channel balanced. This will allow for effective clutter suppression and improvement of the SCR as discussed and observed in subsection 8.2. Co-registration for the DPCA technique is governed by the data collection mode used during the recording of the radar data. The data collection mode used in this investigation is the standard data collection mode. This mode requires that the aft antenna travel half the chosen antenna baseline for it to image the same point in space that the fore antenna imaged at a different time. This is achieved by introducing a delay in the recorded data of the aft antenna. This delay is determined by the chosen antenna baseline, system PRI and the platform speed. The time it takes the aft antenna to travel half the antenna baseline determines the number of pulses to

be shifted in order to introduce the time delay in the recorded data of the aft channel.

Once the required time delay is correctly introduced on the aft antenna, the recorded data of the two channels will be of the same point in space at different time instances hence enabling change to be detected in the imaged area from channel to channel. However, on real measured radar data, it is difficult to maintain constant radar platform velocity which makes it difficult to determine the time delay required to align the aft antenna pulses with that of the fore antenna, hence resulting in co-registration errors.

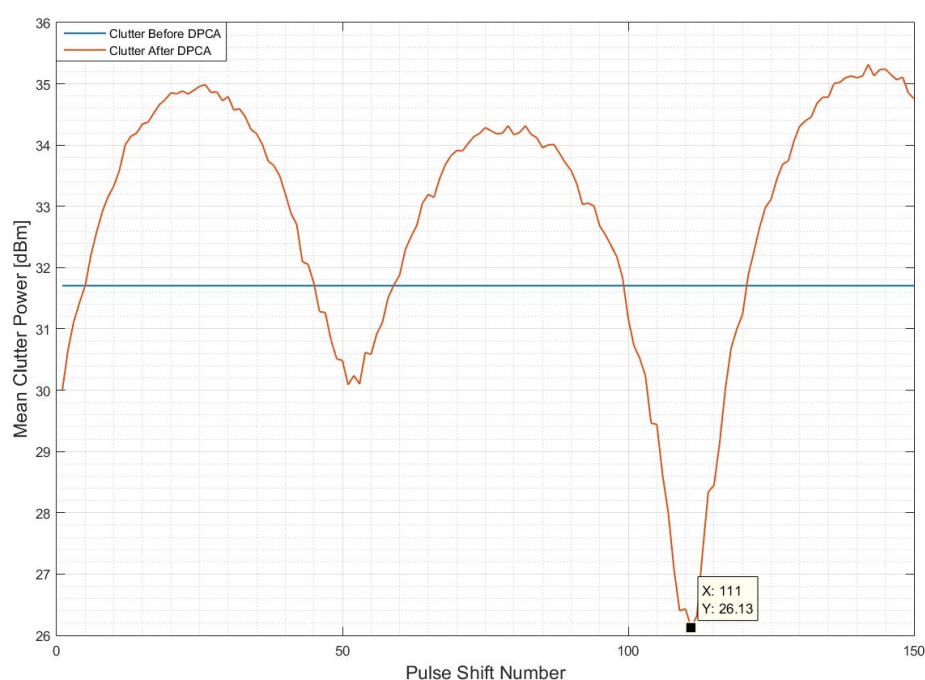


Figure 8.19: Mean clutter power before and after DPCA for data with target moving east along target path 1

Co-registration errors result in the increase of the residual clutter after applying DPCA. An increase in residual clutter means a decreased SCR improvement performance and an increased number of false target detections.

Each data recording session has its own unique co-registration requirements because the radar platform speed was slightly different for each recording session. Figure 8.19 presents the co-registration requirements for optimal clutter suppression on data recorded with a target moving east, parallel and same direction as the radar (target 1). The mean residual clutter power is obtained from several range bins of interest with only clutter present after DPCA processing. The pulse shift number represent the

total amount of pulses to shift in order to introduce the required time delay for optimal clutter suppression. The region with the least mean residual clutter from Figure 8.19 give the optimum number of pulses to discard in order to align and co-register the aft antenna with the fore antenna for clutter suppression. Pulse shift number 111 from Figure 8.19 give a minimum residual clutter power of 26.13 dBm. This pulse shift number was used to introduce a delay on the recorded data of a target moving east (target 1).

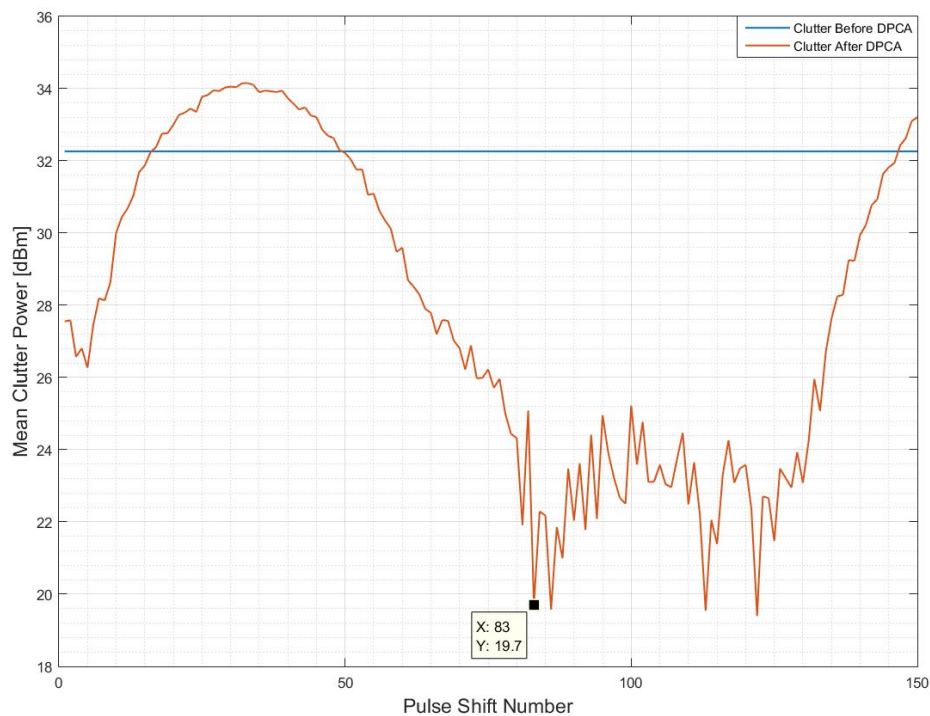


Figure 8.20: Mean clutter power before and after DPCA for data with target moving west along target path 2

The optimum pulse shift number for data recorded with a target moving west, parallel and opposite direction to the radar (target 2), is determined from Figure 8.20. The optimum pulse shift number is 83 pulses which result in a mean residual clutter power of 19.7 dBm. The pulse shift number gave the required time delay to align the aft antenna with the fore antenna for data recorded with a target moving west (target 2). It can be observed from Figure 8.19 and Figure 8.20 that the co-registration requirements for the two cases of the recorded data are unique for each case.

To illustrate the sensitivity of the DPCA technique to co-registration errors in this study, the two radar channels were intentionally miss-aligned by several pulses obtained from Figure 8.20. The radar data were measured in a controlled environment with

a PRF of 1501.5 Hz and an antenna baseline of 118.5 mm. According to Equation 2.8, the required platform velocity was calculated as 1.2 m/s which was the maximum velocity of the radar platform used. To perform channel co-registration of the fore and aft radar channels with the PRF, antenna spacing and platform velocity used, the pulses of the aft antenna are required to be shifted forward by 74 pulses. This is equivalent to a total time of 49.375 ms, which is the time it takes the aft antenna to travel half the chosen baseline and hence image the same point in space as the fore antenna at different times.

Figure 8.19 shows that the required pulse shift for channel co-registration is 111 pulses and not 74 as per theoretical calculation. Figure 8.20 also shows that the required pulse shift for co-registration is 83 pulses. These pulse shifts are different from the theoretically calculated pulse shift due to the fact that the theoretical calculation assumes that the radar platform velocity will remain constant at 1.2 m/s for the whole recording time which is not the case during real radar data measurement. A pulse shift of 111 pulses is equivalent to a time delay of 73.93 ms with a PRF of 1501.5 Hz. This time delay means the radar platform was travelling at an average velocity of 0.80 m/s during the recording of data with a target moving east (target 1). A pulse shift number of 83 pulses equates to a time delay of 55.28 ms which means the radar platform was travelling at an average velocity of 0.999 m/s during the recording of data with a target moving west (target 2).

Figure 8.4 from subsection 8.2.1 presented the results obtained after co-registration of the data recorded with a target moving west (target 2) by shifting the aft channel by 83 pulses. The resulting SCR after applying the DPCA technique was found as 8.8 dB in Figure 8.4. Co-registering the two channels by shifting the aft channel by 145 pulses and applying DPCA technique results in the range-Doppler map of Figure 8.21. The SCR from Figure 8.21 is calculated as -7.22 dB which is less than that of Figure 8.4. The reduction in SCR indicates that there is more residual clutter power (72.13 dBm) in Figure 8.21 than there is in Figure 8.4 after DPCA processing. This is due to the antenna misalignment and co-registration errors. With this co-registration errors, the DPCA technique is unable to suppress clutter and indicate the ground moving target as Figure 8.21 shows.

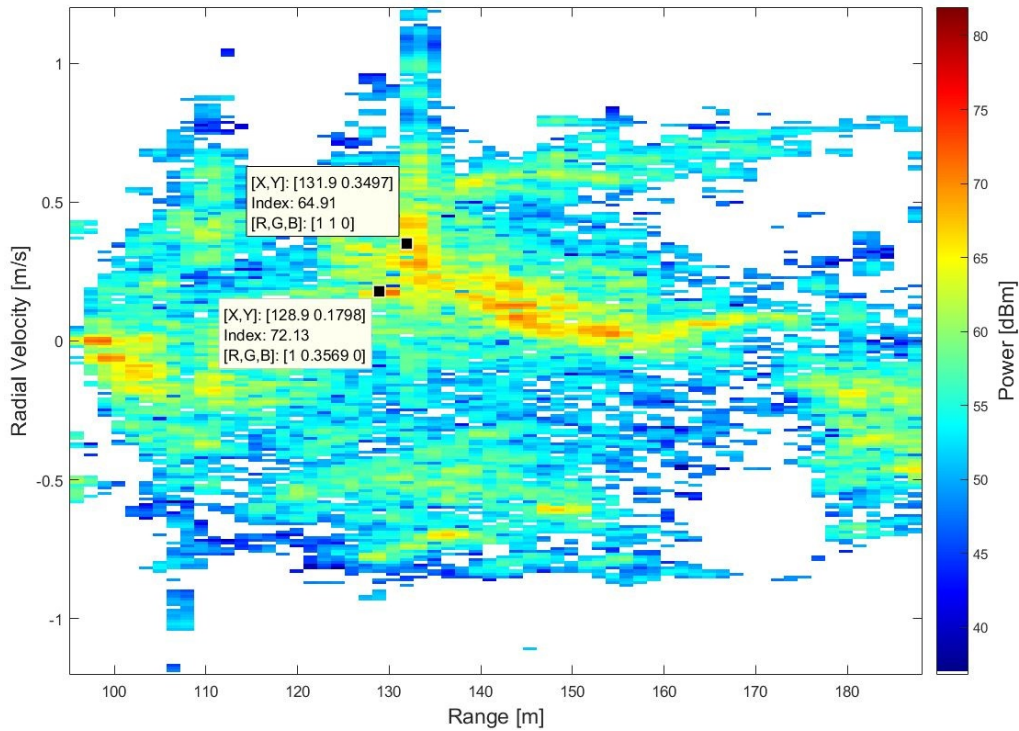


Figure 8.21: Range-Doppler map after DPCA processing with co-registration errors on data with a target moving west (target 2).

### 8.3 GMTI using ATI Technique on Measured Radar Data

ATI is a technique that forms a phase image, also known as an interferogram, using two SAR images obtained from the same point in space at different times. The phase image is formed by a conjugate multiplication of two SAR images obtained with separate radar channels. ATI exploits the fact that the stationary ground scatterers are expected to contribute the same phase on the two radar channels when they image the same point in space. Hence, a conjugate multiplication of the two images from the same point in space will result in cancellation (zeroing) of the phase of the stationary ground scatterers. The ground moving scatterers, however, will have a non-zero phase due to the fact that they contribute a different phase in the two SAR channels imaging the same point in space. This ATI property is used to indicate ground moving targets in the imaged scene.

### 8.3.1 Processing Overview

The ATI technique requires that the measured real radar data from the two channels be co-registered and phase balanced such that the same stationary point in space contribute the same phase in the two channels. Figure 8.22 presents the flowchart followed in applying the ATI technique in real data. The flowchart shows the data pre-processing that needs to be performed before applying the ATI technique. This pre-processing which includes channel co-registration and channel phase balancing is discussed in detail in Chapter 6.

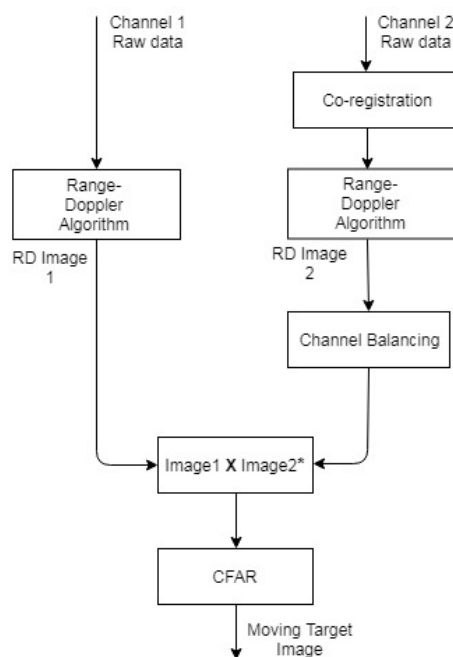


Figure 8.22: Flowchart of the ATI technique (copy of Figure 7.18).

### 8.3.2 ATI Detection of Moving Targets within Clutter

With the correct co-registration and channel balancing, the clutter phase in the fore and aft channel are expected to be equal and hence forming an interferogram (phase difference image) with the two channels should cancel the clutter phase to zero radians. A moving target within the imaged scene will be indicated by a non-zero phase on the interferogram after cancellation of the phase due to stationary clutter. The ability of the ATI technique to zero the phase of clutter and indicate the phase of moving targets in an interferogram was investigated with the same measured data that was used to investigate the DPCA technique. The measured data were processed into complex range-Doppler maps and the ATI technique was applied to form interferograms.

### 8.3.2.1 Scenario 1 Pulse No. 12000: Target moving west, parallel and opposite direction to the radar

The radar data recorded with a target moving west along target path 2 on Figure 5.5 was processed from pulse number 12000 into a complex range-Doppler map. The ATI technique was then applied to form a phase image presented in Figure 8.23 after channel balancing and co-registration of the radar channels. The expected target range and radial velocity at pulse number 12000 was calculated as 131.3 m and 0.3255 m/s respectively.

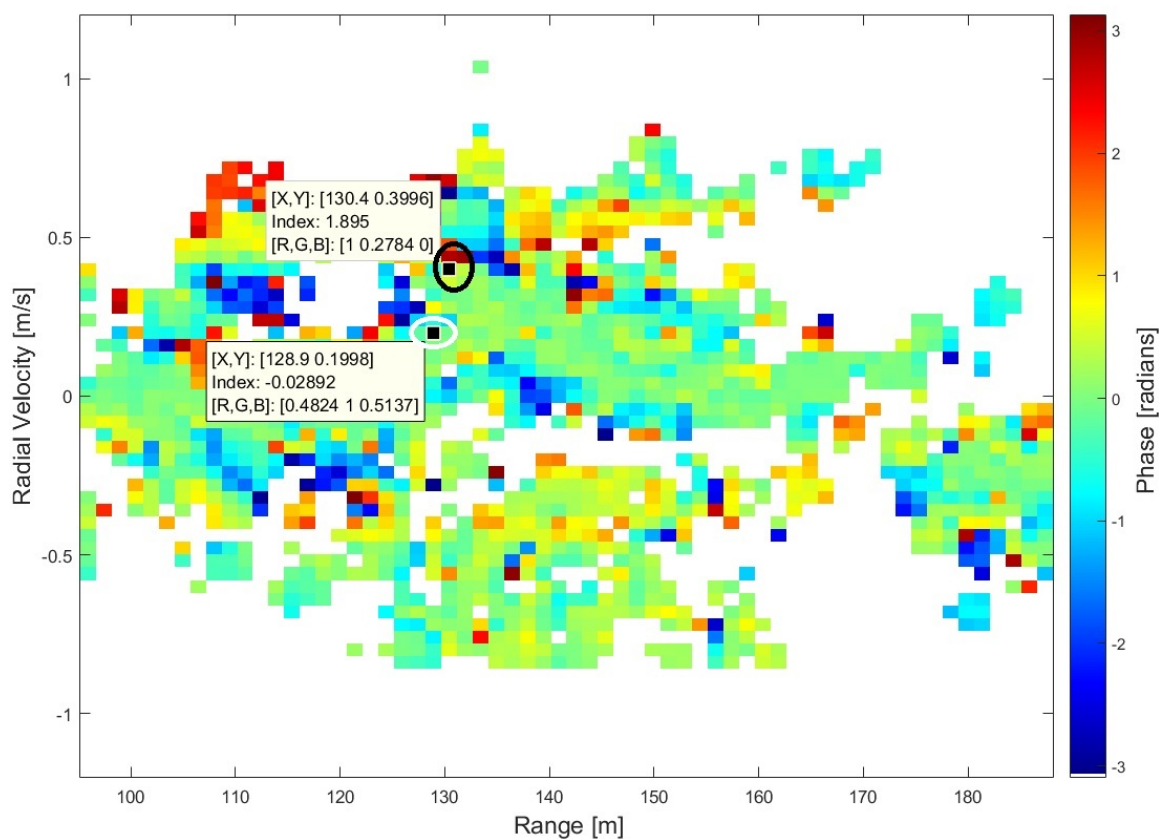


Figure 8.23: Interferogram of a target moving west processed from pulse number 12000.

Figure 8.23 shows the target induced phase of 1.895 radians circled with black. It can be observed from Figure 8.23 that most of the clutter phase difference is close to zero radians. However, for some clutter cells the phase difference remains non-zero. This is due to actual non-stationary clutter (moving tree leaves and branches) as well as the volumetric scattering nature of vegetation [44]. This volumetric scattering results in temporal decorrelation, introducing a phase difference between the radar channels as the radar data is recorded [44]. For cells where the signal power is low,

thermal noise strongly influence the resulting phase difference, leading to a non-zero phase difference result after ATI is applied.

The stationary corner reflector circled with white, which is the object that was inducing static clutter phase, has a phase difference of  $-0.029$  radians as observed in Figure 8.23. Hence, the ATI technique can successfully remove the phase of stationary objects from the interferogram and detect the phase of a ground moving target. This is achieved at a radar azimuth angle of  $81.44^\circ$  and radial velocity of  $0.399$  m/s to the target.

Applying a threshold of 1.6 radians on the interferogram of Figure 8.23 results in Figure 8.24. It can be observed from Figure 8.24 that the ATI technique has a high false alarm rate due to the residual clutter phase caused by the non-stationary clutter and the random independent noise.

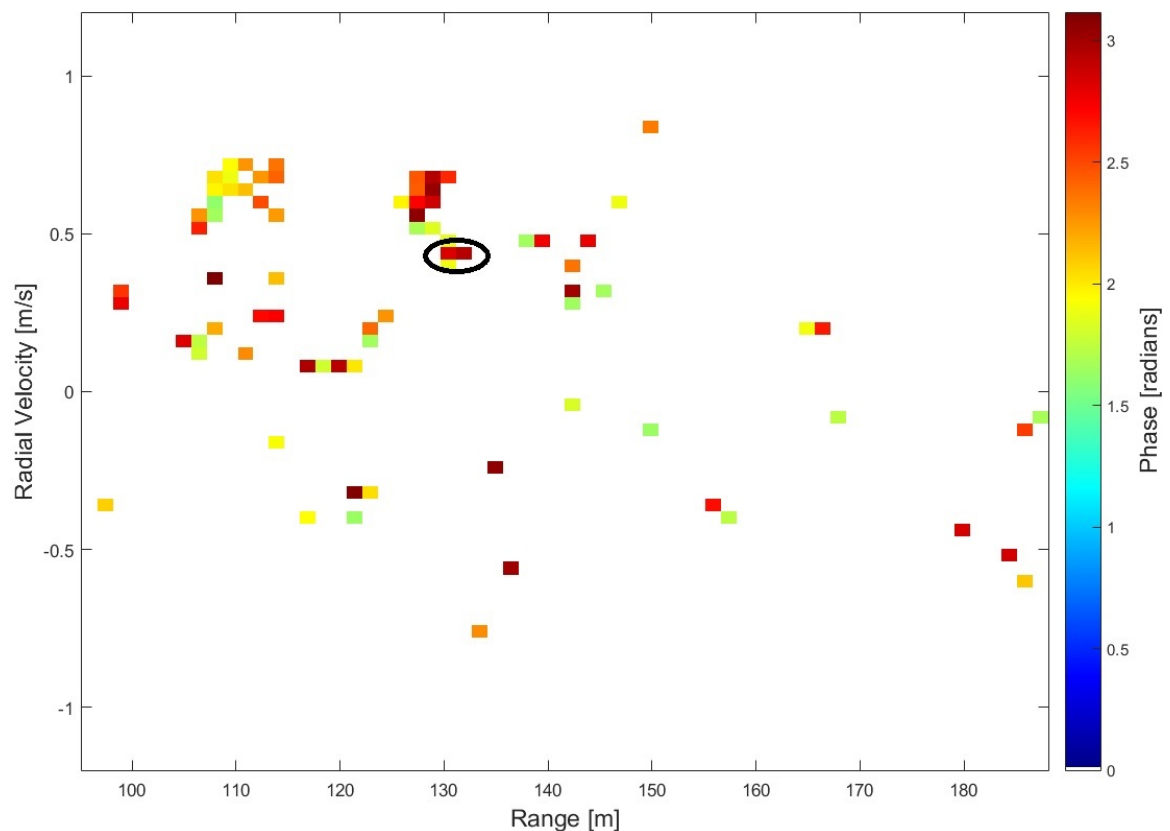


Figure 8.24: Phase image of a target moving west processed from pulse number 12000 with a phase threshold.

### 8.3.2.2 Scenario 1 Pulse No. 24200: Target moving west, parallel and opposite direction to the radar

Figure 8.25 shows an interferogram formed after applying the ATI technique to data processed from pulse number 24200. The data processed is for a target moving west along target path 2 from Figure 5.5. It can be observed from Figure 8.25 that the moving target, circled with black, induced a phase of 1.23 radians at range 131.9 m and radial velocity 0.03996 m/s. This target is not present at this position in Figure 8.23. At this pulse number (24200), the moving target was theoretically calculated to be at range 129.9 m with a radial velocity of 0.02627 m/s. The ATI technique also managed to indicate the phase caused by the stationary corner reflector circled with white in Figure 8.25 as 0.0061 radians, hence indicating that it is not moving from channel to channel. This is obtained at a radar azimuth angle of  $89.32^\circ$  and radial velocity of 0.03996 m/s to the target.

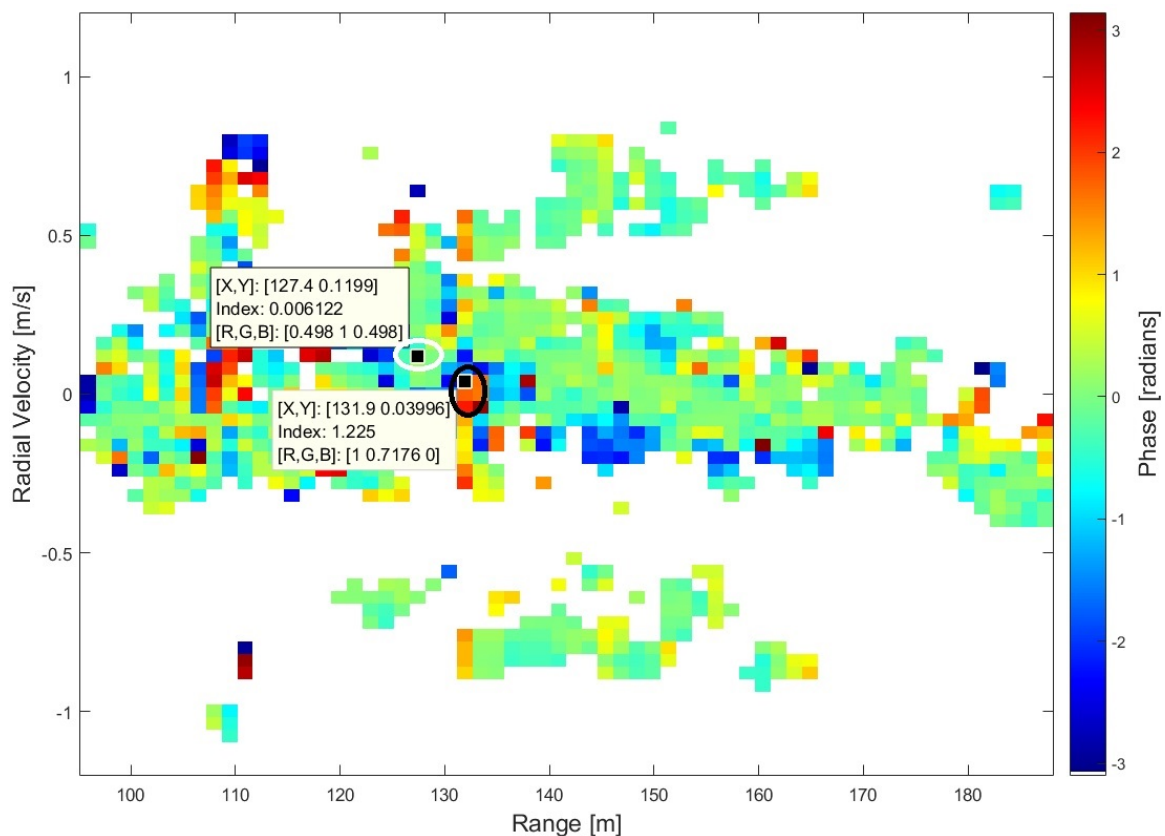


Figure 8.25: Interferogram of a target moving west processed from pulse number 24200.

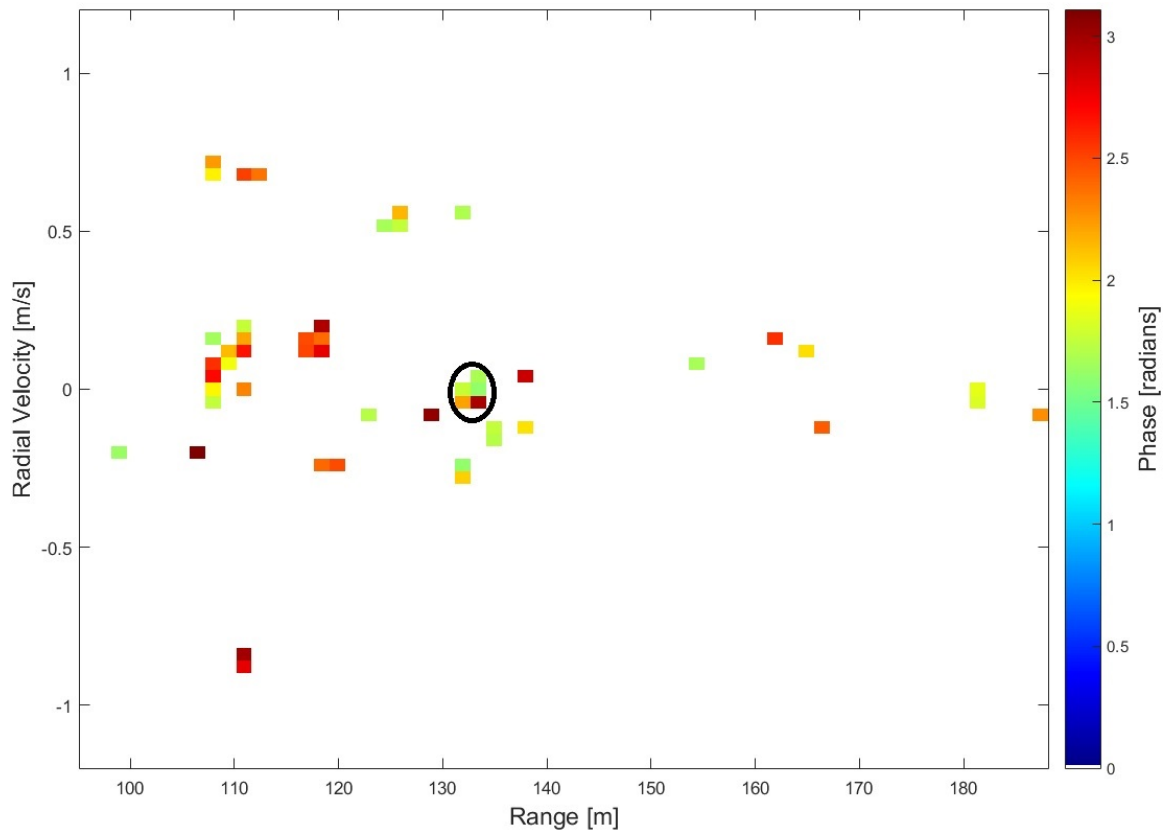


Figure 8.26: Interferogram of a target moving west processed from pulse number 24200 with a phase threshold.

Thresholding the interferogram in Figure 8.25 with a phase of 1.6 radians results in Figure 8.26. The ATI technique can indicate the phase of the moving target as observed, however, the decorrelation caused by noise and non-stationary clutter increases the false alarm rate of the ATI technique.

### 8.3.2.3 Scenario 2 Pulse No. 2048: Target moving east, parallel and same direction as the radar

The ability of the ATI technique to indicate the phase of moving targets within clutter was also investigated on data recorded with a target moving east along target path 1 in Figure 5.5. This data had an additional target (a walking person) moving orthogonal to the radar along target path 3 on Figure 8.10 without holding a corner reflector. This additional target was experimental to assess whether the ATI GMTI technique can detect a person walking on the ground without holding a corner reflector to enhance the radar returns. The data were processed from pulse number 2048 over 4096 pulses into a range-Doppler map, the ATI technique was then applied after co-registration and channel balancing to form an interferogram shown in Figure 8.27.

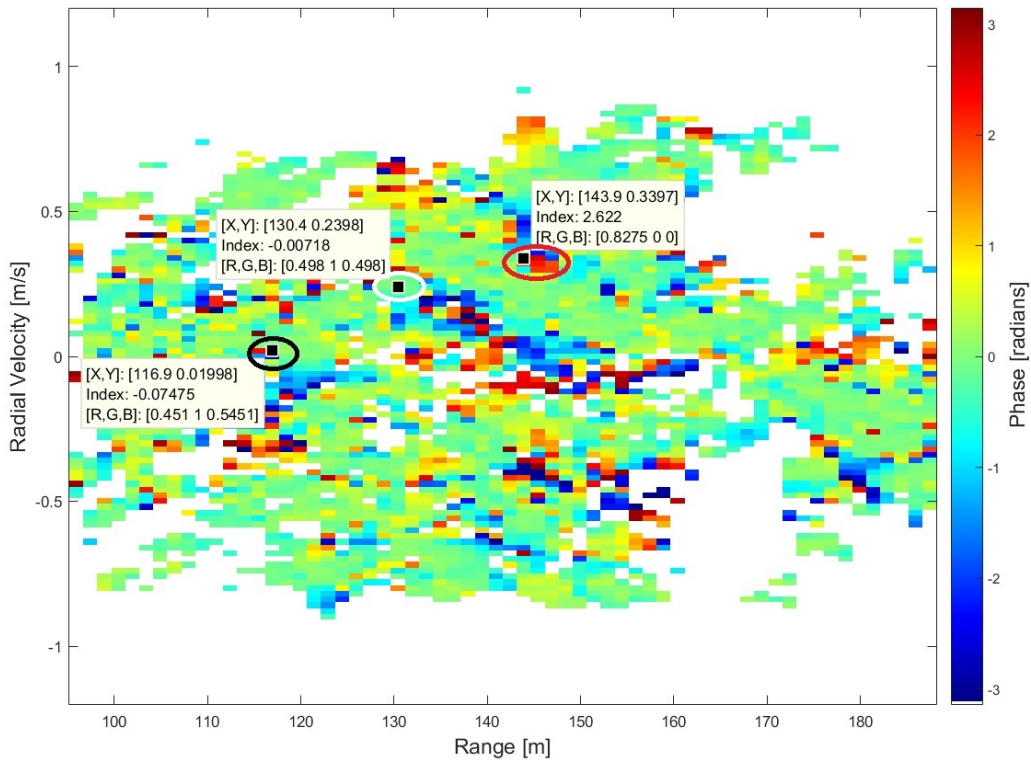


Figure 8.27: Interferogram of a target moving east processed from pulse number 2048.

It is observed on Figure 8.27 that the phase of the stationary corner reflector (static clutter) circled with white is  $-0.007$  radians, this is how much phase change it had between the two radar channels used to form the interferogram. This small phase change indicates that it is stationary. However, in other clutter regions there is some residual clutter phase caused by temporal decorrelation of vegetation and non-stationary clutter. The additional target moving orthogonal to the radar is detected with a phase of  $2.622$  radians as indicated by the red circle. The target moving east and parallel to the radar was theoretically calculated to be at a range of  $116.9$  m and radial velocity of  $0.02$  m/s at pulse number 2048.

The moving target position is circled with black in Figure 8.27 and is detected with a phase of  $-0.075$  radians. This phase is approximately zero radians which means the east moving target is not detected by the ATI technique at this radar and target position with an azimuth angle of  $84.19^\circ$ .

A phase threshold of  $1.6$  radians on the phase image in Figure 8.27 results in the interferogram of Figure 8.28. It can be observed that the false alarm rate is high and the east moving target circled with black together with the orthogonal moving target

circled with red are undistinguishable from the phase image with a phase threshold applied.

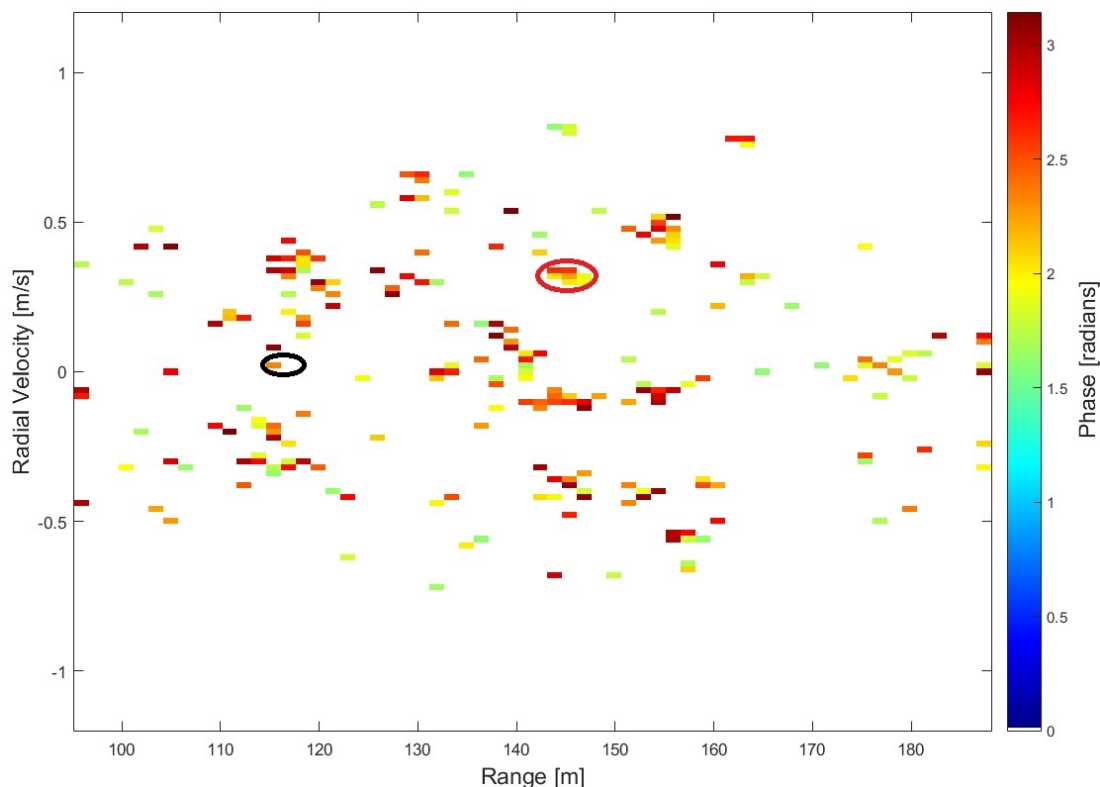


Figure 8.28: Phase image of a target moving east processed from pulse number 2048 with a phase threshold.

### 8.3.2.4 Scenario 2 Pulse No. 18000: Target moving east, parallel and same direction as the radar

The data of a target moving east and parallel to the radar was further processed from pulse 18000. At this pulse number, the azimuth angle of the radar to the target position was calculated as  $85.24^\circ$ .

The interferogram presented in Figure 8.29 was achieved after applying the ATI technique. Figure 8.29 shows that the phase of the stationary corner reflector circled with white is 0.057 radians together with most of the stationary clutter. The additional target moving orthogonal to the radar is detected with a phase of 3.057 radians circled with red in Figure 8.29. The east moving target is circled with black at its expected range with a phase of -2.884 radians. The residual phase of the dynamic clutter is also present in the interferogram of Figure 8.29 after applying the ATI technique.

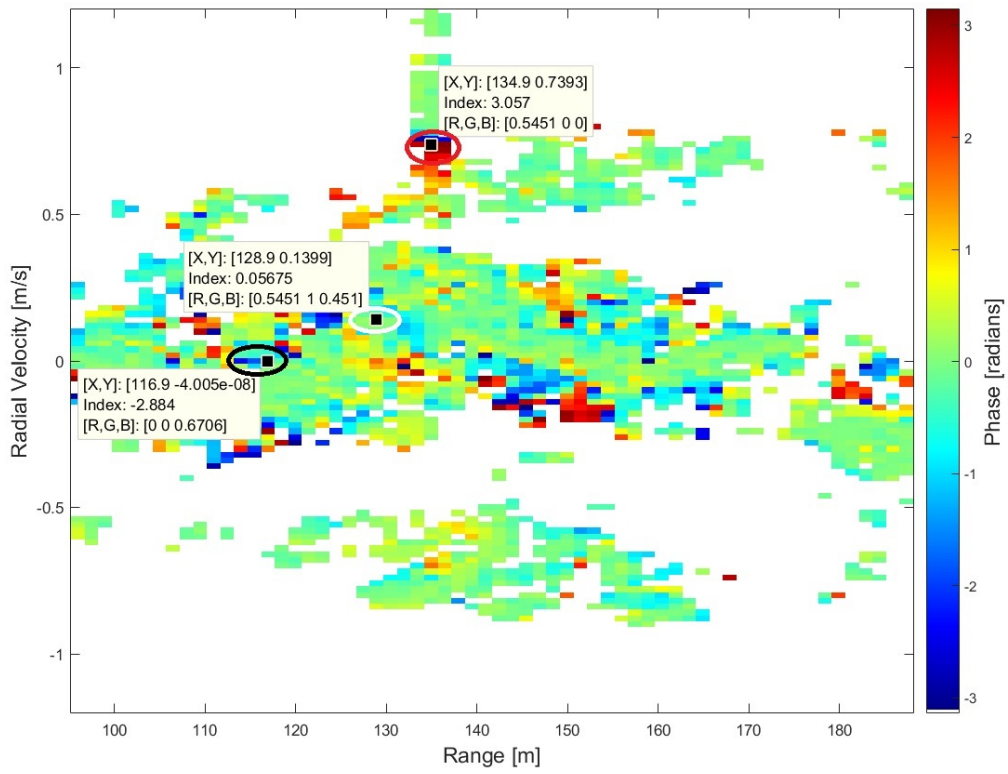


Figure 8.29: Interferogram of a target moving east processed from pulse number 18000.

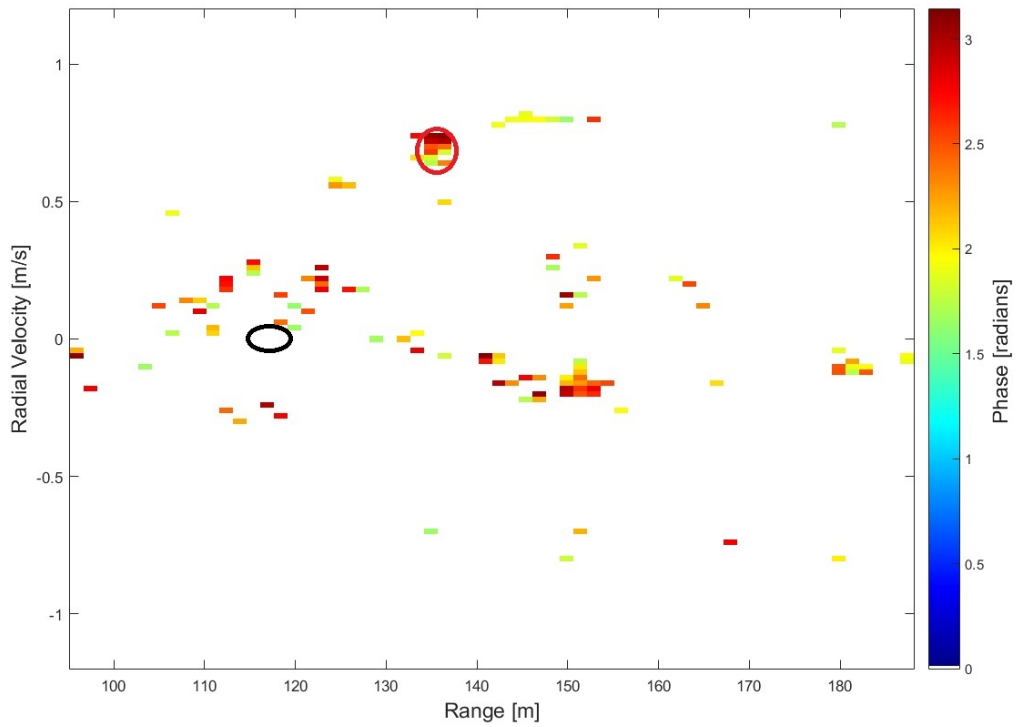


Figure 8.30: Interferogram of a target moving east with a phase threshold.

Figure 8.30 presents the obtained phase image after applying a phase threshold of 1.6 radians. It is observed that the phase of the east moving target has been zeroed at its expected position circled with black. This is due to the fact that its radial velocity is inducing a phase that is below the set phase threshold. The orthogonal moving target circled with red is present. The presence of non-stationary clutter phase and noise is also observed in Figure 8.30.

### 8.3.2.5 Results Summary

The results achieved by the ATI technique on the measured data is summarized in Table 8.2. It is observed that the ATI technique can well show static clutter phase (stationary corner reflector) as approximately zero radians. This is because the phase of the stationary corner reflector is correlated and equal in channel 1 and channel 2 and hence appears as zero radians in the phase difference image (interferogram).

The non-stationary clutter phase caused by the movement of tree branches and leaves together with the random noise phase result in residual clutter phase in the formed interferograms after applying the ATI technique. The non-stationary clutter phase can only be subtracted to a certain level even with correct channel balancing and co-registration. This is because as the tree branches and leaves move, they induce a different phase on each radar channel (temporal decorrelation). This result in unequal phase in the radar channels which does not subtract down to zero radians when the ATI technique is applied. Zebker and Villasenor in [44], found that only 2-3 cm rms motion decorrelates the phase in signals of a C-band system [44]. Hence, with the rapid and random motion of foliage, temporal decorrelation is unavoidable which affects the performance of the ATI technique.

Table 8.2: Summary of the ATI technique clutter cancellation extent achieved on measured radar data.

Target Direction	Pulse Number	Azimuth Angle	Radial Vel. ( $V_r$ )	Radial Vel. ( $V_{rP0}$ )	Clutter Phase After ATI	Target Phase After ATI
West	12000	81.44°	0.39 m/s	0.15 m/s	-0.029 radians	1.895 radians
West	24200	89.32°	0.039 m/s	0.014 m/s	0.0061 radians	1.23 radians
East	2048	84.19°	0.02 m/s	-0.10 m/s	-0.007 radians	-0.075 radians
East	18000	85.24°	0.013 m/s	-0.082 m/s	0.057 radians	-2.884 radians

The east moving target appears not to be well detected by the ATI technique as observed in Table 8.2, however, the west moving target as well as the orthogonal moving target are well detected by the ATI technique with some residual clutter phase present. The radial velocity,  $V_r$ , on Table 8.2 is calculated by taking the radar platform velocity and the moving target velocity into account while the radial velocity,  $V_{rP0}$ , is calculated by only taking into account the moving target velocity with the platform motion arrested.

### 8.3.3 Sensitivity Analysis of ATI Technique

The ATI technique, just like the DPCA technique, is sensitive to channel misalignments or co-registration errors. The co-registration errors could be because of the non-constant platform velocity or an offset in the radar channel spacing. This all result in spatial baseline decorrelation between the receive channels. With a constant system PRF, any change in the initially calculated platform velocity or channel spacing, causes spatial baseline decorrelation which result in co-registration errors according to Equation 2.8. This co-registration errors will result in the non-cancellation of stationary clutter phase on the phase difference image formed by the ATI technique and hence result in false detections of the ground moving targets.

The measured data were recorded with a PRF of 1501.5 Hz, an antenna baseline of 118.5 mm and a radar platform moving at a top velocity of 1.2 m/s. Correct co-registration of the radar channels required for the standard data collection mode requires that the aft radar channel data be delayed by 74 pulses which is an equivalent of 49.375 ms. This is ideally the time it takes the aft antenna to travel half the selected antenna baseline and image the same point in space as the fore antenna. However, the radar platform does not always travel at a constant velocity of 1.2 m/s.

Figure 8.31 shows the resulting residual clutter phase as a result of pulse misalignment as well as noise after applying the ATI technique. It can be observed that the residual clutter is random, which displays the phase sensitivity of the ATI technique to noise and co-registration errors.

Before applying the ATI technique in subsection 8.3.2, the data measured with a target moving west, parallel and opposite direction to the radar (along target path 2) was co-registered by discarding the first 83 pulses of the aft antenna, which is equivalent to introducing a time delay of 55.28 ms to the data of the aft channel. Applying a different time delay to the data of the aft channel results in the interferogram of Figure 8.32.

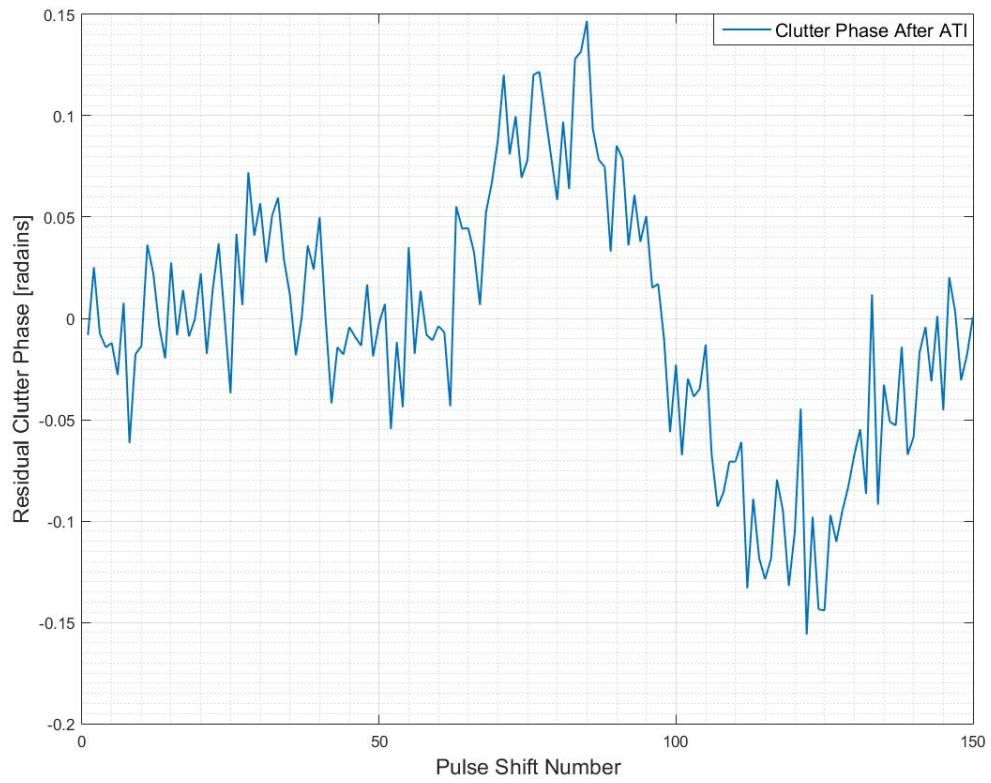


Figure 8.31: Residual clutter phase after applying the ATI technique.

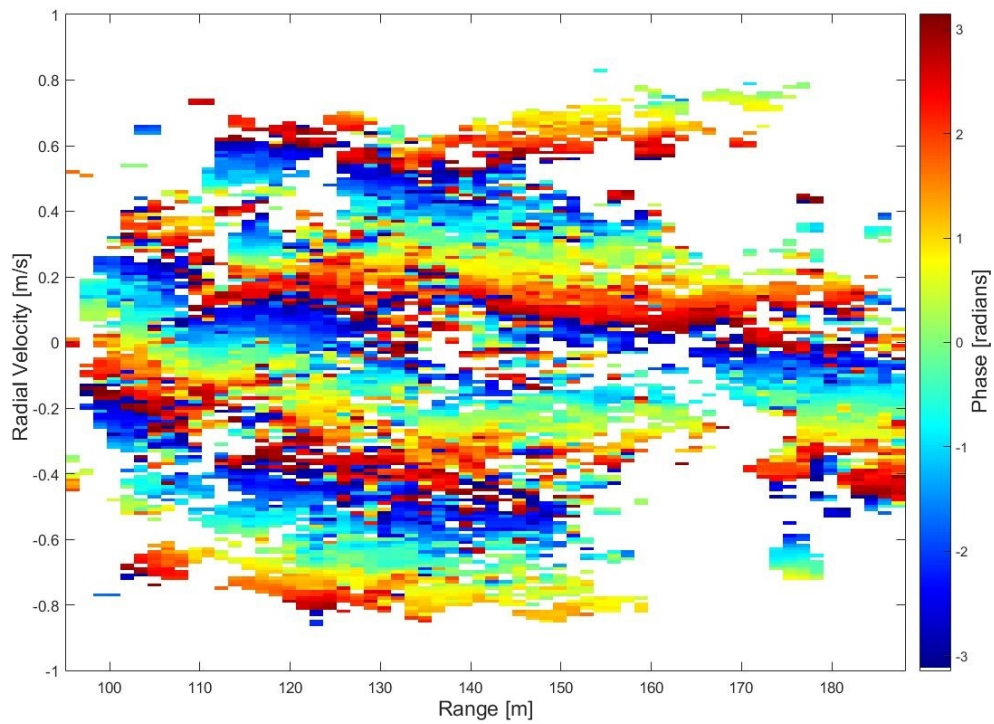


Figure 8.32: Interferogram after applying ATI technique on channel miss-aligned data.

Figure 8.32 shows how spatial baseline decorrelation and co-registration errors affect the performance of the ATI technique. The sensitivity of phase to any 2-3 cm (C-band) position change of objects makes the ATI technique sensitive, hence, any channel alignment errors affect the performance of the technique significantly as observed in Figure 8.32. It is also observed that the target is indistinguishable from the clutter phase and the ATI technique fails in indicating its position in the imaged area.

## 8.4 Comparison of DPCA and ATI Performance on Measured Data

Radar data were measured in a controlled environment with known scene features and co-operating ground moving targets. The DPCA GMTI technique and the ATI GMTI technique were both applied on the measured radar data to indicate and detect the moving targets within the imaged scene. The performance of the two GMTI techniques were assessed in-terms of their ability to indicate moving targets within clutter as well as their sensitivity to system measurement errors. The DPCA technique was evaluated given the received power extracted from the formed range-Doppler maps and the ATI technique was evaluated given the phase difference from the formed interferogram.

The DPCA technique showed that it can improve the SCR from -2.74 dB to 8.8 dB for data recorded with a target moving west along target path 2. This is a SCR improvement of 11.54 dB at a radar detected radial velocity,  $V_r$ , of 0.34 m/s and azimuth angle of  $81.44^\circ$  which corresponds to  $V_{rP0}$  of 0.15 m/s with the motion of the radar arrested. This DPCA SCR improvement is only possible given that the measured radar data is well co-registered and channel balanced before applying the technique. The ground moving target was well detected above clutter and singled out when applying a power threshold of 62 dBm as observed in Figure 8.5. The DPCA technique was also assessed on data with a target moving east along target path 1. For this data, the SCR was improved from -1.69 dB to 14.83 dB resulting in a SCR improvement of 16.52 dB at a radar radial velocity,  $V_r$ , of 0.02 m/s and azimuth angle of  $84.19^\circ$  to the target which correspond to  $V_{rP0}$  of -0.10 m/s with the radar platform motion arrested. With this SCR improvement, the ground moving target was able to be detected and separated from clutter. A GMTI experiment conducted by Coe and White in [45] achieved similar clutter suppression extent and SCR improvement results. It is stated in [45] that the DPCA technique achieved clutter suppression extent of 15 dB. The clutter suppression extent was then increased to about 20 dB

by employing an adaptive DPCA technique in [45].

The DPCA response of a moving target obtained with measured data in this study showed that the SCR improvement decreased as the target radial velocity ( $V_{rP0}$ ) decreased towards zero. This is the theoretically expected DPCA response according to Equation 8.1 which state that the DPCA technique does not only suppress stationary clutter but also attenuates the received power of slow moving targets. Hence, the results obtained with measured radar data agree with the results obtained with the simulated radar data which both agree with the theoretically expected results. The moving targets were calculated to be slow moving when their radial velocity,  $V_r$ , is below 0.069 m/s, hence indicating the minimum detectable velocity of the radar used in this experiment.

The performance of the ATI technique was assessed by its ability to indicate the phase of a moving target and zero the phase of the stationary scatterers (clutter) on the ground. For a target moving west along target path 2, parallel and opposite direction to the radar platform, the ATI technique was able to correctly detect it with a phase of 1.895 radians. The interferometric phase of the stationary dominant clutter scatterer resulted in a phase difference of -0.029 radians as observed in Figure 8.23. This was achieved at a radial velocity,  $V_r$ , of 0.399 m/s and radar azimuth angle of  $81.44^\circ$  to the target which corresponds to  $V_{rP0}$  of 0.15 m/s with the platform velocity arrested.

Most of the clutter phase on the interferogram is down to zero radians indicating that the scatterers are stationary except for some patches with non-zero phase. The non-stationary clutter due to the movement of the tree leaves and the bushes resulted in some clutter phase that did not correlate from channel to channel even after channel co-registration and channel balancing. This non-stationary clutter and noise resulted in patches of non-zero phase in the interferogram formed by the ATI technique. The non-zero phase can trigger the phase detection threshold and result in false target detection by the ATI technique. The ATI technique was, however, able to detect the moving target with non-zero phase and show the phase of the dominant static clutter scatterer (corner reflector) with zero radians. Similar results were achieved by Zhang in [19]. AirSAR ATI data were used in [19] to conduct research on the ability of the ATI technique to be used for GMTI. It was discovered that the ATI technique can detect moving targets, however, the technique had a high false alarm rate due to its sensitivity to slight phase changes caused by non-stationary clutter [19]. A double threshold approach using amplitude-only detection plus phase-only detection

was then implemented to reduce the false alarm rate of the ATI technique in [19].

The ATI technique was also assessed with a target moving east along target path 1 at a radar azimuth angle of  $84.19^\circ$ . At this azimuth angle the target was detected with a radial velocity,  $V_r$ , of 0.02 m/s which correspond to  $V_{rP0}$  of -0.10 m/s with radar platform velocity arrested. The phase of the east moving target was not indicated above the phase of clutter as Figure 8.27 shows. The phase at the range and radial velocity that the target was expected to be was indicated as -0.075 radians in Figure 8.27. This showed that the ATI technique observed the moving target as stationary together with clutter. With the phase of the non-stationary clutter also present, the ATI technique fails in detecting a target moving east, parallel and same direction as the radar. However the DPCA technique, at the same radar azimuth angle ( $84.19^\circ$ ), is able to improve the SCR of a target moving east by 16.52 dB and clearly indicate the moving target above clutter with no false alarms.

Assessing the sensitivity of the DPCA technique to system measurement errors such as channel misalignment and non-constant radar platform velocity resulted in channel co-registration errors which affected the performance of the DPCA technique. It was observed that this co-registration errors resulted in the increase of the residual clutter power while attempting to suppress it. This increase in clutter power was caused by the fact that when DPCA is applied on miss-aligned radar images, The power spectra of one image gets added on that of the second image when the images are subtracted, hence resulting in an increased clutter power because the images are not co-registered. With co-registration errors, the DPCA technique is unable to detect the ground moving target on measured radar data because clutter does not get well suppressed and hence the technique is prone to false detections.

The performance of the ATI technique was also assessed on data with co-registration errors due to non-constant platform velocity and misaligned radar channels. It was observed that clutter phase zeroing does not occur when applying the ATI technique and forming an interferogram on radar data that is not well co-registered. The ATI technique only works when the phase of the aft channel is balanced and co-registered with that of the fore channel, any imbalance or co-registration error results in failure of the ATI technique to distinguish the non-zero phase of the moving target from the phase of the stationary clutter. Hence, co-registration and channel balancing are important when applying the DPCA and the ATI GMTI techniques on measured radar data.

From the investigation of the DPCA and ATI GMTI techniques with measured radar data, it can be observed that both the GMTI techniques are able to indicate the presence of the moving target within clutter, however the ATI technique is prone to false alarms because of the phase caused by fluctuating (non-stationary) clutter and random noise from channel to channel. The DPCA technique showed that it is limited in terms of suppressing clutter from dominant clutter scatterers as residual clutter is present before applying a threshold. The ATI technique on the other hand is robust at zeroing the phase of dominant stationary scatterers (like corner reflectors).

The clutter phase zeroing of the ATI technique is sensitive to non-stationary clutter that is caused by movement of the tree leaves, branches and the bushes. The DPCA technique, on the other hand, is able to suppress the non-stationary clutter well below the set threshold and indicate the moving target with less false alarms. Channel balancing and co-registration errors affect both the techniques when it comes to target detections with less false alarms, however, the resulting phase of the ATI technique is more sensitive to co-registration errors which is compounded by non-stationary clutter and noise. Similar results were obtained in [10] and in [19]. In terms of moving target detection within clutter and noise with less false alarms, the DPCA technique is superior to the ATI technique.

Improved results were obtained in [10] and in [19] when a double threshold approach was used whereby the DPCA and the ATI technique were combined and used to indicate ground moving targets. The double threshold approach is applied on the measured radar data and analysed in the following section.

## **8.5 GMTI using DPCA and ATI Techniques Combined**

The DPCA technique as well as the ATI technique can be combined and used to indicate ground moving targets. Combining this two techniques is known as the double threshold approach [19]. The double threshold detection approach involves a phase threshold from the ATI technique and a magnitude threshold from the DPCA technique. For a detection to be declared as a true target detection, it has to be above both the phase threshold and the magnitude threshold. The pixel that does not pass both the threshold is ignored [19]. This approach was proposed in [19] to improve the probability of detection and decrease the probability of false alarm for the ATI technique since pixels dominated by noise will typically be rejected by the DPCA magnitude threshold.

### 8.5.1 Scenario 1 Pulse No. 12000: Target moving west, parallel and opposite direction to the radar

Figure 8.33 shows an interferogram of a target moving west (target 2) at pulse number 12000. A phase only threshold of 1.6 radians was applied to the interferogram in Figure 8.33 and one can observe that the phase of the moving target is not clearly distinguished from that of non-stationary clutter and noise pixels.

Applying the double threshold approach with the DPCA threshold of 62 dBm to the same data with a target moving west (target 2) results in the phase image presented in Figure 8.34. It can be seen that the phase of noise and non-stationary clutter is ignored and only the phase of the pixel that passes the magnitude threshold obtained from DPCA and the phase threshold from ATI is indicated. Hence the false alarm rate of the ATI technique is reduced.

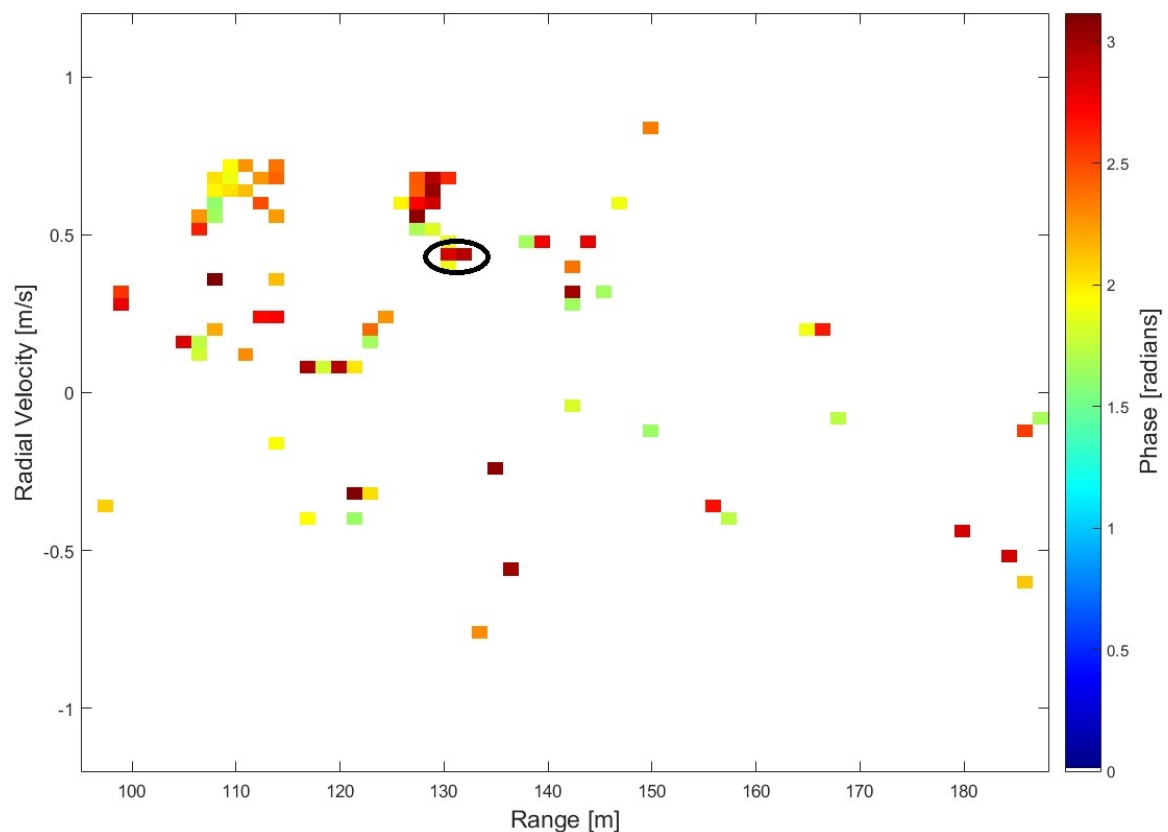


Figure 8.33: Phase image of a target moving west with a phase threshold.

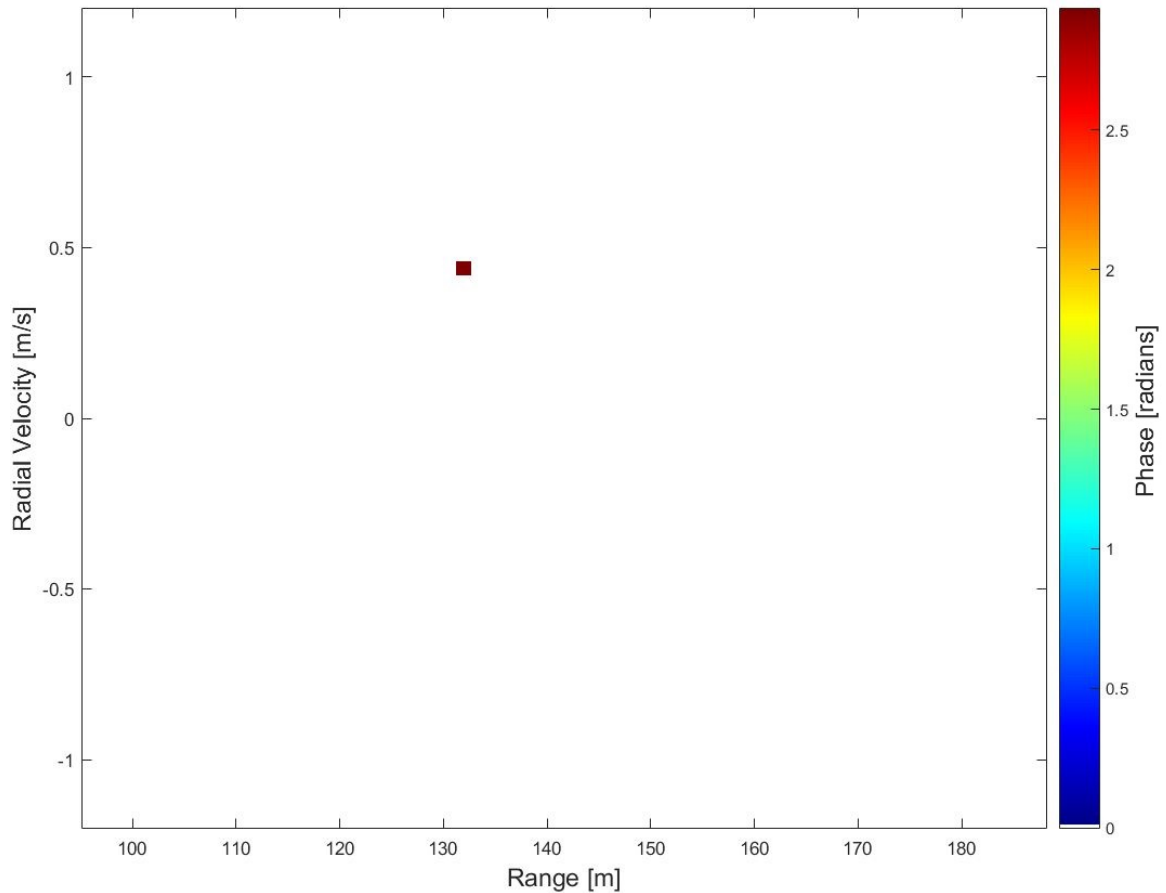


Figure 8.34: Phase image of a target moving west after applying double threshold.

### 8.5.2 Scenario 1 Pulse No. 24200: Target moving west, parallel and opposite direction to the radar

The phase image of a target moving west (target 2) processed from pulse number 24200 is presented in Figure 8.35. A phase threshold of 1.6 radians was applied to this phase image. It is observed from Figure 8.35 that the position of the moving target is not clearly distinguished due to the residual phase after applying the ATI technique.

Applying the double threshold approach reduces the residual clutter and decreases the rate of false alarms for the ATI technique. Figure 8.36 presents the phase image after the double threshold approach with a DPCA threshold of 63 dBm.

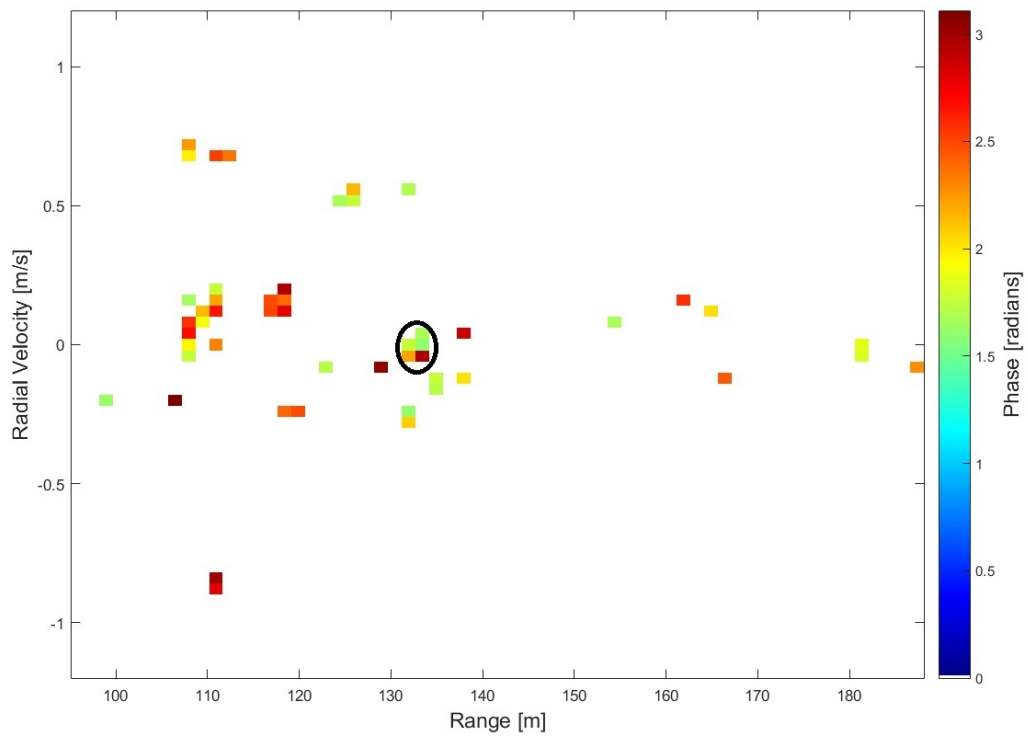


Figure 8.35: Phase image of a target moving west with a phase threshold.

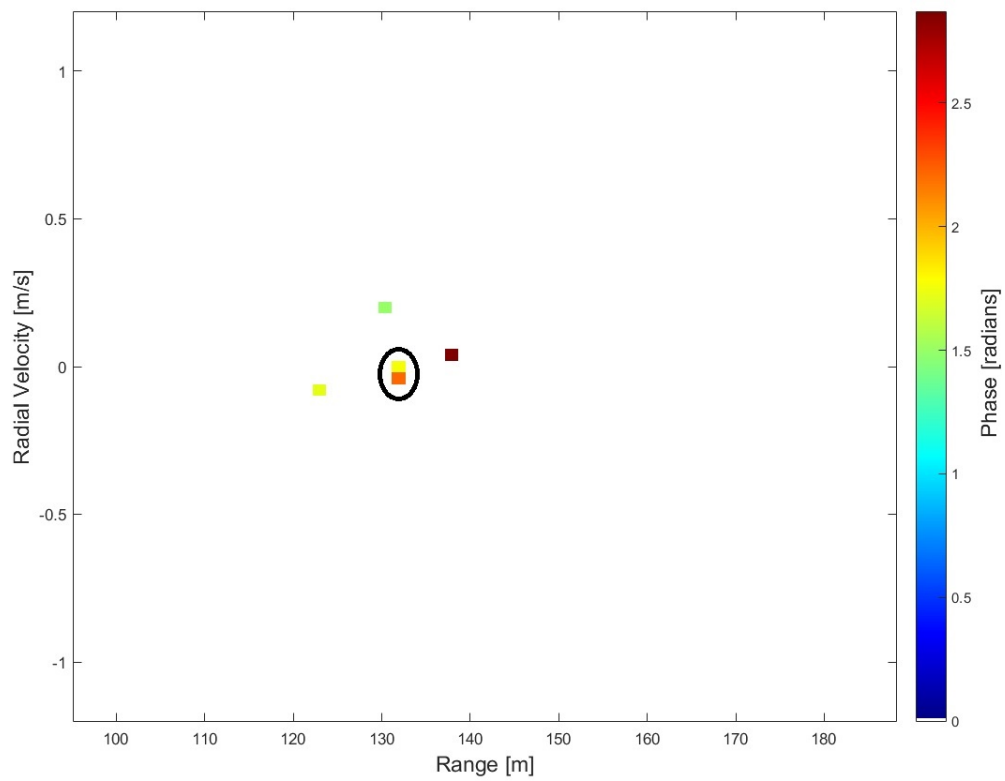


Figure 8.36: Interferogram of a target moving west after double thresholding.

Some residual clutter phase is still present in Figure 8.36 after double thresholding, this is mainly because at this pulse number the target's radial velocity ( $V_{r_{P0}}$ ) is 0.014 m/s which is slow and hence the DPCA technique starts attenuating the target's received power together with that of stationary clutter, so detection is typically missed. However, lowering the DPCA threshold to still detect the moving target allows more stationary clutter and noise through the threshold which increases the false alarm rate. An increased false alarm rate in both the magnitude and phase threshold results in an increased false alarm rate in the double threshold approach. However, the observed false alarm rate when using a double threshold approach is much lower than when using either DPCA or ATI technique alone separately as Figure 8.36 shows.

### 8.5.3 Scenario 2 Pulse No. 2048: Target moving east, parallel and same direction as the radar

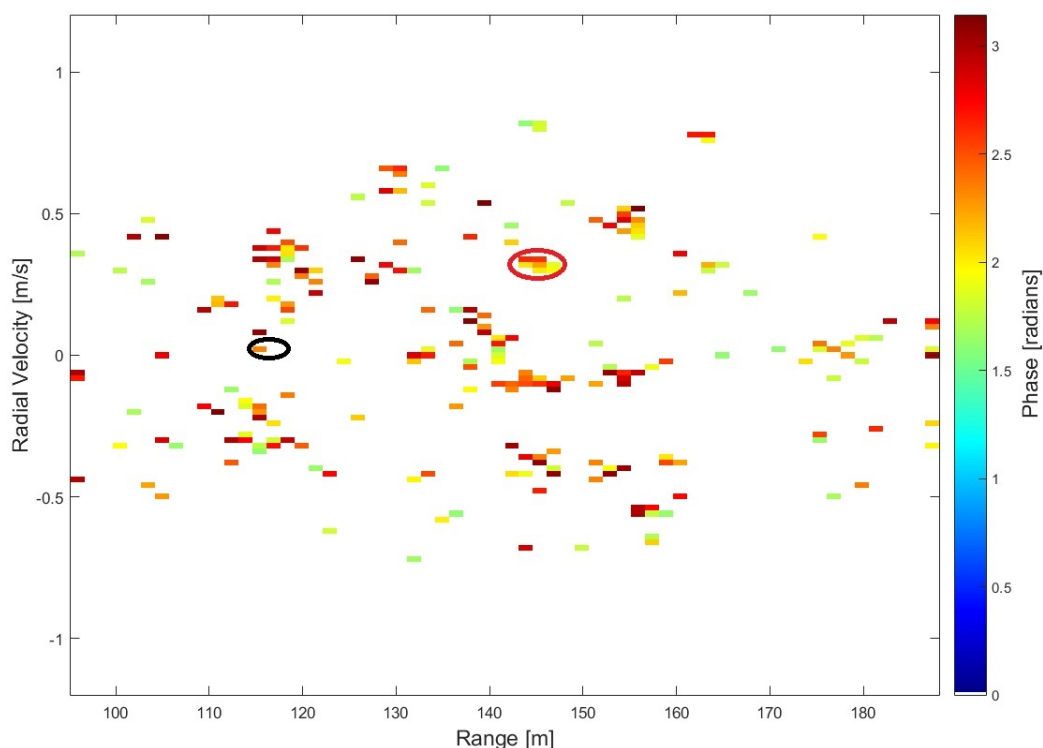


Figure 8.37: Phase image of a target moving east with a phase threshold.

The data recorded with a target moving east, parallel and same direction as the radar (target 1) also had an experimental target walking orthogonal towards the radar

(target 3) without a corner reflector. Figure 8.37 presents the phase image of the two ground moving targets after applying ATI with a threshold of 1.6 radians. The east moving target is circled with black and the orthogonal moving target is circled with red. The residual clutter phase is also present around the moving targets which can trigger the phase threshold.

Figure 8.38 presents the phase image after applying the double threshold approach with a DPCA threshold of 61 dBm. It can be seen that the residual clutter phase have been reduced significantly as compared to the single phase threshold case in Figure 8.37. Hence the double threshold approach reduces the false alarm rate of ATI technique and reduces its sensitivity to non-stationary clutter phase and noise phase.

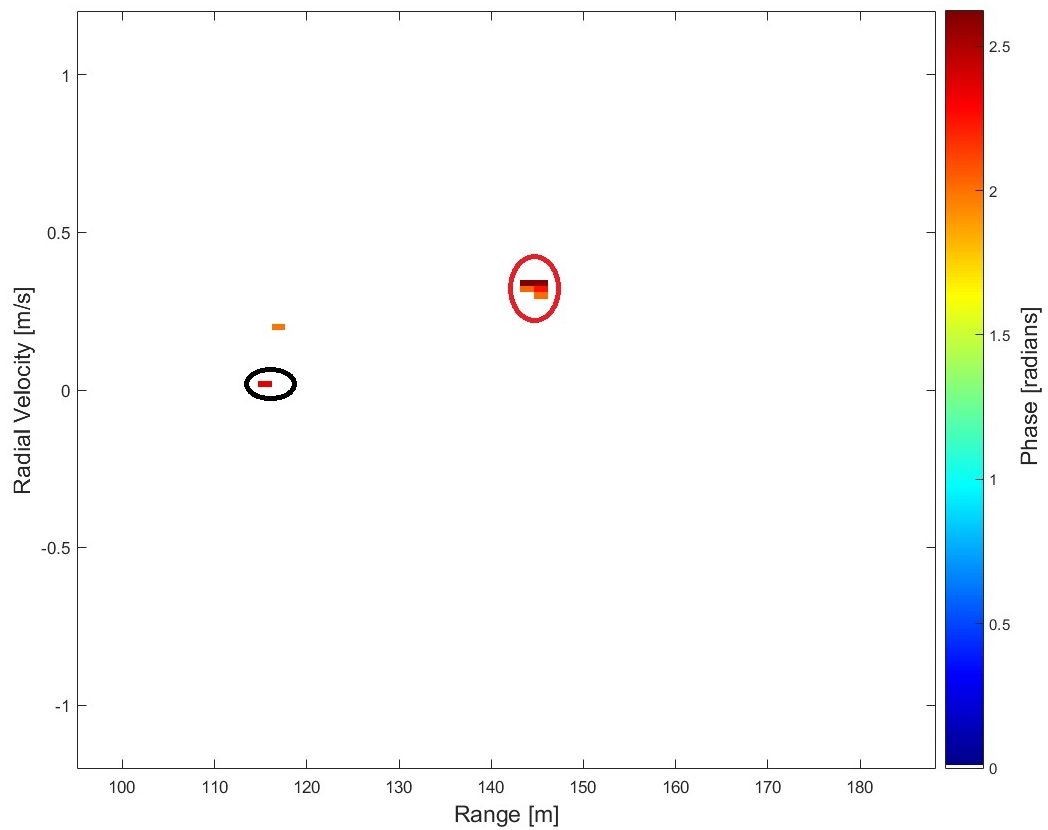


Figure 8.38: Interferogram of a target moving east after double thresholding.

### 8.5.4 Scenario 2 Pulse No. 18000: Target moving east, parallel and same direction as the radar

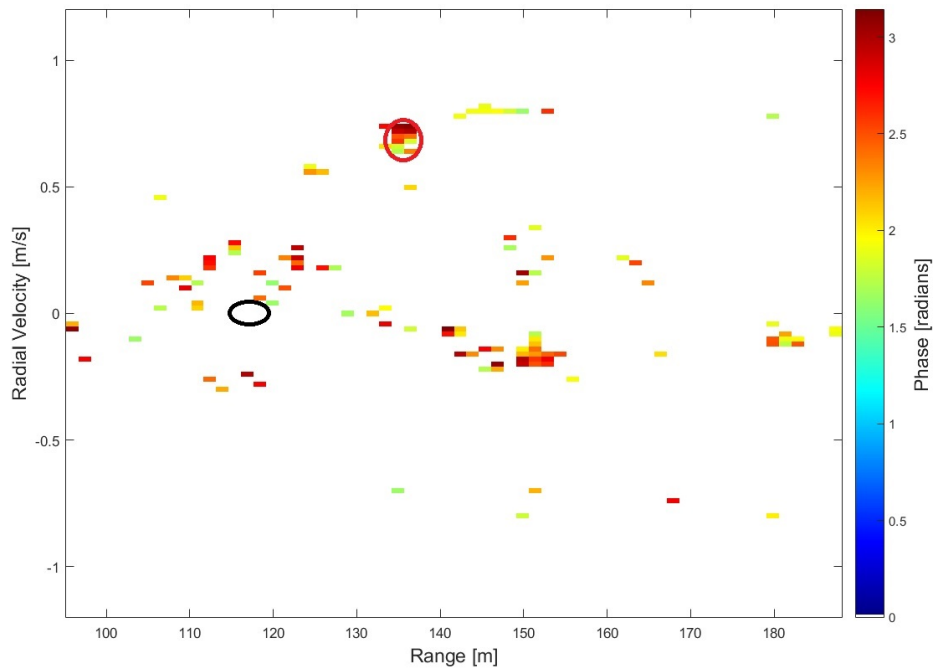


Figure 8.39: Interferogram of a target moving east with a phase threshold.

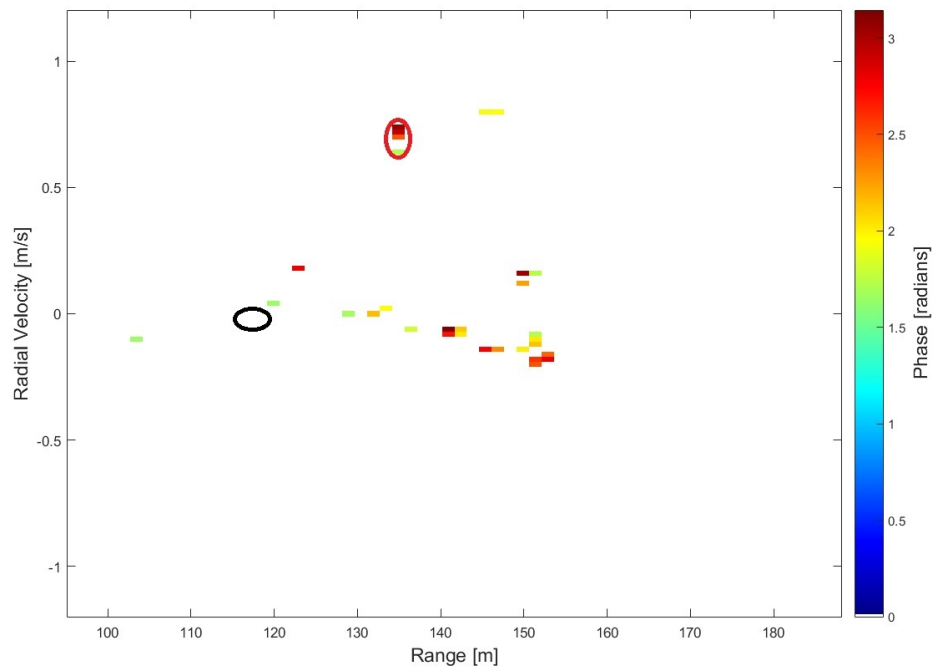


Figure 8.40: Interferogram of a target moving east after double thresholding.

At pulse number 18000, the interferogram of a target moving east and parallel to the radar is presented in Figure 8.39 after applying a phase threshold of 1.6 radians. It is seen that the phase of noise and non-stationary clutter is still present in the interferogram after applying a phase threshold. Applying a double threshold with a DPCA threshold of 54.9 dBm to the interferogram gives the results in Figure 8.40. It is observed that the residual clutter phase is reduced as compared to Figure 8.40 and the orthogonal moving target (target 3) is indicated circled with red while the east moving target (target 1) is cancelled as it did not pass the phase and the magnitude threshold.

## 8.6 Conclusion

The performance of the two selected GMTI techniques were assessed with measured radar data in this chapter. The performance of a double threshold approach which combines the DPCA and the ATI technique was also investigated. The double threshold approach reduced the false alarm rate and detected the moving targets better than DPCA and ATI alone, this is mainly because it uses both the magnitude and phase thresholds for detection. The performance comparison of the DPCA and ATI techniques showed that both the techniques are able to detect and indicate the moving target on measured radar data. However, the obtained results indicated that the DPCA technique alone is robust in performance than the ATI technique alone in terms of indicating moving targets with noise and non-stationary clutter present. The ATI technique is also more sensitive to co-registration errors due to the sensitivity of phase to decorrelation between the channels. The following chapter will summarise and conclude all findings of this study.

# Chapter 9

## Conclusion

In this work, five GMTI techniques were reviewed and investigated in the literature review. The reviewed techniques were DPCA, ATI, IAA algorithm, STAP algorithm and VSAR for GMTI. Two techniques from the five were then implemented and tested with simulated data and measured radar data. The two techniques are DPCA and ATI. A double threshold approach which combines the ATI technique and the DPCA technique was also explored and tested with measured radar data.

The data used to evaluate the performance of the two techniques was simulated using a radar simulator implemented by the CSIR. The simulator only generated raw radar data and the raw radar data were processed into range-Doppler maps in this study. The measured raw radar data were recorded with a C-band FMCW radar in a controlled experiment with known features and also with co-operating ground moving targets. The performance of the techniques on simulated data and on real measured radar were assessed in terms of their ability to indicate moving targets within clutter and noise and their sensitivity to errors in their system setup.

The DPCA technique displayed that it can indicate the presence of moving targets within stationary clutter, non-stationary (fluctuating) clutter and noise. The DPCA technique improved the SCR by more than 8 dB in the measured radar and target scenarios with radial velocity greater than 0.069 m/s. The performance of the ATI technique deteriorated on measured radar data as the technique is sensitive to the phase caused by non-stationary clutter and noise. The ROC curves of both ATI and DPCA on simulated data also displayed that ATI technique is more sensitive to co-registration errors as compared to the DPCA technique. The DPCA technique achieved a Pd of 80.04% while ATI achieved a Pd of 34.53% for the same Pfa of 0.1517. This leads to the conclusion that the DPCA technique alone is a better practical choice in terms of indicating moving targets within clutter with minimum

false alarms and it is also less sensitive to co-registration errors than the ATI technique. The double threshold approach detected ground moving targets with less false alarms than DPCA and ATI alone on measured radar data and it also showed that it is less affected by noise and non-stationary clutter than DPCA and ATI alone. Hence the double threshold approach is more robust than both ATI and DPCA techniques on their own in terms of moving target indication within clutter and noise.

# References

- [1] M. A. Richards, J. A. Scheer, W. A. Holm. *Principles of Modern Radar, Vol. I: Basic Principles*. SciTech Publishing, Edison, NJ. 2010.
- [2] G. A. Akers. *An Approach To Ground Moving Target Indication Using Multiple Resolutions of Multilook Synthetic Aperture Radar Images*. Ph.D dissertation, Electrical Engineering and Computer Science Graduate Faculty, University of Kansas, Kansas, 2010. Accessed on: June 13, 2019. Available: <http://hdl.handle.net/1808/5665>.
- [3] B. G. Avilasha, H. V. Srinivasa Gowda. Class Lecture, Topic: *Military Radar*. Department of Mechanical Engineering, A.P.S. College of Engineering, Bangalore, India, April 2015.
- [4] C. Wolff. *Radar Basics*. November 1998, Accessed on: 10 January 2018. [Online]. Available: <http://www.radartutorial.eu/index.en.html>
- [5] W. L. Melvin, J. A. Scheer. *Principles of Modern Radar, Vol. II: Advanced Techniques*. SciTech Publishing, Edison, NJ. 2013.
- [6] C. Noviello. *Techniques for Inverse Synthetic Aperture Radar Imaging and monitoring of Deformation with Differential Interferometric Synthetic Aperture Radar*. Ph.D dissertation, Department of Electrical Engineering and Information Technologies, University of Naples Federico II, Italy, 2015. Accessed on: January, 2018. [Online]. Available: <https://www.semanticscholar.org/paper/Techniques-for-Inverse-Synthetic-Aperture-Radar-and-Noviello/2fc2dfbd9c670f9535fb3e191943b385dd0b191d>
- [7] K. Jing, J. Xu, Z. Huang, D. Yao, T. Long. *GMTI for Squint Looking XTI-SAR with Rotatable Forward-Looking Array*. Sensors (Basel), Vol. 16, No. 6, June 2016.
- [8] M. Anees *Joint Direct Attack Munition (JDAM), Modern Warfare*. Indian Defence, April 2015. Accessed on: 20 January 2018. [Online]. Available: <http://indiandefence.com/threads/joint-direct-attack-munition-jdam.54264/>

- [9] A. Bacci, M. Martorella, D. A. Gray, S. Gelli, F. Berizzi. *Virtual Multichannel SAR for Ground Moving Target Imaging*. IET Radar, Sonar and Navigation, Vol. 10, No. 1, pp. 50-62, January 2016.
- [10] R. Deming, M. Best, S. Farrell. *Simultaneous SAR and GMTI using ATI/DPCA*. Proceedings of SPIE - The International Society for Optical Engineering, Vol. 9093 90930U 1-19. June 2014.
- [11] W. L. Melvin, J. A. Scheer. *Principles of Modern Radar, Vol. III: Radar Applications*. SciTech Publishing, Edison, NJ. 2014.
- [12] J. Xu, Z. Huang, L. Yan, X. Zhou, F. Zhang, T. Long. *SAR Ground Moving Target Indication Based on Relative Residue of DPCA Processing*. Sensors (Basel), Vol. 16, No. 10, October 2016.
- [13] M. A. Hasan. *Blind Speed Elimination for Dual Displaced Phase Center Antenna Radar Processor Mounted on a Moving Platform*. Patent Number: 4,885,590. General Electric Company, Moorestown, NJ. 5 December 1989.
- [14] M. A. Richards, Class Lecture, Topic: *Space-Based Radar: Introduction to Synthetic Aperture Radar*. School of Electrical and Computer Engineering, Georgia Institute of Technology, Atlanta, Georgia, 2014.
- [15] Y. Hou, J. Wang, X. Liu, K. Wang, Y. Gao. *An Automatic SAR-GMTI Algorithm Based on DPCA*. IEEE Geoscience and Remote Sensing Symposium, Quebec City Canada, pp. 592-595, July 2014.
- [16] E. Chapin, C. W. Chen. *Airborne Along-Track Interferometry for GMTI*. IEEE Aerospace and Electronic Systems Magazine, Vol. 24, No. 5, pp. 13-18, May 2009.
- [17] P. A. Hwang, J. V. Toporkov, M. A. Sletten, S. P. Menk. *Mapping Surface Currents and Waves with Interferometric Synthetic Aperture Radar in Coastal Waters: Observations of Wave Breaking in Swell-Dominant Conditions*. Journal of Physical Oceanography, Vol. 43, No. 3, pp. 563-582, March 2012.
- [18] J. H. G. Ender. *Space-Time Processing for Multichannel Synthetic Aperture Radar*. Electronics and Communication Engineering Journal, Vol. 11, No. 1, pp. 29-38, February 1999.
- [19] Y. Zhang. *Along-Track Interferometry Synthetic Aperture Radar Techniques for Ground Moving Target Detection*. Air Force Research Laboratory, Sensors Directorate, Rome Research Site, Rome. January 2006.

- [20] P. G. Richardson. *Analysis of the Adaptive Space Time Processing Technique for Airborne Radar*. IEEE Proceedings - Radar, Sonar and Navigation, Vol. 141, No. 4, pp. 187-195, August 1994.
- [21] J. Ward. *Space Time Adaptive Processing for Airborne Radar*. 1995 International Conference on Acoustics, Speech, and Signal Processing, Detroit MI, USA, pp. 2809-2812.
- [22] L. E. Brennan, L. S. Reed. *Theory of Adaptive Radar*. IEEE Transactions on Aerospace and Electronic Systems, Vol. AES-9, No. 2, pp. 237-252, March 1973.
- [23] W. Brgrer. *Space-Time Adaptive Processing: Fundamentals*. Advanced Radar Signal and Data Processing, Paper 6, Neuilly-sur-Seine France: RTO, pp. 1-14, 2006.
- [24] T. Yardibi, J. Li, P. Stoica, M. Xue, A. B. Baggeroer. *Source Localization and Sensing: A Nonparametric Iterative Adaptive Approach Based on Weighted Least Squares*. IEEE Transactions on Aerospace and Electronic Vol. 46, No. 1, pp. 425-443, January 2010.
- [25] J. Karlsson, W. Rowe, L. Xu, G. Glentis, J. Li. *Fast Missing-Data IAA With Application to Notched Spectrum SAR*. IEEE Transactions on Aerospace and Electronic Systems, Vol. 50, No. 2, pp. 959-971, April 2014.
- [26] W. Rowe, J. Li, P. Stoica. *Sparse Iterative Adaptive Approach with Application to Source Localization*. 2013 5th IEEE International Workshop on Computational Advances in Multi-Sensor Adaptive Processing, St. Martin, France, pp. 196-199.
- [27] J. Wang, P. Wang. *Sidelobe Suppression Algorithm for SAR Imaging Based on Iterative Adaptive Approach*. 2015 IEEE 5th Asia-Pacific Conference on Synthetic Aperture Radar, Singapore, Singapore, pp. 443-446.
- [28] S. Lou, P. Cheng, Z. Wang, J. Wan, K. Xu. *Moving Target Indication for Multichannel FMCW SAR via Iterative Adaptive Approach*. Proceedings of EUSAR 2016: 11th European Conference on Synthetic Aperture Radar, Hamburg, Germany, pp. 471-474.
- [29] B. Guo, D. Vu, L. Xu, M. Xue, J. Li. *Ground Moving Target Indication via Multichannel Airborne SAR*. IEEE Transactions on Geoscience and Remote Sensing, Vol. 49, No. 10, pp. 3753-3764, October 2011.
- [30] Z. Yang, X. Li, H. Wang, W. Jiang. *Adaptive Clutter Suppression Based on Iterative Adaptive Approach for Airborne Radar*. Signal Processing, Vol. 93, No. 12, pp. 3567-3577, December 2013.

- [31] B. Friedlander, B. Porat. *VSAR: a High Resolution Radar System for Detection of Moving Targets*. IEE Proceedings - Radar, Sonar and Navigation. Vol. 144, No. 4, pp. 205-218, August 1997.
- [32] G. Li, J. Xu, Y.-N Peng, X.-G Xia. *Location and Imaging of Moving Targets using Non-uniform Linear Antenna Array SAR*. IEEE Transactions on Aerospace and Electronic Systems, Vol. 43, No. 3, pp. 1214-1220, July 2007.
- [33] G. Li, J. Xu, Y.-N Peng, X.-G Xia. *Moving Target Location and Imaging using Dual-Speed Velocity SAR*. IET Radar, Sonar and Navigation. Vol.1, No. 2, pp. 158-163, April 2007.
- [34] X. Li, X.-G Xia. *Location and Imaging of Elevated Moving Target using Multi-Frequency Velocity SAR with Cross-Track Interferometry*. IEEE Transactions on Aerospace and Electronic Systems, Vol. 47, No. 2, pp. 1203-1212, April 2011.
- [35] R. Berndt, U. Kathree. *DST UAV SAR Simulator User Guide*. Council for Scientific and Industrial Research, Pretoria, Doc No: 5841-SARDSTTCCBI-10005 GID Rev. 1, February 2016.
- [36] M. C. Garthwaite, M. Thankappan, M. L. Williams, S. Nancarrow , J. Dawson. *Corner Reflectors for the Australian Geophysical Observing System and Support for Calibration of Satellite-Borne Synthetic Aperture Radars*. 2013 IEEE International Geoscience and Remote Sensing Symposium - IGARSS, Melbourne, VIC, Australia, pp. 266-269.
- [37] A. W. Doerry, D. L. Bickel. *Measuring Balance Across Multiple Radar Receiver Channels*. Sandia National Laboratories, Albuquerque, New Mexico, SAND2018-3068, NM 87185-0519, March 2018.
- [38] C. H. Gierull. *Digital Channel Balancing of Along-Track Interferometric SAR Data*. Defence Research and Development Canada, Ottawa, Technical Memorandum, March 2003.
- [39] H. Yan, R. Y. Wang, C. Gao, Y. B. Liu, M. Zheng, Y. Deng. *Channel Balancing Algorithm in Multichannel Wide-Area Surveillance Systems*. IET Radar, Sonar and Navigation, Vol. 8, No. 1, pp. 27-36, June 2013.
- [40] D. Haitao, Z. Changyao. *A Real-Time Signal Processing Method for Air-born Three-Channels GMTI*. 2007 1st Asian and Pacific Conference on Synthetic Aperture Radar, Huangshan, China, pp. 262-265.

- [41] J. H. G. Ender. *The Airborne Experimental Multi-Channel SAR System AER-II*. European conference, Synthetic Aperture Radar: EUSAR'96, Konigswinter, Germany, pp. 49-52, 1996.
- [42] E. Makhoul, S. V. Baumgartner, M. Jger, A. Broquetas. *Multichannel SAR-GMTI in Maritime Scenarios with F-SAR and TerraSAR-X Sensors*. IEEE Journal of Selected Topics in Applied Earth Observations and Remote Sensing, Vol.8, No.11, pp. 5052-5067, November 2015.
- [43] S. Chiu, C. Livingstone. *A Comparison of Displaced Phase Centre Antenna and Along-Track Interferometry Techniques for RADARSAT-2 Ground Moving Target Indication*. Canadian Journal of Remote Sensing, Vol. 31, No. 1, pp. 37-51, 2005.
- [44] H. A. Zebker, J. Villasenor. *Decorrelation in Interferometric Radar Echoes*. IEEE Transactions on Geoscience and Remote Sensing, Vol. 30, No. 5, pp. 950-959, September 1992.
- [45] D. J. Coe, R. G. White. *Moving Target Detection in SAR Imagery: Experimental Results*. Proceedings International Radar Conference, Alexandria, VA, USA, pp. 644-649, May 1995.